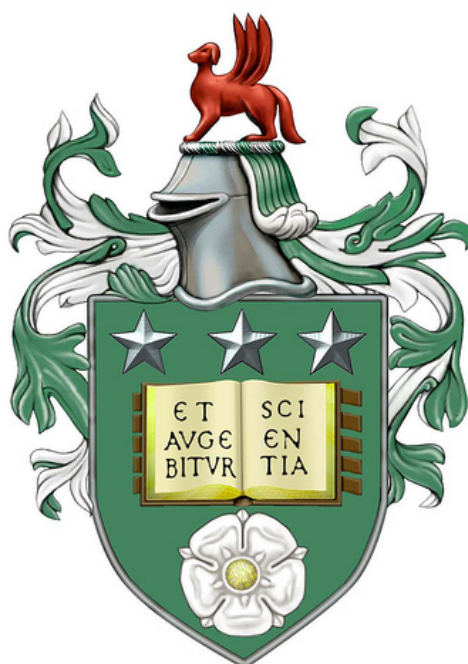


Femtosecond transient absorption to reveal spectroscopically dark dynamic processes



Ingvar Tobias Kraatz

School of Chemistry

University of Leeds

Submitted in accordance with the requirements for the degree of
Doctor of Philosophy

February 2016

To my parents

Declaration

The candidate confirms that the work submitted is his own, except where work which has formed part of jointly authored publications has been included. The contribution of the candidate and the other authors to this work has been explicitly indicated below. The candidate confirms that appropriate credit has been given within the thesis where reference has been made to the work of others.

The work in Chapter 4 of the thesis has appeared in publication as follows:

'Sub-Bandgap Emission and Intraband Defect-Related Excited State Dynamics in Colloidal CuInS₂/ZnS Quantum Dots Revealed by Femtosecond Pump-Dump-Probe Spectroscopy' by Ingvar T. Kraatz, Matthew Booth, Benjamin J. Whitaker, Michael G.D. Nix, and Kevin Critchley in *J. Phys. Chem. C*, 2014, 118 (41), pp 2410224109

I was responsible for the time resolved experiments and data analysis. Matthew Booth was responsible for the synthesis and characterisation of the quantum dots. The contribution of all authors were attributed to data interpretation and manuscript editing.

This copy has been supplied on the understanding that it is copyright material and that no quotation from the thesis may be published without proper acknowledgement.

© 2016 The University of Leeds and Ingvar Tobias Kraatz

The right of Ingvar Tobias Kraatz to be identified as Author of this work has been asserted by him in accordance with the Copyright, Designs and Patents Act 1988.

Ingvar Tobias Kraatz
February 2016

Acknowledgements

First of all I would like to thank my academic supervisor Prof. Ben J. Whitaker and my former supervisor Dr Michael G. D. Nix for their continued and always welcomed support with my research and studies. It has truly been a pleasure and an honour to undertake my PhD at the University of Leeds. I would like to extend a special thanks to Dr Michael Nix, as he still offered advice after he had left the University of Leeds and for offering me the PhD position in the first place.

My thanks also goes to the kind and helpful people that studied alongside me in the Leeds group. I wish Dr Kiera Jones, Dr Alan Sage, Jadwiga Milkiewicz, Dr Manuel Schneider, Khalid M Siddiqui, Michael Horbury and the whole Atmospheric Chemistry group all the best for the future and thank them for the excellent shared time in the laboratory. Also I would like to thank Dr Dmitry Shalashilin and his group, especially Dr Kenichiro Saita for his support with the ab-initio calculations and Christopher Symonds for his help with so many scripts that make life so much easier.

I would like to thank the many great scientists I undertook collaborations with. My thank goes especially to Dr Tolga Karsili, Barbara Marchetti and Prof Michael Ashfold at the University of Bristol and Dr Matthew Booth and Dr Kevin Critchley of the University of Leeds Physics Department.

Also I would like to express my gratitude to my personal tutor Dr Julie Fisher for her continued support, also throughout my undergraduate degree at the University of Leeds, who has sadly passed away too soon.

I am also indebted to the Engineering and Physical Science Research Council (EPSRC), who have kindly provided funding for my PhD work. Without their support I wouldn't have been able to undertake the research in this thesis.

And last but not least I would like to thank my family and friends, who have been very supportive during the whole PhD and have seen me carry it through to the end. A special thanks goes out to Sarah Hinton for her time, editing and helpful comments and my fiancée Sophie Jueterbock for the endless support she has offered.

Abstract

A femtosecond transient absorption spectrometer has been constructed and was used to investigate the carrier dynamics in CuInS₂/ZnS quantum dots and the excited state dynamics of pyrrole, 2-ethylpyrrole and pyrrole-2-carboxaldehyde in a wide excitation range. The time evolution of absorbing population was probed between 320 nm to 1070 nm.

N-H bond fission was observed in pyrrole and its derivatives upon accessing the $1^1\pi\sigma^*$ state. The onset for N-H bond fission in pyrrole-2-carboxaldehyde was determined to be at 222 nm for both the solution phase (ethanol) and experiments conducted in the gas phase with H (Rydberg) atom photofragment translational spectroscopy (PTS). Excitation below the $1^1\pi\sigma^*$ onset in pyrrole-2-carboxaldehyde resulted in triplet state formation with time constants of 2 ps and 4 ps. The observed onset for N-H fission in pyrrole and 2-ethylpyrrole in ethanol solution coincided with the N-H bond fission observed in gas phase studies [23, 48]. Contrary to the H atom PTS data [23, 48], but in agreement with recent dynamics calculations [69, 98], the molecular radical co-fragments (pyrrolyl, 2-ethylpyrrolyl) indicate the formation of electronically excited radical fragments in the $D_1(B_1)$ state. Spectral signatures were assigned to the radical co-fragments and a decay time constant of 1.2 ps (pyrrolyl) and 2.5 ps (2-ethylpyrrolyl) was determined that correspond to the population flow out of the excited radical state into the radical ground state $D_0(A_2)$ state via a conical intersection.

Femtosecond transient absorption and pump-dump-probe spectroscopy was used to follow the carrier dynamics in CuInS₂/ZnS quantum dots (suspended in n-hexane). Evidence is provided that the long-lived photoluminescence is originating from a high-lying intraband donor state. Three time constants were extracted: a 0.5 ps component marking the filling time of the emitting sub-bandgap state, a 1.8 ps time constant associated to the de-excitation via surface sites and a longer 27 ps decay component assigned to Auger recombination.

Contents

Contents	xi
List of Figures	xv
List of Tables	xix
Nomenclature	xxiii
1 Introduction	1
2 Theory	5
2.1 Ultrashort laser pulses	5
2.1.1 Time Domain	6
2.1.2 Frequency Domain	8
2.1.3 Spectral Phase	8
2.2 Nonlinear Optical Interaction	10
2.2.1 Second-order Nonlinear Processes	11
2.2.2 Third-order Nonlinear Processes	12
2.3 Potential Energy Surface	14
2.3.1 Born-Oppenheimer approximation	14
2.3.2 Franck-Condon Principle	15
2.4 Femtosecond Transient Absorption Spectroscopy	17
3 Experimental	21
3.1 Experimental Techniques	21
3.1.1 Femtosecond Transient Absorption Spectroscopy	21
3.1.2 Ultrashort Laser Pulse Characterisation	23
3.1.3 H atom Phototranslational Spectroscopy	26
3.2 Experimental Components	28
3.2.1 Clark-MXR CPA-2110	28

3.2.2	Clark-MXR NOPA	28
3.2.3	TOPAS white and TOPAS-SHG	30
3.2.4	White Light Generation	31
3.2.5	Sample and Detection Scheme	33
3.2.6	Data Acquisition Processing (LabView)	34
4	Excited State Dynamics in CuInS₂/ZnS Quantum Dots	39
4.1	Introduction	39
4.2	Method Development	46
4.2.1	Extension of Probe Continuum to the Infra-Red	46
4.2.2	Pump-Dump-Probe Scheme	47
4.2.3	Sample Preparation	48
4.3	Results and Analysis	49
4.3.1	Quantum Dot Characterisation	49
4.3.2	Femtosecond Transient Absorption Spectroscopy	50
4.3.3	Pump-Dump-Probe Experiments	58
4.4	Conclusion	62
5	Excited State Dynamics of Pyrrole-2-carboxylaldehyde	63
5.1	Introduction	63
5.2	Methodology: Experimental Details, Method Development, Computational Details	65
5.2.1	Transient absorption spectroscopy	65
5.2.2	Extension of Probe Continuum to the Ultra-Violet	65
5.2.3	'Deep'-UV Pump with Sum-Frequency Mixing	66
5.2.4	H atom photofragment translational spectroscopy (H atom PTS)	66
5.2.5	Computational Details	68
5.3	Results	69
5.3.1	Excited State Dynamics in the range 315-225 nm	70
5.3.2	Excited State Dynamics $\lambda < 223$ nm	73
5.3.3	Ab-initio Results	75
5.4	Discussion	79
5.5	Conclusion	91
	Appendix A Tables for Chapter 5	95

6	$\pi\sigma^*$ mediated Photodissociation in Pyrrole and 2-Ethylpyrrole derivatives	99
6.1	Introduction	99
6.2	Methodology: Experiment, Computational Details	103
6.2.1	Sample Preparation	104
6.2.2	Computational Details	104
6.3	Pyrrole	105
6.3.1	Results: fs-Transient Absorption	105
6.3.2	Results: Computational	108
6.4	2-Ethylpyrrole	109
6.4.1	Results: UV Absorption Spectrum	110
6.4.2	Results: fs-Transient Absorption	113
6.4.3	Results: Computational	116
6.5	Discussion	120
6.5.1	Excitation into the S_1 of 2-Ethylpyrrole	122
6.5.2	Excitation above the $S_1(\pi\sigma^*)$ minimum	124
6.6	Conclusion	132
7	Concluding Remarks	135
	References	137

List of Figures

1.1	Common Non-Radiative Intramolecular Photophysical Processes: Internal Conversion (IC), Intersystem Crossing (ISC), Internal Vibrational Relaxation (IVR)	2
2.1	Electric Field, real amplitude and intensity of a Gaussian pulse with constant phase $\phi(t) = 0$	7
2.2	Gaussian-intensity pulse with positive and negative linear chirp	10
2.3	Schematic of the Franck-Condon Principle	16
2.4	General Spectral Features in Transient Absorption Spectroscopy together with Feynman time-line diagrams	19
3.1	Schematic of the Optical Bench showing the fs-Transient Absorption Setup	22
3.2	Second Harmonic Generation - FROG	24
3.3	Pulse Front Tilt Characterisation with SHG-FROG	24
3.4	Polarisation Gating - FROG	25
3.5	H atom Phototranslational Spectroscopy (schematic setup)	26
3.6	H atom Rydberg Tagging Scheme in PTS	27
3.7	Co-linear vs. Non-Colinear Optical Parametric Amplification	29
3.8	Photography of the Clark-MXR NOPA with Components	30
3.9	Schematic of the TOPAS-white with Pulse Shaper and Compressor Unit	31
3.10	Schematic of the main components in the White Light Generation Step	32
3.11	Principle of Temporal Focus in the Generation Step of a White Light Continuum	33
3.12	Flow Chart of the TA Data Acquisition Procedure in LabView	35
3.13	Flow Chart of the LabView Processing component of the Acquisition Procedure	36
3.14	Flow Chart of the LabView De-Glitching routine of the Acquisition Procedure	37

4.1	Unit Cell of a chalcopyrite lattice	42
4.2	Schematic energy level diagram for CIS/CdS and CIS core QD as given by the Klimov group in Li et al. [63].	44
4.3	Schematic energy level diagram for CIS and CIS core QD as given in Nam et al. [77].	45
4.4	Schematic components in the IR-WLC Generation	47
4.5	Pulse Sequence in PDP-Scheme	48
4.6	UV/Vis (black line) and PL (red line) spectra of CIS/ZnS QDs dispersed in hexane.	49
4.7	PL spectra (a) of CIS/ZnS QDs (black) and CIS core (red). TEM (b-e) of CIS/ZnS QDs.	50
4.8	TA spectrum of CIS/ZnS QDs over the first 20 ps after excitation at 540 nm	51
4.9	TA data with spectral cut (at ~ 1 ps) of CIS/ZnS QDs acquired with varying excitation wavelength and pump intensity.	52
4.10	Spectral cuts (at ~ 10 ps) of CIS/ZnS QDs acquired with varying excitation wavelengths and pump intensities.	53
4.11	Spectral cuts with spectral component fitting (at ~ 1 ps) of CIS/ZnS QDs acquired with varying excitation wavelength and illustration of spectral shift based on overall fitting given in this figure (a-d). Indication of spectral shift (curved red arrow) and reduction in ESA signal (red arrow).	55
4.12	Kinetic cuts (a) at 620 nm (circles) with the blue line representing a bi-exponential fit and at 950 nm (triangles) with the red line representing a tri-exponential fit. b: First 5 ps with normalised data points for the fitted range on a logarithmic scale (620 nm data inverted). c: Kinetics showing initial signal amplitude and final amplitude at 2.8 ns for the 620 nm data. Note the break in the linear time delay axis at 10 ps to logarithmic scale.	56
4.13	Magnification (a) of the first 5 ps of the TA data set ($\lambda = 772$ nm) as shown in figure 4.9(d). Colour scale: ± 5 mOD. Raman bands of the solvent (n-hexane) are also visible at time zero. The line at ~ 772 nm is the result of incomplete scattered light subtraction. Kinetic cuts (b) with fitting at 600 nm, 650 nm and 700 nm. Time zero indicated with a dashed line.	57

4.14	TA spectrum of CIS/ZnS QDs (a) dumped at 772 nm, after 6 ps. The kinetics (b) are analysed at the GSB (blue dots), SE (green squares) and ESA (red triangles) spectral fitting positions, resulting from the analysis in figure 4.9. The temporal position of the dump pulse is indicated (dashed line).	60
4.15	Illustration of the proposed recombination pathways involving the intra-gap defect complexes $[\text{Cu}_{\text{In}}^{2-} + \text{In}_{\text{Cu}}^{2+}]$ and $[\text{In}_{\text{Cu}}^{2+} + 2\text{V}_{\text{Cu}}^+]$ in bulk CIS (left) and quantum-confined CIS/ZnS QDs (right). Solid lines represent proposed radiative transitions and dashed lines represent non-radiative transitions.	61
5.1	Cis and trans pyrrole-2-carboxaldehyde	64
5.2	Schematic of the sum-frequency mixing scheme	67
5.3	UV-vis absorption spectra (normalised) of vapour phase PCA and as solution in ethanol, methanol and water	70
5.4	Averaged transient (a) of PCA (in ethanol solution) excited at 300 nm and corresponding contour plot (b) in the range 365 to 625 nm	71
5.5	Averaged transient (a) of PCA excited at 233 nm and corresponding contour plot (b) in the range 465 to 1050 nm	72
5.6	Selected H atom TKER Spectra at (a) 280 nm, (b) 275 nm, (c) 270 nm, (d) 260 nm, (e) 240 nm and (f) 225 nm	74
5.7	Averaged transient (a) of PCA excited at 222 nm and corresponding contour plot (b) in the range 500 to 1070 nm	75
5.8	Selected TKER Spectra at (a) 225 nm, (b) 220 nm, (c) 218.25 nm . . .	76
5.9	Unrelaxed (rigid body) CASPT2 potential energy curves along R_{NH} for (a) pyrrole and (b) PCA	77
5.10	Absorption spectra of vapour and solution phase PCA with fitting . .	80
5.11	Kinetic Time constants of the TA signal at $\lambda_{\text{probe}} = 400$ nm and 500 nm at a range of excitation wavelengths (λ_{pump})	82
5.12	Possible mechanisms of the ultrafast process in PCA at excitation ≥ 225 nm.	85
5.13	Possible mechanisms of the ultrafast process in PCA at excitation ≥ 225 nm.	88
5.14	TD-DFT orbitals involved in ${}^1A_2 \leftarrow {}^1A_1$ type transition in PCA . . .	90
6.1	Pyrrole in C_{2v} Symmetry in Cartesian Coordinates System	99
6.2	Frontier Orbitals of Pyrrole and the energetically low lying singlet transitions	100
6.3	Absorption Spectrum of Pyrrole (vapour phase)	101

6.4	CASPT2(8/7) Calculations of the first three excited electronic states in Pyrrole	102
6.5	Averaged transient (a) of pyrrole excited at 240 nm and corresponding contour plot (b) in the range 315 to 375 nm	106
6.6	Excited state dynamics over the first 50 ps of pyrrole in ethanol solution excited at 240 nm and probed in the near-IR spectral range between 550 to 1070 nm	107
6.7	Selected 2-Ethylpyrrole Conformers in Cartesian Coordinates System	110
6.8	CASPT2(8/7) Calculations of the first three excited electronic states in 2-Ethylpyrrole and CASSCF(8/7) around the dihedral angle of the 2-Ethylpyrrolyl Radical conical intersection	111
6.9	Comparing the UV Absorption Spectrum of 2-Ethylpyrrole and Pyrrole	112
6.10	Excited state dynamics over the first 6 ps of 2-ethylpyrrole in ethanol solution excited at 243 nm and probe in the UV range	113
6.11	Excited state dynamics over the first 50 ps of 2-ethylpyrrole in ethanol solution excited at 243 nm and probed in the near-IR spectral range between 550 to 1070 nm	115
6.12	Excited state dynamics over the first 50 ps of 2-ethylpyrrole in ethanol solution excited at 267 nm and probed in the near-IR spectral range between 510 to 1070 nm	116
6.13	Frontier Orbitals of 2-Ethylpyrrole and the energetically low-lying singlet transitions	118
6.14	SA4-CASSCF(7/6) Calculations showing cuts through the PESs of the pyrrolyl and 2-ethylpyrrolyl radical	121
6.15	Rydberg (3p) to Rydberg (3d) Absorption in 2-Ethylpyrrole	124
6.16	Possible Population Flow upon S_1 Absorption in 2-Ethylpyrrole and Pyrrole	125
6.17	Diabatic Population Flow from $S^1(A_2)$ to $D^0(A_2)$	127
6.18	Adiabatic Population Flow from $S^1(A_2)$ to $D^1(B_1)$	127
6.19	Population flow from Radical 2B_1 to 2A_2 minimum via Conical Intersection	128

List of Tables

5.1	Vertical excitation energies calculated for pyrrole (C_{2v}) and PCA using the (TD)-B3LYP/aug-cc-pVDZ level of theory.	78
5.2	Vertical excitation energies calculated for pyrrolyl and the pyrrolyl-2-carboxaldehyde radical using the (TD)-B3LYP/aug-cc-pVDZ level of theory.	79
5.3	Comparison of TD-DFT energies and oscillator strength for the isolated and ethanol solvated PCA molecule. Key data points for discussion taken from data tables 5.1 and A.1.	81
5.4	TD-DFT energies for the first four triplet states of PCA in ethanol solution. Key data points for discussion taken from data table A.1. . . .	83
5.5	TD-DFT energies for the triplet-triplet states of PCA in ethanol solution. Key data points for discussion taken from data table A.3.	84
A.1	Vertical excitation energies calculated for pyrrole-2-carboxaldehyde with the polarisation continuum model and explicit solvent molecule using the (TD)-B3LYP/aug-cc-pVDZ level of theory.	96
A.2	Vertical excitation energies calculated for pyrrolyl-2-carboxaldehyde radical (2PCyl) with the polarisation continuum model and additional explicit solvent molecule using the (TD)-B3LYP/aug-cc-pVDZ level of theory.	97
A.3	Vertical excitation energies calculated from the T_1 minimum energy geometries for PCA with the polarisation continuum model and explicit solvent molecule using the (TD)-B3LYP/aug-cc-pVDZ level of theory.	98
6.1	Vertical excitation energies calculated for pyrrole with polarisation continuum model and explicit ethanol molecule using the (TD)-B3LYP/aug-cc-pVDZ level of theory.	108

6.2	Vertical excitation energies calculated for pyrrolyl radical with polarisation continuum model and additional explicit ethanol molecule using the (TD)-B3LYP/aug-cc-pVDZ level of theory.	109
6.3	Vertical excitation energies and oscillator strength calculated for 2-ethylpyrrole and 2-ethylpyrrolyl radical using the (TD)-B3LYP/aug-cc-pVDZ level of theory. Also shown is an un-relaxed scan along the N-H stretch (graphic inset).	117
6.4	Vertical excitation energies calculated for 2-ethylpyrrole and 2-ethylpyrrolyl radical with explicit ethanol molecule and PCM using the (TD)-B3LYP/aug-cc-pVDZ level of theory.	119

Nomenclature

Greek Symbols

- Δ change or difference of a changeable quantity e.g. used in combination with τ or λ
- λ wavelength, spatial period of a wave
- μ SI metric prefix 'micro-' used with a measurable quantity of length
- π electronic orbital of π character
- σ electronic orbital of σ character
- τ duration of time

Acronyms / Abbreviations

- 2-EP 2-ethylpyrrole
- 2PCyl pyrrolyl-2-carboxaldehyde radical
- AC auto-correlator
- B3LYP Becke 3-parameter (exchange), Lee, Yang and Parr (correlation) functional
- BBO β -barium borate
- BOA Born-Oppenheimer approximation
- BS beam splitter
- CAM-B3LYP Coulomb-attenuating method - B3LYP
- CASPT2 complete active space - second order perturbation theory
- CASSCF complete active space self-consistent field

CCD	charge-coupled device
CdS	Cadmium sulfide
CdSe	Cadmium selenide
CPA	chirp pulse amplifier
CuInS ₂ /ZnS	Copper indium sulfide with zinc sulfide shell
CuInS ₂	Copper indium sulfide
DFM	difference frequency mixing
DFT	density functional theory
f	SI time unit prefix 'femto-' used with a measurable quantity of time
FROG	frequency-resolved optical gating
fs-TA	femtosecond Transient Absorption
FSRS	femtosecond stimulated Raman spectroscopy
GDD	group delay dispersion
H	hydrogen
HOMO	highest occupied molecular orbital
IC	internal conversion
IP	ionisation potential
IR	infra-red
ISC	intersystem crossing
IVR	intramolecular vibrational energy redistribution
J	Joule - SI derived unit of energy
KER	kinetic energy release
LUMO	lowest unoccupied molecular orbital
m	meter - SI base unit of length

Nd:YAG neodymium-doped yttrium aluminium garnet

n SI time unit prefix 'nano-' used with a measurable quantity of time

NOPA non-collinear optical parametric amplifier

PCA pyrrole-2-carboxaldehyde

PDP pump-dump-probe

PG-FROG polarisation gating - FROG

PL Photoluminescence

PLQY Photo-luminescent quantum yield

p SI time unit prefix 'pico-' used with a measurable quantity of time

PTS phototranslational spectroscopy

SerF stretched erbium fibre

SFM sum frequency mixing

SHG-FROG second harmonic generation - FROG

SHG second harmonic generation

s second - SI base unit of time

TD-DFT time dependent density functional theory

THG third harmonic generation

TKER total kinetic energy release

TOF time-of-flight

TOPAS-SHG TOPAS - second harmonic generation stage

TOPAS non-collinear optical parametric amplifier by Light Conversion Inc

UNEP UN Environment Programme

UV ultra-violet

WMO World Meteorological Organization

YAG yttrium aluminium garnet

Chapter 1

Introduction

The motivation behind solution phase studies of the excited state dynamics of pyrrole and its derivatives is the interest to reveal ultrafast processes that govern the fate of a molecule after light absorption. Pyrrole is a fundamental building block in many important biological molecules, such as heme or the indole moiety of purine DNA bases, and serves as a benchmark molecule with which to study the photophysics of biological systems. Excited state dynamics have revealed prompt N-H photodissociation of pyrrole and substituted pyrroles in the gas phase [15, 22, 23, 48]. Despite a rising interest in the study of solution phase dynamics of heteroaromatics with several research groups, such as Prof. Stephen E. Bradforth from the University of Southern California and Prof. Andrew J. Orr-Ewing from the University of Bristol, moving towards solution phase studies of heteroaromatic molecules, the effect of solvent environment on the dissociation dynamics of pyrrole, as known from the gas phase, has not been studied.

The main focus in this thesis is set on the study of excited state dynamics of pyrrole and its derivatives in solution phase. Studies are conducted with femtosecond transient absorption spectroscopy that allow to examine the evolution of population in electronically excited states. Femtosecond transient absorption spectroscopy allows to examine many photophysical processes. Once a molecule absorbs light the energy is converted to internal energy and can then be redistributed via intramolecular processes and/or intermolecular energy transfer to surrounding solvent molecules. Besides pyrrole and its derivatives this thesis also reports on the carrier dynamics of CuInS₂/ZnS quantum dots (chapter 4). CuInS₂/ZnS quantum dots are known for their luminescent properties, thus the long-lived states enable the emission of a photon. The energy distribution in this semiconductor material was also probed with transient absorption spectroscopy. Common non-radiative photophysical processes that can be observed with transient ab-

sorption spectroscopy are summarised in figure 1.1.

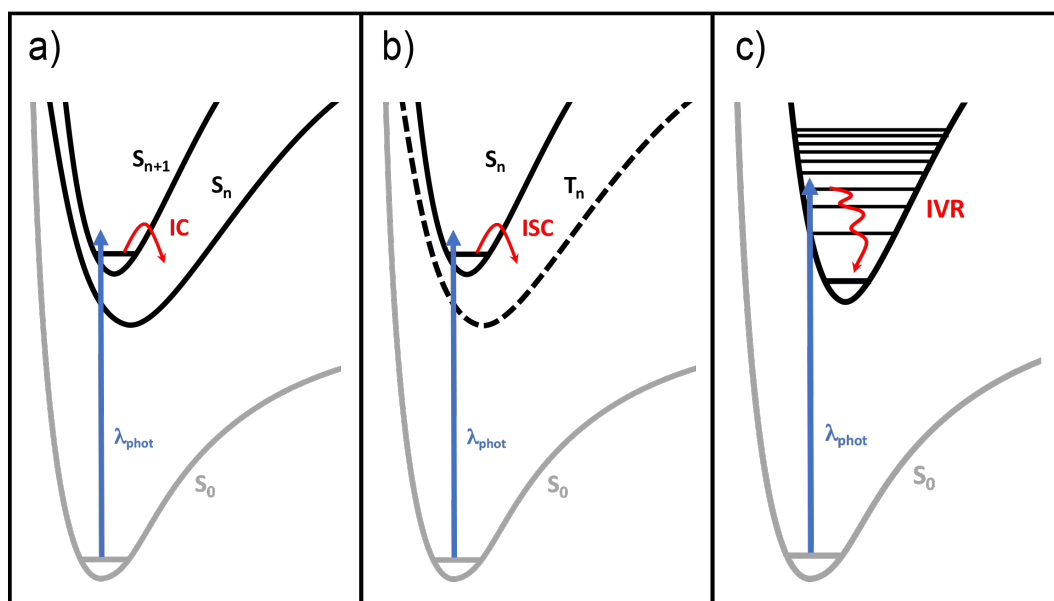


Fig. 1.1 Common Non-Radiative Intramolecular Photophysical Processes: Internal Conversion (IC), Intersystem Crossing (ISC), Internal Vibrational Relaxation (IVR). Singlet states (S_n and S_{n+1}) are radiatively populated (blue arrow) from the ground state (S_0) with λ_{phot} . Non-radiative processes are indicated with red arrows.

Figure 1.1(a) shows the absorption from the singlet electronic ground state (S_0) to the excited S_{n+1} state via promotion with a photon of light (λ_{phot}). The excited singlet state S_{n+1} can undergo internal conversion (IC) to another singlet state S_n (maintaining spin) via redistribution of the internal energy. Absorption from a singlet to a triplet state is unfavourable as the spin is not conserved. So, figure 1.1(b) shows the initial absorption into the singlet state S_n followed by intersystem crossing (ISC) to the triplet state (T_n). The spin is not maintained and thus spin-forbidden, but spin-orbit coupling enables this energy redistribution. Figure 1.1(c) shows the internal vibrational energy redistribution (IVR) within an electronic state by which the excess vibrational energy is gradually redistributed among stable vibrational modes. Shown is the vibrational cooling from the vertical Franck-Condon region to low vibrational states.

The layout of this thesis is such that chapter 2 provides an introduction to ultrashort laser pulses and nonlinear optical interactions to provide the required background information for the optical components used in the femtosecond transient absorption experiments. The theory chapter further touches on potential energy surfaces, the

Born-Oppenheimer approximation and the Franck-Condon principle based on a range of publications [16, 50, 80]. The chapter 3 lists and describes the experimental techniques used together with an explanation of the individual components. Chapter 4 is the product out of a very exciting collaboration with the physics group by Dr. Kevin Critchely from the University of Leeds that extended the work of this thesis by the investigation of the ultrafast energy transfer in CuInS₂/ZnS Quantum Dots. The excited state dynamics of the pyrrole derivative pyrrole-2-carboxaldehyde in solution are provided in chapter 5 and the gas phase photodissociation experiments were conducted together with Dr. Tolga Karsili and Barbara Marchetti as a collaboration with the group by Prof. Michael Ashfold. The chapter 6 is concerned with the excited state dynamics of pyrrole and 2-ethylpyrrole and investigates, whether the gas phase photodissociation dynamics for pyrrole type molecules persists in solution phase.

Chapter 2

Theory

2.1 Ultrashort laser pulses

The duration of ultrashort laser pulses are of the order of 10^{-12} s (picosecond) to 10^{-15} s (femtosecond). The laser pulses generated in the fs-TA experiments reported in this thesis are as short as 40 fs. The advantage of such a short pulses is that they enable the investigation of extremely fast processes. Regardless, if we are aware of it or not, everyday life is determined by ultrafast processes: photosynthesis, molecular vibrations and excited state-lifetimes are just some of the fundamentally important events on an ultrafast timescale. Hence, being able to create and shape ultrashort laser pulses on demand can then be used to examine biological and chemical reaction dynamics and can provide an insight into ultrafast chemistry and biological processes [79]. The fastest observed molecular vibrations in nature have an oscillation of about 10 fs [117]. This underlines the advantage of ultrashort pulses; not only can extremely fast processes be tracked with their aid, but this can also be done with a very high temporal resolution. Thus, this will allow to investigate excited state dynamics and to fulfil the scope as outlined in chapter 1 that states to investigate and reveal dark relaxation pathways upon electronic excitation.

In general, the more frequency components are contained in one pulse the shorter the pulse can be. This has the advantage that in time-resolved optical spectroscopy such as fs-TA or femtosecond stimulated Raman spectroscopy (FSRS) one pulse of light contains the whole spectrum of necessary frequency components to investigate the spectral changes at a given time. On the other hand there are disadvantages, such as in the experimental setup, where the broad optical bandwidth of an ultrashort pulse leads to chromatic dispersion in refractive materials (e.g. lens), requiring the implementation of correcting devices, post-mathematical correction or working predominantly with

reflective media. In general, the propagation of ultrashort pulses through transparent media can lead to interesting nonlinear processes, which are covered in section 2.2.

The relative phase velocity describes that different frequency components contained within a light pulse travel with different velocities in an optical medium (e.g. air, glass), which results from the refractive index of a medium. This gives rise to a shift of the relative position in time of the frequency components within a pulse, which is known as chirp. Therefore, a pulse needs to be described not only by its amplitude, but also by its phase. In conventional continuous-wave light the electric field is solely described by a sine wave form with constant amplitude, whereas the description of an ultrashort pulse requires the amplitude to vary in time and/or space, which is then called the amplitude envelope of a wave or pulse-envelope function. So, an ultrashort pulse can then be described by the product of a sine wave and a pulse-envelope function. Hence, an ultrashort pulse comprises only a few cycles of a sine wave [109]. As it is possible to define the electric field of a pulse in either the time-domain or the frequency domain, the following two sections provide both forms and the information and derivation of the formula is adopted from Trebino [109]. The conversion between those two domains can be achieved with the Fourier transform or with the inverse Fourier transform, respectively.

2.1.1 Time Domain

The electric field of a pulse is defined as a function of space and time $E(x, y, z, t)$. Here, for simplicity, the polarisation is assumed to be linear, i.e. only one space component of the electric field vector is considered in the equation (scalar wave approximation). This leaves the pulse electric field depending on the temporal component as follows:

$$E(t) = \frac{1}{2} \sqrt{I(t)} e^{i[\omega_0 t - \phi(t)]} + \frac{1}{2} \sqrt{I(t)} e^{-i[\omega_0 t - \phi(t)]}, \quad (2.1)$$

where t is the time in the reference frame of the pulse, $I(t)$ is the time-dependent intensity and $\phi(t)$ is the time-dependent phase of the pulse. The angular carrier frequency (at central wavelength of pulse), which is the rate of change (oscillation) of the phase of the wave, is given by ω_0 . The slowly varying envelope approximation can be used for femtosecond pulses, where the assumption holds that $I(t)$ and $\phi(t)$ vary slowly compared to the rapidly oscillating carrier wave given in equation 2.1. Another assumption, called analytic approximation, is made, where the complex conjugate is ignored and as a consequence just the complex electric field part, $E(t)$, multiplied by

two is left. Taking account of both approximations, equation 2.1 is reduced to

$$E(t) = \sqrt{I(t)}e^{-i\phi(t)}. \quad (2.2)$$

using Euler's formula $e^{-i\phi(t)} = \cos(\phi(t)) - i\sin(\phi(t))$ it can easily be shown that $E(t) = \sqrt{I(t)}e^{-i\phi(t)} = |E(t)|(\cos(\phi(t)) - i\sin(\phi(t)))$; Complex number theory then yields that the intensity $I(t)$ is equal to the square of the modulus of the electric field $E(t)$

$$I(t) = |E(t)|^2. \quad (2.3)$$

Figure 2.1 shows a Gaussian pulse with constant temporal phase, which illustrates the relation between the intensity $I(t)$ and the real amplitude $\sqrt{I(t)}$ of a short pulse given in equation (2.2).

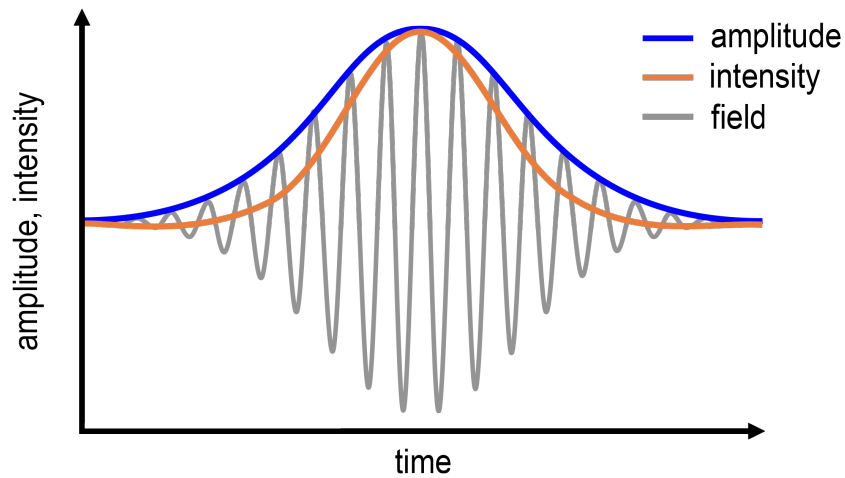


Fig. 2.1 Electric Field, real amplitude and intensity of a Gaussian pulse with constant phase $\phi(t) = 0$. Illustration adopted from Trebino [109]

The complete time-dependent electric field in one dimensional space can be described as follows, using the information above:

$$E(t) = \frac{1}{2}E(t)e^{i\omega t} + \frac{1}{2}E^*(t)e^{-i\omega t} \quad (2.4)$$

2.1.2 Frequency Domain

As already mentioned, the electric field can also be represented in the frequency domain using the Fourier transform of the electric field in the time-domain:

$$E(\omega) = \int_{-\infty}^{\infty} E(t)e^{-i\omega t} dt. \quad (2.5)$$

The inverse Fourier transform is then given by

$$E(t) = \frac{1}{2\pi} \int_{-\infty}^{\infty} E(\omega)e^{-i\omega t} d\omega. \quad (2.6)$$

In analogy to the derivation in section 2.1.1, the spectral intensity is here given by $S(\omega)$ and the spectral phase by $\varphi(\omega)$:

$$E(\omega) = \sqrt{S(\omega)}e^{-i\varphi(\omega)}. \quad (2.7)$$

Then the spectrum is given by

$$S(\omega) = |E(\omega)|^2. \quad (2.8)$$

2.1.3 Spectral Phase

The spectral phase is essential to describe a short pulse and especially its shape. As initially stated, the position of the individual spectral components of a pulse in time can vary, and can be described by the group delay

$$T_{group}(\omega) = \frac{d\varphi}{d\omega}, \quad (2.9)$$

i.e. the chirp of a pulse can be extracted, and in order to extract information about the individual terms contributing to the overall spectral phase $\varphi(\omega)$ it can be resolved into its individual components by writing a Taylor series for $\varphi(\omega)$:

$$\varphi(\omega) = \varphi_0 + \varphi_0^{(1)}(\omega - \omega_0) + \frac{\varphi_0^{(2)}}{2!}(\omega - \omega_0)^2 + \frac{\varphi_0^{(3)}}{3!}(\omega - \omega_0)^3 + \dots + \frac{\varphi_0^{(n)}}{n!}(\omega - \omega_0)^n \quad (2.10)$$

In this power series the absolute phase is $\varphi_0 = \varphi(\omega_0)$ and the higher differential terms are $\varphi_0^{(n)} = \left(\frac{d^n \varphi}{d\omega^n}\right)_{\omega_0}$, in short $\varphi(\omega) = \sum_{n=0}^{\infty} \frac{\varphi_0^{(n)}}{n!}(\omega - \omega_0)^n$.

The first term in the Taylor expansion is the zeroth-order phase term (φ_0), which is also called the absolute phase. The absolute phase needs to be considered in the generation of higher harmonics in nonlinear interactions, when the pulse is so short that only a very few cycles lie within the envelope [74]. The femtosecond pulses considered in this work contain many cycles, so that a change in absolute phase is negligible. The first-order phase term ($\varphi_0^{(1)}$) corresponds to a linear shift in time, when the Fourier transform is applied, i.e. it can lead to a delayed pulse. This shifting property of Fourier transforms also applies for its inverse, and applying it to a linear term in the temporal phase ($\varphi_0^{(1)}$) results in a frequency shift. As shown, the first-order spectral phase affects only the time point, when a pulse 'arrives' and the first-order temporal phase leads to a shift in frequency. Hence, the first order phase does not affect the overall shape of a pulse but leads to a temporal delay or frequency shift [109]. The second-order phase term ($\varphi_0^{(2)}$) is quadratic. Calculating the first derivative using equation 2.5 results in a linear function for the group delay. Hence, the second-order phase is responsible for linear chirp, also called group delay dispersion (GDD). An example of positive linear chirp is shown in figure 2.2a, where the frequency of the electric field increases with time. Similarly, an example for negative linear chirp is given in figure 2.2b. The consequence of positive linear chirp is that it stretches the pulse in time, so the pulse duration is longer. This is a standard effect that is observed, when an ultrashort pulse propagates through a material: the pulse duration increases due to positive chirp. In ultrafast spectroscopy it is usually attempted to compensate for linear chirp with pulse shaping devices or mathematical corrections, as a longer pulse duration leads to a reduced temporal resolution.

As the spectral phase is cubic ($\varphi_0^{(3)}$), the group delay yields a quadratic chirp function. Since materials induce higher-order phase distortions $\varphi_0^{(n)}$, it is once again necessary to correct for such effects, if one desires to create short pulses near the transform limit. Positive quadratic chirp leads to the effect that the central frequency of the pulse arrives first and the other frequency components lag behind.

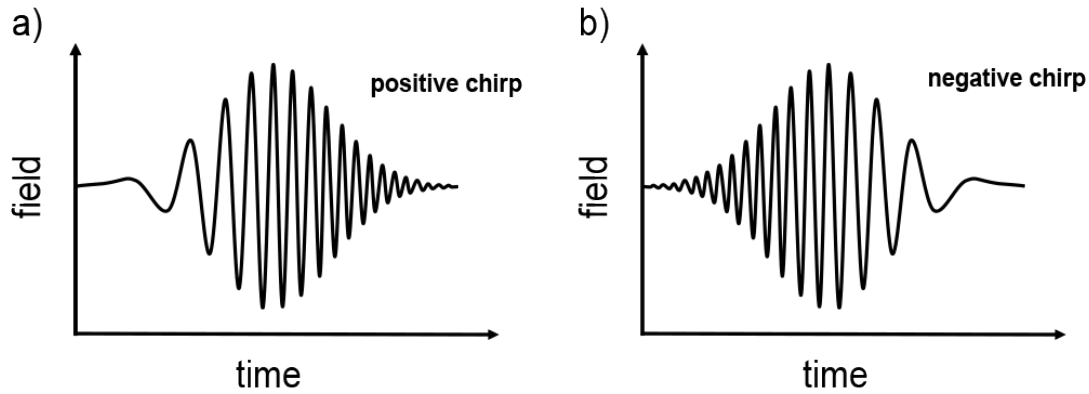


Fig. 2.2 Gaussian-intensity pulse with a) positive and b) negative linear chirp. Illustration adapted from [109]

2.2 Nonlinear Optical Interaction

This chapter provides a brief introduction into the relevant aspects of nonlinear optics that are noteworthy in respect to the experimental framework. The majority of information and formulae are adopted from Traeger et al. [107]. Nonlinear optics is the area of optics that deals with the interaction of light in nonlinear media. This is known as light induced polarisation. Nonlinear effects arise, when the light intensity, for instance, provided by a laser source is sufficient high to modify the optical properties of a material. As a consequence, light waves interact with each other and result in higher-order nonlinear processes such as second order harmonics and optical Kerr effects.

In conventional optics the induced polarisation vector, $\mathbf{P}_L(\omega)$, depends linearly on the electric field vector, $\mathbf{E}(\omega)$, and is described by the following well-known formula in linear optics

$$\mathbf{P}_L(\omega) = \varepsilon_0 \chi_{ij}^{(1)} \mathbf{E}(\omega) \quad (2.11)$$

This describes a linear response between the polarisation and the electric field. It applies to weak electric fields only. The electric permittivity of free space, ε_0 , and the dimensionless electric susceptibility tensor, $\chi_{ij}^{(1)}$, provide the proportionality relation between the polarisation vector and the electric field vector. The j and i element of the susceptibility stands for the incident and the created electric field each in the direction of the three Cartesian coordinates. The order of the second rank tensor is first order (linear) and is given in brackets. In practical terms, the linear susceptibility tensor can

be used to extract information about the refractive index and absorption properties of a material.

The polarisation vector can be derived as a power-series for the nonlinear processes of higher order that are relevant at higher electric field strength

$$\mathbf{P}_{NL}(\omega) = \epsilon_0 \chi^{(2)} \mathbf{E}^{(2)}(\omega) + \epsilon_0 \chi^{(3)} \mathbf{E}^{(3)}(\omega) + \dots + \epsilon_0 \chi^{(n)} \mathbf{E}^{(n)}(\omega) \quad (2.12)$$

or equivalently

$$\mathbf{P}_{NL}(\omega) = \mathbf{P}^{(2)} + \mathbf{P}^{(3)} + \dots + \mathbf{P}^{(n)} \quad (2.13)$$

The second-order, third-order and higher-order nonlinear susceptibilities in equation 2.12 are responsible for the observed nonlinear processes during the interaction of light with matter at high electric field strength. This is understandable considering that the newly created field depends on the incident electric fields interaction with a molecule, which polarises the molecule i.e. the molecule experiences a distortion in its electronic charge distribution. The degree of this interaction is determined by the differential Raman-cross section of a molecule, which in turn is directly related to the nonlinear susceptibility tensor by density matrix calculations [5, 59]. So, the origin of the observed nonlinear-optical phenomena is comprised of the nature of the nonlinear susceptibilities.

The following subsections explain some of the nonlinear-optical phenomena that can be observed in ultrafast laser spectroscopy in more detail.

2.2.1 Second-order Nonlinear Processes

The second-order nonlinear polarisation

$$\mathbf{P}^{(2)}(\omega_i) = \epsilon_0 \chi_{ijk}^{(2)}(\omega_i; \omega_j, \omega_k) \mathbf{E}(\omega_j) \mathbf{E}(\omega_k) \quad (2.14)$$

is governed by the nonlinear susceptibility tensor $\chi_{ijk}^{(2)}(\omega_i; \omega_j, \omega_k)$, which is responsible for three-wave mixing processes. In the case of both incident electric fields being of the same angular frequency $\omega_j = \omega_k$, and defining $\omega_j = \omega_k = \omega_0$, then the nonlinear susceptibility tensor $\chi_{ijk}^{(2)}(\omega_i = \omega_j + \omega_k)$, yields second-harmonic generation (SHG) $\chi^2(\omega_{SHG} = 2\omega_0)$. In the case of $\omega_j \neq \omega_k$ (setting $\omega_j = \omega_1$ and $\omega_k = \omega_2$) the three-

wave mixing process gives rise to sum-frequency generation $\chi^2(\omega_{SFG} = \omega_1 + \omega_2)$ or difference-frequency generation $\chi^2(\omega_{DFG} = \omega_1 - \omega_2)$. The number of possible elements contributing to the nonlinear susceptibility tensor $\chi_{ijk}^2(\omega_i)$ in three-wave mixing processes is the permutation result b^a , in this particular example $3^3 = 27$. The base (b) is the sum of the possible three directions (x, y, z) in Cartesian coordinates and the integer (a) in the exponent accounts for the sum of the two incident fields and the resulting field [36]. The number of possible elements contributing to the nonlinear susceptibility tensor in three-wave mixing processes can be limited by symmetry effects. In an extreme case the second-order nonlinear tensor is zero and the overall polarisation for second-order processes vanishes. This happens in centrosymmetric bulk media i.e. materials, such as some crystals, whose space group structure contains a centre of inversion or isotropic liquids. This also applies to any higher even-order polarisation term in the general form

$$\mathbf{P}^{2n} = \varepsilon_0 \chi^{(2n)} \mathbf{E}^{(2n)} \quad (2.15)$$

which becomes obvious, when \mathbf{P} and \mathbf{E} change their signs, in other words the polarisation goes in the opposite direction of the electric field (x switches to $-x$, y to $-y$ and z to $-z$), while ε_0 remains a positive constant. $\mathbf{P}^{2n} = -\mathbf{P}^{2n}$ then results in the trivial solution $\chi^{(2n)} = \mathbf{0}$, which applies to all even-order polarisation terms in the general equation 2.12 [67].

Second-harmonic generation is frequently used in combination with frequency-resolved optical gating (FROG) for the characterisation of ultrashort pulses. This autocorrelation method is commonly abbreviated as SHG-FROG. The latter and other pulse characterisation methods are described in more detail in the experimental method section 3.1.2. The main idea is that a time-delayed pulse is scanned over an identical copy of this very pulse, which results in SHG in an χ^2 material, when the pulses overlap in time and space. The gain in signal is evident for the described overlaps and the intensity signal and its shape can be used to gather information about the pulse duration [74].

2.2.2 Third-order Nonlinear Processes

In analogy to the preceding section, four-wave mixing (FWM) processes are determined by the third-order nonlinear polarisation vector

$$\mathbf{P}^{(3)}(\omega_i) = \epsilon_0 \chi_{ijkl}^{(3)}(\omega_i; \omega_j, \omega_k, \omega_l) \mathbf{E}(\omega_j) \mathbf{E}(\omega_k) \mathbf{E}(\omega_l) \quad (2.16)$$

which in turn is governed by the nonlinear susceptibility tensor $\chi_{ijkl}^3(\omega_i; \omega_j, \omega_k, \omega_l)$. A general case of four-wave mixing processes is given when the frequency components are non-degenerate $\omega_j \neq \omega_k \neq \omega_l$, then $\chi_{FWM}^3(\omega_i = \omega_j + \omega_k + \omega_l)$. Coherent anti-Stokes Raman spectroscopy (CARS) is a special case when the frequency of a Raman-active mode of a material is coherent with the difference in frequency between two incident electric fields. The angular frequency for CARS is $\omega_{CARS} = \omega_j - \omega_k + \omega_l$. Degenerate four-wave mixing (DFWM) involves four fields of the same frequency and the nonlinear susceptibility is $\omega_{DFWM} = \omega - \omega + \omega$. Third-harmonic generation (THG) occurs if the angular frequencies of the incident electric fields are identical i.e. $\omega_j = \omega_k = \omega_l = \omega_0$, then the susceptibility tensor $\chi_{ijkl}^3(\omega_i = \omega_j + \omega_k + \omega_l)$ results in $\chi_{THG}^3(3\omega_0)$.

The optical Kerr effect is also deduced from the third-order nonlinear polarisation and can be understood as an induced change of the refractive index of a nonlinear material, which is caused by an intense laser beam propagating through the material. Three of the main effects summarised under optical Kerr effect are self-phase modulation (SPM), self-focusing (SF) and cross-phase modulation (XPM). In brief, SPM is an effect that increases the refractive index of a material with increasing electric field intensity, which results in a phase shift and spectral broadening. SF is similar to SPM with the exception that the increase in the refractive index in SF is dependent on a nonlinear spatial-related intensity factor and in SPM on a nonlinear time-related intensity factor. XPM is caused when two distinguishable laser pulses interact in a nonlinear material. The change in the refractive index of the nonlinear material caused by one pulse leads to a phase shift of the other pulse. The number of possible elements contributing to the nonlinear susceptibility tensor $\chi_{ijkl}^3(\omega_i)$ in four-wave mixing processes is $3^4 = 81$. Once again, the base is determined by the three directions in Cartesian coordinates and the exponent is the sum of the three incident electric fields and the created field. Polarisation gating (PG)-FROG is one standard method to gain information about an ultrashort pulse. In PG-FROG a copy of a pulse is time-delayed and used for self-referencing in a χ^3 medium. The interpretation of the measured intensity profile with a spectrometer is easier than in SHG-FROG as the experimental setup uses a wave plate before intersecting with the original pulse in order to set the polarisation of the referencing pulse. A polariser behind the Kerr medium ensured that the spectral information (such as chirp and time duration) of the original pulse can be retrieved

using the intensity profile [74].

2.3 Potential Energy Surface

The introduction showed already a selection of photophysical processes evolving on potential energy surfaces. Understanding the potential energy changes as a result of electronic excitation and nuclear responses is key to assess dynamic processes in molecular systems. Upon excitation diverse routes from the prepared electronically excited states are possible to redistribute the gained energy as shown in the 2D cuts in figure 1.1 and are depending on the potential energy surface. Those processes showed a simplistic view along one nuclear coordinate only. The complexity of polyatomic systems makes it difficult to represent the potential energy surfaces accurately as the number of vibrational degree of freedom is increasing dramatically with the number of nuclei M and can be calculated with $3M - 6$ (or $3M - 5$ for linear molecules). The subtrahend is made up of the three possible translations in cartesian space and three degrees of freedom for rotation (or two for linear molecules). Thus even relatively small molecules quickly result in complex multidimensional potential energy surfaces. But an accurately represented potential energy surface is required to describe dynamics. The potential energy surface can be calculated by solving/approximating the electronic Schrödinger equation. In order to be able to calculate the potential energy surface an approximation is made that assumes the nuclear and electronic wavefunction of the Schrödinger equation can be separated. This approximation was proposed by Born and Oppenheimer in 1927 [13] and is shown in the next subsection.

2.3.1 Born-Oppenheimer approximation

An important approximation that allows to separate the nuclear and electronic part of the time-independent Schrödinger equation

$$\hat{H}\psi_{(r,R)} = E\psi_{(r,R)} \quad (2.17)$$

is the Born-Oppenheimer approximation, which takes advantage of the difference in relative mass between nuclei and electrons. The molecular energy Hamiltonian operator (\hat{H}) with M nuclei and N electrons in R nuclear and r electronic coordinates is given with

$$\hat{H} = - \sum_{\alpha=1}^M \frac{\hbar^2}{2M_{\alpha}} \nabla_{\alpha}^2 - \sum_{i=1}^N \frac{\hbar^2}{2m_e} \nabla_i^2 + V(r, R). \quad (2.18)$$

The Born-Oppenheimer approximation is made by separating the electronic and nuclear wavefunction, that assumes that electrons adjust instantly with nuclear changes. The wavefunction is given as the product of the electronic and nuclear wavefunction

$$\psi^{BOA} = \psi_{el}(r, R)\phi(R) \quad (2.19)$$

At any given fixed nuclear geometry the following solution of the electronic Schrödinger equation is valid and the electronic eigenstate with the corresponding wavefunction can be calculated:

$$\left\{ - \sum_{i=1}^N \frac{\hbar^2}{2m_e} \nabla_i^2 + V(r, R) \right\} \psi_{el}(r, R) = E_{el}(R) \psi_{el}(r, R) \quad (2.20)$$

Equation 2.20 is the result of replacing the Hamiltonian in equation 2.18 with the electronic Hamiltonian. With a change in the nuclear coordinates the electronic wavefunction changes as well and with it the eigenvalues, which allows to calculate the potential energy surfaces. The corresponding nuclear wavefunction does not depend on the electronic coordinates as only the nuclear coordinates R are part of equation 2.21:

$$\left\{ - \sum_{\alpha=1}^M \frac{\hbar^2}{2M_{\alpha}} \nabla_{\alpha}^2 + E_{el}(R) \right\} \phi(R) = E_{BOA} \psi(R) \quad (2.21)$$

As can be seen in the equation 2.20 the breakdown of the Born-Oppenheimer approximation is given when a simultaneous change is given in the nuclear coordinates and the electronic state. This can happen during vibronic excitation via intensity 'borrowing' from higher electronic states such as in the case of the $\pi\sigma^*$ absorption in pyrrole or at conical intersections.

2.3.2 Franck-Condon Principle

The Franck Condon principle is an approximation that is used to calculate the probability of vibrational states being populated upon electronic excitation. The probability

is calculated based on the overlap between the initial ground state vibronic wavefunction and the individual vibronic states in the upper excited state. The approximation treats the nuclear configuration as fixed and allows an instantaneous response of the electron, based on the high difference in relative mass between nuclei and electrons. Figure 2.3 shows a schematic with the blue arrow (λ_{phot}) marking the electronic excitation into the upper excited state. For simplicity the vibrational distribution is shown to be at $v'=0$ in the ground state (S_0) and the vibrational states of the excited state are explicitly sketched for the $v=0$ to $v=4$. The grey shaded wavefunctions for the vibrational states symbolise the region that can overlap with the orange wavefunction of the vibrational ground state population $v'=0$. The resulting overlap between the wavefunctions is called Franck-Condon overlap and is illustrated to the right of the potential assuming a densely vibrational state arrangement (orange shaded) and explicitly for the four drawn vibrational states (grey bars).

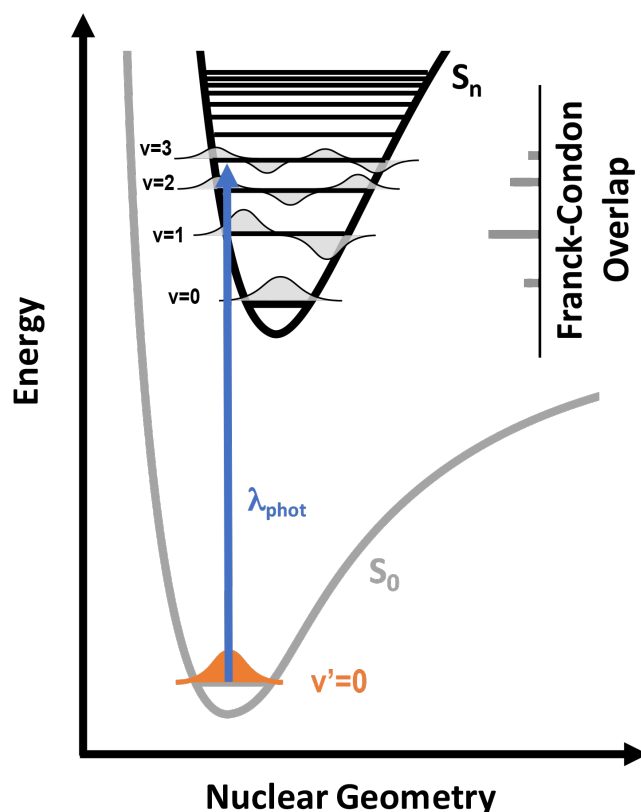


Fig. 2.3 Schematic of the Franck-Condon Principle (see text).

2.4 Femtosecond Transient Absorption Spectroscopy

Transient absorption in general is a four-wave mixing process, but due to strong time-ordering of the pulses the formation of the observed signal is this of linear absorption spectroscopy. Linear absorption spectroscopy is briefly mentioned in 2.2 together with the important polarisation term $\mathbf{P}^{(1)} = \epsilon_0 \chi^{(1)} \mathbf{E}$. This shows that the susceptibility tensor $\chi^{(1)}$ is the important element in the signal generation. The spectral features that can contribute towards the spectrum of a transient absorption experiment are listed below. Each of the spectral features described below is illustrated with help of one of many possible Feynman diagram.

Signal Calculation

The signal in transient absorption is expressed as optical density (OD), which is the absorbance of a solution at a particular wavelength (λ) and concentration (c) at given path length (l). The equation for the optical density is given by Beer-Lambert Law

$$OD = A(\lambda) = -\log \left(\frac{I(\lambda)}{I_0(\lambda)} \right) = \epsilon(\lambda)lc \quad (2.22)$$

wherein the wavelength dependent molar extinction coefficient is denoted as ϵ , the initial light intensity as $I_0(\lambda)$ and the intensity after the sample as $I(\lambda)$. In transient absorption a change in optical density (ΔOD) is detected. This is possible as both the initial intensity $I_0(\lambda)$ and the intensity $I(\lambda)$ after the sample is known for each time delay (Δt).

Excited state absorption

Excited state absorption (ESA) (gain, positive ΔOD) can be represented as it is given in the Feynman diagram (figure 2.4A). The Feynman dual time line diagrams shows the interaction on bra (right time line) and ket side (left time line) of the wavefunction with time evolving from bottom to top. The pump pulse transfers a population from the ground state (g) to the excited state (e). The grey shaded time period indicates the created population in the electronic excited state. The population then gets probed with the white light continuum. Transitions that are optically allowed from the excited state result in an absorption at the corresponding energy and a gain signal is detected. Assuming that the probe pulse is relatively weak it is not going to affect the excited state population significantly. The actual interesting part in TA studies is to follow the

dynamics that a molecule undergoes after excitation. This means that the absorption signal changes as a function of delay time (Δt) and is recorded as gain. The features contributing to a TA spectrum can be manifold. Some of the absorption signals that can be observed in TA experiments are the result of singlet state population, triplet state formation or solvation effects.

Ground state bleach

Ground state bleach (GSB) (loss, negative ΔOD) is shown in figure 2.4B. After excitation with the pump pulse a fraction of molecules have been lifted to the excited state and thus the number of molecules in the ground state is reduced. The signal calculated in TA spectroscopy compares the absorption spectrum before and after excitation in form of a ratio. As a result the removal of ground state population is registered as a loss feature in TA spectroscopy, as the fraction of ground state molecules is reduced and thus its absorption.

Stimulated Emission

Stimulated Emission (SE) (loss, negative ΔOD) occurs after excitation with the pump pulse and is induced by the probe pulse. The energy provided by the probe pulse induces the emission of a photon from an excited molecule, which returns to the ground state by emitting light in the direction of the probe field [8]. This is in contrast to fluorescence, where the excited molecule can emit light without external influence by returning to the ground state. The phase and direction (but not polarisation) of emitted light in fluorescence is then randomly oriented.

Coherence Spike

At experimental time delays, when the pump pulse and the probe continuum are overlapping in time, the contributions to the signal will not only be governed by $\chi^{(1)}$ but also by $\chi^{(3)}$. In other words four-wave mixing processes are involved and for the time of pulse overlap all resonant and non-resonant processes contribute towards the absorption spectrum. This is seen as a coherence spike over the whole wavelength range of the probe continuum, which can be very intense for solvents with large $\chi^{(3)}$ such as toluene or cyclohexane.

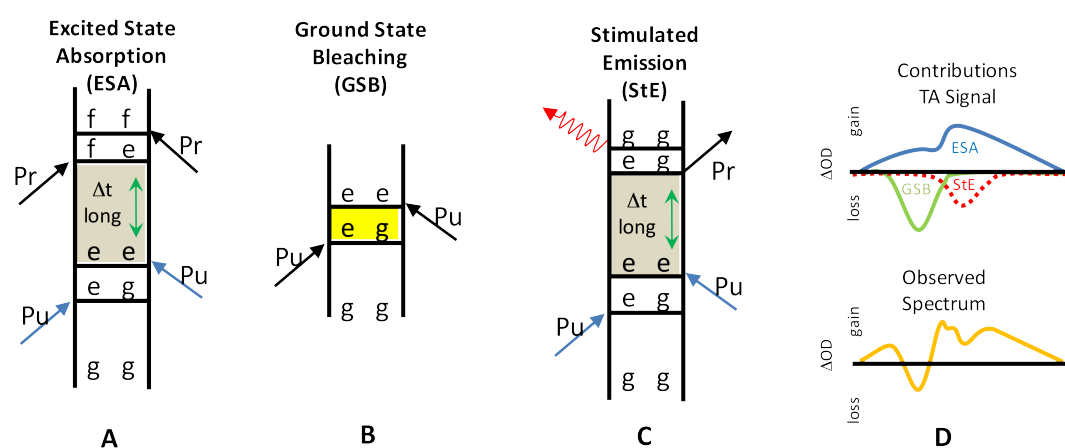


Fig. 2.4 General Spectral Features in Transient Absorption Spectroscopy together with Feynman time-line diagrams. A: ESA, with excited state (e) population (grey shading) prepared from the ground state (g) with the pump pulse (Pu) and is successively probed (Pr). B: GSB, interaction on ket side (left time line) creates coherence between g and e until second interaction on bra side is completed to create the excited state population. C: StE, typical four-wave mixing process, probe field is acting as emitting field on bra side and stimulates emission (red, curved arrow) (coherence collapses). D: shows the individual components contributing to a TA signal (top) and the resulting spectrum (bottom).

Chapter 3

Experimental

3.1 Experimental Techniques

The aim of this chapter is to provide a descriptive outline of the experimental techniques used in the study of quantum dots and pyrroles, as outlined in the results chapters 5 to chapter 6.

The femtosecond spectrometer that was constructed is described in section 3.1.1. Section 3.1.2 describes the methods used to characterise the laser pulses. The related theory, with regard to femtosecond pulse characterisation and transient absorption spectroscopy, is outlined in the theory section in 2.2.

3.1.1 Femtosecond Transient Absorption Spectroscopy

The transient absorption experiments were performed with a Clark-MXR femtosecond laser system that involved two laser pulses: the pump and the probe. A part of the CPA output ($320 \mu\text{J}$) was used to generate the temporally short (40 fs) pump pulse in a non-linear parametric amplification step, followed by pulse compression (TOPAS-white). The pump wavelength is variable in the range 480 to 700 nm with an energy of up to $25 \mu\text{J}$ (peaking around 550 nm) and can, optionally, be frequency doubled. During the instances when frequency doubling is carried out in the TOPAS-SHG, an extension unit to the commercially available TOPAS-white is used. The TOPAS-white and the TOPAS-SHG are described in the components section 3.2 in more detail. After frequency doubling, a wavelength range between 255 to 350 nm can be accessed with a pulse duration as short as 40 fs and pulse energies up to $5 \mu\text{J}$. The pulse energy can be adjusted by means of a variable neutral density filter prior to the TOPAS-SHG stage to allow a pulse energy range between $0.1 \mu\text{J}$ and $5 \mu\text{J}$. The beam waist at the sample is

estimated to be approximately $50 \mu\text{m}$ based upon a Gaussian beam waist calculation. A modification to the commercially designed TOPAS-SHG allows access to shorter pump wavelengths in the range of 220 to 245 nm by sum frequency mixing of the TOPAS-white output and a separately generated second-harmonic source at 386 nm. A schematic setup of the sum-frequency mixing stage is given in section 5.2.1. The layout of the optical bench, as used throughout the transient absorption experiments, is depicted in figure 3.1, with its main components being described in section 3.2.

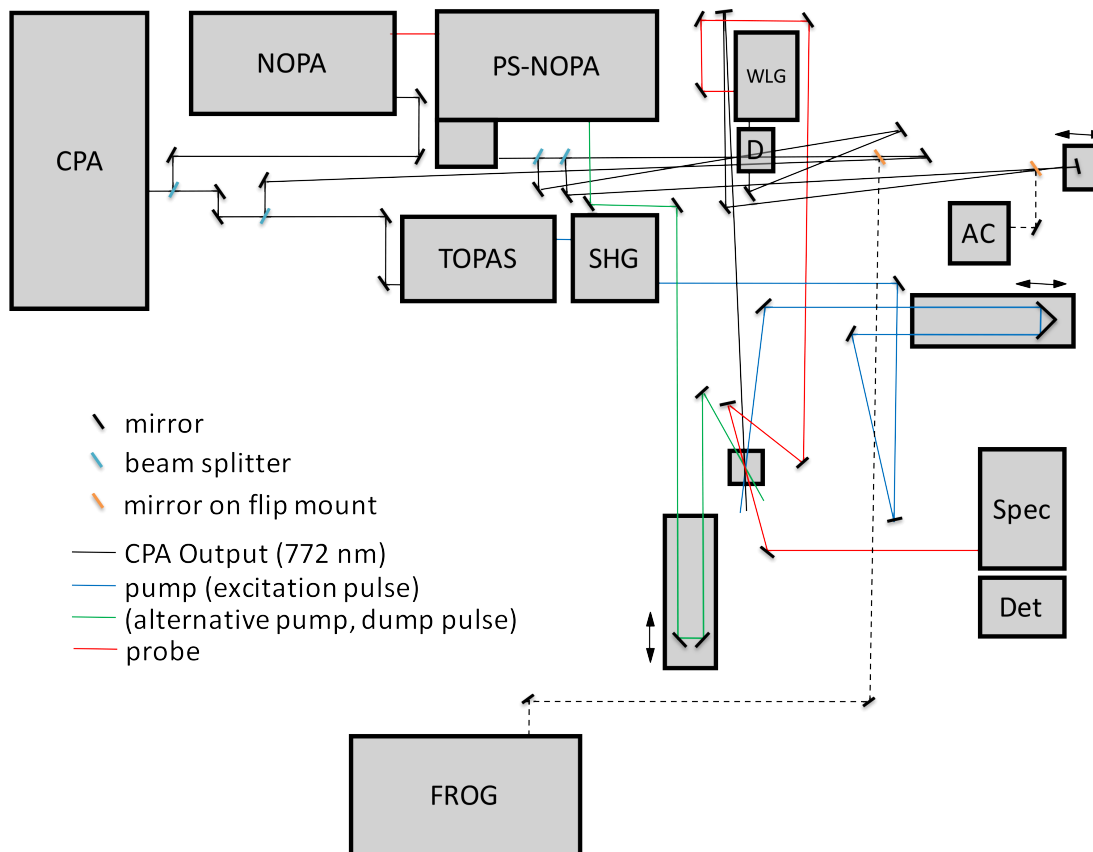


Fig. 3.1 Schematic of the Optical Bench showing the fs-Transient Absorption Setup. Components: CPA: chirp-pulse amplifier; (PS-)NOPA: (picosecond-) non-linear optical parametric amplifier; TOPAS: non-linear optical parametric amplifier with temporal pulse compression; SHG: second-harmonic generator; WLG: white-light generator; D: Dazzler - acoustic optic modulator for pulse shaping; FROG: frequency-resolved optical gating; Spec: prism-based spectrometer; Det: line array detector. Additionally shown are three delay lines (indicated with double-sided arrows) and diverse mirrors as well as flip-mirrors to guide the laser beam lines.

The probe pulse in a white light continuum stage supports three wavelength regions that focus a beam at 1150 nm, 772 nm or 386 nm into a nonlinear medium (e.g. water or sapphire) in order to generate a probe continuum in the range of 430 to 1100 nm, 380 to 730 nm or 300 to 380 nm respectively. The power of the probe pulse is below

the detection threshold of the power meter ($<0.1 \mu\text{J}$). The beam diameter of the pump pulse at the overlap position with the probe pulse in the sample is adjusted to cover the whole of the white-light spot size by optimising the signal amplitude of the coherence spike over the whole spectral range of the probe continuum.

3.1.2 Ultrashort Laser Pulse Characterisation

Several pulse characterisation techniques are employed. The intensity auto-correlator (pulseCheck, APE GmbH) represented by 'AC' in the schematic layout (figure 3.1) is used to check the pulse duration of the CPA on a daily basis. The characterisation and iterative tuning of the pulse duration and spectral shape is conducted prior to each experiment with two frequency-resolved optical grating (FROG) methods: second harmonic and polarisation gating. The pulse front tilt of the CPA output is measured with a slightly modified second-harmonic generation-FROG (SHG-FROG) and is shown as part of figure 3.3.

Second-Harmonic Generation-FROG

The spectral phase of an ultrashort pulse can be measured by frequency-resolved optical gating. In this method, a time-delayed pulse is generated for self-referencing in order to gain information about the pulse duration and the spectral phase. In SHG-FROG this is achieved by phase matching the two laser pulses in an SHG crystal, such as β -barium borate. The spectrum of the frequency doubled output of the cross-correlation is detected as a function of delay time between the replica pulses. SHG-FROG produces symmetrical time traces and hence has an ambiguity in the direction of time [109]. A schematic SHG-FROG set-up is shown in figure 3.2. This method is used to characterise both the fundamental 772 nm laser pulse and the visible laser pulses generated by the nonlinear optical parametric amplifiers; however it cannot be used to characterise the UV pump pulses (see Polarisation Gating-FROG).

The SHG-FROG setup depicted in figure 3.2 is blind to pulse front tilt. In a pulse with pulse front tilt, the arrival time varies across the beam profile, i.e. the pulse travels with an angle to the beam propagation direction [92]. A slight modification is required to measure the pulse front tilt of a laser pulse (see figure 3.3). An important difference in the setup for the pulse front tilt characterisation is that the lens is removed, as itself can introduce pulse front tilt itself and thus make the measurement impossible. The green lines would cross each other when propagating through the crystal. Due to the tilt, the cross correlation time is substantially longer than in the case shown in

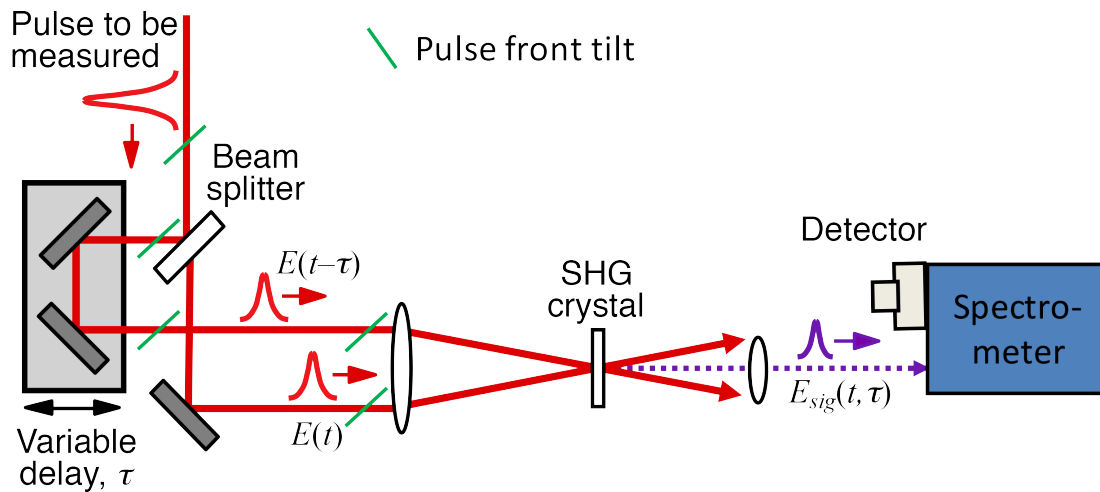


Fig. 3.2 Second Harmonic Generation - FROG. The setup allows for the measurement of the pulse duration by self-referencing the laser pulse and measuring the generated SHG signal as a function of time.

figure 3.2, where the pulses are overlapping in parallel within the SHG crystal. In order to be sensitive to pulse front tilt in the vertical plane a periscope is needed.

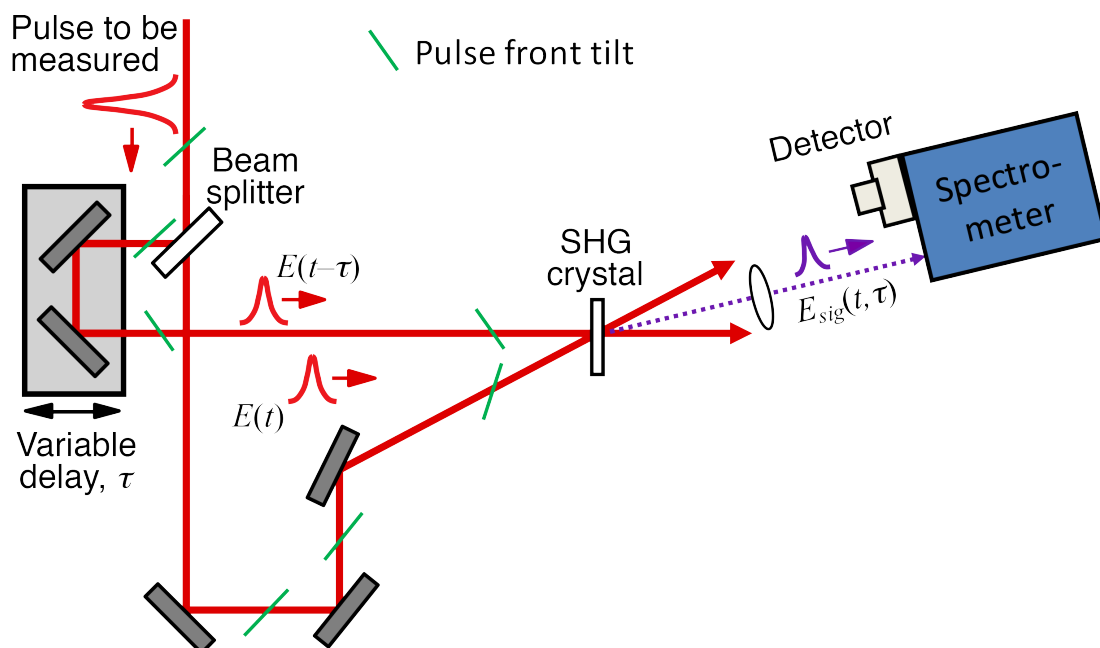


Fig. 3.3 Pulse Front Tilt Characterisation with SHG-FROG. Insertion of an additional mirror and removal of the lens from the setup shown in figure /reffig:shgfrog allows for characterisation of the pulse front tilt. Besides a temporal measurement, this technique permits a spatial map of the laser pulse on a 2D detector (such as a CCD camera) as a function of time.

Polarisation Gating-FROG

The PG-FROG setup depicted in 3.4 is based on the optical Kerr effect, which is touched upon in section 2.2.2, and is a third-order nonlinear effect in which the sample is made birefringent by a polarised laser field. The polarised laser field becomes the gate pulse and is plane polarised by 45° with respect to the probe pulse.

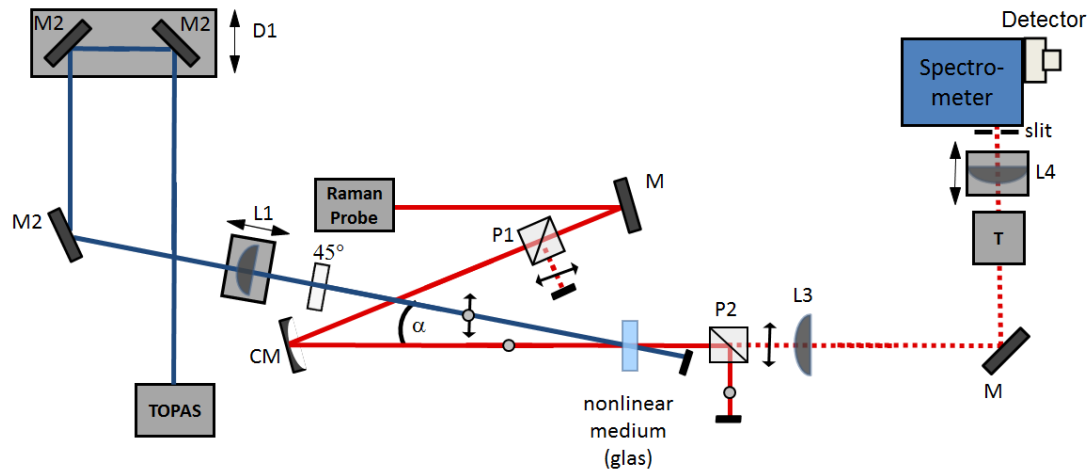


Fig. 3.4 Polarisation Gating - FROG. Characterisation of the weak laser pulse (e.g. probe pulse) by gating with a 'strong' laser pulse sufficient to 'access' the third-order nonlinear susceptibility tensor in order to flip the polarisation of the weaker probe pulse and thus open the gate to the detector.

The probe pulse is then (de)polarised by the induced birefringence and the change in polarisation is detected. The schematic setup depicts the actual table setup and is just slightly modified by introducing a beam splitter (BS) into the pump pulse line before the delay stage (D1). This not only allows to characterise the probe pulse as with help of two additional mirrors a fraction of the pump pulse can be directed onto the former probe beam path. With this arrangement, little modification to the beam alignment setup is required and the self-referencing PG-FROG is complete. This PG-FROG method is used to optimise the pulse duration of the excitation pump pulse in the UV range, which cannot be characterised with SHG-FROG based on BBO (which is below the SHG phase matchable range, the limit of which is approximately 410 nm).

Despite its advantage in reliably determining the pulse duration and phase of a pulse, the polarisation gating technique requires a polariser with a very high extinction ratio [90] and laser pulses with high pulse intensity. The peak power needs to be in the order of 1 MW in order to access the third-order nonlinear terms of the susceptibility tensor [25] and generate a detectable signal strength. As a consequence, this method is unsuitable for PG-FROG via self-referencing with the weak white light continuum

(<0.1 MW); however cross-referencing with a characterised short laser pulse, such as a short, close-to-transform-limited pump pulse, is possible.

3.1.3 H atom Phototranslational Spectroscopy

The schematic setup of the H atom phototranslational spectroscopy experiment as installed in the laboratory of Prof. Dr. M. Ashfold at the University of Bristol is shown in figure 3.5. The optical bench shows the setup of the photolysis laser (shaded green), the Lyman- α laser (shaded blue) and the Rydberg tagging laser (shaded red), which overlap with the molecular beam in the vacuum chamber. The tunable photolysis laser is generated by frequency doubling the output of a dye laser which is pumped by a YAG laser. Similarly, the Rydberg tagging laser at 366 nm and the 364.8 nm laser (the latter being required to generate the Lyman- α) are generated with YAG pumped dye lasers and successive frequency doubling and mixing, respectively.

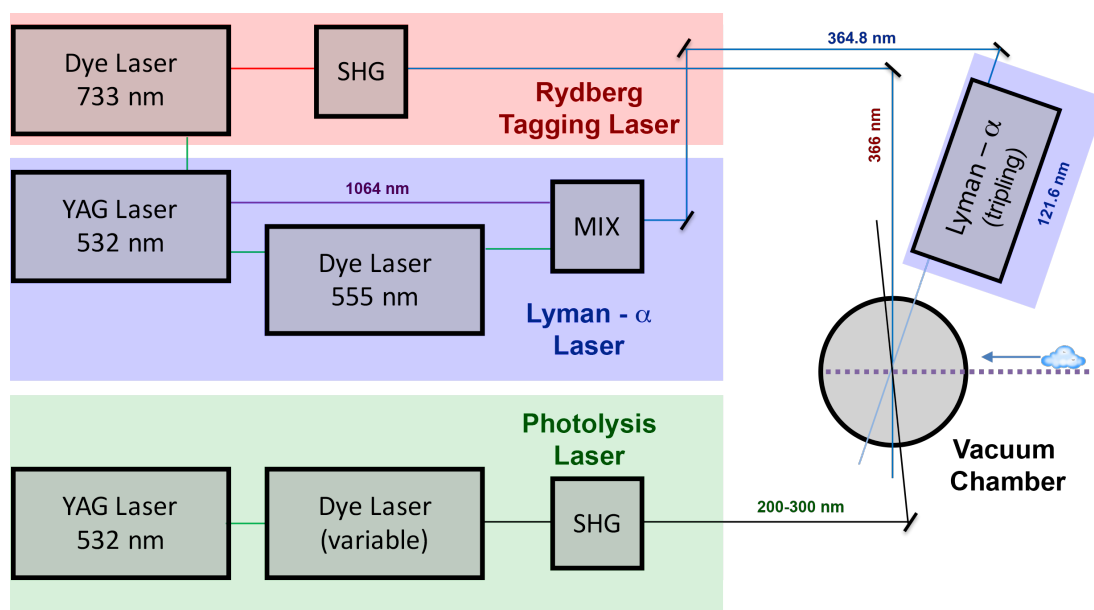


Fig. 3.5 H atom Phototranslational Spectroscopy (schematic setup). Optical bench of the H atom PTS setup at the University of Bristol. The above shows the main laser components and crossing of the photolysis laser with the molecular beam in a vacuum chamber. Generated H atoms are probed with the temporally and spatially overlapping Lyman- α (121.6 nm) and Rydberg tagging (366 nm) lasers.

The sample is seeded in Ar carrier gas (stagnation pressure ~ 1 bar), supersonically expanded and skimmed before being intersected by a pulsed photolysis laser beam in the vacuum chamber. After a time delay ($\Delta t \sim 10$ ns), the H atoms are probed in a two-colour double-resonant process comprising of the Lyman- α and Rydberg tagging

lasers that are spatially and temporally overlapped. The first, the 121.6 nm Lyman- α pulse (generated by tripling 364.8 nm radiation in a phase matched Ar/Kr gas mixture), promotes the H atoms to the $2p$ level; the second ($\lambda \sim 366$ nm) promotes the H atoms to a higher Rydberg state ($n \sim 80$). The time-of-flights (TOFs) of these Rydberg H atoms from the interaction volume (defined by the three laser pulses) to the front face of the detector are then measured. An extraction field (~ 50 V cm^{-1}) is used to remove unwanted H^+ ions formed in the interaction region. Figure 3.6 shows the spatial overlap of the three laser beams together with the overlapping molecular beam in the vacuum chamber. The spherically-expanding molecular fragments after photolysis, together with the Rydberg tagged H atoms, are indicated by the cone. The figure also indicates the H atom quantum state accessed with the Lyman- α and the Rydberg tagging lasers in an energy level diagram. The continuum (grey shaded), reaching ionisation of the H atom is achieved as stated with an extraction field, allowing finally to detect the created H atom from the photodissociation event indirectly by the generated electron.

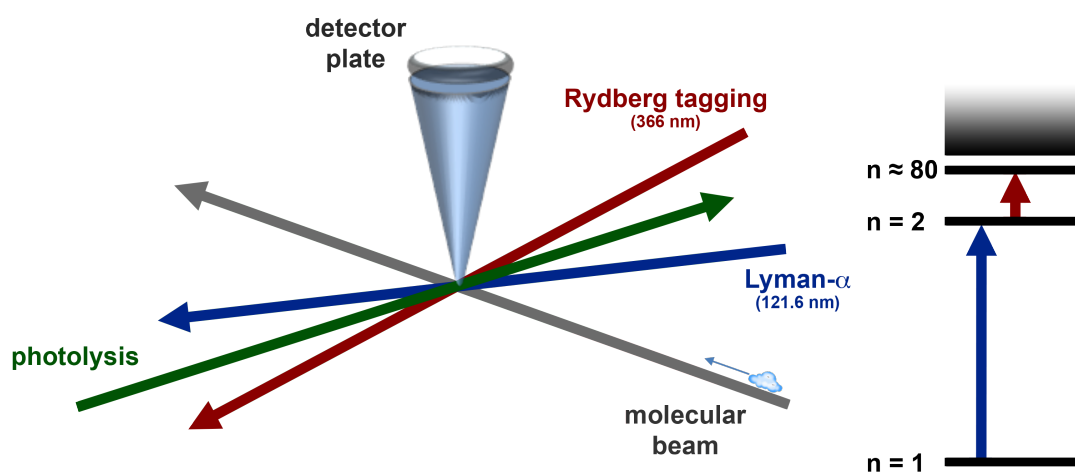


Fig. 3.6 H atom Rydberg Tagging Scheme in PTS. The H atom is released due to photolysis and subsequently undergoes Rydberg tagging with temporally and spatially overlapping Lyman- α (121.6 nm) and Rydberg tagging (366 nm) lasers. The quantum states accessed with the Lyman- α and Rydberg lasers are shown in separate diagrams.

3.2 Experimental Components

3.2.1 Clark-MXR CPA-2110

The Clark-MXR CPA-2110 is a chirped pulse amplifier which generates 150 fs pulses at a central wavelength of approximately 775 nm at a repetition rate of up to 1 kHz and a pulse energy of 1 mJ. The CPA-2110 consists of two main components: Firstly, there is an erbium fibre laser (SErF) with stretcher optics that generate strongly-stretched seed pulses at 1.55 μm with a bandwidth of about 8 nm and an average power of 3 mW (30 MHz, i.e. 10^{-7} mJ per pulse), which are subsequently frequency doubled in a periodically-poled lithium niobate (PPLN) crystal to generate the seed pulse train at 775 nm. And secondly, there is a pump laser that amplifies the weak seed pulse. The pump pulse itself is generated in a series of steps. A DC arc lamp pumps a neodymium-doped yttrium aluminium garnet (Nd:YAG) rod that creates a population inversion and continuously lases at 1064 nm. The output is then frequency doubled in the z-shape IR cavity and the 532 nm portion is used to pump the stretched seed pulse in a Ti:Sapphire crystal. The Ti:Sapphire amplifying cavity precedes a pulse compression unit that compresses the output pulse to 150 fs.

3.2.2 Clark-MXR NOPA

The non-collinear optical parametric amplifier (NOPA) produces broadband sub-30 fs pulses with tunable wavelengths. The Clark-MXR NOPA consists of a white light continuum generation stage, which is pumped by a small fraction ($<1 \mu\text{J}$) of the CPA output (150 fs, 772 nm), and two amplification stages that are pumped by the frequency doubled fundamental CPA output.

In traditional collinear optical parametric amplification (OPA), the pump and seed pulses are sent collinearly into the nonlinear crystal. The seed pulse is then amplified by a short UV pump pulse via OPA and an infrared (IR) idler is also generated due to the difference in frequency mixing. The group velocity of the IR idler is higher than that of the amplified seed pulse, i.e. the different frequency components travel at different velocities through the nonlinear material. As the short signal pulse propagates with a higher group velocity through the crystal than the comparably longer and slower pump pulse, the OPA takes place at the leading edge of the signal pulse front. As a result, the signal pulse spreads in time as it is continuously generated at its pulse front. Correspondingly, the coinciding generation of the idler takes place at the trailing edge of the idler pulse. This group velocity mismatch that leads to pulse lengthening in a collinear setup can be circumvented by using a non-collinear beam arrangement.

To achieve this, the pump beam is sent into the nonlinear crystal at an angle with respect to the signal beam, so that the group velocities of pump, signal and idler are matched. They are phase-matched because each of the three pulses travel through a slightly different amount of nonlinear material, which compensates for the velocity mismatch. As such, a suitable angle of incidence can be found so that the signal pulse is amplified throughout the crystal at its centre temporal position. The idler and pump beams are then spatially offset from the amplified signal beam. This is another benefit of the non-collinear setup, because spectral filtering of the idler and pump pulse is not necessary. [6]

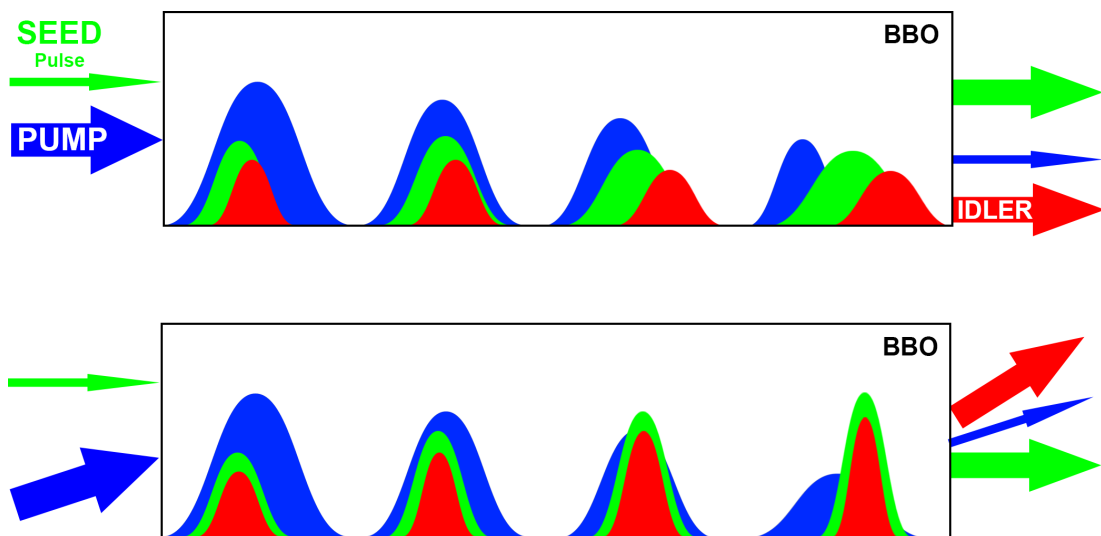


Fig. 3.7 Co-linear vs. Non-Collinear Optical Parametric Amplification. a) Co-linear OPA, signal field amplification at leading edge of pulse and pulse broadening in time due to group velocity mismatch indicated across crystal. b) Non-collinear OPA, with the incident angle between pulses chosen to allow phase-matching, amplification throughout crystal without pulse broadening in time and spatially separated beam lines after the pulse leaves the crystal is discernable.

Figure 3.8 shows the modified Clark-MXR NOPA with its central components. The white light generator (WLG) combines two lenses, an adjustable neutral density filter and a sapphire plate. The first lens focusses the beam into the sapphire plate, which generates the white light continuum, followed by a beam collimation with the second lens. A portion of the CPA output ($250 \mu\text{J}$) is frequency doubled in a β -barium borate (BBO) crystal and $8 \mu\text{J}$ of 387 nm are used to pre-amplify a portion of the chirped visible white light continuum in the first nonlinear crystal (1^{st} crystal). After the pre-amplification stage, $0.6 \mu\text{J}$ are received (at 550 nm) and further amplified with the remaining $75 \mu\text{J}$ of 387 nm light initially generated in the frequency doubling stage. The final 'signal' NOPA pulse is created in the second nonlinear crystal (2^{nd} crystal)

with a bandwidth of approximately 40 nm and a pulse energy of approximately $10 \mu\text{J}$. The wavelength range embraces the visual-to-near infra-red (450 to 700 nm) for the 'signal' output.

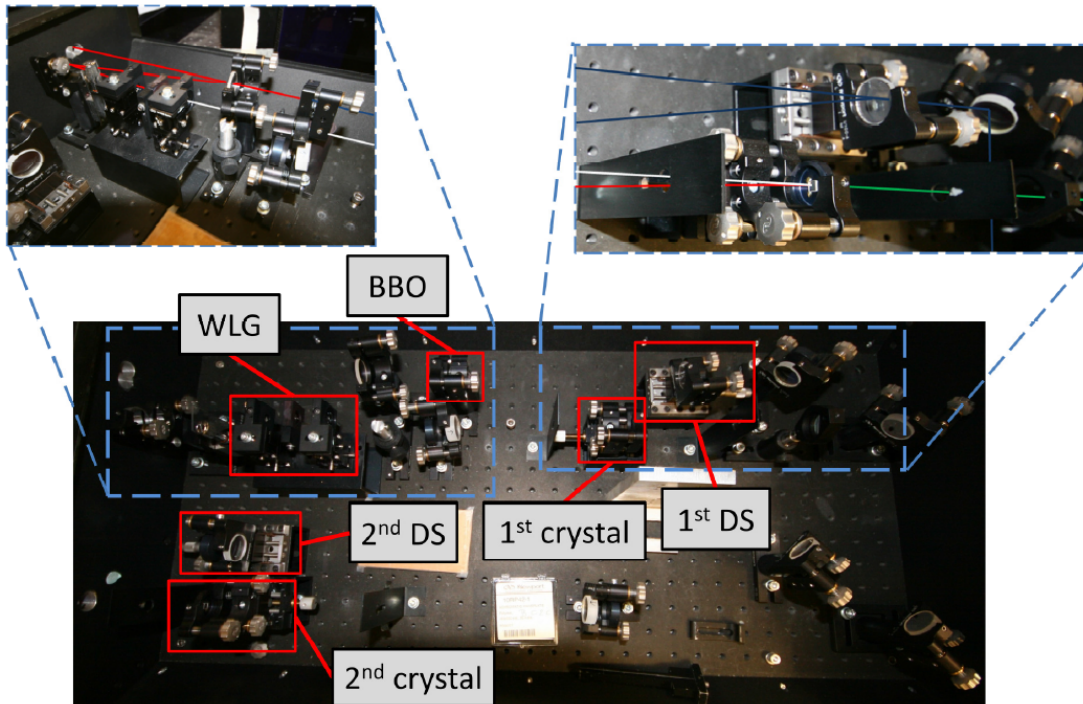


Fig. 3.8 Photography of the Clark-MXR NOPA with Components. Components: WLG, white light generator; BBO, β -barium borate, frequency doubling crystal; 1st delay, first delay stage; 2nd delay, second delay stage; 1st crystal, pre-amplifier crystal; 2nd crystal, amplifier crystal; beam path is indicated in different colours.

The NOPA can also be operated in the IR range between 870 to 1600 nm, by amplification of the 'idler' output instead of the 'signal'. The maximum 'idler' NOPA output is approximately $8 \mu\text{J}$. The available spectrometers (Ocean Optics) in our laboratory are not suitable to operate efficiently in a spectral range exceeding 1000 nm. Thus the central wavelength of the IR laser pulses generated with the idler in the range of 1100 to 1600 nm are calculated by measuring the signal wavelength and making use of the conservation of energy. An output laser centred at approximately 1100 nm, is used to generate the probe pulse (this is explained in more detail in section 4.2.1).

3.2.3 TOPAS white and TOPAS-SHG

The excitation pump pulse is generated with the TOPAS-White, which is a commercially available nonlinear optical parametric amplifier from Light Conversion Ltd. The difference between the TOPAS-White and the Clark-NOPA is that the TOPAS uses

only one BBO crystal for the first and second stage amplifications of the white light continuum. The white light continuum is generated in sapphire as in the Clark-NOPA. A schematic setup is given in 3.9. The advantage of the TOPAS is that it allows pulse compression to transform-limited pulses. This is achieved by negatively chirping the WLC with a pulse-phase shaper so that positive chirp can be added on demand to the output pulse with two fused silica wedges, labelled as compressor in 3.9. The TOPAS output covers the wavelength range from 500 nm to 650 nm. The TOPAS-SHG allows for frequency doubling of the TOPAS output in a BBO crystal in order to generate UV pulses in the range between 250 nm and 325 nm. In addition, the two delay lines, the BBO crystal angle and the pulse compressor in the TOPAS are all equipped with computer-controlled stepping motors; these motors allow easy selection of the desired excitation wavelength. The optional TOPAS-SHG allows a computer-controlled adjustment of the BBO crystal angle for optimum phase matching.

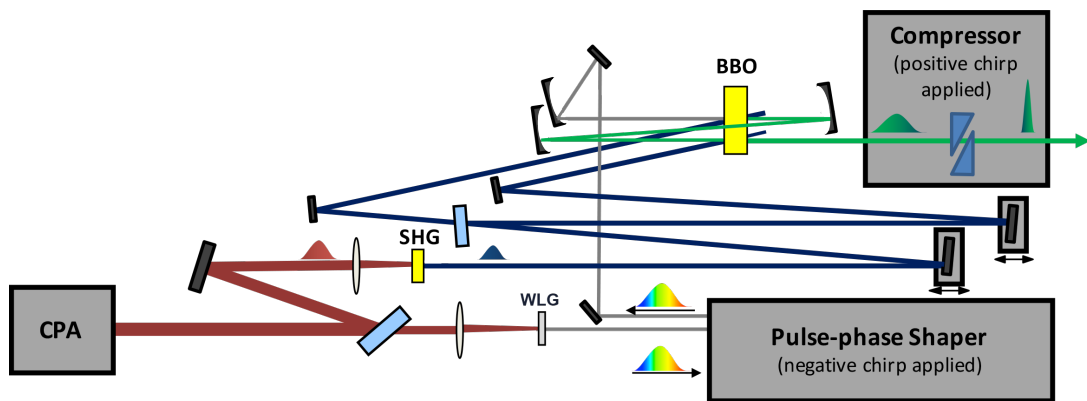


Fig. 3.9 Schematic of the TOPAS-white with Pulse Shaper and Compressor Unit. Components: WLW: white-light generation with fraction of 772 nm light in sapphire; Pulse-phase Shaper: adds negative chirp to white light continuum; SHG: frequency doubling of 772 nm to 386 nm; BBO: 1st - parametric amplification of fraction of white light with 386 nm (grey to green line), then 2nd - pre-amplified fraction (thin green line) is amplified in second step with 386 nm light in a second pass through the BBO crystal (thin line to thick green line); Compressor: silica wedges, which add positive chirp to compress the output pulse to a transform-limited pulse.

3.2.4 White Light Generation

The continuum is generated by focussing ($f = 50$ mm) a small fraction ($1-5 \mu\text{J}$) of the 772 nm laser light into a nonlinear material. The white light continuum spectrum is dependent upon the choice of nonlinear material. Stable continua covering different

sections in the range from 360 nm to about 720 nm are generated in a 1 cm fused silica cuvette filled with deionised water. Local heating effects that lead to lensing issues at the foci position are avoided by placing a heating block under the water cell to generate convection. The strongly-diverging light is collimated with an off-axis parabolic mirror (silver, $f = 50$ mm) as indicated in the schematic in figure 3.10.

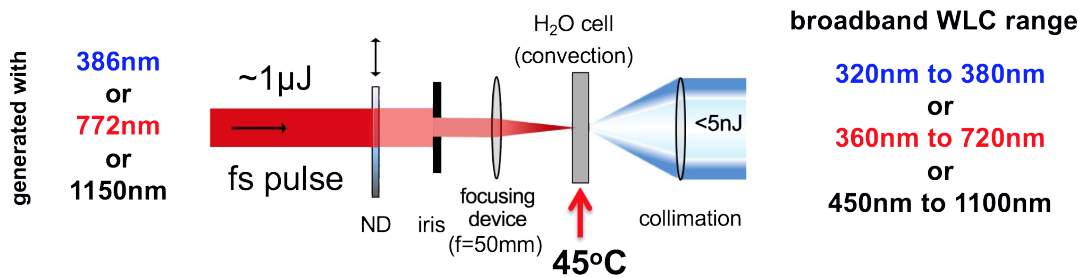


Fig. 3.10 Schematic of the main components in the White Light Generation Step. Components: ND: neutral density for power adjustment; iris: iris for beam profile adjustment; focusing device: off-axis parabolic mirror with focal length of 50 mm; H_2O cell: continuum generation medium with convection; collimation: diverging white-light is collimated with an off-axis parabolic mirror (contrary to schematic) in order to avoid chromatic aberration.

In order to generate a stable, single filament of white light, the spatial focus is set at the back of the nonlinear material and the latter is then moved towards the foci position until a stable continuum is observed on a standard spectrometer (Ocean Optics, HR4000). Fine-tuning is achieved with an iris to send only the central part of the Gaussian fundamental beam into the nonlinear material. In addition, a neutral density filter is used to adjust the fundamental beam power for the white light generation. Further improvements to the white light stability are achieved by applying negative pre-chirping to the 772 nm light before the white light generation. This is achieved with help of an acoustic optic modulator (Dazzler) that applies a negative chirp to the laser pulse and thus provide access to a temporal focus in the white light continuum medium, improving the stability of the white light continuum. The schematic in figure 3.11 illustrates the difference between normal chirp and negative chirp of the 772 nm laser pulse. The figure indicates the problem associated to multiple temporal focal points (stars) creating multi-filaments (coloured waves) i.e. several white light generation spots in the nonlinear medium can lead to instabilities in the white light continuum.

The anti-stokes side of the visible white light continuum in either material cuts off rapidly, and hence it is very weak and insufficient for experiments at wavelengths

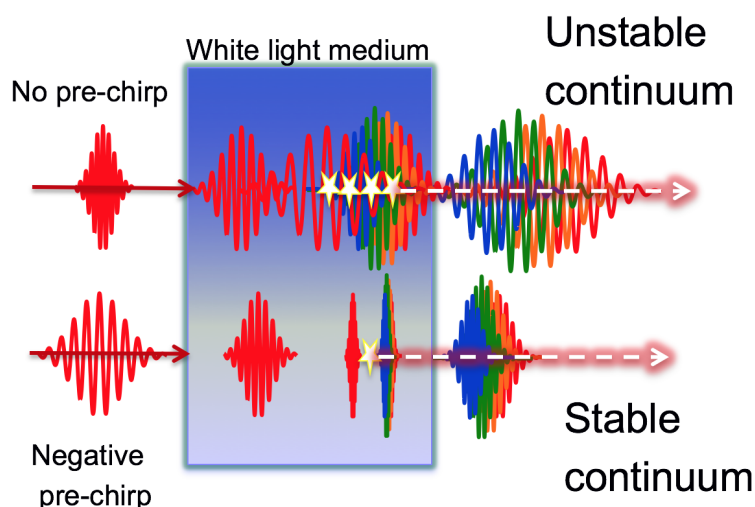


Fig. 3.11 Principle of Temporal Focus in the Generation Step of a White Light Continuum.

larger than 772 nm. As indicated in figure 3.10, and as will be seen in sections 4.2.1 and 5.2.3, slight modifications to the standard white light generation setup can allow continua in the near-IR (up to approximately 1100 nm) and slightly deeper UV range, such as making use of the 772 nm laser pulse.

3.2.5 Sample and Detection Scheme

The pump and probe pulses are spatially overlapped in the sample flow cell. A TCS micro pump (M100S) is used to circulate the sample at a flow rate of about 50 mL min^{-1} . The 1 mm flow cell itself is made of fused silica (Starna, Q48) to avoid the absorption of UV light. The sample thickness is artificially decreased by adjusting the sample concentration to absorb about 90 % of the excitation light (pump pulse) in the first $100 \mu\text{m}$ of the sample. This minimises the group velocity mismatch between the pump and probe pulses in the sample medium. The grating spectrograph (ISA Jobin Yvon Spex HR320) has been modified to support both a grating and a prism to disperse the light transmitted through the sample.

The transmitted probe light and spatially offset reference light (optional) are separately collimated and then focused onto the spectrometer slit. After collimation in the spectrometer, the incident light is dispersed with help of a calcium fluoride prism or with a grating for a higher spectral resolution. After a second collimation step, the probe light and the reference light are separated with a D-shaped aluminium mirror and detected in the focal plane of the spectrometer by diode array line scan cameras (ISG

Camera, LW-ELIS-1024A-1394), each with 1024 diodes. The prism configuration is the standard setup for transient absorption experiments and provides a spectral resolution of approximately 17 cm^{-1} . The optional grating configuration results in a spectral resolution of just a few wavenumbers, depending on the grating chosen. Details of the data processing are given in the next section.

3.2.6 Data Acquisition Processing (LabView)

A simplified data acquisition scheme that shows the delay stage control and the LabView response is given as flow chart in figure 3.12. With the 'Start LabView' input, the TA acquisition begins and the software records the number of laser shots per time delay as specified by the user. The vital component of the data acquisition procedure is the block labelled 'LabView Processing' in figure 3.13 containing the 'De-Glitching' component (details in figure 3.14). Laser shots are recorded at a 1 kHz data rate on the reference ISG Camera (DCam_{Ref}) and the signal ISG Camera (DCam_{Sig}) simultaneously. The DCam_{Sig} records the laser shots that propagate through the sample medium and the DCam_{Ref} records the pulse that is split off before travelling through the sample material. Both cameras are set to record 100 laser shots (i.e. 100 'lines', with each line covering 1024 diode array points that record the spectral information) that are bound into one 'frame'. These will subsequently be referred to as 'lines' and 'frames'. The two frames (one per camera) are then sent to LabView for processing. The excitation pump pulse is chopped at 500 Hz, so every second line in a frame is a pump on or off spectrum, as is shown in the 'LabView Processing' figure 3.13. Each frame consists of 50 lines with pump on and 50 lines with pump off. This means that there are four different types of spectra in general:

- signal pump on (SigON)
- reference pump off (RefOFF)
- signal pump off (SigOFF)
- reference pump on (RefON)

Each frame, with its corresponding 50 lines, is fed into the 'De-Glitching' component of the LabView code (figure 3.14). The 'De-Glitching' code calculates the standard deviation (STDEV) within each frame and deletes the corresponding lines from all four frames if the standard deviation exceeds the De-Glitch Input Value. The LabView code continues to acquire frames from the cameras until the actual number of 'Line Counts' reaches the 'Line Count Input Value'. It then either drives to the next delay step or stops the program if the process is completed. If the program is affected

by an unexpected termination or a stopping procedure (stop), the randomised delay steps are sorted and an output data file is written. The output file (*.csv) is optimised for the evaluation software (Transient Absorption Template 4.5) in Igor 6.22A.

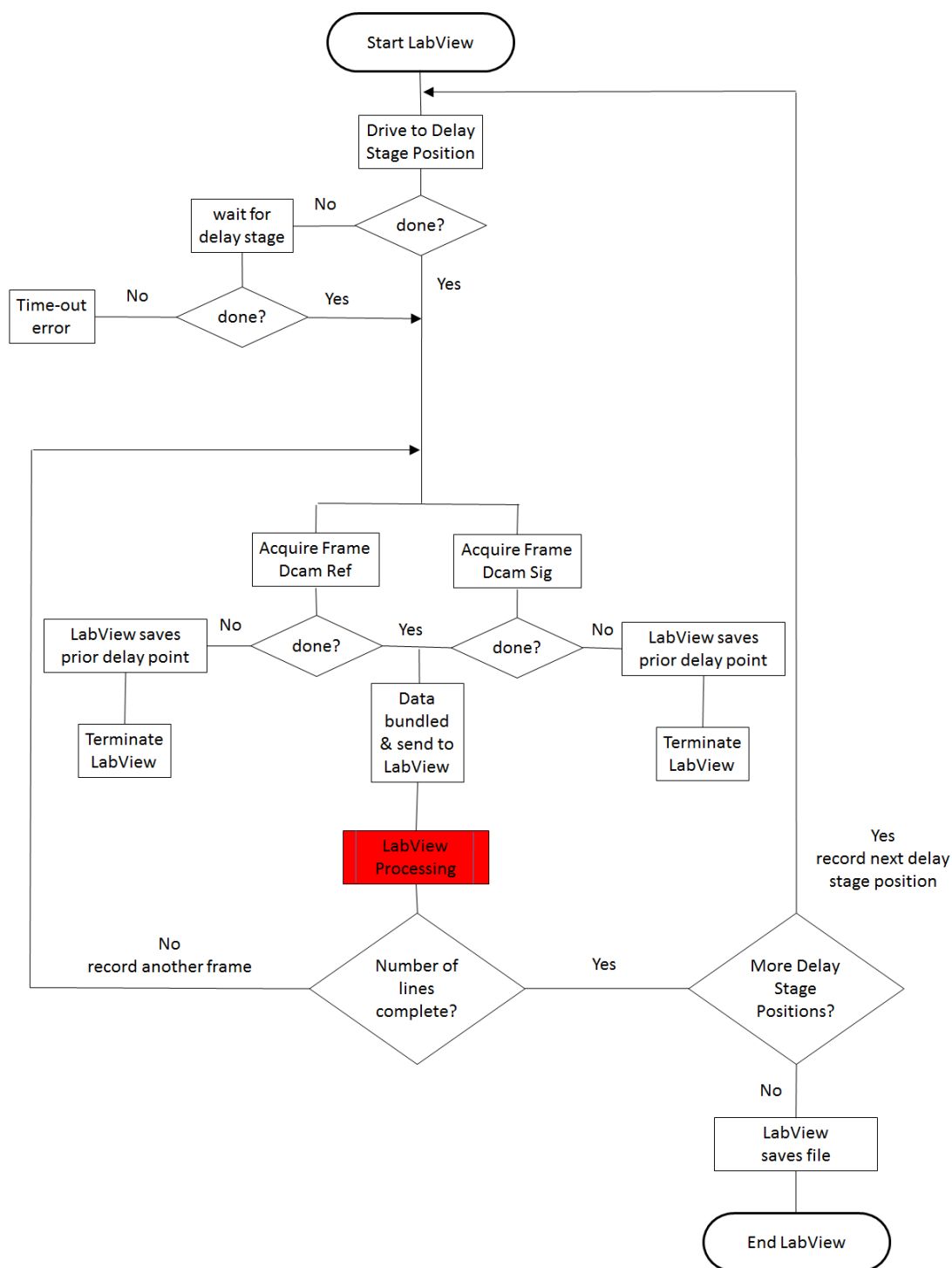


Fig. 3.12 Flow Chart of the TA Data Acquisition Procedure in LabView

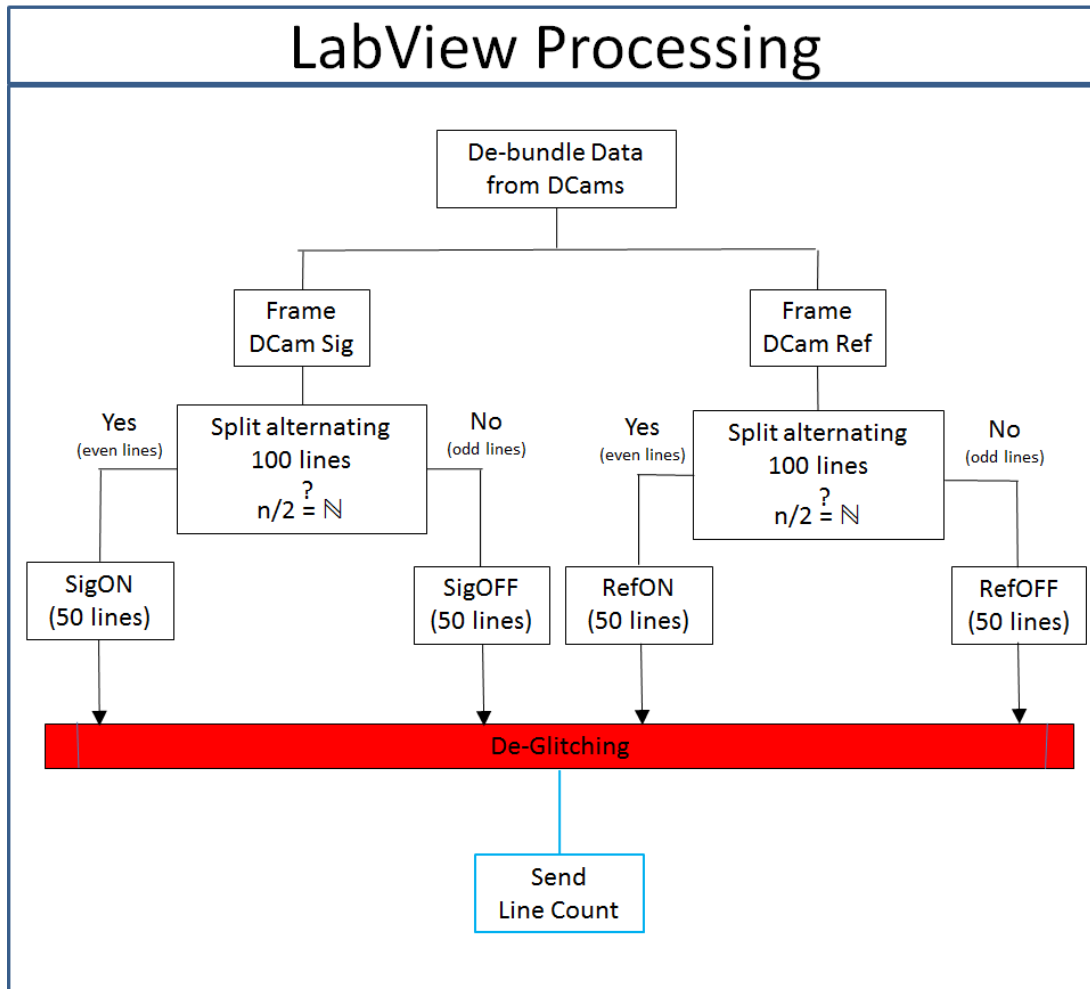


Fig. 3.13 Flow Chart of the LabView Processing component of the Acquisition Procedure

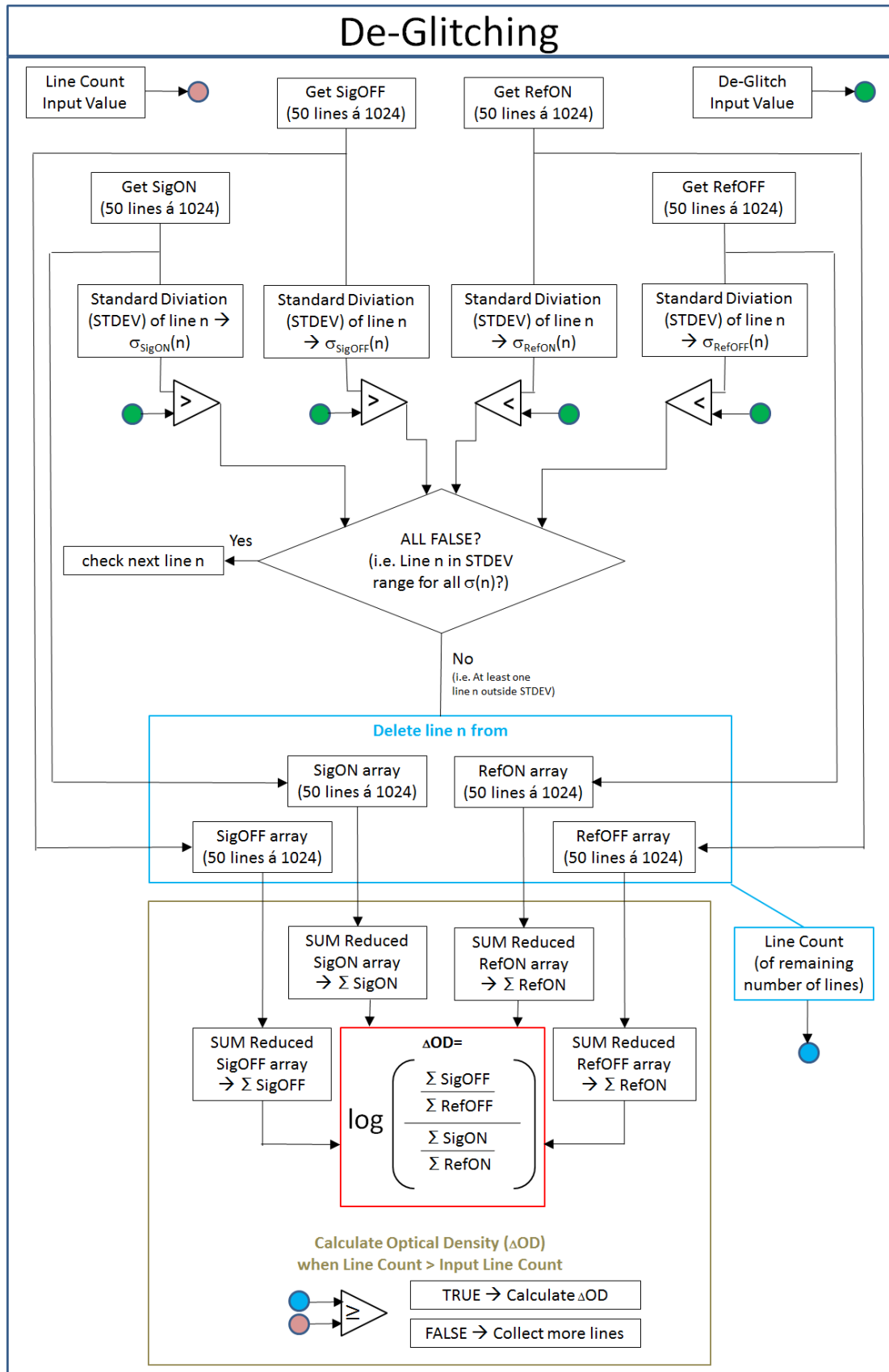


Fig. 3.14 Flow Chart of the LabView De-Glitching routine of the Acquisition Procedure

Chapter 4

Excited State Dynamics in CuInS₂/ZnS Quantum Dots

4.1 Introduction

Nanotechnology and nanomaterials have been receiving increasing attention over the last few decades. This is in part related to their great potential as has been proven in applications such as one's favourite electronics being made even smaller and more portable or in the form of composite materials in dental implants and charge carriers in solar panels. The increased focus on nanomaterials is thus being built on scientific advances in nanotechnology; however there is a corresponding rise in awareness of their potential harm to health and the environment. Consequently, governing bodies are toughening regulations with the aim of reducing unforeseen side-effects related to the production and use of nanomaterials. An example of the rising awareness and its consecutive regulation is the precautionary principle that was included in the EU Treaties and made public in a communication in 2000 [29]. Since then, research has been driven towards finding alternative materials to substitute nanomaterials that are suspected of producing toxic effects in humans and nature. Cadmium-based solar cell devices, as used in photovoltaics, are known to be toxic. Nevertheless, photovoltaics remain an integral feature of our a sustainable and green energy mix. In photovoltaics electric power is generated by converting the incident sun's radiation on a semiconductor surface, or more precisely on an interface layer between two types of semiconductor materials. In the case of Cadmium sulfide (CdS), a substance frequently used in thin-film solar cell devices [122], the CdS layer forms the n-type layer, whereby 'n-type' indicates that a larger 'negative' electron concentration than hole concentration is present in the semiconductor, as opposed to p-type systems where the 'positive'

charged hole concentration is dominant. The opposing p-type layer is required for the charge separation. More recently developed examples of such solar cells are doped thin-film CdTe/CdS [122] or CdS/TiO₂ quantum dot-based solar cells [91, 101]. Two new terms have been introduced here: quantum dots and doping. Doping is the process of including impurities in the lattice structure of the material to alter the conductivity of a semiconductor, which is often used to fine-tune the type (n- or p-type) of a semiconductor material. Quantum dots (QDs) are semiconductor nanoparticles that exhibit electrical and optical properties between those of bulk material and discrete molecules. This effect is described as quantum confinement, and is the result of the very small size of QDs of just a few nanometers. Thus, QDs are spatially confined and can exhibit unusual properties, such as a size-dependent shift in their emission spectrum contrary to the emission spectrum of bulk material. The remarkable properties of QDs gave rise to the development of a high resolution scanning optical microscope [44] and are still being applied in new ways in the areas of light emitting devices, laser technology and optical switches [57].

As already indicated, a QD, and more generally a semiconductor material, contains holes and electrons which form the charge carriers. The band structure of a QD is made up of such holes and electrons. In the simplest case the band structure can be described as having a valence band containing a sea of electrons and a conduction band containing holes. This is, in part, similar to the molecular picture of a ground and an excited state, but a direct comparison fails when the discrete occupation of electrons in the HOMO and LUMO is taken into account. In contrast to a metal, a semiconductor's valence and conduction bands are separated sufficiently to form a band gap i.e. the Fermi level lies between the bands as in an insulator. However, in a semiconductor the Fermi level can be thermally populated. Specific to the notation, in a p-type semiconductor the band edge is close enough to the Fermi level to be populated with electrons, and in an n-type semiconductor the band edge is close enough to the Fermi level to be populated with holes. Upon light absorption (photon) an electron can be promoted from the valence band to fill partially the conduction band, thus leaving a positively charged electron hole in the valence band. This generated excited electron is called exciton and is defined as a bound state of an electron and an electron hole which are attracted to each other by the Coulomb force. The exciton can return to the valence band hole via one of several possible channels to conserve energy. One option for conserving energy is the emission of a photon, by which the excited electron emits the excess energy in order to 'collapse' back to the valence band hole. Alternatively, the excess energy can equilibrate with the surrounding environment, e.g. phonon vibration to a solvent, and thus a pathway back from the conduction band to the valence band is

found. Auger recombination provides another frequent pathway for energy distribution in semiconductors by which an electron and electron hole recombine by giving the energy to a third carrier in the conduction band, which in turn is excited to a higher energy level. The excess energy of the third carrier is usually distributed vibrationally to surrounding carriers and/or solvents.

Each quantum dot can be made up of hundreds or even thousands of atoms forming the lattice structure of a nanocrystal. In light-emitting devices the desired property is a high efficiency to emit light, or in other words a high photo-luminescent quantum yield (PLQY). On the contrary, a solar cell device should have a high efficiency in extracting the charge carriers to an external circuit. Both practical examples can suffer severely from the inclusion of impurities or imperfections in the lattice structure. Surface related traps can arise in quantum dots, and these provide a pathway to non-radiative deactivation, similar to a relaxation pathway via a 'dark state' in a molecule. Those surface sites can be thought of as imperfections in the lattice structure along the surface of the QD with, for example, missing atoms in the lattice structure that form vacancies. A shell layer can 'fill' those vacancies along the surface and can prevent the electron-hole recombination via such surface sites, i.e. they get passivated. Moreover, further exogenous impact (such as an oxidising environment or light) can also be minimised with a shell layer. Thus, QDs without a shell layer are often referred to as core-only QDs. Despite the fact that impurities alter the properties and efficiency of QDs for particular applications, they also provide an opportunity for other future applications. Overall, the combination and composition of core-only and shell QDs can be further used to tune and control the properties of a QD, along with their size and shape.

A relatively new, 'non'-toxic alternative to Cd-based semiconductors and quantum dots is CuInS_2 . Its lattice structure is that of a ternary I-III-VI₂ chalcopyrite, as shown in figure 4.1. The old group notation I-III-VI₂ is more recently represented by the actual positions of the components in the periodic table by group number (11-13-16, ascending order). In this thesis, CuInS_2 is studied by fs-TA spectroscopy in the form of CuInS_2 QDs and $\text{CuInS}_2/\text{ZnS}$ QDs in order to investigate the relaxation dynamics upon energy absorption in the visible spectrum.

The work in this chapter forms part of a collaboration with the Critchley Group in the School of Physics and Astronomy at the University of Leeds. The aim is to investigate ultrafast non-radiative and radiative pathways of QDs upon excitation. The QDs of interest are CuInS_2 (CIS core) and $\text{CuInS}_2/\text{ZnS}$ (CIS/ZnS core/shell, short CIS/ZnS) particles dissolved in n-hexane. Due to the small dimensions of QDs the surface-to-volume ratio is very large and their surface properties affect their potential applications [123]. The general interest in these particles is related to applications in

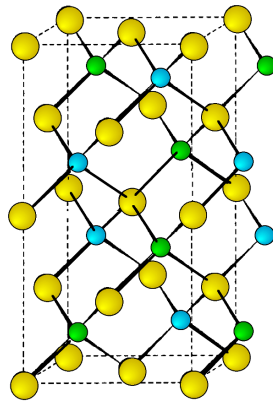


Fig. 4.1 Unit cell structure of a chalcopyrite lattice. Copper atoms are shown in blue, indium atoms are shown in green and sulfur atoms are shown in yellow. The dashed lines show the unit cell. Courtesy to reference [4].

biolabeling [58, 63] and as 'active components in optoelectronic devices' [58]. Several studies [58, 62, 63, 77, 108, 123, 124] have investigated the highly luminescent nature and long-lived emission of these QDs by means of photoluminescence. Surprisingly, CIS QDs show a large Stokes-shift, meaning that 'the emission peaks (..) are significantly red-shifted relative to their absorption peaks' [77], moreover, the emission band is very broadband. This unusual relaxation process is not yet fully understood and the possible states involved are not all identified yet. It is suggested [18, 35, 40, 62, 77] that the strong Stokes-shift and the broadband emission is caused by defect states that lead to donor-acceptor pair (DAP) recombination. Nam et al. [77] summarise the possible donor states as a sulphur vacancy (V_S), an interstitial copper (Cu_i) and an indium substituted at a copper site (In_{Cu}). The possible acceptor states are named as a copper vacancy (V_{Cu}), an indium interstitial (In_i) and a copper substituted at an indium site (Cu_{In}). A coupling between the conduction band and the emitting donor state is required to allow for DAP recombination and must be accompanied by an energy transfer, either radiatively or non-radiatively. Diverse time-resolved (nanosecond) studies related to CIS/shell QDs frequently conclude that the emission upon excitation is 'instant' and therewith originating from the CB, which, in part, disagrees with the DAP recombination suggested previously. Nevertheless, population transfer between the CB and the possible donor states could occur on an ultrafast time-scale, which can be rationalised by suggesting a mechanism of fast moving electrons and 'electron deficient' donor states. Nonetheless, the population transfer will be limited by the overlap between the wavefunctions of the involved states. Information about the early relaxation dynamics might be helpful in gaining a better understanding of the states involved in the recombination process. A first attempt to gain information about possible ultra-

fast non-radiative contributions in the relaxation process following photoexcitation has been undertaken by Li et al. [63] in the form of time-resolved (femtosecond) transient absorption spectroscopy. The journal papers by Li et al. [63] from the Klimov group and Nam et al. [77] are particularly notable. In the first instance, this is because the investigated QDs are comparable to the CIS QD synthesised in the Critchley Group, and secondly the described relaxation dynamics differ between the authors of these two journal papers. As a further literature introduction, the main experimental results and conclusion by Li et al. [63] and Nam et al. [77] are summarised and the similarities as well as differences are highlighted.

The study by Li et al. [63] investigates the QDs both with and without a CdS or ZnS shell. A schematic representation, as provided by Klimov et al. for the possible relaxation pathways, is given in figure 4.2. The figure shows the decay mechanism for the coated and uncoated CIS. The different decay mechanisms are highlighted in the figure with red and blue shaded areas respectively. Our TA experiments allow us to study the strongly luminescent CIS, which is the coated species. This is the reason why the findings by Li et al. [63] for the CIS core study are not given in full detail; the focus is instead on the CIS with ZnS or CdS shell. The defect structure between the CIS/ZnS and CIS/CdS is not likely to be very different, as both coatings are expected to remove any surface trapping centres and increase the quantum yield (QY) [63, 124]. Nevertheless, coating the CIS with ZnS leads to a spectral blue-shift [63], while coating with CdS leads to an initial blue-shift followed by a red-shift [63, 124] in the photoluminescence.

The Klimov group, in the publication by Li et al. [63], proposes a three-level system for the CIS/shell, wherein upon excitation from the valence to the conduction band the population is radiatively emitted to an energetically low-lying internal defect state, where it undergoes non-radiative decay back to the valence band. These findings were rationalised on the basis of time-resolved photoluminescence (TRPL) studies with nanosecond time resolution. The TRPL showed single-exponential decays with a time constant of 500 ns upon excitation ($\lambda_{\text{pu}} = 400$ nm) for CIS/CdS and red light emission (~ 700 nm). The reported TA data at 4 ps after excitation ($\lambda_{\text{pu}} = 400$ nm) shows a loss feature only, which has been attributed to the ground state bleach (GSB) since its centre frequency matches that of the ground state UV/Vis absorption spectra and does not match the maximum emission peak obtained from other TRPL studies. The TA of the CIS core shows 'a similar feature' [63] to the coated species, i.e. a GSB signal only. On the other hand, their findings for the CIS core species (blue area in figure 9.1) show a weak emission in the yellow range (~ 670 nm) of the PL spectra with a fast decay ($\tau_{640 \text{ nm}} = 6.5$ ns) component, indicating the role of surface

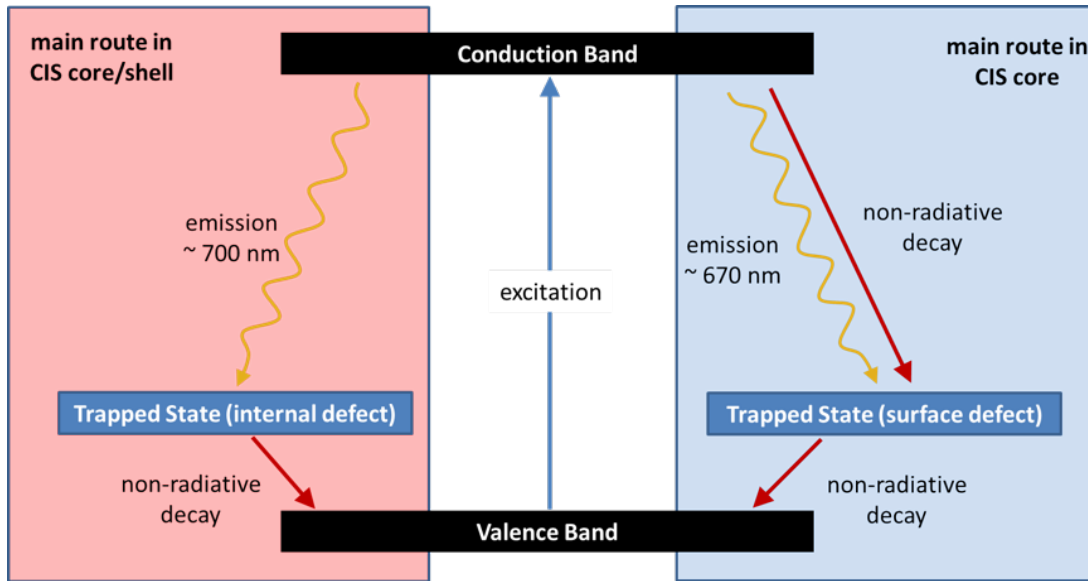


Fig. 4.2 Schematic energy level diagram for CIS/CdS and CIS core QD as given by the Klimov group in Li et al. [63]. Straight and wavy arrows show non-radiative and radiative relaxation pathways, respectively. The proposed decay mechanism contributing mostly in CIS/CdS and CIS core species are highlighted with red and blue shaded areas, respectively.

defects in uncoated QD. The latter fast process was greatly reduced upon coating with either CdS or ZnS, and the red-shaded process in figure 9.1 becomes dominant. As the TRPL data of CIS/ZnS retained some biexponential character it is concluded that some population still follows the fast decay route. Nam et al. [77] are more precise in identifying possible internal defect states as a sulphur vacancy (V_S) and an indium substituted at a copper site (In_{Cu}) for energetically high-lying states, and a copper vacancy (V_{Cu}) for energetically low-lying states. They propose two main radiative decay routes: firstly, a recombination pathway between the donor-acceptor pair (DAP) from V_S -to- V_{Cu} , and secondly a recombination route from CB-to- V_{Cu} . Both routes contribute to the emission observed in PL studies of CIS core. The V_S -to- V_{Cu} route seems to be the dominant pathway in CIS core, as evidenced by the high density of V_S and V_{Cu} at the surface. This goes along with the interpretation by Klimov et al. that surface trapping states are the dominant recombination route in CIS core. It also explains the low QY with competitive non-radiative pathways related to surface states. Upon ZnS shell growth in Nam's study the second recombination route CB-to- V_{Cu} becomes more dominant. This can be explained by a reduction of V_S and V_{Cu} sites on the surface, leading to the fast channel via V_S effectively being switched-off, and making the recombination CB-to- V_{Cu} favourable. Nevertheless, the DAP route (V_S -to- V_{Cu}) is still present to an extent in the CIS/ZnS and is even enhanced with closure of the previously

dominant non-radiative channel. This is because the prepared QDs in Nam's work are In-rich, so they can contain a large number of acceptor states (i.e. V_{Cu}) in the whole domain of the QDs. The large amount of acceptor states allows for relatively more frequent DAP recombination that is relatively seen larger than in CIS/core, but overall it is still outweighed by the favourable CB-to- V_{Cu} recombination. Furthermore, this also explains the spectrally observed blue-shift emission and increased QY in PL studies, as the energy gap in CB-to- V_{Cu} is larger than in V_S -to- V_{Cu} .

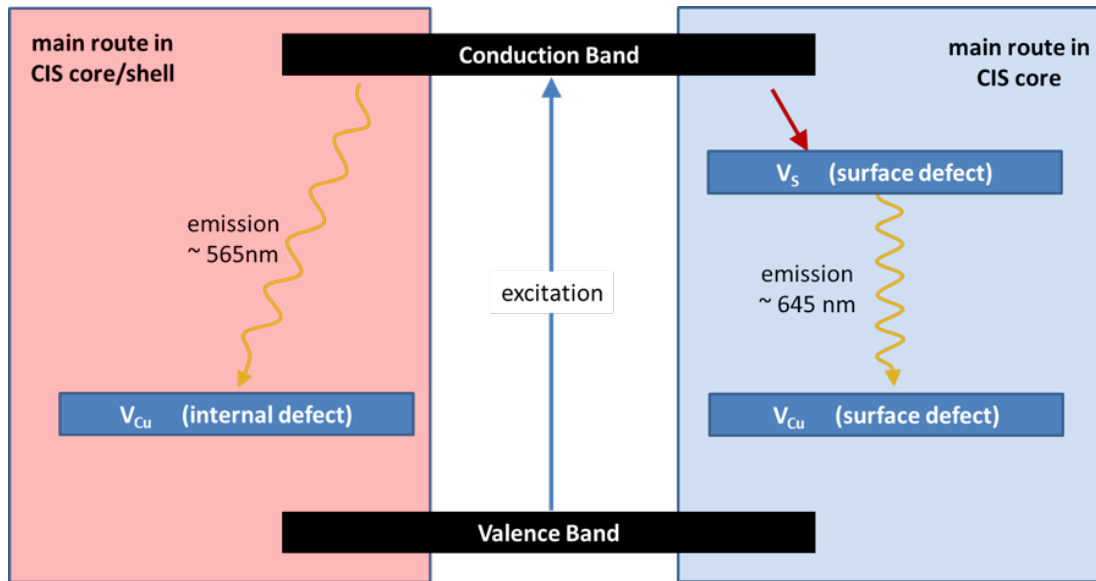


Fig. 4.3 Schematic energy level diagram for CIS and CIS core QD as given in Nam et al. [77]. Straight and wavy arrows show non-radiative and radiative relaxation pathways, respectively. The proposed decay mechanism for the CIS and CIS core species are highlighted with red and blue shading, respectively.

At this point the similarity between the interpretation by the Klimov group and Nam should be pointed out: both suggest a radiative decay from the CB to an internal defect state for the CIS/shell. Nam et al. specify this internal defect state as the copper vacancy (V_{Cu}) centre. Klimov associates the fast decay component to a surface state that quenches the fluorescence and is drastically reduced upon shell growth. Nam et al.'s interpretation once again agrees with that of Klimov and identifies the V_S site as being the important surface defect. However, they differ in their energetic representation of the recombination route that is dominated by the surface states (i.e. mainly present in CIS/core). Klimov solely describes the recombination process originating at the CB as a low-lying surface state with a competing non-radiative and emitting process (figure 4.2, (blue area)), whereas Nam invokes a four-level system with photoemission from the surface defect V_S to its acceptor V_{Cu} ; no comment is made on how the surface state is populated in the first place. Further to this, Nam does not

address the evident lower QY of the CIS Core in comparison to CIS/shell, which in Klimov's paper is rationalised by the ultrafast non-radiative decay component. The opposing frequency shift (blue-shift in Nam vs. red-shift in Klimov) in the emission of the CIS/shell is directly related to the surface passivation (ZnS vs. CdS) and is well established in literature [63, 124]. Nam et al. [77] reject a possible recombination pathway via an energetically high-lying In_{Cu} donor state on energetic grounds, as a DAP recombination from In_{Cu}-to-V_{Cu} would give rise to a near infrared emission, which does not match the observed 647 nm emission in their study. The In_{Cu} state is assumed to be energetically invariant from CIS bulk to CIS QD with respect to band gap changes as a consequence of shell growth (and subsequent size variation). This can be explained by the limited mobility of this deep In_{Cu} trap state. Nam et al. do not mention any non-radiative processes in their interpretation nor any recombination originating from other defect states except the sulphur vacancy. The In_{Cu} defect has been identified as an effective trap state in spray-deposited CIS [35, 40]. Possible recombination routes are manifold and the dominant recombination pathway will also depend on stoichiometry, i.e. In-rich versus Cu-rich CIS [19, 35, 40, 77]. The differences in interpretation and lack of ultrafast (femtosecond) studies have prompted this investigation into the relaxation dynamics of CIS QD in more detail.

4.2 Method Development

Modification of the standard experimental methods as outlined in chapter 3 were necessary and are outlined in the following two subsections. As is known from photoluminescence studies, the emitting range of CuInS₂ quantum dots is in the visible-to-near-IR range. The white light stability near the IR and the spectral ranges created with the fundamental CPA output at 772 nm as described in section 3.2.5 are not sufficient to study the expected emitting range. As a result, the probe continuum is extended into the IR range and the required modifications are detailed in section 4.2.1. A further addition to the experimental setup is the inclusion of a third laser pulse, a dump laser, which is used to depopulate carriers at an arbitrary selected delay time position after excitation. The latter adaption to the setup is required to acquire a deeper insight into the relaxation dynamics of the quantum dots investigated. The pump-dump-probe (PDP) scheme is described in section 4.2.2.

4.2.1 Extension of Probe Continuum to the Infra-Red

In order to generate a stable continuum covering the visible-to-near-IR range a separate laser pulse is used with a centre wavelength of approximately 1060 nm. This laser pulse is generated in the Clark-MXR NOPA stage as already indicated and described in section 3.2.2. The essential components of the optical bench used in the IR-WLC are shown in figure 4.4. Importantly, the residual light from the NOPA stage is filtered with a long-pass 850 nm filter (RG850, Schott Ltd.) to avoid cross-phase modulation in the white light medium and generation of a second continuum that would otherwise occur with the strong residual 772 nm pulse from the NOPA and the desired amplified idler at 1060 nm. To further attenuate the power of the 772 nm residual and to compensate for the different beam length with respect to the Vis-WLC, two highly reflective 1064 nm (HR1064, 0°) mirrors are used in the beam line after the long-pass filter.

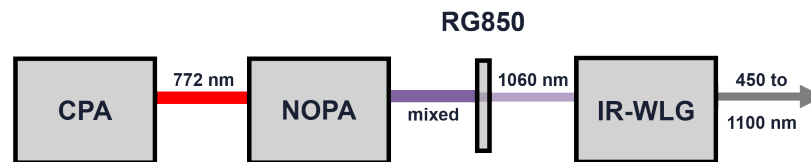


Fig. 4.4 Schematic components in the IR-WLC Generation. Experimental components required to generate the IR-WLC are the Clark-MXR CPA-2110 laser (short: CPA), the infra-red pulse generation in the Clark-MRX NOPA (short: NOPA) and the WLC generation stage (IR-WLG). An additional long-pass filter (RG850, Schott Ltd.) is also used.

4.2.2 Pump-Dump-Probe Scheme

The pump-dump-probe (PDP) scheme (figure 4.5) used in the experiment is shown in a simple schematic to show the implementation of the third laser pulse (dump pulse) and the corresponding pulse sequence used in the experiment. The delay times between the pump and dump pulses ($\Delta\tau_1$) and between the pump and probe pulses ($\Delta\tau_2$) are shown. Further to this, an illustration of a potential population flow and the effect on it by the dump laser is indicated. The dump laser pulse used in the experiments is a fraction of the 772 nm CPA laser pulse. The fraction is isolated with help of a 4 % beam splitter (BS). A variable neutral density (ND) allowed for fine-tuning of the dump laser pulse energy in a range between 0.1 to 4 μJ . Similarly to the excitation pulse that shifts population from a relaxed ground state population into an excited state, the dump laser is used to shift population states once the QDs are excited. The final probe pulse is then

used to measure the change in absorption as per a standard pump/probe experiment. The wavelength choice of the dump pulse is critical. The dump wavelength chosen for the experiments outlined in this chapter are set to 772 nm and thus are outside the ground state absorption range of the CuInS₂/ZnS QDs used in this experiment (see figure 4.6). The time delay $\Delta\tau_1$ is fixed for each PDP experiment, with $\Delta\tau_2$ being scanned over the whole time delay range.

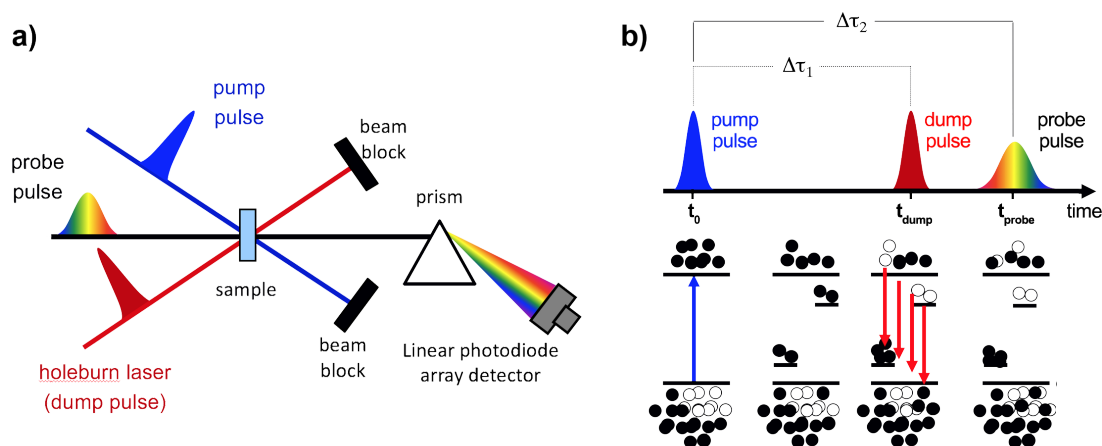


Fig. 4.5 Pulse Sequence in PDP-Scheme. a: Additional dump pulse (red) is shown together with the pump pulse (blue) and probe pulse (coloured). b: Pulse sequence of the PDP-Scheme with the pump pulse at t_0 , followed by the dump pulse at t_{dump} and the probe pulse at t_{probe} . Time delay between the pump and dump pulse ($\Delta\tau_1$) allows population to evolve after excitation and is set at a chosen time delay $\Delta\tau_1$. The dump pulse at t_{dump} moves population between absorbing states as indicated with the hollow dots and filled dots. The final probe pulse at t_{probe} measures the change in population at any given delay time ($\Delta\tau_2$) between the pump and probe pulse.

4.2.3 Sample Preparation

The QDs used in the experiment were synthesised by Dr. M. Booth from the Critchley group. A detailed description of the materials used, together with the synthesis of CIS/Zns QDs, can be found in Booth et al. [12] and also in the published version of this chapter, available in Journal of Physical Chemistry C [55]. The CIS/ZnS QDs are suspended in n-hexane to form a purple solution. The hydrophobic QDs are stored at 8 °C.

4.3 Results and Analysis

4.3.1 Quantum Dot Characterisation

Static Spectral Data

The UV/Vis absorption spectrum (black, solid line) and the photoluminescence (PL) spectrum (red, solid line) are shown in figure 4.6. The second derivative (black, dashed line) of the CIS/ZnS QDs data indicates that the first excitonic transition is centred at approximately 540 nm. Upon excitation at this wavelength the steady-state PL spectrum shows a single broadband emission centred at 693 nm with FWHM of approximately 100 nm. Based on an empirically-determined relationship [12] between the length of the triangular projection of CIS QDs in TEM images and their PL spectral peak positions, the height of the pyramid of the QD cores is estimated to be 3.4 nm.

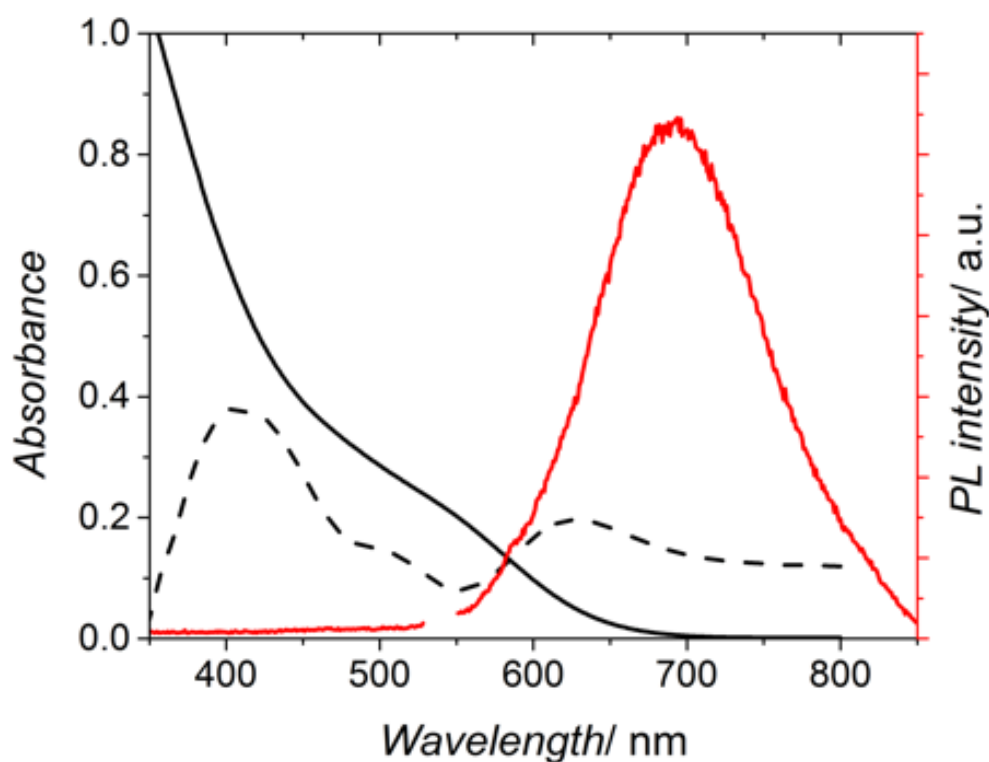


Fig. 4.6 UV/Vis (black line) and PL (red line) spectra of CIS/ZnS QDs dispersed in hexane. The dashed line shows the second derivative of the absorption spectrum, revealing the first band centre at ~ 540 nm.

The PL and UV/Vis absorption spectra of the CIS/ZnS QDs are consistent with literature [19, 63, 77, 108] and, as expected, the formation of a ZnS shell significantly enhances the PL intensity and slightly blue-shifts the emission, as reported elsewhere [12]. The PL recorded for core-only CIS QDs (red, solid line) in comparison to

CIS/ZnS QDs (black, solid line) is shown in figure 4.7(a) and highlights the dramatic increase in PL upon shell growth. The triangular shape of the CIS QDs determined with TEM is shown in figure 4.7(b-e) (courtesy of Dr. M. Booth [11]).

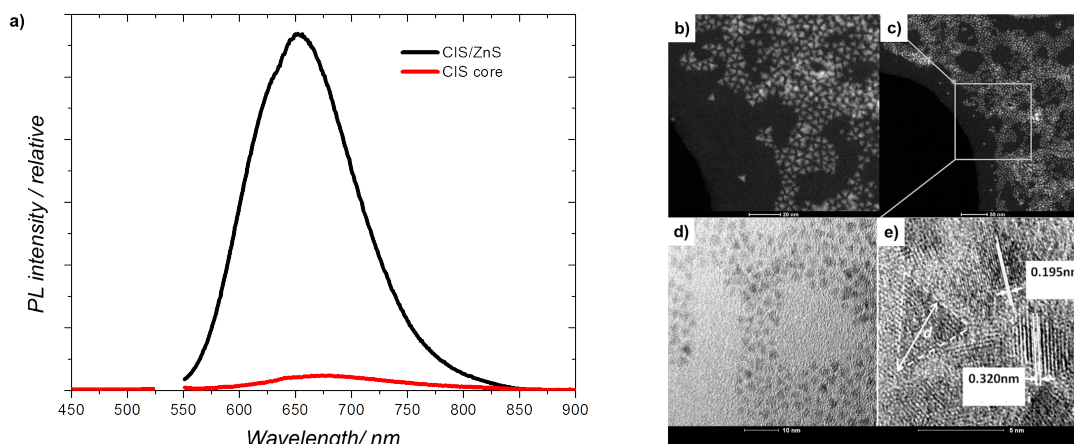


Fig. 4.7 PL spectra (a) of CIS/ZnS QDs (black) and CIS core (red). TEM (b-e) of CIS/ZnS QDs.

4.3.2 Femtosecond Transient Absorption Spectroscopy

Figure 4.8 shows the spectral transient absorption data as a function of time delay (Δt). The change in optical density (ΔOD) is calculated according to the formula given in figure 3.14. The strong loss in optical density ($\Delta OD < 0$) between 550 nm and 700 nm corresponds to a reduction in absorption or a gain due to stimulated emission. This band aligns with the first excitonic feature seen in figure 4.6, and indicates a GSB (that slowly recovers over the first 20 ps). A significant but rapidly-decaying positive signal ($\Delta OD > 0$) is observed within 5 ps at longer and shorter wavelengths, and is associated with ESA.

Besides the GSB, which results in reduced absorption following the partial removal of the ground state population, a negative signal can also result from an emission process stimulated by the probe light. Such an SE signal is expected in photoluminescent samples and should, in principle, resemble the steady state PL spectrum. Despite the large Stokes-shift observed in CIS/ZnS QDs, the features in the absorption and the PL spectra are both broad enough to overlap significantly between 550 nm and 700 nm. Thence the negative TA signal in this region might therefore be expected to contain contributions due to both SE and GSB.

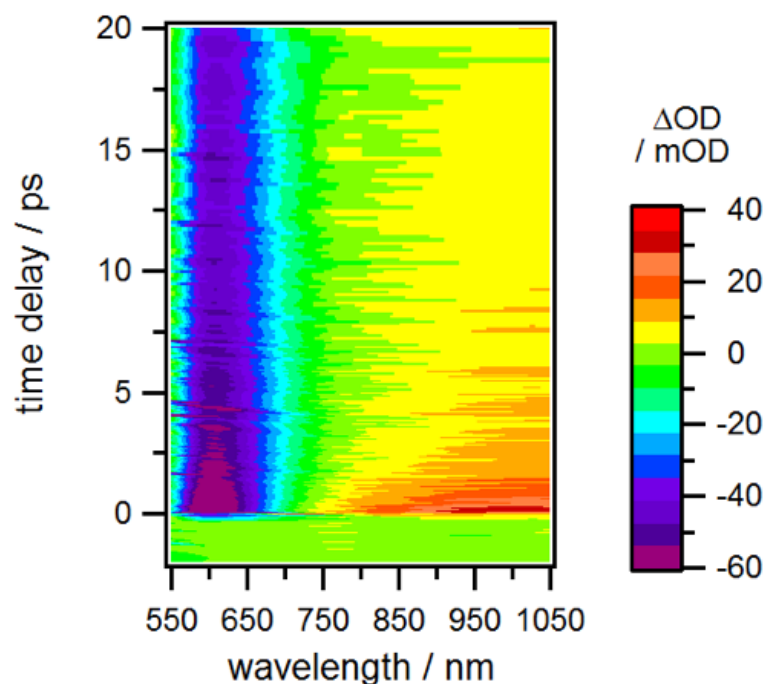


Fig. 4.8 TA spectrum of CIS/ZnS QDs over the first 20 ps after excitation at 540 nm

Spectral Data and Analysis

The transient data in figure 4.9 show the excited state evolution over the first 20 ps after excitation, at various pump wavelengths in the range 540 to 772 nm (a-d). Spectral profiles through the transients at ~ 1 ps show that the combined negative signal is red-shifted and apparently broader with increased pump wavelength. Since the GSB component is not expected to shift with pump wavelength, the observed red-shift could be related to an SE component stretching out to longer wavelengths.

In fact, initial fitting done on spectral cuts at 10 ps reveal such a negative band around 700 nm. The initial spectral fitting is carried out on spectral cuts at 10 ps taken from the TA data sets pumped at 540 nm, 625 nm, 655 nm and 772 nm, as shown in figure 4.9. The scattered light from the pump laser is removed manually for the data sets for 625 nm, 655 nm and 772 nm. In the initial spectral fitting the minor (1-3 mOD) ESA contribution in the range 510 to 900 nm is treated as a linear offset (i.e. a broadband background) and subtracted from all spectral cuts. Subsequently, the strong negative band is fitted with two Gaussian components with no constraints in the range between 510 and 900 nm, with the exception of the 540 nm data set to which is applied a fitting range between 600 to 900 nm (due to scattered light from the 540 nm pump pulse). The fit results in two spectral components with significant amplitude: one centred close to 615 nm and another centred at about 685 nm. This is consistent

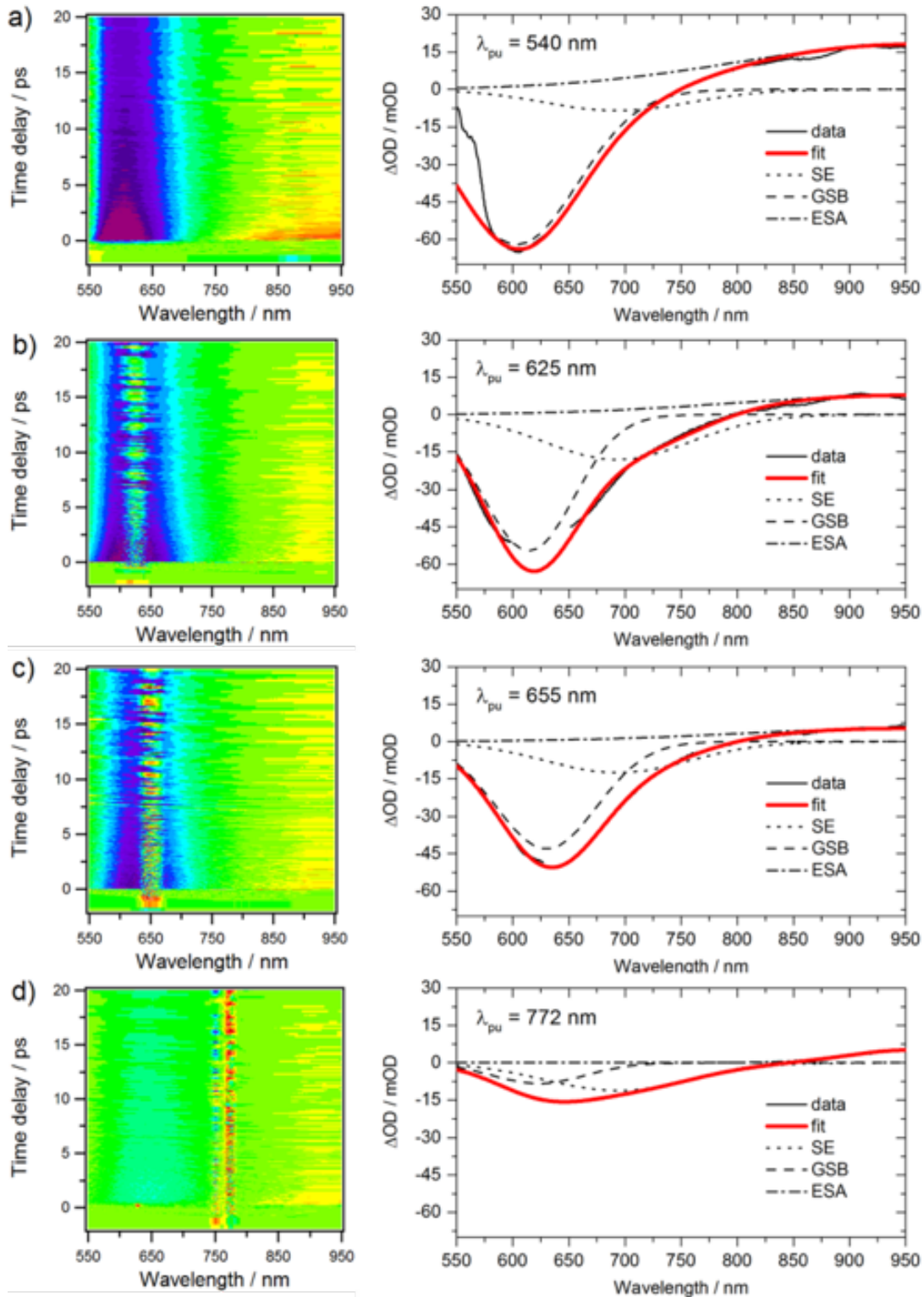


Fig. 4.9 TA data with spectral cut (at ~ 1 ps) of CIS/ZnS QDs acquired with varying excitation wavelength and pump intensity. a: $\lambda = 540$ nm, $1.1 \mu\text{J}$; b: $\lambda = 625$ nm, $0.6 \mu\text{J}$; c: $\lambda = 655$ nm, $0.7 \mu\text{J}$; d: $\lambda = 772$ nm, $4.5 \mu\text{J}$. TA data colour scale as in figure 4.8.

over all four spectral cut data sets (see figure). Based on the steady-state PL data, the peak at 685 nm is assigned to the expected emission from the highly luminescent QDs and the peak at 620 nm is assigned to GSB.

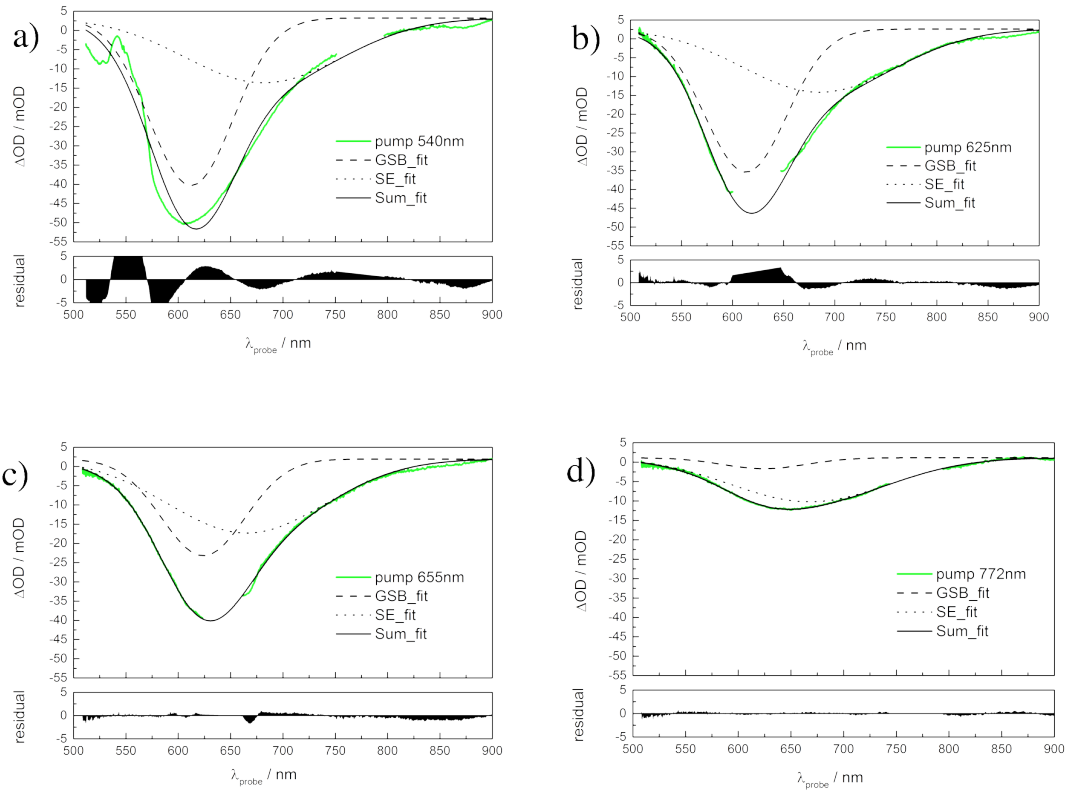


Fig. 4.10 Spectral cuts (at ~ 10 ps) of CIS/ZnS QDs acquired with varying excitation wavelength and pump intensity. a: $\lambda = 540$ nm, $1.1 \mu\text{J}$; b: $\lambda = 625$ nm, $0.6 \mu\text{J}$; c: $\lambda = 655$ nm, $0.7 \mu\text{J}$; d: $\lambda = 772$ nm, $4.5 \mu\text{J}$.

The ~ 1 ps spectral cut data in figure 4.9 are then fitted in a second step using three Gaussian components: one positive, centred at 950 nm, representing ESA, and two negative, representing GSB and SE. No constraints are imposed on the GSB component. The centre position (693 nm) and FWHM (100 nm) are fixed for the SE component on the basis of the steady state PL spectrum, but no constraints are imposed on the amplitude of any of the three components. A strong positive signal at the excitation wavelength, an artefact of the incomplete subtraction of scattered excitation light, is removed manually from each profile prior to fitting. The ~ 1 ps cuts (solid bold line) with fitting (black dashed and dotted lines) are shown in figure 4.11 (a-d) together with the overall fit (solid red line) per spectral cut. As is revealed from the initial fitting, the long wavelength component of the negative signal is centred at ~ 700 nm and stretches out to about 850 nm, which is consistent with the steady state luminescence spectrum. The second negative component is assigned to the GSB signal. The red-shift of the neg-

ative band as a function of excitation wavelength can thus be understood as a change in the relative intensity of the GSB and the SE components. The spectral peak shift is shown in the illustration in figure 4.11 (b), depicting the sum of the fitting curves containing the components GSB, SE and ESA as received from the fittings shown in figure 4.11(a-d). The peak shift of the overall negative component is indicated with a red arrow. The shift from 610 nm to 640 nm is the result of a shift in relative amplitude mostly between the GSB and the SE component. Also shown with a second red arrow at 950 nm is the reduced ESA signal with increased excitation wavelength. The relative area of the SE component increases with pump wavelength, although the overall absorption cross-section falls rapidly (see figure 4.6), suggesting that saturation of the emitting state is occurring at shorter excitation wavelengths. With 772 nm excitation, direct absorption to the CB should not be energetically possible, yet a weak GSB signal is observed and the SE component remains relatively strong. Two-photon excitation may be weakly populating the CB, which subsequently decay to the trap states with high efficiency, avoiding saturation due to the low absorption cross-section.

Kinetic Data

Time-zero, scattered-light corrected kinetic traces close to the GSB and ESA centre positions of 620 nm and 950 nm respectively are shown in figure 4.12. Both signals appear instantaneously within the temporal resolution of the excitation laser (60 fs). Figure 4.12 (b) shows the first 5 ps of the 950 nm and 620 nm data points that have been used in the initial fitting (n.b. the 620 nm data set and its corresponding fitting function have been inverted in the normalisation step for easier comparison). The 620 nm data are fitted with a bi-exponential recovery function with offset (blue) and the 950 nm data with a tri-exponential decay function with offset (red). The extracted time constants for the bi-exponential recovery function at 620 nm are (27 ± 1) ps and (1.8 ± 0.1) ps.

After 2.8 ns the transient at 620 nm levels off to an intensity of -31 mOD (see figure 4.12(c)), which corresponds to 45 % of the initial value at time zero. That the GSB recovery is incomplete is consistent with a fraction of the excitons being trapped in the emitting state on a timescale of 10-100 ns, as previous time-resolved PL studies have also suggested [63]. The kinetic data at 950 nm (figure 4.12(a)) are fitted with the two time constants derived from the 620 nm data (i.e. 1.8 ps and 27 ps), but require an additional fast (0.5 ± 0.2) ps component, which makes up 43 % of the overall signal amplitude at 950 nm, to describe the early decay seen in figure 4.12(b). We therefore assign this ultra-fast component that is only present in the ESA signal to a non-radiative

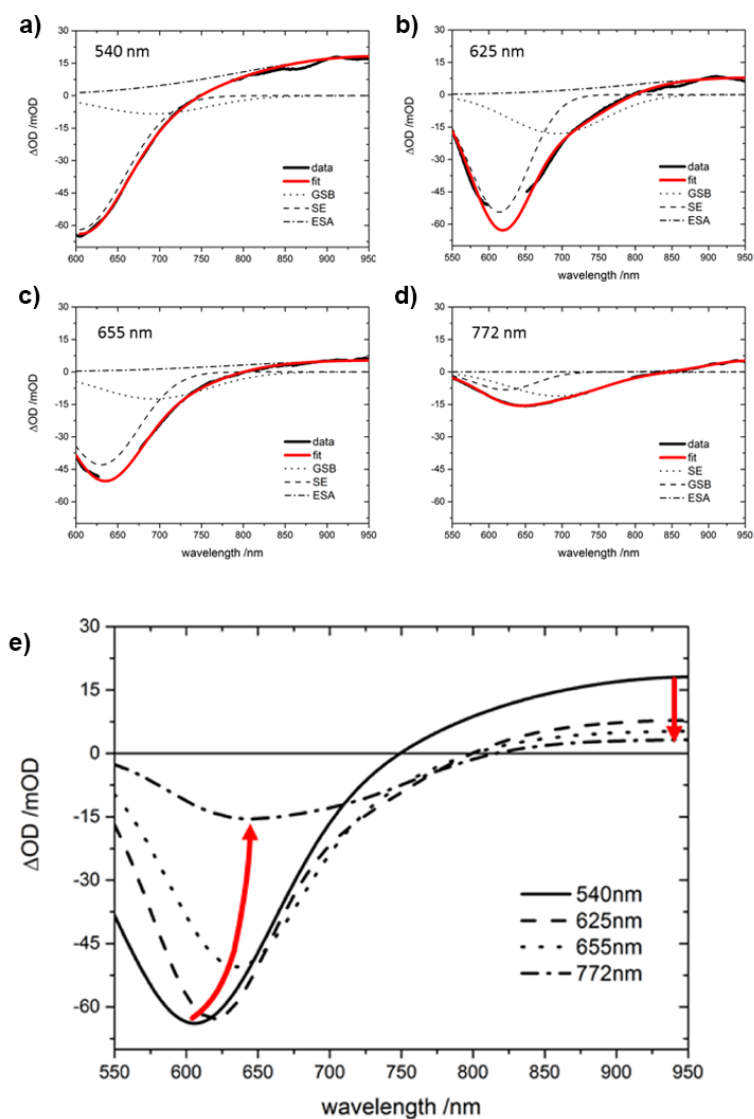


Fig. 4.11 Spectral cuts with spectral component fitting (at ~ 1 ps) of CIS/ZnS QDs acquired with varying excitation wavelength - a: $\lambda = 540$ nm; b: $\lambda = 625$ nm; c: $\lambda = 655$ nm; d: $\lambda = 772$ nm. e: Illustration of spectral shift based on overall fitting given in this figure (a-d). Indication of spectral shift (curved red arrow) and reduction in ESA signal (red arrow).

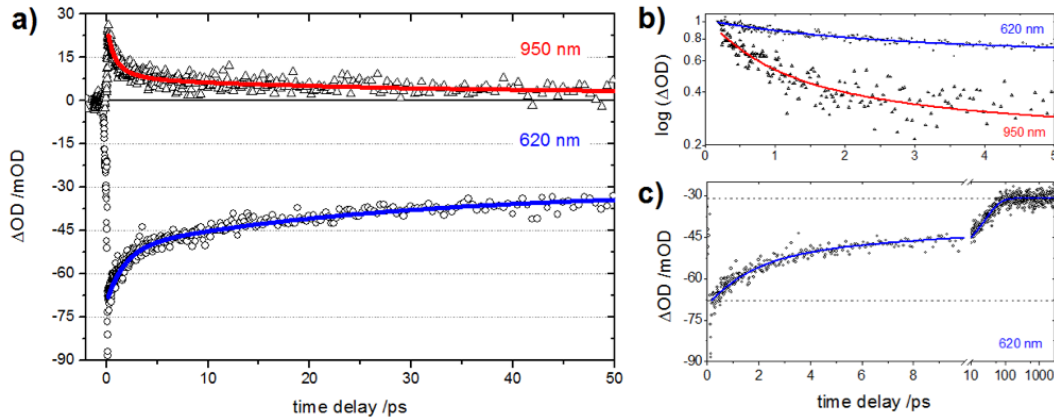


Fig. 4.12 Kinetic cuts (a) at 620 nm (circles) with the blue line representing a bi-exponential fit and at 950 nm (triangles) with the red line representing a tri-exponential fit. b: First 5 ps with normalized data points for the fitted range on a logarithmic scale (620 nm data inverted). c: Kinetics showing initial signal amplitude and final amplitude at 2.8 ns for the 620 nm data. Note the break in the linear time delay axis at 10 ps to logarithmic scale.

decay into the long-lived emissive state, most likely a deep donor state arising from an internal point defect. Kinetic analysis of the data presented in figure 4.9(d) also indicates a growing SE signal component with $\tau = \sim 0.4$ ps (at ~ 700 nm), a further indication of a relaxation mechanism via a sub-bandgap state. A magnification of the first 5 ps of the data set shown in figure 4.9(d) is given in figure 4.13(a), together with a series of spectral cuts at 600 nm, 650 nm and 700 nm (figure 4.13(b)). The approximate rise time of the fitting (single exponential) is 185 fs, 265 fs and 360 fs for the cuts at 600 nm (black solid line), 650 nm (red solid line) and 700 nm (green solid line) in figure 4.13(b).

A correlation between the amplitudes of the 27 ps component in the 620 nm and the 950 nm signals is observed, each making up 30 % of the total amplitude, once the data is normalised to exclude the carriers trapped in the long-lived state. This indicates a direct coupling between the CB and VB that can be described by Auger recombination. Multi-excitation processes, such as Auger effects, require high pump fluence, which our experimental conditions provide; the average occupation number of the 1s electron state, $\langle n_{1S} \rangle$, is calculated and found to be close to unity as shown in the following calculation:

The average occupation number is calculated for an excitation wavelength of 540 nm and pulse energy of 1.1 μJ as used in the experiment:

The pump fluence (j_p) is estimated based on a Gaussian beam waist calculation.

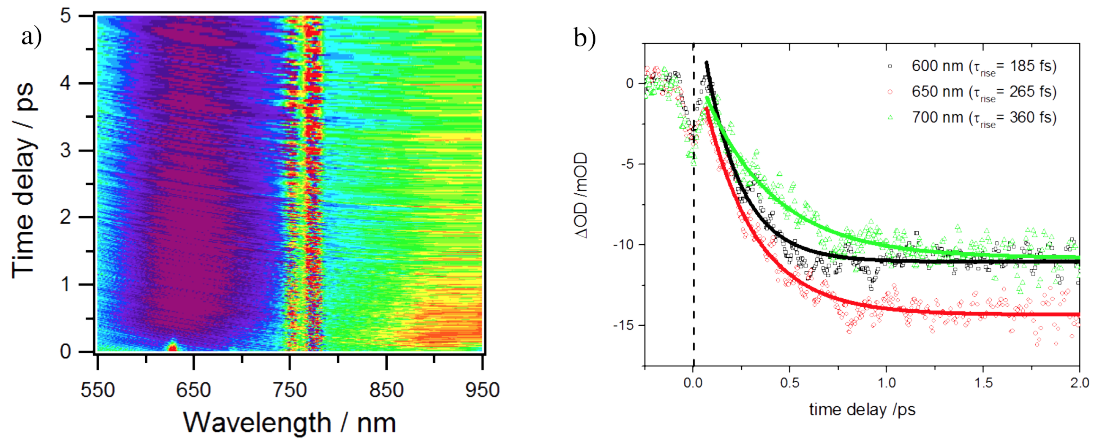


Fig. 4.13 Magnification (a) of the first 5 ps of the TA data set ($\lambda = 772$ nm) as shown in figure 4.9(d). Colour scale: ± 5 mOD. Raman bands of the solvent (n-hexane) are also visible at time zero. The line at ~ 772 nm is the result of incomplete scattered light subtraction. Kinetic cuts (b) with fitting at 600 nm, 650 nm and 700 nm. Time zero indicated with a dashed line.

The fluence is given for a spot size radius of about 50 to 60 μm with ~ 10 mJ cm^{-2} .

$$j_p = 2.72 \times 10^{16} \text{ cm}^{-2} \quad (4.1)$$

Comparing the high pump fluence with figure 2(b) and 4(b) in the work by Sun et al. [103] and Li et al. [63] respectively, indicates that the experiments are conducted in the saturated regime.

The absorption cross section (σ_α) for CIS QDs is converted from the extinction coefficient as determined following the method outlined in a previous publication [12] for a wavelength of 540 nm.

$$\sigma_\alpha = 2.12 \times 10^{-15} \text{ cm}^2 \quad (4.2)$$

The average number of photons absorbed is therefore given by

$$\langle N \rangle = j_p \times \sigma_\alpha = 58 \quad (4.3)$$

If it is assumed that every photon absorbed leads to the generation of an electron-hole pair (as expected in the low fluence regime) then the state occupation probability

$\langle n \rangle$ is estimated for the 1S state [52, 103]

$$\langle n_{1S} \rangle = 1 - e^{-\langle N \rangle} \left(1 + \frac{\langle N \rangle}{2} \right) \cong 1 \quad (4.4)$$

However, in our case this is not representative of the number of excitons per QD. This is likely to be because the calculation above is only valid in cases where either the pump fluence is small or the excitation energy is significantly greater than the band gap energy [52]. The large pump fluence and the excitation energy close to the band gap energy used here suggest that this model is therefore not applicable. However, this implies that the experiments were performed in the saturated regime, which is further confirmed when comparing our pump fluence of $\sim 10 \text{ mJ cm}^{-2}$ with figure 2 (b) in the paper by Sun et al. [103]. Thus, the offset in the 620 nm data could also include a contribution from Auger recombination. The faster component of $\sim 1.8 \text{ ps}$ could be explained by either carrier cooling or additional carrier trapping, most likely at the remaining surface defects due to incomplete surface passivation with ZnS. However, the excitation wavelength in this study is such that single-photon excitation into higher quantised states is unlikely based on energetic grounds. Carrier cooling is therefore expected to be minimal and we attribute the 1.8 ps component to surface trapping. This is corroborated by a lack of characteristic derivative-shaped spectral features in the GSB (see figure 4.8).

4.3.3 Pump-Dump-Probe Experiments

To confirm that the 0.5 ps time constant is related to the observed PL in CIS/ZnS QDs, a dump laser centred at a wavelength longer than the absorption band edge is used to drive the stimulated emission process. The TA spectrum shown in figure 4.8(a) is pumped at 540 nm and dumped, after 6 ps, at 772 nm. Kinetic profiles at 600 nm, 695 nm and 950 nm are shown in figure 4.8(b). At the dump time position, of the total signal intensity at 600 nm and 695 nm are reduced to $\sim 42 \%$ and $\sim 75 \%$ relative to the previous values respectively, whereas the ESA at 950 nm is unaffected. No spectral decomposition is performed, however the latter qualitative observation is the most interesting, as it provides direct evidence that the absorbing excited state is not depopulated by the dump laser and is therefore not the emissive state. The instant appearance of the ESA signal with the excitation laser implies it originates in the CB, whilst the delayed rise of the SE component ($\sim 0.4 \text{ ps}$), which fits well with the 0.5 ps time constant assigned to a decay into an intra-gap state, implies that the SE originates from a

sub-bandgap state. Therefore, the traditional picture of both ESA and SE originating from the CB [103] is not consistent with the pump-dump-probe data. The TA signal in the wavelength region of 750 nm to 850 nm shows a small increase in absorption, which is interpreted as a loss of the SE signal upon population dump. This observation lends support to the idea that the observed room temperature PL in CIS/ZnS QDs can be attributed to the fraction of electrons undergoing an ultra-fast, non-radiative relaxation from the CB into a long-lived, high-lying donor state. Whether the PL originates from a coupling with a low-lying acceptor state or with the valence band remains an open question. However, the instantaneous response of the GSB signal to the dump laser indicates either direct coupling to the valence band or ultrafast decay of the populated low-lying acceptor state on a sub-150 fs timescale. In either case, it is clear that the emission cannot originate from the CB edge, but rather it must involve high-lying intra-gap donor states. Our results point towards an electron-hole recombination via a trapped electron, which is contradictory to the conclusion drawn in a recent publication by Cadirci et al. [17] that also investigates relaxation dynamics with femtosecond TA spectroscopy. Cadirci et al. [17] point out that 'the maximum bleach should be twice the value after electron trapping', which is in agreement with the data presented here in figure 4.12(c) where the bleach amplitude increases from -70 mOD to a plateau of approximately -32 mOD after 50 ps. Admittedly, a direct comparison between the study by Cadirci et al. [17], carried out on CIS core-only QDs, and the work presented in this thesis is difficult since the experimental conditions, such as excitation wavelength and pump fluence, are different. Further to this, the ZnS surface passivation layer on the QDs in our work is known to influence the trapping behaviour. Nevertheless, our findings are further supported by a recently published study by Omata et al. [85], who carry out a detailed size-dependent photoluminescence study on CIS core-only QDs, and who attribute the origin of the PL emission to either indium-copper anti-site defects (In_{Cu}) and/or sulphur vacancy (V_{S}) defect states. It is argued that the V_{S} -to- V_{Cu} (copper vacancy, V_{Cu}) non-radiative coupling is the dominant recombination pathway in CIS core-only QDs as the density of V_{S} and V_{Cu} at the surface is high [77]. This agrees with the interpretation by Klimov et al. and explains the low PLQY with competitive non-radiative pathways related to surface states [53]. It is thus generally accepted that V_{S} trap states at the QD surface provide a very efficient de-excitation channel in CIS QDs, and that they can be suppressed by surface treatment [49, 51, 53, 77, 100, 110]. Based on the dramatic gain in PLQY upon surface passivation, along with the observed effect of $[\text{Cu}]/[\text{In}]$ ratio on PLQY, it is clear that V_{Cu} states at the surface are not involved in the highly radiative recombination route in fully passivated CIS/ZnS QDs. The fs-TA data reveal a minor (~ 3 mOD) residual ESA component, even after 2.8 ns.

The insensitivity of this signal to the dump laser precludes the emitting trap states as the origin of this signal.

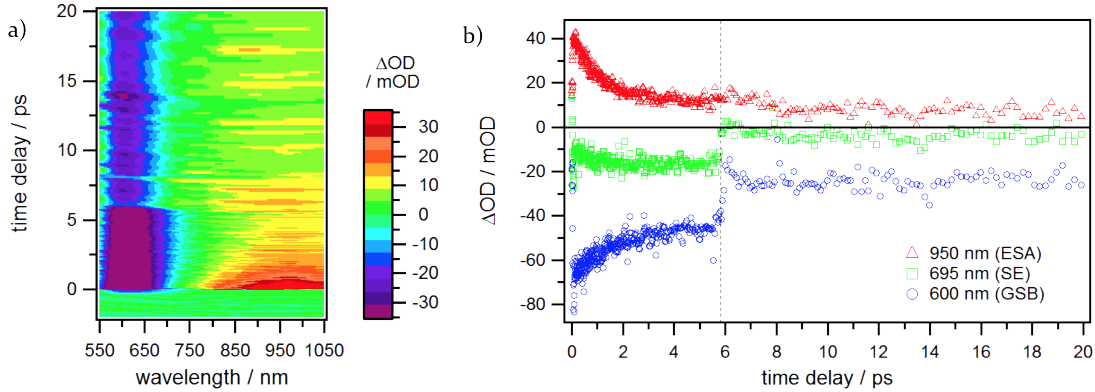


Fig. 4.14 TA spectrum of CIS/ZnS QDs (a) dumped at 772 nm, after 6 ps. The kinetics (b) are analysed at the GSB (blue dots, SE (green squares) and ESA (red triangles) spectral fitting positions, resulting from the analysis in figure 4.9. The temporal position of the dump pulse is indicated (dashed line).

There remain two possible origins for the long time offset in the ESA. Internal defect sites may trap a small fraction of the CB population in the interior of the QDs and in the absence of efficient non-radiative decay via surface V_{Cu} sites, these traps may be long lived. Alternatively, the formation of a photoproduct could give rise to this offset after a long time delay. There is some evidence in the 950 nm data (figure 4.8(b)) for a picosecond timescale decay of the ESA residual following the dump pulse, which might suggest a refilling of the depopulated trap states. However, the effect is weak and our data are not conclusive in this regard. Furthermore, this effect would not occur under weaker illumination, as would be the typical conditions for relevant applications. Based on studies of the similar semiconductor $Cu_{In}Se_2$ the neutral defect complexes $[In_{Cu}^{2+} + 2V_{Cu}^+]$ and $[Cu_{In}^{2-} + In_{Cu}^{2+}]$ can be expected to have relatively low formation energies in CIS, especially in the copper-poor phase [46]. Furthermore, the formation of $[Cu_{In}^{2-} + In_{Cu}^{2+}]$ anti-site dimers is promoted in the vicinity of $[In_{Cu}^{2+} + 2V_{Cu}^+]$ defects, and large defect 'clusters' tend to form around sulphur anions, especially in nanocomposite CIS [78]. The identification of In_{Cu} or Cu_{In} defects being involved in the highly radiative recombination process is therefore consistent with observations of the effects of off-stoichiometry on the PLQY. [19] From μs -TA studies in the bulk it is known that the In_{Cu} state is an effective trap state (20 μs) [35] that can emit to the valence band, as can Cu_{In} states. Nam et al. have previously discounted both DAP recombination and transitions directly into the valence band (VB) on the grounds that the dependency on QD size of the VB and intra-gap states cannot account for the size dependence of the

observed PL spectrum. They therefore conclude that CB emission must be involved in the radiative transition [77]. However, the extent to which the individual VB, CB and intra-gap state energies depend upon QD size is not well known. Cyclic voltammetry studies performed on CIS QDs of various sizes indicate that the CB and VB actually shift much more evenly than predicted from confinement models that are based on the effective-mass approximation [86, 123]. We therefore propose a model of the relaxation dynamics of CIS/ZnS QDs involving emission from deep In_{Cu} trap states, as shown in figure 4.15.

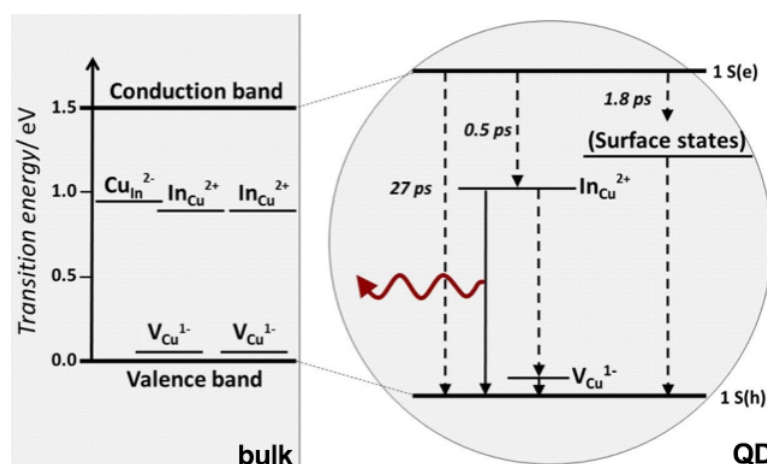


Fig. 4.15 Illustration of the proposed recombination pathways involving the intra-gap defect complexes $[\text{Cu}_{\text{In}}^{2-} + \text{In}_{\text{Cu}}^{2+}]$ and $[\text{In}_{\text{Cu}}^{2+} + 2\text{V}_{\text{Cu}}^{1-}]$ in bulk CIS (left) and quantum-confined CIS/ZnS QDs (right). Solid lines represent proposed radiative transitions and dashed lines represent non-radiative transitions.

In figure 4.15, the defect states are represented by their reported positions (in bulk CIS) relative to the valence band maximum [20], which is taken as the zero-energy level, although the shifts in energy shown in figure 4.15 for the CIS QDs are only estimated. The observed PL maximum at 693 nm corresponds to 1.79 eV, which appears to be consistent with a donor state to VB transition. The corresponding Stokes shift of ~ 0.5 eV (based on a band gap of ~ 2.3 eV) is consistent with the expected relative positions of In_{Cu} or Cu_{In} defects to the CB, assuming such deep trap states move only weakly with the CB energy as the particle size is reduced. It is known that the electronic structure of ternary chalcopyrite compounds, in particular the hybridised p and d orbitals near the VB edge, lead to an increased VB energy in bulk CIS. As the QD dimensions are reduced, the energetic overlap and thus the exchange integrals between the S $4p$ and Cu $3d$ orbitals will be reduced due to confinement. Therefore, the extent of p - d hybridisation can be expected to be reduced, lowering the VB energy and increasing the observed band gap [45, 120]. Similar effects have been demonstrated in

copper-doped CdSe QDs [118] and HgTe nanoparticles [93]. Our model of In_{Cu}-VB emission in CIS QDs, based on our femtosecond dump data, is consistent with theoretical models of size dependence in ternary chalcopyrite systems, once hybridisation effects are considered.

4.4 Conclusion

Steady state spectroscopy performed on CIS QDs indicates the involvement of intra-gap states in the photoluminescence process, which is consistent with studies on CIS in thin film and bulk [18, 35, 40, 56, 68]. In this study, transient absorption (TA) spectroscopy was performed on CIS/ZnS QDs, revealing two time constants (27 ps and 1.8 ps) in the recovery of the negative component. We identify the 27 ps time constant as Auger recombination and the 1.8 ps time constant as population flow into a surface defect state. A third time constant (0.5 ps), observed only in the infra-red excited state absorption (ESA) signal, is related to a non-radiative decay into an internal defect state. A dump laser was used to depopulate the upper state of the radiative transition. Significantly, the excited state absorption at long wavelengths was unaffected by the dump pulse, confirming that the radiative transition does not involve the conduction band, as has previously been proposed by others [17, 63, 77, 103], but involves one of the high-lying donor states. This clarification highlights the ability of standard fs-TA spectroscopy, modified by the inclusion of a third dump laser, to control carrier populations. This enables extended insight into excited state dynamics, as we have shown here. Based on recent literature discussing the enhanced PLQY of CIS/ZnS QDs and copper-deficient CIS QDs compared to stoichiometric CIS QDs, together with the time constant assignment in this work, we identify the indium-copper anti-site as being the origin of the observed photoluminescence. The anomalous Stokes-shift and broad non-band-edge emission in CIS and CIS/ZnS QDs are explained by this model. The results presented in this work may be of potential importance to charge extraction in CIS QDs sensitised solar cells and to the optimisation of the PLQY for biological imaging applications.

Chapter 5

Excited State Dynamics of Pyrrole-2-carboxylaldehyde

5.1 Introduction

The comparison between molecular dissociation dynamics in the gas and solution phases has become a recent topic of interest. It is often assumed that significant changes to the isolated molecule dynamics occur upon solvation. However, recent results from tests on heteroaromatic systems suggest that an important class of dissociations, occurring via $1^1\pi\sigma^*$ states persist in solution [95]. Pyrroles are the prototypical N-heterocyclic chromophores and are of fundamental interest because of their photodynamics. In the gas phase, pyrrole itself is known to dissociate via the H atom loss channel at ≤ 254 nm [23], showing significant vibrational adiabaticity (i.e. maintaining the initially excited vibrations) in the dissociation channel, proceeding via several exit channel conical intersections. More recently, the role of these non-adiabatic couplings has been examined by Ehrenfest Quantum Dynamics [98] and it is likely that the pathway to the dissociated pyrrolyl products involves more than one electronic state. Pyrrole-2-carboxaldehyde (PCA) is the simplest carbonyl-substituted pyrrole. Its dimers were the preferred prototype for beta-sheet peptide models [94]. PCA was also used in the first synthesis of porphines, the parent compound of porphyrins [32]. The best-known porphyrin is the red colouring pigment heme, a co-factor of haemoglobin found in blood cells necessary for oxygen transport in blood cells. PCA is a clear crystalline material at room temperature (mp 43-46 °C) and readily soluble in protic solvents, such as water and alcohols. PCA is expected to exhibit absorption at longer wavelengths than bare pyrrole due to the extended π -system created by the conjugation of the C=O group with the 4 π electron system of the pyrrole ring. PCA can form two

flat conformers: cis-PCA and trans-PCA (figure 5.1).

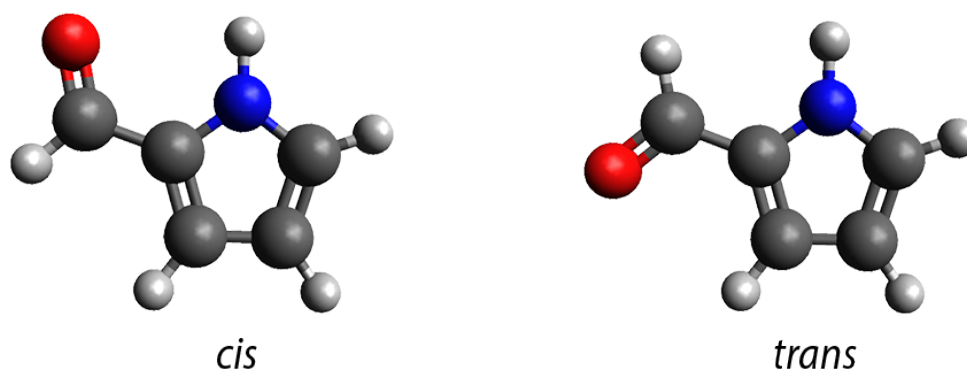


Fig. 5.1 Cis and trans pyrrole-2-carboxaldehyde

Several experiments in the gas and solution phases suggest that the cis-conformer is the more stable form at room temperature [70]. The torsional potential of PCA around the C-C bond linking pyrrole and the aldehyde group is computed as part of the study by Rice et al [94] with optimisation of all other structural parameters. The relative energy of the trans-conformer is reported to be approximately 15 kJ mol^{-1} higher in energy than the cis-conformer [34, 94]. From this, one estimates the population of the cis-conformer to be greater than 99 % at room temperature.

Transient absorption (TA) spectroscopy allows femtosecond time-resolved probing of the electronic state evolution following photoexcitation. However, wavelengths shorter than $\sim 260 \text{ nm}$ are difficult to access, and would require sum frequency mixing processes. One of the primary aims of this study is to determine the energetic threshold for the onset of $1^1\pi\sigma^*$ mediated H atom loss in the gas and solution phases. The $1^1\pi\sigma^*$ onset in pyrrole is known to exist at 257 nm [23], with very weak absorption occurring until the $1^1\pi\pi^*$ absorption onset at approximately 225 nm is accessed. As such the extended π -system in PCA appears to be ideal as a subject of investigation, as the absorption is expected to be shifted to lower energy. In addition, the TA experiments should give an indication of the role of other non-radiative pathways both above and below the $1^1\pi\sigma^*$ threshold, which are not observable in the gas phase H atom detection experiment. Other aromatic carbonyl systems have been studied in detail by solution phase [72] and gas phase [2, 37, 60, 89] transient methods and all exhibit ultrafast intersystem crossing dynamics. However, pyrrole compounds are intermediate in terms of their degree of aromaticity [43] and there exists little previous work on the deactivation dynamics of its excited states. In particular, the question of triplet participation in the deactivation of this pyrrole-based aromatic carbonyl is not addressed in the literature. Recent ab-initio computational studies [24, 30, 31, 47, 61, 87] identify

three-state crossings from the singlet to the lowest triplet state via a relay triplet state in aromatic carbonyl compounds such as benzaldehyde, acetophenone and benzoic acid. PCA is iso-electronic with benzaldehyde, so the analysis of excited state relaxation in aromatic carbonyl compounds is potentially useful.

This chapter reports primarily on solution phase experiments that are conducted with femtosecond transient absorption (fs-TA) spectroscopy at the University of Leeds and links the recorded observations with N-H photodissociation dynamics observed in the gas phase with H atom phototranslational spectroscopy (H atom PTS), performed in collaboration with Dr. T. Karsili and B. Marchetti in the group of Prof. M. Ashfold at the University of Bristol. Ab-initio calculations are used to assist in the spectral assignment of the fs-TA data and to derive potential energy cuts. The reported potential energy cuts presented in figure 5.9 were computed by Dr. T. Karsili.

5.2 Methodology: Experimental Details, Method Development, Computational Details

5.2.1 Transient absorption spectroscopy

A detailed description of the femtosecond transient absorption setup is provided in section 3.1.1. Solid PCA (Sigma Aldrich, purity >99 %) is dissolved in ethanol (Sigma Aldrich, purity ≥ 99.5 %) to form clear solutions of $c \simeq 15 \text{ mmol L}^{-1}$ and $c \simeq 40 \text{ mmol L}^{-1}$ for experiments in the excitation range $\lambda_{\text{pump}} > 240 \text{ nm}$ and $\lambda_{\text{pump}} \leq 240 \text{ nm}$, respectively. Modifications to the standard transient absorption setup described previously are provided in the following two sub-sections:

5.2.2 Extension of Probe Continuum to the Ultra-Violet

In order to study the absorption spectrum in the UV range the probe continuum generation stage (as outlined in section 3.2.4) is modified. A fraction (10 μJ) of the 772 nm is frequency doubled in a 200 μm -thick BBO crystal to produce about 3 μJ of 386 nm light. A highly reflective (HR800) mirror set before the continuum generation stage is used to remove the residual 772 nm light. As described previously, the continuum generation is then carried out in water and the stability of the white light source is optimised with the use of an iris and a variable neutral density filter. The UV continuum provides the ability to probe a wavelength range between approximately 310 nm and 390 nm.

5.2.3 'Deep'-UV Pump with Sum-Frequency Mixing

The TOPAS-SHG stage is modified to support a sum frequency mixing scheme in a co-linear optical parametric amplification step as shown in figure 5.2. A part ($200 \mu\text{J}$) of the CPA output is frequency doubled to give $70 \mu\text{J}$ at 386 nm and is then mixed with the tunable TOPAS-white output, which is then made co-linear to the second harmonic pulse in a BBO crystal ($200 \mu\text{m}$). The sum-frequency mixing (SFM) scheme allows for the generation of excitation pulses in the wavelength range between 220 nm and 245 nm with an output energy of up to $1 \mu\text{J}$ at 245 nm at the sample. The typical excitation power used in an experiment is attenuated to be less than $0.1 \mu\text{J}$. Along the beam path from the pump pulse generation to the sample, highly reflective dichromatic mirrors are installed, with the exception of the retro-reflector (Newport, UV enhanced aluminium coated) that is mounted to the delay stage and the final focusing mirror (silver, $f = 100 \text{ mm}$) set before the sample cell. The known limitations of the power output and temporal resolution can be addressed in the following ways: The low reflectivity of the retro-reflector and the final focussing mirror can be improved to get a higher pulse intensity at the sample by using highly reflective mirrors more suitable for the UV range. Moreover, the co-linear beam setup limits the amplified bandwidth and leads to a temporal stretching of the generated pulse in comparison to the traditional co-linear OPA described in section 3.2.2. Amplifying a larger spectral width in a non-colinear setup should in principle enable temporally shorter pulses and might allow access to even shorter wavelengths than the current limit of about 220 nm .

5.2.4 H atom photofragment translational spectroscopy (H atom PTS)

A schematic diagram of the H atom PTS experimental set-up is given in section 3.1.3 and has already been described in detail [22, 23, 80]. The solid PCA sample (Sigma Aldrich, purity $>99 \%$) is packed in a stainless steel inline filter positioned upstream of a pulsed valve (General Valve, series 9) and heated to $\sim 50 \text{ }^\circ\text{C}$ in order to generate sufficient vapour pressure for the photodissociation experiments. At selected photolysis wavelengths in the range of 218 nm to 280 nm , the polarisation vector (ϵ_{phot}) of the photolysis laser radiation is typically aligned at an angle $\Theta = 0^\circ$, 90° or 54.7° (defined with respect to the TOF axis) using a double Fresnel rhomb in order to assess the H atom photofragment recoil anisotropy.

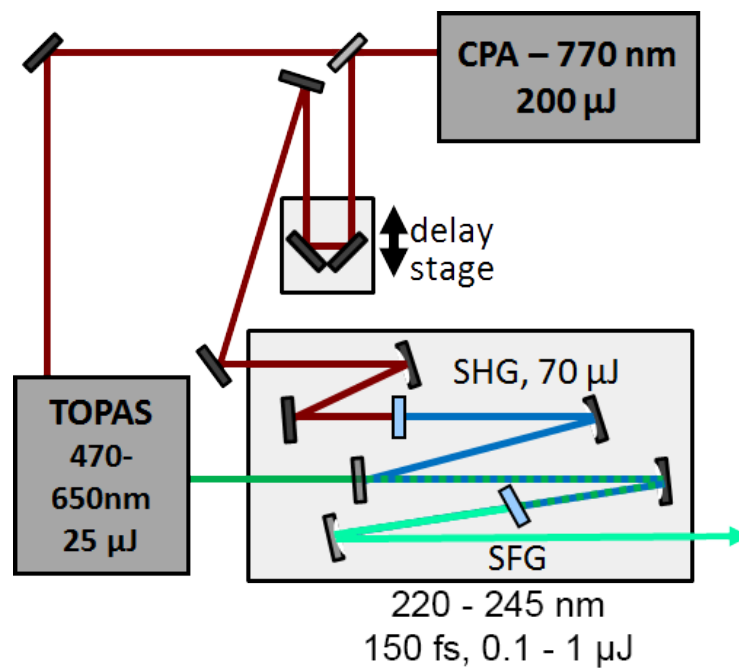


Fig. 5.2 Schematic of the sum-frequency mixing scheme. Modified TOPAS-SHS stage to support SFM in a close to co-linear configuration with components: input laser beams shown for TOPAS (green, solid line) and CPA laser beam (red, solid line) via delay stage; Second Harmonic Generation (SHG) of CPA input in first BBO crystal (indicated with blue rectangle); Sum-Frequency Generation (SFG) via mixing of SHG pulse (dark blue, solid line) with variable TOPAS input pulse (green, solid line) in second BBO crystal (indicated with slight blue rectangle).

5.2.5 Computational Details

The minimum energy geometry of the ground state of PCA is optimised using Møller-Plesset second order perturbation theory (MP2), along with Dunning's augmented correlation consistent basis set of triple- ζ quality: aug-cc-pVTZ (AVTZ) [26] using the Gaussian 09 computational package [Frisch et al.]. As a comparison, calculations are also carried out on bare pyrrole, the geometry of which is also optimised at the same level of theory. Planar geometries are imposed on both molecules throughout the optimisation process so the follow-up calculations are undertaken with C_{2v} (for pyrrole) and C_s (for PCA) symmetries. Using the MOLPRO 2010.1 computational package [116], transition dipole moments (TDMs) and vertical excitation energies to, respectively, the first four (for pyrrole) and first five (for PCA) excited singlet states are calculated using a state averaged complete active space self-consistent field (SA-CASSCF) method with the AVTZ (pyrrole) and AVDZ (PCA) basis sets, but with extra even-tempered sets of s and p diffuse functions on the N atoms in order to describe the Rydberg-valence mixing more effectively. For pyrrole, an active space comprising of 10 electrons in 10 orbitals is used following the earlier work by Domcke and co-workers [111] and Karsili et al.[48]. These orbitals are comprised of the three ring-centred (Hückel type) π bonding orbitals and the two π^* antibonding orbitals, the N centered 3s Rydberg orbital and two occupied σ and two virtual σ^* orbitals, one of each of which is localised around the N-H bond. For PCA, the choice of active space is non-trivial and requires rigorous investigation. Test calculations show that the optimum active space consists of 14 electrons in 13 orbitals (14/13). These include all of the orbitals used for bare pyrrole, plus one occupied π orbital centred on the C=O moiety along with its virtual π^* counterpart and the p_y orbital localised on the O atom. Unfortunately, the addition of these extra orbitals coupled with an SA6-CASSCF results in a vast increase in computational expense and requires the elimination of an extended ζ function. Thus the CASSCF calculations for PCA are undertaken using the smaller AVDZ basis set and, for internal consistency, the pyrrole PECs are then recalculated using this smaller basis set.

'Unrelaxed' (rigid body) potential energy cuts (PECs) along the NH stretch coordinate, R_{N-H} , are then computed for the ground (1^1A_1), 1^1A_2 , 1^1B_1 , 1^1B_2 and 2^1A_1 electronic states of pyrrole; followed by the ground ($1^1A'$) and the lowest three A' and two A'' singlet excited states of PCA using complete active space with second order perturbation theory (CASPT2), based on a fully SA-CASSCF reference wavefunction with the remainder of the nuclear framework fixed at the optimised ground state geometry. In both cases, a small imaginary level shift of 0.5 a.u. is applied to encourage

convergence and circumvent intruder state effects.

Further DFT calculations for PCA and pyrrolyl-2-carboxaldehyde radical (2CPyl) as isolated gas phase species and in solvent solution are carried out at the TD-DFT/B3LYP/aug-cc-pVDZ level of theory to derive (vertical) excitation energies and the associated oscillator strengths, f . Those that are computed in solution are calculated using the IEFPCM polarisation continuum model (PCM) embedded within Gaussian 09, using a dielectric constant of $\epsilon = 24.852$, $\epsilon = 32.613$ and $\epsilon = 78.3553$ for ethanol, methanol and water, respectively. The latter calculations are also carried out with one explicit solvent molecule in order to account for possible charge transfer effects between the solvent and the PCA or 2CPyl molecule. Vertical excitation energies are calculated from the ground (1^1A_1), first triplet (T_1) and radical ground state (D_0) minima.

5.3 Results

PCA is readily soluble in ethanol, methanol and water to form a clear and colourless solution. Figure 5.3 presents static UV-vis absorption spectra of vapour phase PCA (heated to ~ 60 °C, [blue, dot-dash line]) and of PCA in ethanol solution [red solid line], methanol solution [black dotted line] and water solution [green dashed line]. The spectra are normalised to the most intense peak in the wavelength range shown.

The normalised vapour phase spectrum features four components: a shoulder centred at ~ 295 nm, an obvious peak at ~ 269 nm, a higher energy shoulder centred at ~ 242 nm and another feature that appears to peak at wavelengths below 200 nm. The most intense peak recorded in the solution spectra appears to be shifted to a lower energy with a peak centred at ~ 290 nm in the two alcohols and ~ 295 nm in water, the latter being the most protic solvent used. The low energy shoulder, as observed at ~ 295 nm in the vapour phase spectrum, is not distinguishable from the dominant peak in solvent and the actual onset is blue-shifted. The high energy shoulder is slightly red-shifted to about 250 nm in solvent. By comparing the vapour phase absorption spectrum with the solution phase spectrum (regardless of the solvent), it can also be observed that the high energy shoulder at 242 nm in the vapour phase appears to be significantly lower in intensity.

Solution phase fs-TA and gas phase H atom PTS data are recorded at many excitation wavelengths (λ_{pump}) in the range $315 > \lambda_{\text{pump}} \geq 218.25$ nm to investigate the time evolution of photo-excited PCA and potential N-H bond fission. Guided by the UV-vis absorption spectrum, experiments are initially carried out in the excitation range covering the most intense absorption features observed in the gas and solution spectrum

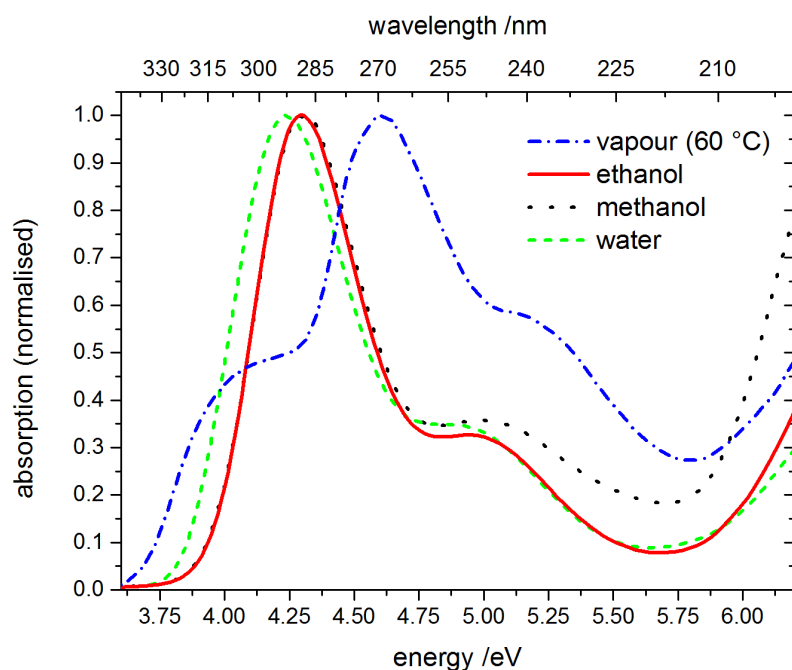


Fig. 5.3 UV-vis absorption spectra (normalized) of vapour phase PCA (blue, dot-dashed line) and as solution in ethanol (red, solid line), methanol (black, dotted line) and water (green, dashed line)

in the range between 315 nm and 225 nm (section 5.3.1). The results related to experiments with excitation wavelengths below 225 nm are given in section 5.3.2 for both the solution phase and the gas phase experiments.

5.3.1 Excited State Dynamics in the range 315-225 nm

Transient absorption spectroscopy

The TA data for PCA in ethanol solution are shown in figure 5.4 for an excitation wavelength at $\lambda_{\text{pump}} = 300$ nm, thus close to the absorption maximum known from the UV-Vis absorption spectrum (figure 5.3). The TA data shown are recorded with the VIS probe continuum (figure 5.4(b)).

The data set features two growing absorption bands. The first band is strongest at the short wavelength edge, appearing with a centre wavelength of ~ 400 nm) in figure 5.4(b). The second band is approximately centred at ~ 500 nm in the VIS probe continuum with a fwhm of approximately 75 nm. The apparent cut-off in figure 5.4(b) is the result of the weak probe light intensity at a short wavelength in the VIS probe continuum. These spectral features observed in the range 365 to 425 nm and 450 to 550 nm are representative for the excitation range $\lambda_{\text{pump}} \geq 225$ nm and are the only two

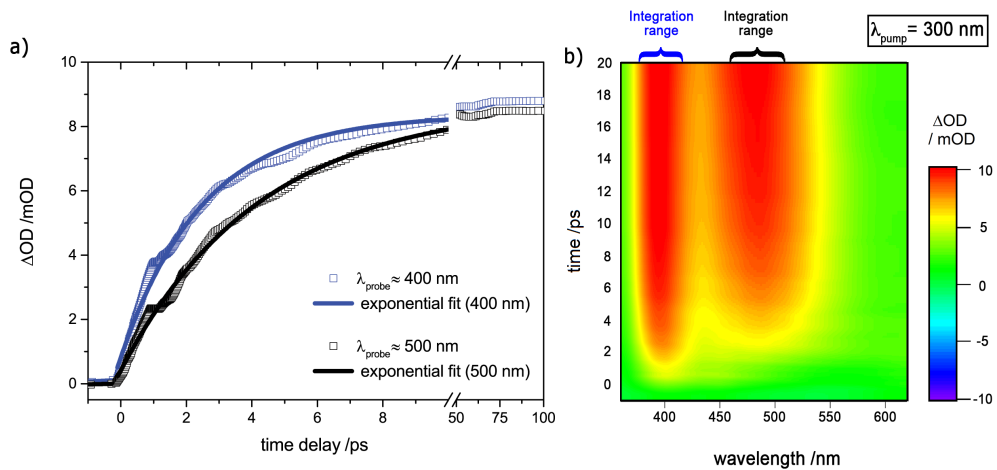


Fig. 5.4 Averaged transient (a) of PCA excited at 300 nm and corresponding contour plot (b) in the range 365 to 625 nm. Transient (a) shows a single exponential rise component for each of the broadband absorption bands observed in the contour plot (b) at ~ 400 nm and ~ 500 nm, respectively. Note the break in the time ordinate between 10 and 50 ps

bands observed in the probe range from 365 to 1070 nm. The kinetics shown in figure 5.4(a) are average kinetics by integration over the spectral domain range between 375 to 425 nm and 475 to 525 nm for the 400 nm (hollow blue squares) and 500 nm (hollow black squares) components, respectively. The kinetics are fitted with a single exponential with a resulting time constant of ~ 2.5 ps for the 400 nm and ~ 4.2 ps for the 500 nm component.

For consistency, a dataset is shown in figure 5.5 that uses the excitation light source of the SFM scheme as described in section 5.2.3. The dataset is recorded at $\lambda_{\text{pump}} = 233$ nm with the IR probe continuum. The chirp-corrected dataset features the rising absorption band at approximately 500 nm as has already been seen in figure 5.4. The oscillation is the result of pump light instability, due to the sum-frequency mixing process being highly non-linear to laser power.

A series of experiments in the excitation range $315 > \lambda_{\text{pump}} \geq 225$ nm is carried out with the TOPAS-SHG and TOPAS-SFM excitation light generated as outlined in sections 3.2.3 and 5.2.3 respectively. All experiments are conducted with an average pump energy of $\leq 1.2 \mu\text{J}$ and a spot size of $\sim 100 \mu\text{m}$ at the sample. A non-linear power dependence in the signal contribution is not observed even at an estimated pump fluence as high as 15 mJ cm^{-2} .

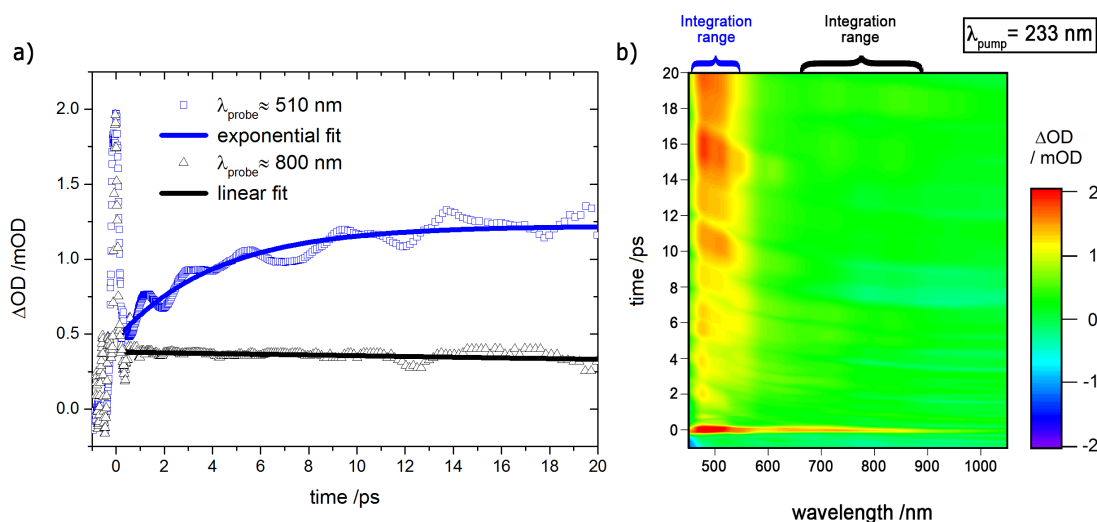


Fig. 5.5 Averaged transient (a) of PCA excited at 233 nm and corresponding contour plot (b) in the range 465 to 1050 nm. Transient (a) shows a single exponential rise component over a time window of 20 ps. Contour plot (b) shows a broadband absorption band centred at ~ 500 nm

H atom photofragment translational spectroscopy

H atom PTS data are recorded at a series of excitation wavelengths from near the absorption maximum at 280 nm to 218.25 nm. The TKER data are obtained from H atom TOF profiles according to the equation 5.1:

$$TKER = \frac{1}{2} m_H \left(1 + \frac{m_H}{m_R} \right) \left(\frac{d}{t} \right)^2 \quad (5.1)$$

The partner fragment is assumed to be the pyrrolyl-2-carboxyaldehyde radical with a mass of 94.020 amu (m_R), which corresponds to the parent molecule less an H atom ($m_H = 1.0079$ amu) produced *via* N-H bond fission. The distance between the detector plate and source of the H atom formation in the interaction is given by d in equation 5.1. The TKER calculation also requires a t^3 Jacobian transformation to account for the spherical expansion of the molecular fragments upon the photodissociation event and to map these into cartesian space, along with a re-binding procedure to ensure the correct distribution of intensities. The Microsoft Excel program 'TOF to TKER convert' provided by the University of Bristol is used to carry out the calculation step from raw H atom TOF data to TKER data. The full procedure is described in the thesis by Cook [21]. Figure 5.6(a-f) shows selected TKER spectra for PCA photolysis at several wavelengths 280 nm (a), 275 nm (b), 270 nm (c), 260 nm (d),

240 nm (e) and 225 nm (f) with ϵ_{phot} aligned at $\Theta = 90^\circ$ aligned to the TOF axis. It is noted that all spectra recorded at $\lambda_{\text{phot}} \geq 240$ nm peak at TKER ~ 3500 cm^{-1} and show an extended tail to TKER of ~ 12000 cm^{-1} . The observed tail becomes less pronounced with increasing excitation energy (see figure 5.6(f)).

5.3.2 Excited State Dynamics $\lambda < 223$ nm

Transient absorption spectroscopy

A significant change in the TA spectra is observed at $\lambda_{\text{pump}} = 222$ nm. The transient shown in figure 5.7 features an instant broadband absorption component in the IR region that is centred around 800 nm.

The excitation wavelengths $\lambda_{\text{pump}} < 250$ nm are accessed via the TOPAS-SFM scheme. Recording transient spectra at excitation wavelength as short as ~ 222 nm is challenging. This is in part due to the weak absorption of the target molecule in this wavelength range (figure 5.3). Generating such short excitation wavelengths leads to power fluctuations due to the series of nonlinear processes involved, and is generally an inefficient process. The power of the excitation light source is not detectable at the sample position, the fluorescence of a strongly absorbing dye coated card is barely visible. An acquisition time of up to 10,000 laser shots per time-delay step is used to improve the signal-to-noise ratio. The transient in figure 5.7(a) is derived from the chirp-corrected data set as shown in figure 5.7(b). The transient is averaged over the spectral range $620 \text{ nm} \geq \lambda_{\text{probe}} \leq 825$ nm as indicated in the contour plot (figure 5.7(b)). The instant component can be described with a single exponential decay of approximately 3.7 ps. It is noteworthy that at $\lambda_{\text{pump}} = 222$ nm the instant component is the only component observed in the probe region between 400 nm to 1070 nm. Thus the previously dominant and growing absorption feature at probe wavelengths 400 and 500 nm are only observed at $\lambda_{\text{pump}} \geq 223$ nm.

H atom photofragment translational spectroscopy

A new signal component in the form of a pedestal becomes apparent at $\lambda_{\text{phot}} \leq 222$ nm at high TKER with an approximate centre position of 9000 cm^{-1} , which is consistent with the change observed in solution phase at this wavelength. The spectrum at 220 nm (figure 5.8(b)) shows some structure in the broad, high kinetic energy pedestal in the form of three peaks: the strongest at the highest kinetic energy onset of approximately 9950 cm^{-1} , then at ~ 9725 cm^{-1} and a third with very low intensity at ~ 9500 cm^{-1} . The 225 nm data set is shown for comparison in order to highlight the

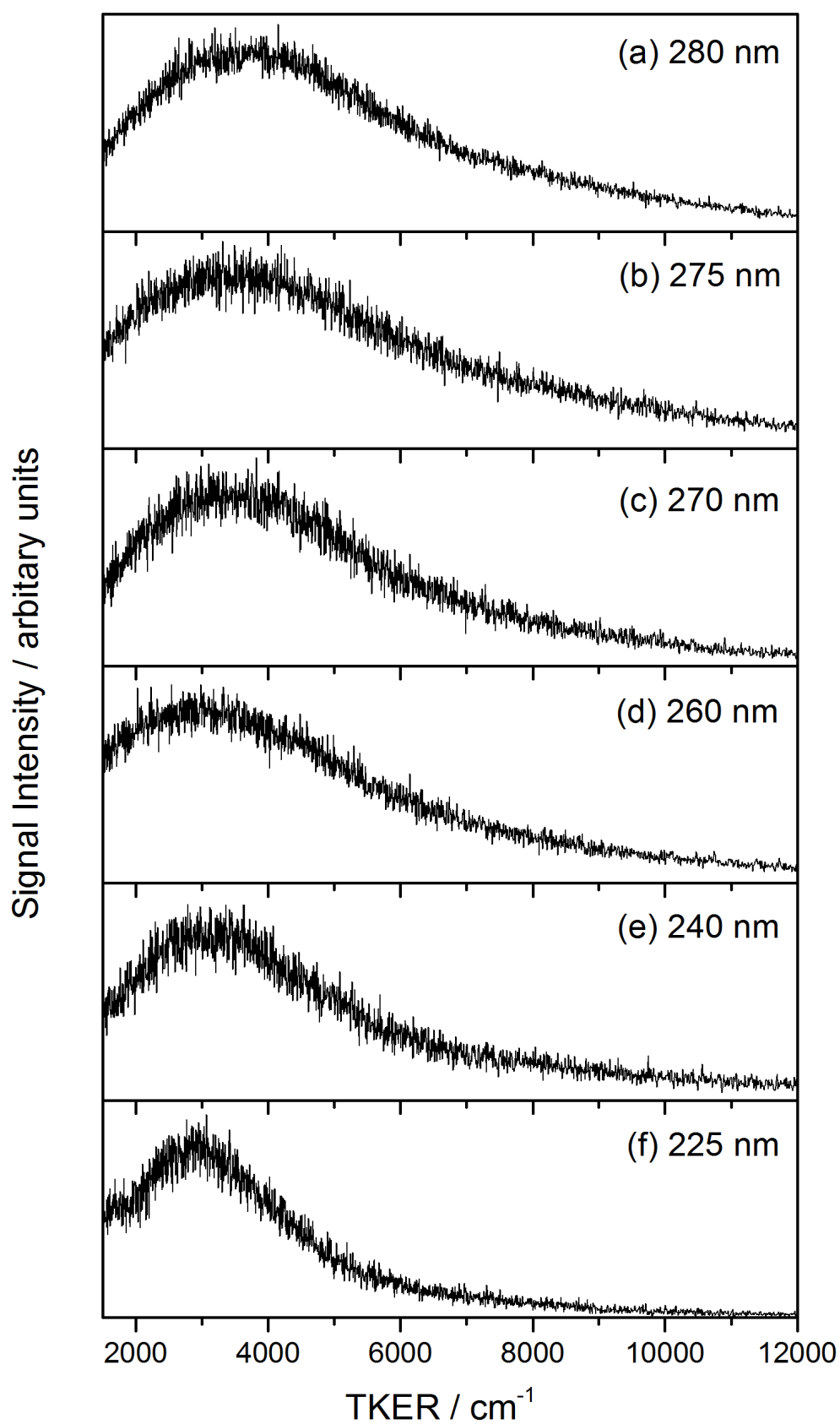


Fig. 5.6 Selected TKER Spectra at (a) 280 nm, (b) 275 nm, (c) 270 nm, (d) 260 nm, (e) 240 nm and (f) 225 nm.

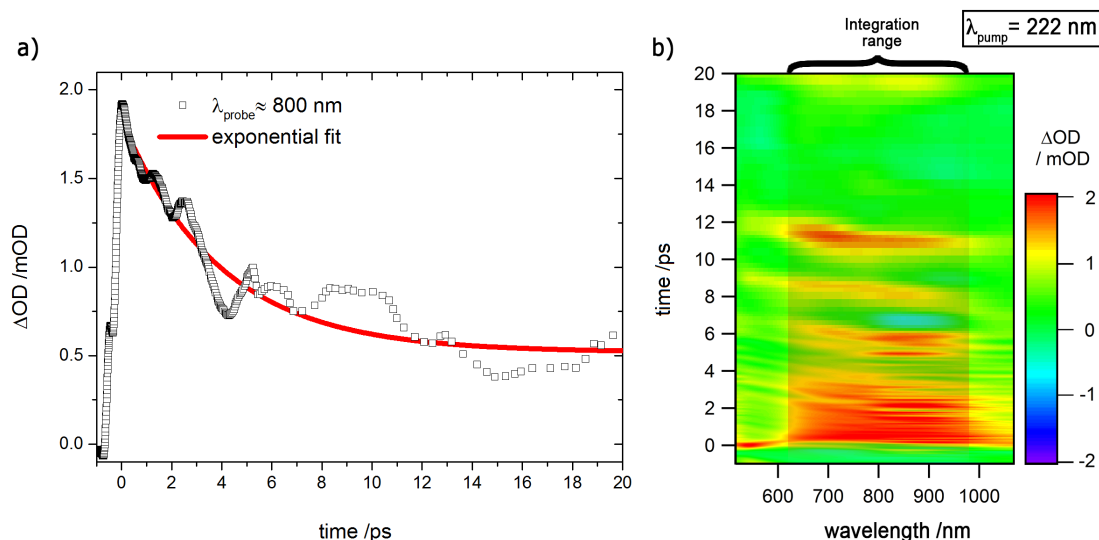


Fig. 5.7 Averaged transient (a) of PCA excited at 222 nm and corresponding contour plot (b) in the range 500 to 1070 nm. Transient (a) shows a single exponential decay profile with offset over a decay window of 20 ps. Contour plot (b) shows broadband absorption band centred at ~ 800 nm

observable difference in the TKER data presented in figure 5.8(b,c). The fast hydrogen release in the form of a pedestal is observed at $\lambda_{\text{phot}} \leq 222$ nm in all experiments. However, the observed fine structure shown in figure 5.8(b) is, as expected, strongly dependent upon the experimental conditions (e.g. wavelength, pressure, sample temperature), with the majority of spectra recorded between 222 and 218 nm showing a featureless, high TKER profile (as can be seen in figure 5.8(c)). However, the observed pedestal, such as in figure 5.8(b,c) is more intense when ϵ_{phot} is aligned at $\Theta = 90^\circ$ to the TOF axis.

5.3.3 Ab-initio Results

CASPT2 Potential Energy Cuts

The potential energy cuts (PECs) along the NH stretch coordinate calculated for pyrrole (C_{2v}) and cis-PCA (C_s), as described in section 5.2.5, are presented in figures 5.9(a) and (b) respectively.

Figure 5.9(a) shows the first four excited states of pyrrole. In the vertical Franck-Condon region the lowest two energy surfaces are the $1^1\pi\sigma^*$ and $2^1\pi\sigma^*$ states, corresponding to A_2 and B_1 symmetry (as has been established in the literature [23, 81, 102]), are the result of electron promotion from the HOMO and HOMO-1 to the LUMO. Adhering to the electric-dipole forbidden nature of the $^1A_2 \leftarrow ^1A_1$ transi-

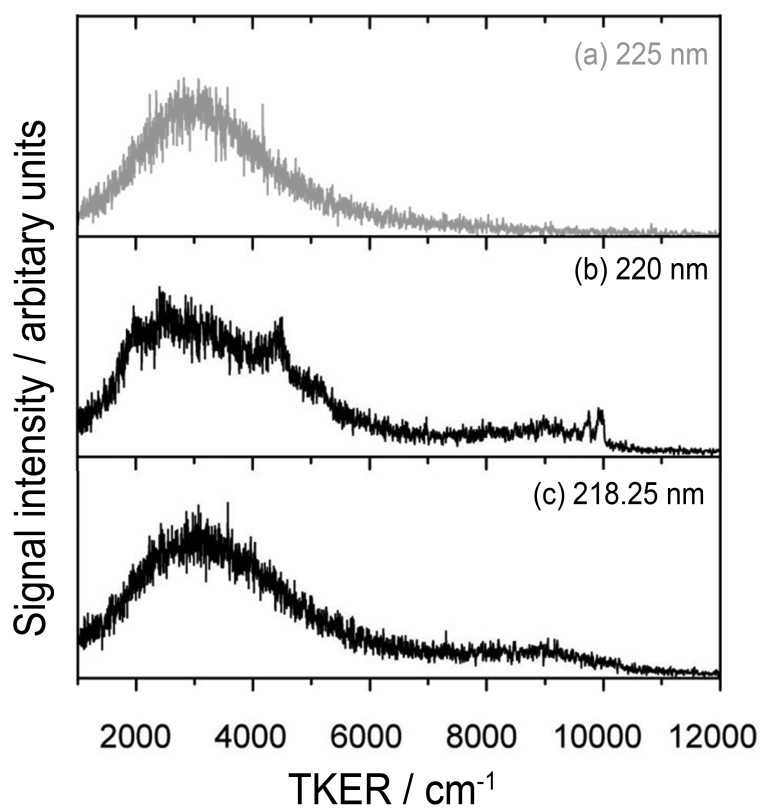


Fig. 5.8 Selected TKER Spectra at (a) 225 nm, (b) 220 nm, (c) 218.25 nm. Fast hydrogen release observed at $\lambda_{\text{phot}} \leq 222$ nm with pedestal at ~ 9500 cm⁻¹. Spectrum a) at 225 nm (grey) shows the TKER of the statistical low kinetic energy release for comparison. All spectra shown were recorded with ϵ_{phot} aligned at $\Theta = 90^\circ$.

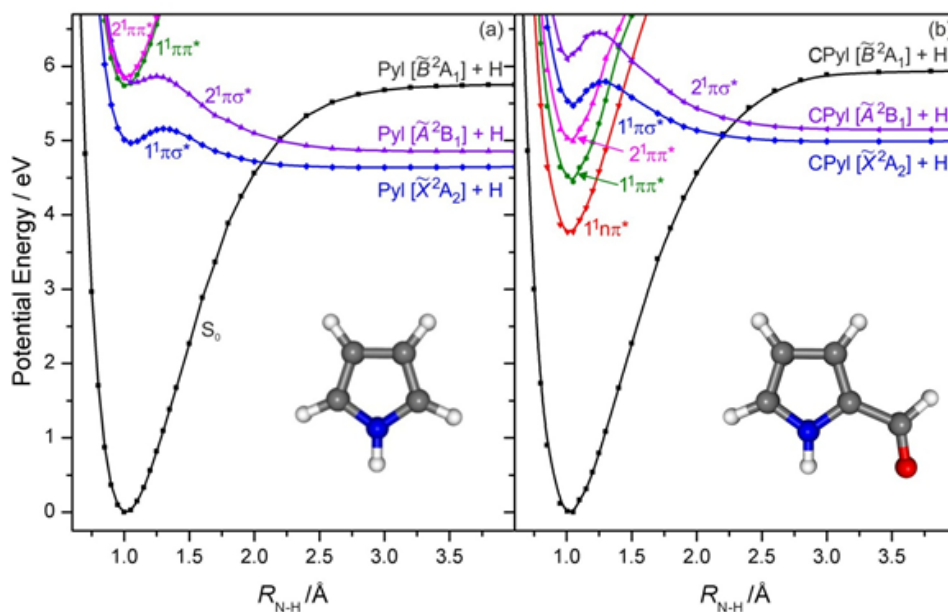


Fig. 5.9 'Unrelaxed' (rigid body) CASPT2 potential energy curves along R_{NH} for (a) pyrrole and (b) PCA

tion [23, 48], the oscillator strength is calculated to be zero for $S_1 \leftarrow S_0$ in the vibrational adiabatic limit. As is stated in the literature [23, 81, 102], vibronic mixing (Herzberg-Teller coupling) permits these transitions via intensity borrowing for certain vibronic transitions of appropriate symmetries. The $S_3(1^1\pi\pi^*)$ and $S_4(2^1\pi\pi^*)$ bound states both arise from $\pi^* \leftarrow \pi$ excitations and are dipole-allowed, yielding strong absorption features.

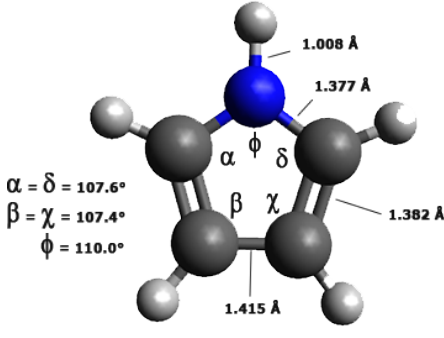
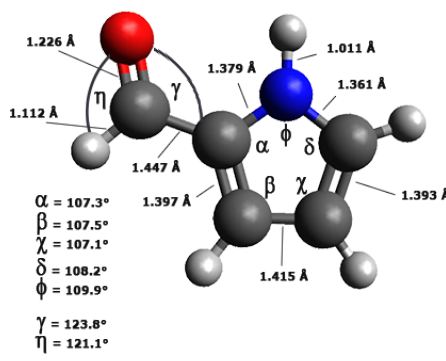
The S_1 state in isolated PCA, in contrast to pyrrole, is the bound $1^1n\pi^*$ indicated by the red solid PEC in figure 5.9(b) at approximately 3.75 eV followed by two more bound states at 4.5 eV (S_2) and 5.0 eV (S_3) both being of $\pi\pi^*$ character. Besides the apparent difference in state ordering and the inclusion of a new $n\pi^*$ state, when comparing pyrrole with PCA, the repulsive $S_4(1^1\pi\sigma^*)$ and $S_5(2^1\pi\sigma^*)$ states are not only calculated to lie ~ 0.5 eV higher in energy than their counterparts in pyrrole, they also both exhibit a minimum in the vertical Franck-Condon region that is more pronounced than in the case of pyrrole. Both molecules show a crossing of their corresponding $\pi\sigma^*$ surfaces with their ground state surface at an approximate bond length of 2.1 Å that corresponds to a conical intersection.

TD-DFT

The TD-DFT calculations for the isolated species of pyrrole and PCA are summarised in table 5.1 with their relative vertical excitation energies and oscillator strengths, cal-

culated from the optimised ground state geometry. The optimised structures for pyrrole and PCA are shown as inset in table 5.1, accompanied by selected bond lengths and angles. Both molecules are constrained to be planar (C_{2v} and C_s symmetry respectively).

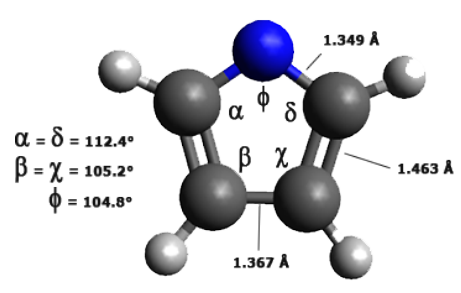
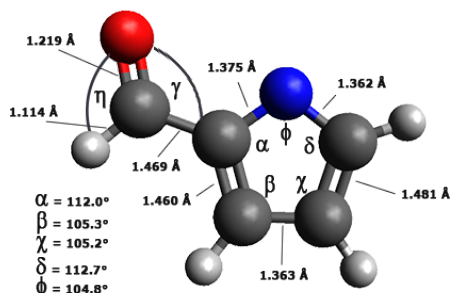
Table 5.1 Vertical excitation energies calculated for pyrrole (C_{2v}) and PCA using the (TD)-B3LYP/aug-cc-pVDZ level of theory.

(TD)-B3LYP / aug-cc-pVDZ Vertical Excitation Energies / eV						
Transition from S_0						
	State	Gas phase Vertical Excitation Energy / eV	f	State	Gas phase Vertical Excitation Energy / eV	f
	S_1	$^1\pi\sigma^*$	4.7185	0.0000	$^1n\pi^*$	3.8969
S_2	$^1\pi\sigma^*$	5.4692	0.0269	$^1\pi\pi^*$	4.7549	0.2984
S_3	$^1\pi\pi^*$	5.5717	0.0033	$^1\pi\pi^*$	5.1555	0.1010
S_4	$^1\pi\pi^*$	5.9943	0.1787	$^1\pi\sigma^*$	5.4930	0.0000
T_1				$^3\pi\pi^*$	2.9630	
T_2				$^3n\pi^*$	3.3732	
T_3				$^3\pi\pi^*$	4.0924	
T_4				$^3\pi\pi^*$	5.1856	

TD-DFT calculations for the pyrrolyl and the pyrrolyl-2-carboxaldehyde radical (2CPyl) are carried out at an identical level of theory, taking into account the unpaired electron ($S = 1/2$) that dictates a multiplicity of 2 for the free radical. The optimised structures for the pyrrolyl and an pyrrolyl-2-carboxaldehyde radical are shown as an inset in table 5.2.

TD-DFT calculations carried out for PCA using the IEFPCM polarisation continuum model for ethanol, methanol and water to simulate a solvent bath are given in table A.1 of Appendix A to this chapter. Additionally, the vertical excitation energies and oscillator strengths are calculated for PCA including one explicit solvent molecule.

Table 5.2 Vertical excitation energies calculated for pyrrolyl and the pyrrolyl-2-carboxaldehyde radical using the (TD)-B3LYP/aug-cc-pVDZ level of theory.

Transition from D_0	(TD)-B3LYP / aug-cc-pVDZ Vertical Excitation Energies / eV			
				
	Gas phase		Gas phase	
	Vertical Excitation Energy / eV	f	Vertical Excitation Energy / eV	f
D_1	1.4138	0.0010	1.0986	0.0000
D_2	2.0463	0.0000	1.2662	0.0008
D_3	4.6738	0.0071	3.8266	0.0000
D_4	4.8925	0.0008	3.8499	0.0003
D_5	5.4226	0.0000	4.2684	0.0022
D_6	5.5839	0.0005	4.3764	0.0004

Additional solvent molecules have a minimal effect on calculated energies at large additional computational expense. Similarly, the calculations for the pyrrolyl radical and the pyrrolyl-2-carboxaldehyde radical, with the polarisation continuum model and explicit solvent molecules, are given in table A.2 of Appendix A to this chapter.

A list of triplet state energies and oscillator strengths calculated from the T_1 minimum energy geometries are presented in table A.3 of Appendix A to this chapter. These are calculated using the IEFPCM polarisation continuum model for ethanol, methanol and water to simulate a solvent bath, as before, in a separate set of calculations one explicit solvent molecule is included to take into account the direct interactions between the PCA and the solvent molecule.

5.4 Discussion

Guided by the PECs in figure 5.9 and the calculated oscillator strengths shown in table 5.1, the features in the vapour phase UV-vis shown in figure 5.3 are assigned

in terms of transitions to the $1^1n\pi^*$, $1^1\pi\pi^*$, $2^1\pi\pi^*$ and higher lying $\pi\pi^*$ states, respectively. Many of these features are still evident in the solution phase spectra, but their relative energies are different. The $\pi^* \leftarrow \pi$ excitations show the expected [83] bathochromic (red) shift in these protic solvents (which is greatest in the most polar solvent, water), to the extent that the $\pi^* \leftarrow n$ feature is apparently buried under the more intense $1^1\pi\pi^* \leftarrow S_0$ absorption. This qualitative observation can be confirmed by fitting the vapour phase spectrum shown in figure 5.3 with a series of Gaussian components.

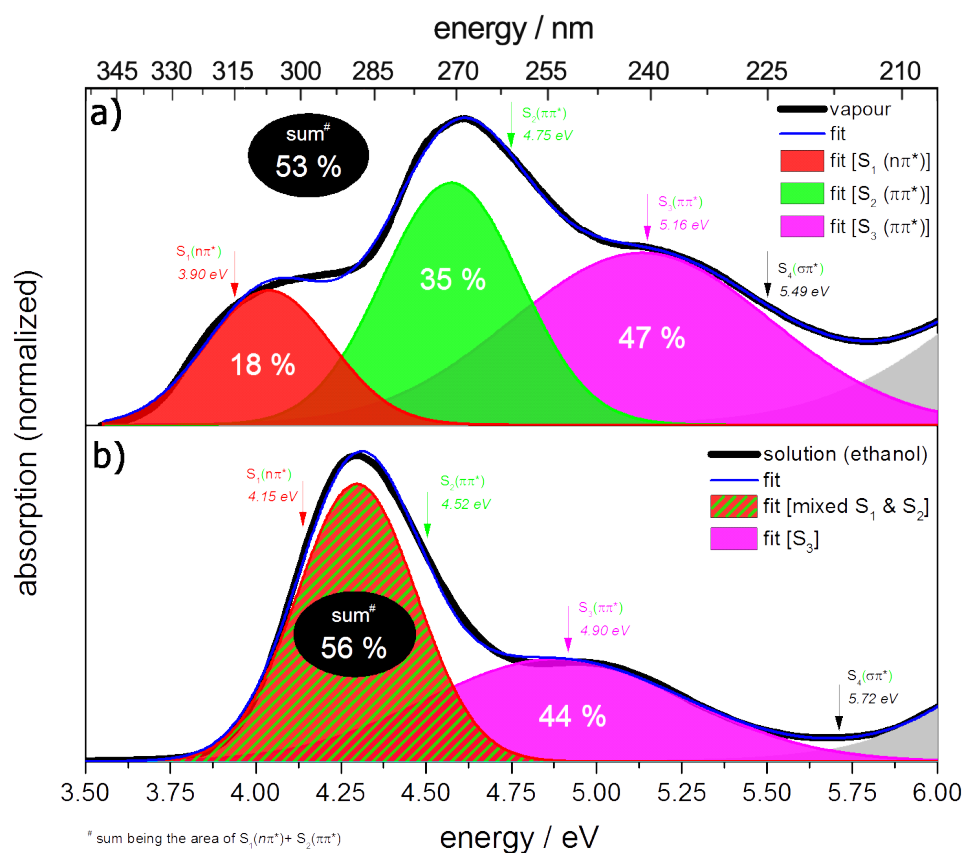


Fig. 5.10 Absorption spectra of PCA (a) vapour and (b) in ethanol solution. Absorption bands are indicated with coloured shading. Arrows indicate the corresponding TD-DFT energies as shown in tables 5.1 and A.1

Figure 5.10(a) shows three clear components centred at 4.0 eV, 4.6 eV and 5.1 eV, with relative areas of 18%, 35% and 47% respectively. The $S_n \leftarrow S_0$ energies calculated for the isolated species via TD-DFT are 3.90 eV, 4.75 eV and 5.1 eV, and are thus within 6% deviation to the fitted vapour phase transition energies. The TD-DFT energies are indicated with arrows in figure 5.10(a) for the isolated species and in figure 5.10(b) for the corresponding data shown in table A.1 with the explicit sol-

vent molecule (ethanol). The solution phase UV-vis in figure 5.10(b) shows only two clearly distinguishable peaks, centred at 4.3 eV and 4.8 eV and with areas of 56% and 44% respectively. Thus, the sum area (53%) of the two low energy components in the vapour phase UV-vis closely match the solution phase data. Together with the relative shift of the normalised peak height of the $S_3(\pi\pi^*)$ component to a lower relative height in the solution phase UV-vis compared to the vapour phase data, this further demonstrates the (partial) overlap of the two low energy states. Additional evidence is provided by the TD-DFT calculations that show a 0.25 eV red shift of the $1^1\pi\pi^*$ and $2^1\pi\pi^*$ states and a 0.25 eV blue shift of the $1^1n\pi^*$ state when comparing the isolated species to the 'solution phase' calculations (see data excerpt in table 5.3).

Table 5.3 Comparison of TD-DFT energies and oscillator strength for the isolated and ethanol solvated PCA molecule. Key data points for discussion taken from data tables 5.1 and A.1.

Transition from S_0	Pyrrole-2-Carboxylaldehyde					
	State	Gas phase		State	Solution phase	
		Vertical Excitation Energy / eV	f		Vertical Excitation Energy / eV	f
S_1	$1^1n\pi^*$	3.8969	0.0002	$1^1n\pi^*$	4.1480	0.0004
S_2	$1^1\pi\pi^*$	4.7549	0.2984	$1^1n\pi^*$	4.5220	0.3548

Based on the UV-vis data and the TD-DFT calculations, excitation at >260 nm results in population of the energetically close-lying $S_1(1^1n\pi^*)$ and $S_2(1^1\pi\pi^*)$ states in solution phase. In principle the lowest three triplet states can be accessed at an excitation energy of ~ 4.76 eV (~ 260 nm), but direct absorption into the triplet manifold is forbidden by the spin selection rules for the absorption of a photon. The calculated oscillator strength for the $\pi^* \leftarrow \pi$ transition is significantly larger than the $\pi^* \leftarrow n$ transition, both in the solution phase (table A.1) and for the isolated molecule (table 5.1). This trend is reflected in the UV-vis data. However, the low energy absorption that is assigned to $\pi^* \leftarrow n$ appears to be more intense in the UV-vis data, than the calculations suggest. This discrepancy can be explained on the grounds of symmetry. The TD-DFT calculations for the isolated molecule are performed close to C_s symmetry, resulting in a very low oscillator strength for the $\pi^* \leftarrow n$ transition. Furthermore, the electronic structure calculation also ignores potential intensity borrowing via vibronic coupling from higher electronic states. Breaking the symmetry, as has been done by adding an explicit solvent molecule, results in an increased oscillator strength. This is demonstrated in table A.1, where the oscillator strength increases for both the $\pi^* \leftarrow \pi$ and $\pi^* \leftarrow n$ transition.

The extracted time constants from the exponential fitting (figure 5.4) of the experiments at $\lambda_{\text{pump}} = 300$ nm are ~ 2.5 ps and ~ 4.2 ps for the 400 nm and 500 nm transitions, respectively. These two preceding time constants are shown together with all of the extracted kinetics from a series of TA experiments in the range $315 > \lambda_{\text{pump}} \geq 225$ nm (figure 5.11). Figure 5.11 shows weighted average values of the time constants at 400 nm (open red circles) and 500 nm (filled black triangles) as a function of excitation energy (E_{phot}). Each point represents a weighted average of all available data

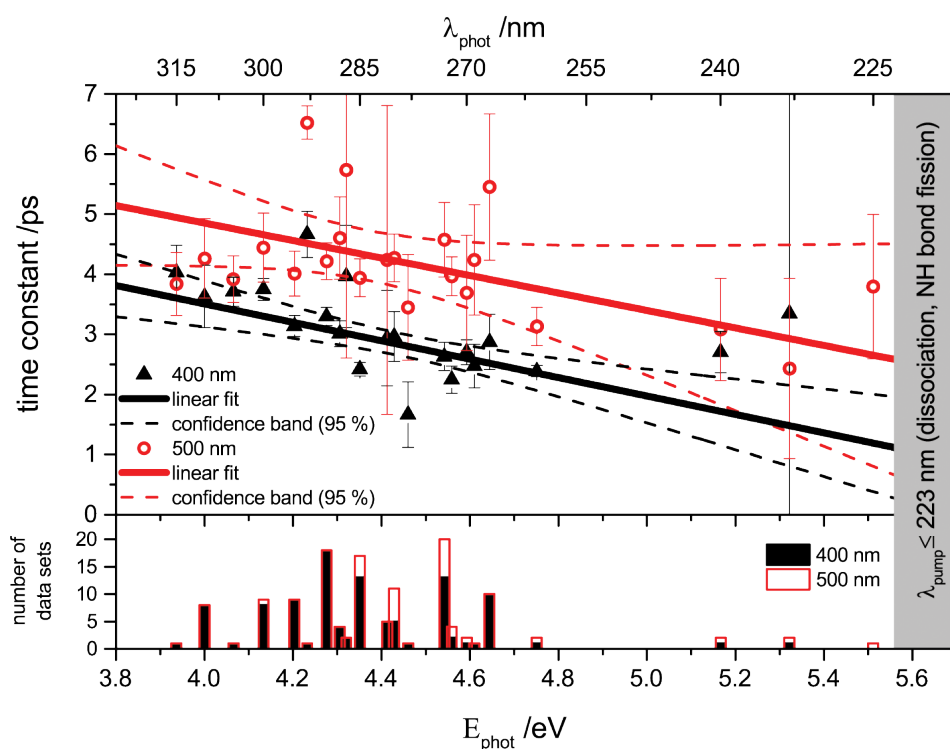


Fig. 5.11 Kinetic Time constants of the TA signal at $\lambda_{\text{probe}} = 400$ nm and 500 nm at a range of excitation wavelengths (λ_{pump})

at a given pump energy. The determined average value per excitation wavelength and its associated error are weighted based on the individual error determined from each initial single exponential fit. The number of data sets used to derive the linear weighted average kinetics for the 400 nm and 500 nm transitions is indicated in the bar graph section of figure 5.11 in the form of filled black and hollow red columns, respectively. Also shown is a linear error-weighted fit for the 400 nm (solid red line) and 500 nm (solid black line) transitions as a function of excitation energy together with their 95 % confidence band (dashed lines). From figure 5.11 it is evident that the absorbing states are not initially populated: the growing signal represents population flow from the pho-

to excited states. The growing absorption bands at 400 nm and 500 nm are observed at the absorption onset, as is determined by the UV-Vis and the TD-DFT data. As such, it is assumed that the population giving rise to the growing absorption bands originated in the two lowest singlet states, ($S_1(1^1n\pi^*)$ and $S_2(1^1\pi\pi^*)$) in PCA. The only lower-lying excited states are the triplet states calculated in table 5.1. After comparing the electronic states of PCA with structurally similar aromatic carbonyl molecules such as benzaldehyde, formaldehyde or benzophenone (Zewail and coworkers [89]), it is interesting to note that all of these aromatic carbonyls show the involvement of triplet states in their excited state relaxation. Remarkably, the intersystem crossing for aromatic carbonyls described in the literature is of the order of several picoseconds to tens of picoseconds [24, 87, 89]. Assuming for now that the population receiving state is one or more of the triplet states as calculated in table 5.1, the time constants that determine the population flow from the singlet states to the triplet states will be inversely dependent upon the excitation energy. Both linear fits show a wavelength dependence with very similar gradients, the 400 nm kinetics being faster compared to the 500 nm component. Excitation into the higher singlet manifold of vibrational states is expected to favour the ISC rate, since the density of states is higher and consequently the coupling between energetically close-lying energy states is enhanced. Only the lowest three triplet states can be populated from the singlet states via ICS, based upon the triplet state energies presented in table A.1. An excerpt of the data shown in table A.1 is shown for reference in table 5.4.

Table 5.4 TD-DFT energies for the first four triplet states of PCA in ethanol solution. Key data points for discussion taken from data table A.1.

Transition from S_0	Pyrrole-2-Carboxylaldehyde	
	State	Solution phase Vertical Excitation Energy / eV
T_1	$^3\pi\pi^*$	2.8947
T_2	$^3n\pi^*$	3.6937
T_3	mixed	3.8539
T_4	$^3\pi\pi^*$	5.3626

This is because the T_4 state is not accessed until the calculated excitation energy of 5.36 eV (~ 230 nm) is reached. The energy separation between $T_2(1^3n\pi^*)$ and T_3 is of the order of 0.15 eV, and as such it is sufficiently difficult to separate the origin of the observed transitions based on energetic grounds in the broadband TA data. However experiments performed close to the absorption edge of PCA in ethanol solution show

two absorption bands very similar to the data set shown in figure 5.4. At the absorption edge of PCA in the experiment the population of the T_3 state is less likely on energetic grounds, as the energy threshold required to get into T_3 is barely accessible. As a consequence the origin of the observed transitions in the TA data has been assigned to be $T_1(1^3\pi\pi^*)$ and $T_2(1^3n\pi^*)$. In order to guide the assignment of the observed transitions the data table A.3 shows the transition energies and oscillator strengths from the geometry optimised T_1 state. An excerpt of the data shown in table A.3 is given for reference in table 5.5 to guide the following discussion.

Table 5.5 TD-DFT energies for the triplet-triplet states of PCA in ethanol solution. Key data points for discussion taken from data table A.3.

Transition from T_1	Pyrrole-2-Carboxylaldehyde	
	Solution phase	
	Vertical Excitation Energy / eV	f
T_5	2.8894 (~430 nm)	0.0125
T_7	3.4523 (~360 nm)	0.0063
T_{11}	3.8480 (~320 nm)	0.0752

With these in mind, the high energy transition centred at ~400 nm in the TA data and stretching further into the blue spectral range is deduced to be the $T_5 \leftarrow T_1$ transition. This transition is calculated to be at 430 nm (~2.9 eV) and shows a large oscillator strength. Further transitions with large oscillator strengths that can explain the observed absorption in the blue spectral range down to ~320 nm in the TA data with a triplet state rise time very similar to the ~400 nm component are $T_7 \leftarrow T_1$ at 360 nm (~3.45 eV) and $T_{11} \leftarrow T_1$ at 320 nm (~3.85 eV). The origin of the absorption band observed at ~500 nm cannot be assigned to the same origin triplet state as the 400 nm transition due to the different rise-time constant observed in the TA data. Using the transition energies shown in table A.3, with low oscillator strengths as an orientation for the assignment of the ~500 nm (~2.5 eV) component, the absorption is likely to be from $T_8 \leftarrow T_2$, $T_9 \leftarrow T_2$ and $T_{10} \leftarrow T_2$ transitions, as their energy gaps correspond to 2.42 eV, 2.47 eV and 2.65 eV respectively, and thus can account for the broadband absorption observed at ~500 nm. Further to this, the data in table A.3 do not show any transition originating from T_1 that can account for the transition observed at ~500 nm.

The next section discusses how the two low-lying triplet states that give rise to the observed TA data are populated in the first place. As mentioned at the beginning of this chapter, the UV-vis data show an overlap of the absorption bands and the TD-DFT

calculation shows an energy separation of approximately 0.37 eV between the S_1 and S_2 states (see table A.1).

The TA data presented in figure 5.4 can be interpreted as follows: the TA band at ~ 400 nm can be assigned to a triplet-to-triplet absorption originating from the $T_1(1^3\pi\pi^*)$ state, following intersystem crossing (ISC) mediated population flow from the initially prepared $S_1(1^1n\pi^*)$ state. Similarly, the band at ~ 500 nm can then be assigned to a further triplet-to-triplet absorption originating from T_2 , following ISC from $S_2(1^1\pi\pi^*)$ to $T_2(1^3n\pi^*)$. In the above case the population via ISC may be treated independently in kinetic modelling, and this has been done with single exponential fitting in figure 5.4(a) and in the summary figure 5.11. Given El-Sayed's rules of spin-orbit coupling in ISC transitions, the $1^3\pi\pi^*$ (T_1) state is reasonably expected to receive population from the $1^1n\pi^*$ (S_1) state, whilst T_2 would primarily be populated by coupling from S_2 [27]. This model, which is also shown in figure 5.12, can account for the difference in time constants that is associated with the triplet state filling dynamics, though it ignores potential coupling between the singlet states in the form of internal conversion. The transition from the higher S_2 to the lower S_1 electronic state would need to be sufficiently slower than the recorded number of picoseconds for the ISC process to allow for internal conversion in this model.

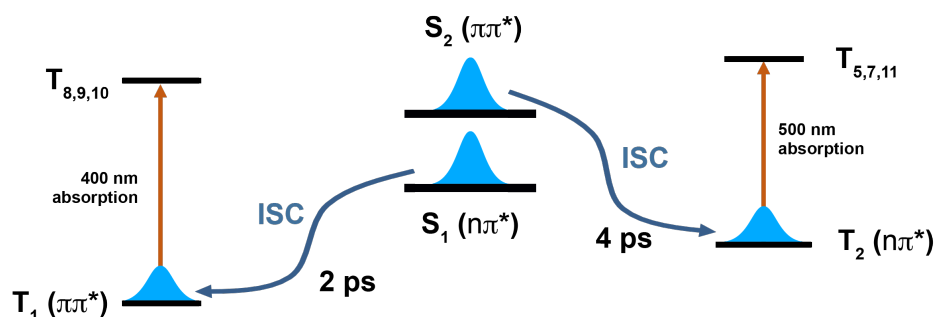


Fig. 5.12 Possible mechanisms of the ultrafast process in PCA at excitation ≥ 225 nm. Excitation into the energetically close-lying $S_1(1^1n\pi^*)$ and $S_2(1^1\pi\pi^*)$ states leads to separated population flow from $S_2(1^1\pi\pi^*)$ to $T_2(1^3n\pi^*)$ and $S_1(1^1n\pi^*)$ to $T_1(1^3\pi\pi^*)$ assuming slow internal conversion between S_2 and S_1

The observed triplet population is similar in part to the dynamics that occur in other aromatic carbonyls, such as benzaldehyde and acetophenone. Benzaldehyde is of particular interest as it is iso-electronic with respect to PCA and is used here to identify the possible underlying triplet filling mechanism. Some of the most notable experimental results for benzaldehyde and related aromatic carbonyl compounds are sum-

marised by Zewail and co-workers [89]. Early studies performed by Berger [9, 10] and Ohmori [82], together with more recent femtosecond pump-probe time-of-flight mass spectroscopy results by Liu [66], provide a good indication of the underlying mechanism for the closely related aromatic carbonyl PCA. The dynamics of isolated benzaldehyde and acetophenone of isolated molecules in the gas phase have been studied by Park et al. [89] using electron diffraction. Comparing the energetic state ordering of the $^3\pi\pi^*$ and $^3n\pi^*$ in PCA with that of benzaldehyde, the $^3n\pi^*$ state is the lowest triplet state in benzaldehyde, contrary to PCA. The study by Park et al. for isolated molecules shows that excitation into the $S_2(1^1\pi\pi^*)$ leads to population of the $S_1(1^1n\pi^*)$ state by internal conversion with a time constant of ~ 250 fs ([60]), which is consistent with the time constant (238 fs) determined by Liu et al. [66], and is sufficiently faster than the observed triplet state filling time constants for PCA. Park et al. assign an ISC from the finally populated $S_1(1^1n\pi^*)$ state to the $T_2(1^3\pi\pi^*)$ in benzaldehyde. In the absence of collisions, the $T_2(1^3\pi\pi^*)$ state is identified as the origin of the dissociation to form benzene and CO in its triplet state with a long time constant of ~ 80 ns. The study by Park et al. is conducted in the gas phase of isolated molecules, unlike the solution phase study presented in this thesis, so despite the fact that the observable time frame lies outside the detectable delay range of the fs-TA setup, the results by Park et al. would not allow for collisional relaxation. The experiments by Berger et al. [9] confirm a long-lived T_2 state in the absence of vibrational relaxation, based upon the spatially orthogonal orbitals that can account for the low coupling, since this transition from $T_2(1^3\pi\pi^*) \leftarrow T_1(1^3n\pi^*)$ requires the transfer of an n electron to the π orbital. Berger et al. point out that, based on the experimentally confirmed selection rules by Koyanagi et al. [54], $T_1(1^3n\pi^*) \not\leftarrow S_1(1^1n\pi^*)$ and $T_2(1^3\pi\pi^*) \leftarrow S_1(1^1n\pi^*)$, there could be competition between the ISC from $T_1(1^3n\pi^*) \leftarrow S_2(1^1\pi\pi^*)$ and the IC from $S_1(1^1n\pi^*) \leftarrow S_2(1^1\pi\pi^*)$. Combining this with the experimental results by Park et al., who name a fast ~ 250 fs IC process and do not assign their results to ISC from $S_2(1^1\pi\pi^*)$ to $T_1(1^3n\pi^*)$, it is safe to say that the IC is out-competing the slower ISC in benzaldehyde. This is further validated with the sufficiently longer 46 ps time constant assigned to the ISC from $S_1(1^1n\pi^*)$ to $T_2(1^3\pi\pi^*)$ in the study by Park et al. In the case of collisions, vibrational relaxation leads to $T_1(1^3n\pi^*)$ population followed by phosphorescence in Park et al.'s study.

A series of computational studies performed by Fang et al. [30, 31], Li et al. [61], Ou et al. [87], Huix-Rotllant [47] and Cui et al. [24] investigate the role of singlet and triplet state involvement in benzaldehyde, acetophenone and other aromatic carboxyl compounds and attempt to link their results to experimental observations in the literature. Many of those ab-initio studies result in a very similar outcome; as such only

some of the key results are given. The study by Ou et al. [87] investigates the electronic relaxation of the $S_1(1^1n\pi^*)$ state in benzaldehyde via TD-DFT. Ou et al. note that the origin of the fast ISC from $S_1(1^1n\pi^*)$ to $T_2(1^3\pi\pi^*)$ is the result of strong spin-orbit coupling. Their computational results highlight the coupling of the T_1 and T_2 state via a conical intersection. In their conclusion the $T_2(1^3\pi\pi^*)$ state takes the form of a relay state to funnel population into the lowest energy state $T_1(1^3n\pi^*)$. In the case of PCA this would imply population flow from T_2 to the lowest triplet, i.e. T_2 population grows and then decays away to T_1 , which is not observed in the TA data. The computations by Cui et al. [24] use a state-averaged CASSCF calculation with a very similar outcome to the results by Ou et al. and Cui et al. identify a three-state intersection region in benzaldehyde and acetophenone for $S_1/T_2/T_1$, which allows efficient electron population from the formally forbidden transition S_1 to T_1 as a consequence of the T_2 state acting as a relay state. The coupling efficiency to T_1 is described as being very efficient due to the structural and energetic similarity of the $S_1/T_2/T_1$ three state geometry to the S_1 minimum energy geometry. The ab-initio results appear contrary to the experimental results as they allow for a $T_1(1^3n\pi^*) \leftarrow S_1(1^1n\pi^*)$ transition by means of coupling via T_2 with the aid of a conical intersection. Nevertheless, Park et al. [89] and Berger et al. [9] indicate the possibility of a population transfer to the low-lying T_1 state in the form of internal conversion once the small energy gap between the T_2 and T_1 state is overcome by removing the excess energy via vibrational collision ([89]). Similarly, Berger et al. [9] indicate the possibility of a $T_2(1^3\pi\pi^*)$ 'relay' state that would allow for a $T_1 \leftarrow S_1$ crossing. One of the more recent publications by Liu et al. [66] investigates the ultrafast dynamics in benzaldehyde, and the possible mechanism for the benzaldehyde relaxation is considered to be a fast (600 fs) internal conversion, which populates the $S_1(1^1n\pi^*)$ state from $S_2(1^1\pi\pi^*)$, followed by a bifurcation at a three state crossing between $S_1/T_2/T_1$ to allow efficient population to flow into the $T_1(1^3n\pi^*)$ state, with $T_2(1^3\pi\pi^*)$ acting as a relay state.

The excited state dynamics of benzophenone in methanol are reported in the study by Merz et al. [72] and in the supporting information of the investigation into the charge transfer in benzophenone linked to one of the natural nucleosides (adenine, guanine, thymine, cytosine) by a phosphodiester. The study is conducted with time-resolved femtosecond transient absorption spectroscopy. The supporting information for this study shows solely the transient absorption data of benzophenone in methanol. The data show a growing absorption band in the visible region around 530 nm, which is assigned in the main publication to an ISC from the lowest singlet state to the lowest triplet state with a singlet state lifetime of 12.5 ps. Similarly, the study by Aloise et al. [1] measures a time constant of 11.6 ps for the triplet state population. The direct

transition from $S_1(1^1n\pi^*)$ to $T_1(1^3n\pi^*)$ in benzophenone is forbidden by El-Sayed intersystem crossing rules, and Aloise et al. [1] indicate that the most likely transition involves coupling via $T_2(1^3\pi\pi^*)$ and hot vibrational levels in $T_1(1^3n\pi^*)$ to allow for the observed fast ISC rate. As such, the state ordering of the two low-lying triplet states in PCA appear to be reversed in comparison to the well characterised dynamics of benzophenone, but the observed time constants are similar to the assigned triplet components in the study, providing some verification to the observed fast intersystem crossing rate. The similarity in electronic structure of PCA with benzophenone, i.e. that they both exhibit the aromatic carbonyl character seems to have a dramatic effect on the intersystem crossing rates. As touched upon in the last two paragraphs the involvement of an intermediate ('relay state') appears to play a significant part in the fast population flow.

Taking into account the main conclusions of the studies by Park, Cui, Ou [24, 87, 89] and others [1, 30, 31, 47, 61, 72] of dynamics and the involvement of singlet and triplet states in aromatic carbonyls, when interpreting the dynamics observed in PCA, the second model suggested appears to be consistent with the general dynamics observed in aromatic carbonyl molecules. The following schematic figure 5.13 summarises the suggested mechanism for PCA for the excitation range ≥ 224 nm.

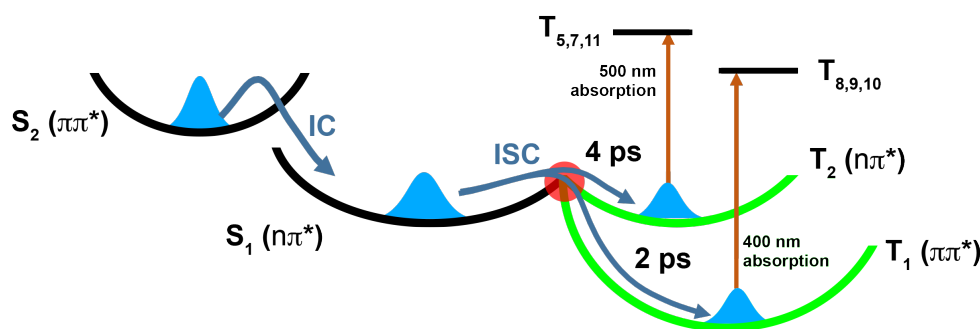


Fig. 5.13 Possible mechanisms of the ultrafast process in PCA at excitation ≥ 225 nm. Excitation into the $S_2(1^1\pi\pi^*)$ or higher singlet states lead to ultrafast IC to the $S_1(1^1n\pi^*)$ state, followed by bifurcation via ISC to build up population in $T_2(1^3n\pi^*)$ and $T_1(1^3\pi\pi^*)$ at the $S_1/T_2/T_1$ three state crossing

The solution phase data are consistent with the H atom PTS data that show statistical TKER data (figure 5.6) with no fast hydrogen release observed at excitations ≥ 224 nm. This being said, the unstructured long tail that is observed when photon excitation of PCA takes place at long wavelengths such as 280 nm (figure 5.6(a)), as the H

atom spectrum extends to TKER $\sim 12000 \text{ cm}^{-1}$, should not be ignored. Those long-tail data at high TKER energy are barely accessible with one-photon excitation of PCA at 280 nm, since at this energy the bond dissociation energy of the N-H bond is not overcome. This is rationalised with the ab-initio calculations which suggest that in the vertical Franck-Condon region an energy of approximately 5.7 eV ($\sim 217 \text{ nm}$) is required to access the repulsive N-H bond-breaking surface. The structured high kinetic energy peak at an approximate energy of 9950 cm^{-1} in figure 5.8(c) that is excited at 220 nm ($\sim 45450 \text{ cm}^{-1}$) can assist in deriving the N-H bond strength. Making the assumption that the observed high TKER feature in figure 5.8(c) is the result of the 2PCyl radical fragment vibration in its ground ($v=0$) vibrational level, then the N-H bond strength is around $\sim 35500 \text{ nm}^{-1}$. The value derived for N-H fission in PCA is approximately 2650 cm^{-1} larger than the literature value for pyrrole ($32850 \pm 40 \text{ cm}^{-1}$ [22]). Thus, it is concluded that the H atoms observed at long wavelengths ($>240 \text{ nm}$) are largely (if not exclusively) the result of multiphoton excitation processes. The tail at high TKER fades away upon tuning to shorter wavelengths (compare figure 5.6(d-f)), showing energy release data consistent with those expected for PCA molecules that undergo one photon excitation, followed by rapid, radiationless decay to high vibrational levels of the S_0 state and subsequent 'statistical' unimolecular decay.

Based on the solution phase TA data, it is evident that the molecular relaxation dynamics change dramatically at $\lambda_{\text{pump}}=222 \text{ nm}$. A new, dominant relaxation channel is accessed that takes precedence over the slower ISC channel. On the time-scale of the TA experiment with a temporal resolution of $\sim 100 \text{ fs}$ the fast channel appears to be instantaneous. The absence of the triplet channel at $\lambda_{\text{pump}}=222 \text{ nm}$ further validates the effective coupling onto an ultrafast pathway that out-competes the triplet state formation. This dramatic change at very short wavelengths is also observed in the HRPTS data at $\lambda_{\text{photo}}=220 \text{ nm}$ that shows the release of fast H atoms. To be specific, the $\pi\sigma^*$ onset, which is known to 'trigger' N-H bond fission in pyrrole, is shown in the PEC in figure 5.8 and predicted in the TD-DFT 'gas phase' calculation (table 5.1) to have an energy of $\sim 5.5 \text{ eV}$, both in the vertical Franck-Condon region, which corresponds to $\sim 226 \text{ nm}$. The UV-vis absorption is at a minimum at 226 nm, as is indicated in figure 5.10. The calculated oscillator strength for the gas phase PCA in the TD-DFT is zero, which is expected for pyrrole-type molecules. The orbitals that are involved in this transition correspond to the pyrrole-typical, electric-dipole forbidden ${}^1A_2 \leftarrow {}^1A_1$ type transition, which is forbidden on symmetry grounds. As PCA is of C_S symmetry this transition is not strictly forbidden. However, the majority of orbital density is on the pyrrole ring and therefore the PCA molecule is close to C_{2v} . The carbonyl group plays a weak role in the HOMO and the ${}^1\pi\sigma^*$ orbital, so symmetry breaking is weakly

present and the transition is observed weakly, and more strongly than in pyrrole.

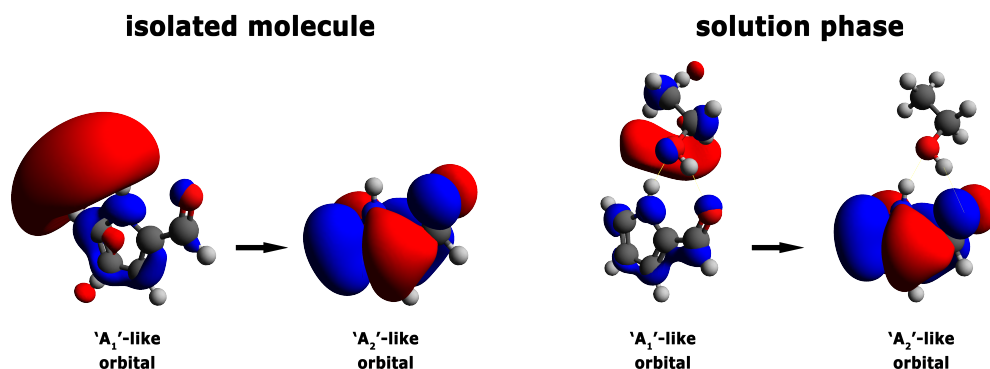


Fig. 5.14 TD-DFT orbitals involved in ${}^1A_2 \leftarrow {}^1A_1$ type transition in PCA. Shown are the orbitals for the a) 'gas phase' type calculation of the isolated PCA molecule and b) the orbital contribution for the 'solution phase' type calculation with explicit solvent.

The carbonyl group is just slightly perturbing the electron density, though not sufficiently enough to alter the density significantly. Even with the inclusion of the solvent (as shown in figure 5.14(b)) the orbitals are just slightly more perturbed, which is also evident in the fraction of increased oscillator strength seen in the 'solution phase' TD-DFT with explicit solvent (table A.1). The similarities between pyrrole and PCA with regard to the ${}^1\pi\sigma^*$ state preclude that the A_2 state in PCA is also gaining oscillator strength due to vibronic (Herzberg-Teller) coupling, as in the case for pyrrole. The TD-DFT solution phase onset is calculated to be at ~ 5.72 eV (~ 217 nm), which is remarkably consistent with the observed sudden spectral change in the solution phase data at ~ 222 nm. The H atom PTS data show the typical high kinetic energy pedestal determined from the N-H bond fission in pyrrole. For comparison the H atom onset in pyrrole is at 254 nm with a centre TKER of approximately 7000 cm^{-1} [23] showing vibrational adiabaticity. The PCA N-H bond fission data show a centre total kinetic energy of about 9500 cm^{-1} and thus the H atom fragment is released with a higher kinetic energy than in the case of pyrrole. The reasoning for this is the higher initial excitation energy relative to the plateau energy for the 2PCyl radical. The PECs in figure 5.9(a,b) reflect this trend, showing a larger energy gap for the vertical Franck-Condon region at $\sim 1.0\text{ \AA}$ to the plateau at $\sim 3.5\text{ \AA}$ of the ${}^1\pi\sigma^*$ cut relatively to the ${}^1\pi\sigma^*$ cut of pyrrole. The vertical ionisation potential of PCA is (8.93 ± 0.05) eV [64] and of ethanol is (10.41 ± 0.05) eV [41]. Excitation at 222 nm (5.6 eV) is therefore unable to induce vertical ionisation of either PCA or the solvent via a single photon absorption process. The low fluence used at these short wavelengths in the transient absorption experiment make multiphoton absorption processes unlikely. Moreover, measurements conducted

in pure ethanol confirm the absence of the IR signal even at the shortest wavelength used in the transient absorption experiments.

The TA data show that once an energy of ~ 5.6 eV is accessed, which coincides with the $^1\pi\sigma^*$ state in PCA, the triplet channel disappears. It is tempting to assign this transition to the N-H bond fission event. The bond-breaking in the most closely-related molecule to pyrrole is known to be faster than the molecular rotation in the gas phase recorded by means of the anisotropy in the TOF data, indicating that bond fission occurs on an ultrafast tens-of-femtosecond time scale. This is consistent with N-H bond fission time constants determined experimentally (~ 15 fs [76]) and ab-initio on-the-fly Ehrenfest calculations that give a time constant of ~ 20 fs [98] in pyrrole to reach an N-H bond length of ~ 2 Å. The temporal resolution in the fs-TA data of ~ 100 fs is insufficient to measure an N-H bond fission process in real time with the experimentally-limited time resolution. The origin of the instantly appearing IR transient absorption component in the femtosecond solution phase experiment at an energy of 5.56 eV (223 nm) closely coincide with the sudden change observed in the TKER gas phase data. Ab-initio calculations for the potential photodissociation product, the 2PCyl fragment, have been performed in order to assign the solution phase absorption.

The TD-DFT calculations performed for the 2PCyl fragment as an isolated species, with PCM and one explicit solvent molecule in table A.2, show some transitions in the visual to IR range. In particular the 'solvent'-like calculation show three transitions at 1020 nm (~ 1.22 eV), 935 nm (~ 1.33 eV) and 750 nm (~ 1.66 eV), which are close to the experimentally-observed transition, but all have no or negligible oscillator strength. Despite the possibility that the observed absorption in the visible range at ~ 800 nm may be related to the radical absorption (which appears to be consistent with the computational data (both the TD-DFT and CASSCF) in that around 220 nm the repulsive $\pi\sigma^*$ surface is accessed, and the TKER data show the 'pyrrole'-like fast H atom photo-detachment kinetics for PCA) the low oscillator strength of the TD-DFT data presented in A.2 jars with this assignment.

5.5 Conclusion

The excited state dynamics of pyrrole-2-carboxaldehyde have been investigated with solution phase femtosecond transient absorption spectroscopy and gas phase H atom photo translational spectroscopy. Condensed phase studies of PCA in ethanol solution were conducted in an excitation range between $315 > \lambda_{\text{pump}} \geq 222$ nm with broad-

band probing between 320 and 1050 nm. The studies of the isolated molecule in the gas phase were carried out at several excitation wavelengths in the range between $280 > \lambda_{\text{pump}} \geq 218.25$ nm. The experimental data were complemented by ab-initio calculations to assign the rich dynamics observed in this aromatic pyrrole carbonyl molecule. The observed dynamics can be separated based on the excitation range that show two behaviours for PCA, resembling on one hand the dynamics that appear typical for aromatic carbonyls and on the other hand dynamics that potentially mimic the photodissociation behaviour known for pyrrole in the gas phase. As such, the conclusion is separated into two 'groups', based on excitation below and above the $\pi\sigma^*$ state:

Firstly, excitation below the $\pi\sigma^*$ onset, as determined by CAS and TD-DFT, resulted in a fast ISC to the two low-lying $T_1(1^3\pi\pi^*)$ and $T_2(1^3n\pi^*)$ triplet states with population time constants of approximately 2.5 and 4.2 ps, depending upon the initial excitation energy. The pathway that finally populated those long-lived triplet states is still a matter for discussion, but the extensive literature research indicates the involvement of an $S_1/T_1/T_2$ three-state crossing, since this has been observed in other aromatic carbonyl compounds that show remarkably similar intersystem crossing behaviour both in terms of the observed time constants and the transient absorption signatures in the visual spectral range. The absorption out of the $T_1(1^3\pi\pi^*)$ and $T_2(1^3n\pi^*)$ states at 400 and 500 nm respectively have been assigned on basis of the TD-DFT data with a simulated 'solvent bath' (PCM) and an explicit ethanol molecule to account for potential charge transfer states. The broadband component at 400 nm is assigned to transitions out of the T_1 to one or a mixture of the T_8 , T_9 and T_{10} states, and correspondingly, the 500 nm component from T_2 to T_5 , T_7 and/or T_{11} states. The TKER data in the excitation range >225 nm show no evidence of a distinct high kinetic energy release channel. Only a low hydrogen KE release is observed at an energy, centred at 3500 cm^{-1} , that corresponds to a statistical kinetic energy release. The H atom release data appear consistent with the TA data that show only the triplet state population and no indication of an instantly-activated channel. The TKER data are insufficient to describe the dynamics observed in the molecule upon excitation in this energy range, as the H atom PTS technique is specifically designed to detect H atoms.

Secondly, excitation above the $\pi\sigma^*$ threshold resulted in a dramatic change in both the observed TA data as well as the TKER data. The TKER data showed structured high TKER peaks at approximately 9950 cm^{-1} , 9725 cm^{-1} and 9500 cm^{-1} , clearly indicating the high kinetic H atom release. The vibrational fine structure in the TKER data cannot be assigned to any specific vibration of the parent molecule, but the sep-

aration of the three peaks is of the order of 225 cm^{-1} . As in the case of the TKER data a dramatic change was also observed in the TA data at an excitation wavelength less than 223 nm. The picosecond intersystem crossings that were previously observed with two spectral components at longer excitation wavelengths vanished, and a new, instantly-appearing broadband absorption component was observed between 650 and 1050 nm characterised by a single exponential decay profile of a few picoseconds. The exact origin of the IR signal is not entirely clarified. The potential origin might be an absorbing radical species which was the result of the N-H bond fission yielding a pyrrolyl-2-carboxaldehyde radical (2PCyl) in solution. Chapter 6 focuses on the excited state dynamics of pyrrole and 2-ethylpyrrole in the solution phase to clarify them further and to compare them with the dynamics observed in pyrrole-2-carboxaldehyde.

Appendix A

Tables for Chapter 5

Table A.1 Vertical excitation energies calculated for pyrrole-2-carboxaldehyde with the polarisation continuum model and explicit solvent molecule using the (TD)-B3LYP/aug-cc-pVDZ level of theory.

Transition	Solvent	(TD)-B3LYP / aug-cc-pVDZ Vertical Excitation Energies / eV					
		PCA			PCA with explicit solvent molecule		
		State	in solution (PCM)		State	in solution (PCM)	
			Vertical Excitation Energy / eV	<i>f</i>		Vertical Excitation Energy / eV	<i>f</i>
S ₁	ethanol	¹ nπ*	4.0041	0.0003	¹ nπ*	4.1480	0.0004
	methanol	¹ nπ*	4.0064	0.0003	¹ nπ*	4.1562	0.0004
	water	¹ nπ*	4.0096	0.0003	¹ nπ*	4.1884	0.0005
S ₂	ethanol	¹ ππ*	4.5809	0.4011	¹ ππ*	4.5220	0.3548
	methanol	¹ ππ*	4.5880	0.3934	¹ ππ*	4.5277	0.3543
	water	¹ ππ*	4.5847	0.3947	¹ ππ*	4.5468	0.3676
S ₃	ethanol	¹ ππ*	5.0178	0.1140	¹ ππ*	4.9022	0.1472
	methanol	¹ ππ*	5.0173	0.1160	¹ ππ*	4.9051	0.1539
	water	¹ ππ*	5.0137	0.1167	¹ ππ*	4.9246	0.1530
S ₄	ethanol	¹ πσ*	5.6509	0.0034	¹ πσ*	5.7244	0.0026
	methanol	¹ πσ*	5.6545	0.0034	¹ πσ*	5.719	0.0026
	water	¹ πσ*	5.6575	0.0033	¹ πσ*	5.6717	0.0017
T ₁	ethanol	³ ππ*	2.8845		³ ππ*	2.8947	
	methanol	³ ππ*	2.8845		³ ππ*	2.8993	
	water	³ ππ*	2.8819		³ ππ*	2.8349	
T ₂	ethanol	³ nπ*	3.5115		³ nπ*	3.6937	
	methanol	³ nπ*	3.5137		³ nπ*	3.7006	
	water	³ nπ*	3.5179		³ nπ*	3.7247	
T ₃	ethanol	³ ππ*	3.9589		mixed	3.8539	
	methanol	³ ππ*	3.9553		mixed	3.9232	
	water	³ ππ*	3.9508		³ ππ*	3.8271	
T ₄	ethanol	³ ππ*	5.2747		³ ππ*	5.3626	
	methanol	³ ππ*	5.2761		³ ππ*	5.3820	
	water	³ ππ*	5.2791		³ ππ*	5.3546	

Table A.2 Vertical excitation energies calculated for pyrrolyl-2-carboxaldehyde radical (2PCyl) with the polarisation continuum model and additional explicit solvent molecule using the (TD)-B3LYP/aug-cc-pVDZ level of theory.

Transition from D ₀ to	Solvent	(TD)-B3LYP / aug-cc-pVDZ Vertical Excitation Energies / eV					
		2PCyl			2PCyl with explicit solvent molecule		
		State	in solution (PCM)		State	in solution (PCM)	
			Vertical Excitation Energy / eV	<i>f</i>		Vertical Excitation Energy / eV	<i>f</i>
D ₁	ethanol	–	1.2017	0.0016	–	1.2150	0.0018
	methanol	–	1.2014	0.0016	–	1.2167	0.0018
	water	–	1.1996	0.0016	–	1.2170	0.0019
D ₂	ethanol	–	1.3595	0.0000	–	1.3254	0.0000
	methanol	–	1.3640	0.0000	–	1.3280	0.0000
	water	–	1.3730	0.0000	–	1.3611	0.0000
D ₃	ethanol	–	1.9373	0.0000	–	1.6603	0.0001
	methanol	–	1.9415	0.0000	–	1.7300	0.0001
	water	–	1.9498	0.0000	–	2.1312	0.0000
D ₄	ethanol	–	3.7944	0.0014	–	2.0578	0.0000
	methanol	–	3.7948	0.0014	–	2.0642	0.0000
	water	–	3.7953	0.0016	–	2.5955	0.0001

Table A.3 Vertical excitation energies calculated from the T_1 minimum energy geometries for PCA with the polarisation continuum model and explicit solvent molecule using the (TD)-B3LYP/aug-cc-pVDZ level of theory.

Transition from T_1 to	Solvent	(TD)-B3LYP / aug-cc-pVDZ Vertical Excitation Energies / eV			
		PCA in solution (PCM)		PCA with explicit solvent molecule in solution (PCM)	
		Vertical Excitation Energy / eV	f	Vertical Excitation Energy / eV	f
T_2	ethanol	0.8626	0.0000	1.0913	0.0000
	methanol	0.8687	0.0000	1.1063	0.0000
	water	0.8803	0.0000	1.1424	0.0000
T_3	ethanol	1.5331	0.0014	1.4478	0.0012
	methanol	1.5319	0.0014	1.4456	0.0012
	water	1.5285	0.0014	1.4439	0.0012
T_4	ethanol	2.7804	0.0121	2.2409	0.0006
	methanol	2.7850	0.0119	2.316	0.0006
	water	2.7923	0.0119	2.9044	0.0120
T_5	ethanol	2.9604	0.0012	2.8894	0.0125
	methanol	2.9626	0.0012	2.898	0.0120
	water	2.9662	0.0012	3.0149	0.0009
T_6	ethanol	3.3801	0.0133	3.0903	0.0013
	methanol	3.3852	0.0127	3.0863	0.0012
	water	3.3924	0.0124	3.2499	0.0016
T_7	ethanol	3.4602	0.0001	3.4523	0.0063
	methanol	3.4642	0.0001	3.4656	0.0069
	water	3.4713	0.0001	3.4746	0.0028
T_8	ethanol	3.5464	0.0003	3.5098	0.0006
	methanol	3.5493	0.0003	3.5510	0.0008
	water	3.5544	0.0003	3.4974	0.0057
T_9	ethanol	3.9102	0.2521	3.5661	0.0011
	methanol	3.9167	0.2478	3.5794	0.0006
	water	3.9166	0.2495	3.6008	0.0002
T_{10}	ethanol	4.0536	0.0067	3.7450	0.0008
	methanol	4.0584	0.0066	3.8067	0.0034
	water	4.0672	0.0065	3.9452	0.2327
T_{11}	ethanol	4.1667	0.0000	3.848	0.0752
	methanol	4.1701	0.0000	3.8597	0.0638
	water	4.1766	0.0001	4.0992	0.0142
T_{12}	ethanol	4.2100	0.0001	3.9596	0.0058
	methanol	4.2151	0.0000	4.0076	0.1771
	water	4.2245	0.0000	4.2407	0.0084
T_{13}	ethanol	4.3710	0.0030	4.0075	0.0736
	methanol	4.3741	0.0030	4.1221	0.0120
	water	4.3795	0.0030	4.3084	0.0177

Chapter 6

$\pi\sigma^*$ mediated Photodissociation in Pyrrole and 2-Ethylpyrrole derivatives

6.1 Introduction

The photostability of pyrrole has been investigated in a number of theoretical and experimental [15, 23, 65, 95, 98, 102, 115] studies. Pyrrole serves as a benchmark molecule with which to study the photophysics of biological systems, such as the indole moiety in the purine DNA bases. It is a five-membered, heterocyclic ring compound. The nitrogen atom donates an electron pair (lone pair in $2p_x$ orbital) to the ring structure, creating an aromatic six π -electron system (aromatic sextet).

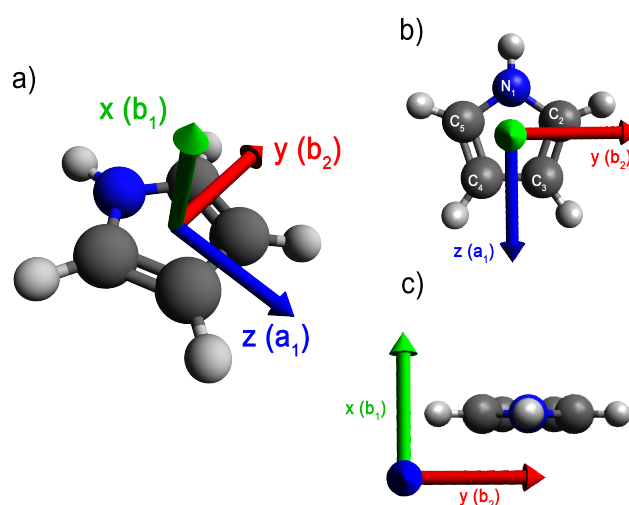


Fig. 6.1 Pyrrole in C_{2v} Symmetry in Cartesian Coordinates System. a) Three dimensional representation of pyrrole with coordinate axes, b) pyrrole in yz -mirror plane and c) molecule shown in xy -plane.

The flat pyrrole molecule is shown in figure 6.1 together with the Cartesian coordinate system. By convention the principle rotation axis defines the z -axis in pyrrole going along the N-H bond with the molecular plane being defined to lie in the yz -mirror plane as shown in figure 6.1(b). The equilibrium geometry of pyrrole possesses a twofold symmetry axis $C_2(z)$ together with two mirror planes ($\sigma_v(xz)$ and $\sigma_v(yz)$) resulting in an overall C_{2v} symmetry. A Hartree-Fock calculation with a minimum STO-3G basis set predicts a ground state molecular orbital configuration of $[\dots](b_1\pi)^2(a_2\pi)^2(a_1\sigma^*)^0(b_1\pi^*)^0$. These orbitals are shown schematically together with their lowest energy transitions from the HOMO and HOMO-1 to the three LUMOs in figure 6.2.

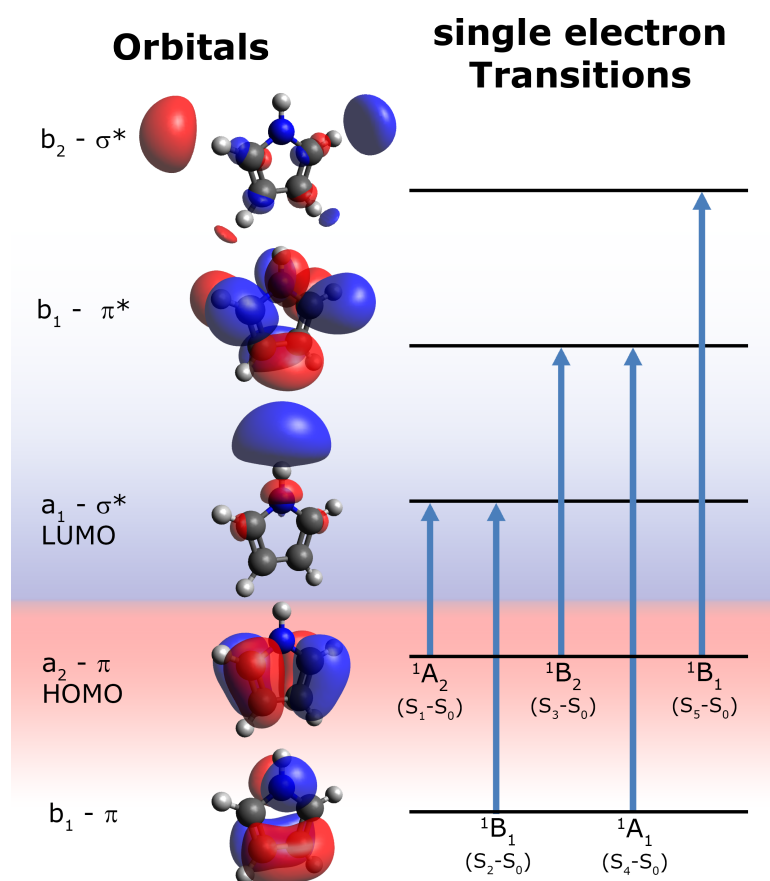


Fig. 6.2 Frontier Orbitals of Pyrrole and the energetically low lying singlet transitions.

The lowest two molecular orbitals are of π character with the HOMO being of a_2 symmetry and the HOMO-1 of b_1 symmetry. The LUMO+1 π^* is the corresponding antibonding orbital of the HOMO-1 and thus of b_1 symmetry. The π^* virtual orbital corresponding to the $a_2 \pi$ (HOMO) is higher in energy and not shown in figure 6.2. Transitions out of the b_1 and $a_2\pi$ valence orbitals to the $b_1 \pi^*$ orbital are bound in the N-H stretch. Two more low-lying unoccupied molecular orbitals are shown in

figure 6.2. These correspond to $a_1\sigma^*$ and $b_2\sigma^*$ orbitals and are described by a mixture of low-lying Rydberg states with valence states. The LUMO lies below the π^* orbital and is a mixture of the nitrogen 3s orbital with the σ^* antibonding orbital. The $3s/\sigma^*$ orbital is unbound in the N-H stretch coordinate and thus in principle can lead to N-H bond fission. Excitation out of either of the two π HOMOs thus leads to two low energy transitions: The lowest energy excitation from the π HOMO (a_2) to the σ^* LUMO (a_1) is of A_2 symmetry and forbidden by electronic dipole symmetry considerations since the configuration [...] $(b_1\pi)^2(a_2\pi)^2$ is necessarily of A_1 symmetry overall. The second lowest (from the π HOMO-1 (b_1) to the LUMO (a_1)) energy transition is of B_1 character which is dipole allowed. The LUMO+2 is another Rydberg valence state that is of $3p_y/\sigma^*$ character.

The above considerations allow us to understand the UV gas phase absorption spectrum of pyrrole shown in figure 6.3.

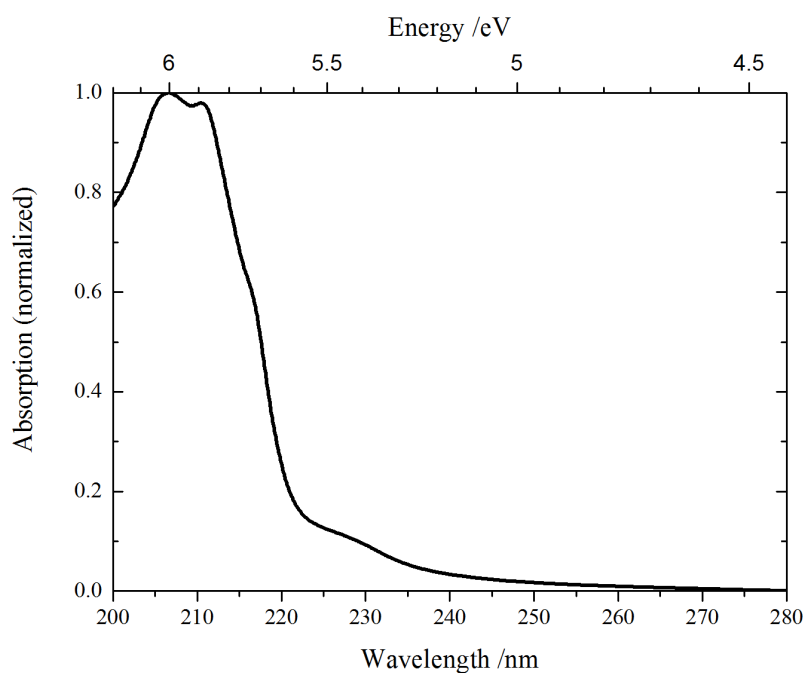


Fig. 6.3 Absorption Spectrum of Pyrrole (vapour phase)

The prominent absorption at wavelengths shorter than 220 nm can be interpreted as an allowed transition out of the ground S_0 (π^2) configuration to the B_1 valence and B_2 Rydberg states. The weak tail in the absorption spectrum at wavelengths longer than 220 nm can be explained as the transition to the energetically low-lying $S_1(\pi\sigma^*)$ state that is formally electric dipole forbidden ($A_2 \leftarrow A_1$) but gains in oscillator strength through Herzberg-Teller coupling. Due to the lack of heavy atoms in pyrrole and the spin selection rules, all possible transitions in the absorption spectrum can be assigned

to singlet state absorptions. Detailed studies in assigning the absorption features have been carried out among others by Palmer [88]. In order to confirm the spectroscopy, un-relaxed four state averaged (SA4) electronic structure calculations along the $R_{\text{N-H}}$ coordinate were performed at the CASPT2(8/7)/aug(N)-cc-pVDZ level of theory (see figure 6.4) using the molpro ab-initio quantum chemistry package.

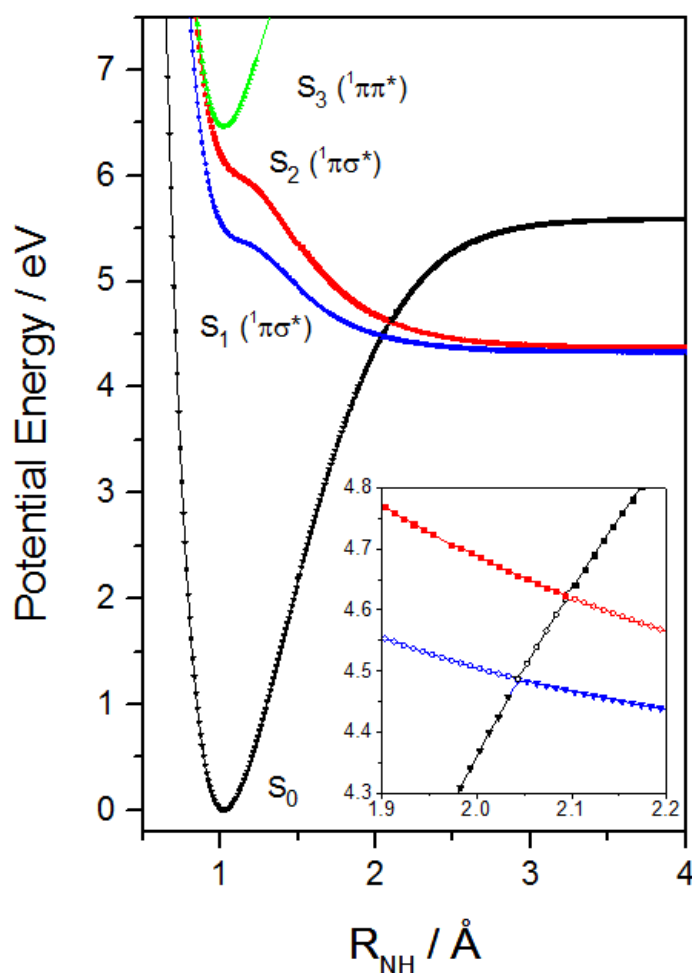


Fig. 6.4 CASPT2(8/7) Calculations of the first three excited electronic states in Pyrrole. Showing the first two repulsive $\pi\sigma^*$ and the bound $\pi\pi^*$ states

As also predicted by Sobolewski and Domcke [102] the low-lying $\pi\sigma^*$ state is repulsive in the N-H bond breaking coordinate, which has been confirmed experimentally in gas phase studies of isolated pyrrole molecules that detected the formation of H atoms upon excitation to the lowest-lying excited state surface [23, 81]. The presented CAS calculation (figure 6.4) reflects this repulsive character for the $S_1(\pi\sigma^*)$ potential energy cut (blue curve). The repulsive character of the S_1 surface is essentially barrierless and leads to rapid dissociation of the excited pyrrole molecule along the N-H stretch as shown for isolated molecules in the gas phase and result in pyrrolyl and H

atom radicals. The repulsive state inevitably crosses the ground state surface ($S_0(\pi^2)$) at long N-H stretch (see inset of figure 6.4) to form a conical intersection as also confirmed experimentally by Lippert et. al [65]. The inset also shows another conical intersection between the ground state surface and the bright $S_2(\pi\sigma^*)$ surface, S_1 being of B_1 character. The involvement of the second conical intersection upon excitation to the S_1 state is little understood. Most gas phase experiments have been carried out with nanosecond time resolution and thus probed the final state of the system. The lack of time resolved femtosecond studies is related to the low absorption cross section of pyrrole at the S_1 absorption onset and the low number density in the gas phase. These considerations together with the low number of photons provided in a femtosecond laser pulse made it challenging to achieve a signal-to-noise ratio sufficient to study the dynamics with femtosecond time resolution. Understanding differences and similarities in the photochemistry between gas and solution phases is crucial to translate conclusions drawn from isolated systems to molecular systems in a solvent environment. The aim of this chapter is to investigate the excited state dynamics of pyrrole and 2-ethylpyrrole (2EP) in the solution phase. 2-ethylpyrrole has recently been studied by Karsili et al. [48] in the gas phase with H atom phototranslational spectroscopy (PTS) and photodissociation was confirmed upon excitation onto the repulsive S_1 surface. Besides an improved understanding of how the excited state dynamics are affected by solvent environment, the femtosecond transient absorption experiment provides additional information over the nanosecond H atom PTS gas phase experiments reported in the literature, as the transient absorption setup allows one to follow the population flow of all absorbing species that are formed upon photoexcitation, provided the species are absorbing in the range of the probe continuum.

6.2 Methodology: Experiment, Computational Details

Similarly, to chapter 4 a slight modification to the experimental setup, as outlined in chapter 3, was required in order to access a probe range in the IR and UV range. Details on the modification of the IR and UV probe continuum are given in sections 4.2.1 and 5.2.2, respectively. Further to the modification of the probe continuum setup, the sum-frequency mixing scheme as described in section 5.2.3 was used in order to access the UV excitation range below 250 nm.

6.2.1 Sample Preparation

Pyrrole and 2-ethylpyrrole were used as received. Pyrrole (Sigma Aldrich, purity >98 %) and 2-ethylpyrrole (TCI Chemicals, purity >96 %) were dissolved in ethanol (Sigma Aldrich, purity ≥ 99.5 %) to form clear solutions of $c \simeq 84 \text{ mmol L}^{-1}$ and $c \simeq 62 \text{ mmol L}^{-1}$, respectively.

6.2.2 Computational Details

Time-dependent density functional theory (TD-DFT) calculations were conducted with the Gaussian 09 computational package [Frisch et al.]. It was used to calculate the minimum energy of the ground state geometry of pyrrole and 2-ethylpyrrole in C_{2v} and C_1 symmetry, respectively. Extensive calculations in Karsili et al. [48] showed a minimum energy geometry for the gauche conformer in 2-ethylpyrrole. Thus a starting geometry close to the gauche conformer in 2-ethylpyrrole was chosen for the optimisation. The minimum energy geometry was calculated using Becke's three-parameter hybrid functional with the Lee-Yang-Parr exchange-correlation functional (B3LYP) [7] together with Dunning's augmented correlation consistent basis set of double- ζ quality (aug-cc-pVDZ) [26]. At the same level of theory the pyrrolyl and 2-ethylpyrrolyl radical minimum energy geometries were calculated. In addition to the geometry optimisations of isolated gas phase species, calculations were also carried out with one explicit ethanol molecule and an ethanol 'solvent bath' simulated with the integral equation formalism variant (IEFPCM) polarisation continuum model (PCM) that used a dielectric constant of $\epsilon = 24.852$ as embedded within Gaussian 09. The geometry optimisations in solvent environment were free of symmetry restrictions. The optimised geometry of each species was used to calculate the vertical excitation energies and the associated oscillator strengths, f .

The MOLPRO 2010.1 computational package [116] was used to calculate the transition dipole moments (TDMs) and vertical excitation energies for the three lowest excited states in pyrrole and 2-ethylpyrrole. In the case of 2-ethylpyrrole a four-state averaged complete active space self-consistent field method with eight electrons over seven orbitals (SA4-CAS(8,7)) together with Dunning's cc-pVDZ basis set with additional diffuse functions centred around the nitrogen atom (aug(N)-cc-pVDZ) was used to describe the low-lying $\pi\sigma^*$ state. The choice of basis set was adapted from pyrrole calculations in Saita et al. [98]. The active space of 2-ethylpyrrole consists of three π and two π^* orbitals on the heteroaromatic ring frame and one σ and a corresponding σ^*

orbital to describe the repulsive character along the N-H coordinate. Potential energy cuts (PECs) along the N-H stretch coordinate ($R_{\text{N-H}}$) with otherwise rigid structure were calculated from the optimised ground state 2-ethylpyrrole geometry. The PECs used the SA4-CAS(8,7) described above and calculated CASPT2 energies. For comparison the PECs for pyrrole with CASPT2 energies are also shown based on the CAS space as described in Saita et al. [98].

The MOLPRO 2010.1 computational package was also used to calculate the intrinsic coordinate that links the radical ground and the first excited radical state via a conical intersection for the pyrrolyl and 2-ethylpyrrolyl fragment. SA4-CAS(7,6)-SCF calculations were conducted on the pyrrolyl and 2-ethylpyrrolyl radical by optimising both on the D_0 (2A_2) minimum and the intersection point. The active space was almost identical to the calculations described above and only differs in the absence of the dissociative H atom together with its single electron and the associated σ^* orbital. For comparison the aug(N)-cc-pVDZ basis set was not changed. The intrinsic coordinate was constructed by linearly interpolating between the D_0 minimum and the conical intersection with consecutive SA4-CAS(7,6)-SCF calculations along this coordinate in order to recover the potential energy curves, very similar to the SA3-CAS(7,7)-SCF calculation reported for the pyrrolyl radical in the publication by Saita et al. [98]. Additionally to these calculations [98] the oscillator strength and excitation energies have been recovered.

6.3 Pyrrole

6.3.1 Results: fs-Transient Absorption

Femtosecond transient absorption experiments for pyrrole in ethanol solution were conducted in a wide probe range stretching from the near UV (~ 315 nm) to the near IR (~ 1000 nm) range. The TA data shown in figure 6.5 were excited at $\lambda_{\text{pump}} = 240$ nm close to the absorption onset as known from the UV-Vis absorption spectrum (figure 6.3) and its time evolution was probed over the first 6 ps. The chirp corrected data were averaged over 25 data points in the time domain. The TA plot (6.5(b)) was recorded with the UV probe continuum and averaged kinetics with an integration range indicated in the TA plot are shown in figure 6.5(a) which results in a kinetic centre wavelength of approximately 350 nm.

The data show an instant absorption signal with the coherence spike at time zero

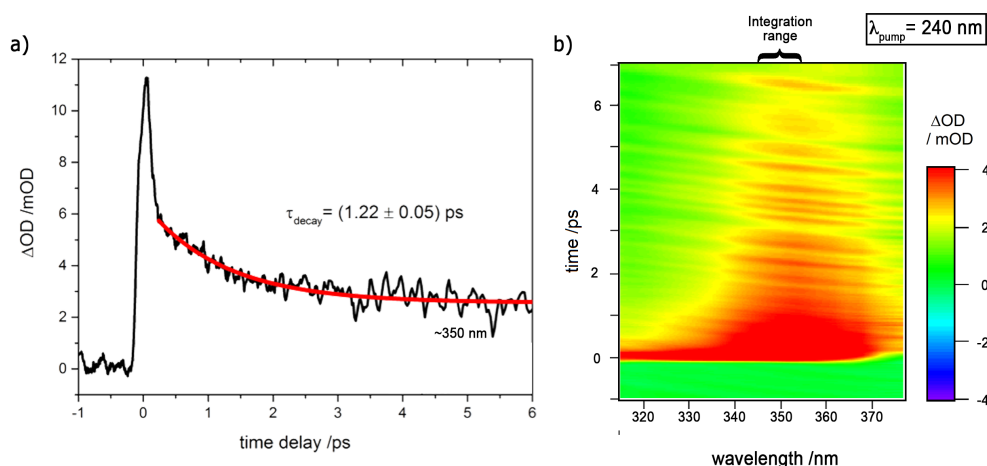


Fig. 6.5 Averaged transient (a) of pyrrole excited at 240 nm and corresponding contour plot (b) in the range 315 to 375 nm. Transient (a) shows a single exponential decay component for the broadband absorption band observed in the contour plot (b) centred at ~ 350 nm.

followed by a decay component that appears to level off after a decay time of a few picoseconds. The extracted kinetic shown in figure 6.5(a) was fitted with a single exponential decay function with offset. A decay time constant of (1.22 ± 0.05) ps was determined. Over the first 6 ps the absorption signal decayed to about 50 % of its magnitude.

The data shown in figure 6.6 show the evolution over the first 50 ps after excitation at 243 nm with the IR probe continuum with a three dimensional representation in figure 6.6(a). No signal components were observed between approx. 400 to 650 nm in the visual range as probed with the VIS probe continuum with the exception of the coherence spike at time zero. The dynamics shown in the data set related to figure 6.6(c) feature a decaying absorption signal and an initial frequency sweep from the near-IR into the visible. The graph in figure 6.6(b) was generated by fitting each spectral cut shown in figure 6.6(c) with a free floating Gaussian with no constraints. The centre wavelength as well as Gaussian full width half-maximum (FWHM) is plotted as a function of delay time. The frequency sweep can be described with a single-exponential with a time constant of (9.1 ± 0.4) ps. The origin of this spectral sweep at time zero is determined to be at ~ 1020 nm and equilibrates to ~ 725 nm at a time delay of 50 ps. The Gaussian width (blue hollow circles) shown in figure 6.6(c) narrows from initially ~ 400 nm to ~ 125 nm within a few picoseconds. A single exponential fit recovers a time constant of approx. 3 ps for the change in Gaussian width.

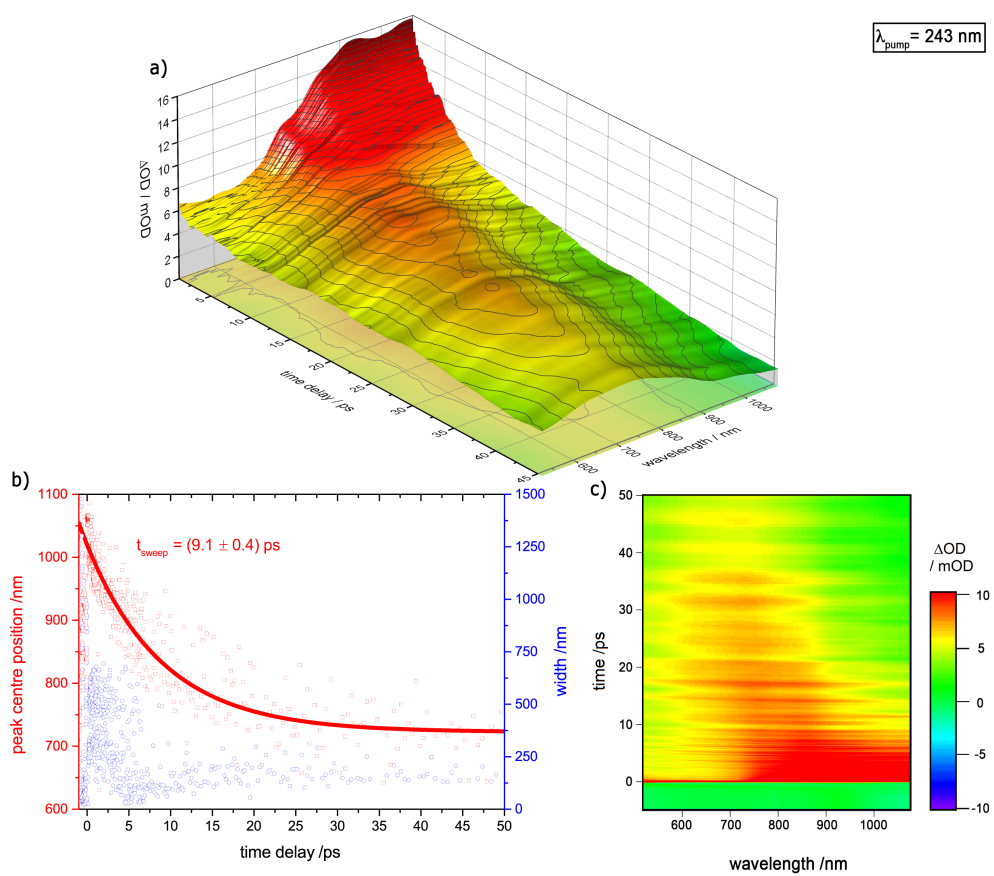


Fig. 6.6 Excited state dynamics over the first 50 ps of pyrrole in ethanol solution excited at 240 nm and probed in the near-IR spectral range between 550 to 1070 nm as (a) 3D representation, (b) fitting of broadband frequency sweep and (c) and as contour plot.

6.3.2 Results: Computational

CASSCF-(SA4) Potential Energy Cuts

The potential energy cuts (PECs) along the NH stretch coordinate calculated for pyrrole (C_{2v}) and the TD-DFT calculations for the isolated molecule have been presented as part of figure 5.9 and table 5.1. The CAS-SCF calculation was recalculated for internal consistency to allow for comparison to 2-ethylpyrrole presented in section 6.4. The four state averaged CAS-SCF calculation along the NH stretch coordinate is given in the introduction to this chapter in figure 6.4, showing the first two repulsive $S_1(\pi\sigma^*)$ surfaces (blue and red) and the bound third excited state (green).

TD-DFT State Energies and Oscillator Strengths

As outlined in section 6.2.2 TD-DFT calculations carried out for pyrrole using the IEFPCM polarisation continuum model for ethanol to simulate a solvent bath are given in table 6.1. Additionally, the vertical excitation energies and oscillator strengths were calculated for pyrrole including one explicit solvent molecule.

Table 6.1 Vertical excitation energies calculated for pyrrole with polarisation continuum model and explicit ethanol molecule using the (TD)-B3LYP/aug-cc-pVDZ level of theory.

Transition from S_0 to	solvent	(TD)-B3LYP / aug-cc-pVDZ Vertical Excitation Energies / eV					
		Pyrrole			Pyrrole with explicit ethanol molecule		
		State	in solution (PCM)		State	in solution (PCM)	
			Vertical Excitation Energy / eV	f		Vertical Excitation Energy / eV	f
S_1	ethanol	$^1\pi\sigma^* / A_2$	5.0505	0.0000	$^1\pi\sigma^*$	4.9363	0.0000
S_2	ethanol	$^1\pi\sigma^* / B_1$	5.6836	0.0466	$^1\pi\sigma^*$	5.4723	0.0321
S_3	ethanol	$^1\pi\pi^* / B_2$	5.9096	0.0024	$^1\pi\pi^*$	5.6052	0.0680
S_4	ethanol	$^1\pi\pi^* / A_1$	5.9325	0.2185	$^1\pi\pi^*$	5.7741	0.0073

The dominant orbital transitions involved in the above calculations for the first four states in pyrrole with PCM are identical to the isolated pyrrole species (in table 5.1) and depicted in figure 6.2. However, they show a slightly different excitation energy for the S_1 to S_3 states which is 0.2 to 0.3 eV above the corresponding calculations for the isolated pyrrole species and the oscillator strength follows the trend of the isolated species. The calculations with explicit ethanol molecule show a reversed ordering for the third and fourth state, which is caused by the mixing of the explicit solvent molecule and also evident in the oscillator strength value.

Calculations were repeated for the pyrrolyl radical fragment. The TD-DFT calculations for the isolated species were already presented in table 5.2 and table 6.2 extends these calculations with PCM and one explicit ethanol molecule in C_{2v} and C_s symmetry, respectively.

Table 6.2 Vertical excitation energies calculated for pyrrolyl radical with polarisation continuum model and additional explicit ethanol molecule using the (TD)-B3LYP/aug-cc-pVDZ level of theory.

Transition from D_0 (A_2 / A'') to	(TD)-B3LYP / aug-cc-pVDZ Vertical Excitation Energies / eV					
	Pyrrolyl Radical			Pyrrolyl Radical with explicit ethanol molecule		
	Sym	in solution (PCM)		Sym	in solution (PCM)	
Vertical Excitation Energy / eV		f	Vertical Excitation Energy / eV		f	
D ₁	B ₁	1.4157	0.0010	A''	1.4546	0.0018
solvent	–	–	–	A''	2.3057	0.0002
D ₂	A ₁	2.0465	0.0000	A'	2.3992	0.0000
solvent	–	–	–	A'	4.1215	0.0000
D ₃	B ₁	4.6742	0.0071	A''	4.7227	0.0056
solvent	–	–	–	A'	4.8548	0.0007
D ₄	B ₂	4.8929	0.0000	A''	5.1003	0.0001

6.4 2-Ethylpyrrole

2-Ethylpyrrole is made up of a five membered heteroaromatic ring structure and is structurally similar to pyrrole as shown in figure 6.7. The numbering of the atoms has been taken over from pyrrole for consistency. In pyrrole a hydrogen is connected to the carbon in the second position (labelled C₂ in figure 6.7b) that in the case of 2-ethylpyrrole is substituted with an ethyl group.

The orientation of the ethyl group with regards to the planar pyrrole ring frame structure effects the symmetry of the molecule. In the case where the ethyl group lies in the molecular plane it possesses a yz -mirror plane, as shown for the syn-conformer in figure 6.7a and for the anti-conformer in figure 6.7d. Those two conformers are of C_s symmetry. Rotation of the ethyl group around the C2-C7 bond moves the alkyl chain out of the molecular plane and as a consequence breaks the C_s symmetry. Thus an orientation other than the two planar conformers results in an overall C_1 symmetry. As in the case of pyrrole symmetry considerations are important in the spectroscopy of 2-ethylpyrrole. Un-relaxed four state averaged (SA4) electronic structure calculations

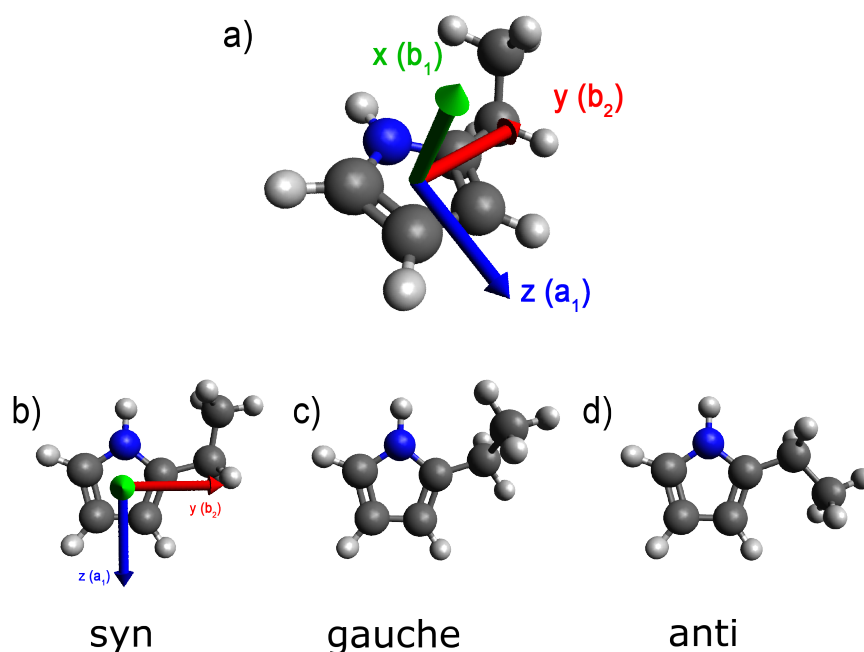


Fig. 6.7 Selected 2-Ethylpyrrole Conformers in Cartesian Coordinates System. a) shows 2-ethylpyrrole in free space together with its cartesian coordinates, b-d) show three possible conformers of 2-ethylpyrrole in syn (0°), gauche (60°) and anti (180°) conformation in the zy -mirror plane.

along the R_{N-H} coordinate in analogy to pyrrole were performed at the CASPT2(8/7)/aug(N)-cc-pVDZ level of theory (see figure 6.8) using the molpro ab-initio quantum chemistry package.

The CAS calculation (figure 6.8)(a) show two low-lying repulsive potential surfaces $S_1(\pi\sigma^*)$ (blue curve) and $S_2(\pi\sigma^*)$. The S_2 cut shows a very small barrier, followed by the pyrrole-typical repulsive character along the N-H stretch coordinate. Figure 6.8(b) shows the energy separation of the first and second conical intersection as a function of dihedral angle. The following subsection 6.4.1 compares the UV absorption spectrum between pyrrole and 2-ethylpyrrole.

6.4.1 Results: UV Absorption Spectrum

Static UV-vis absorption spectra of 2-ethylpyrrole and pyrrole in the vapour phase (20°C) are shown in figure 6.9. The absorption axis was normalised to the maximum absorption peak for easier comparison of the absorption spectra of 2-ethylpyrrole with pyrrole. The gas phase UV-vis suggests a slight shift of the absorption onset to about 267 nm for 2-ethylpyrrole in comparison to the absorption onset in pyrrole (257 nm).

The shift has been related to the inductive effect of the alkyl group that acts desta-

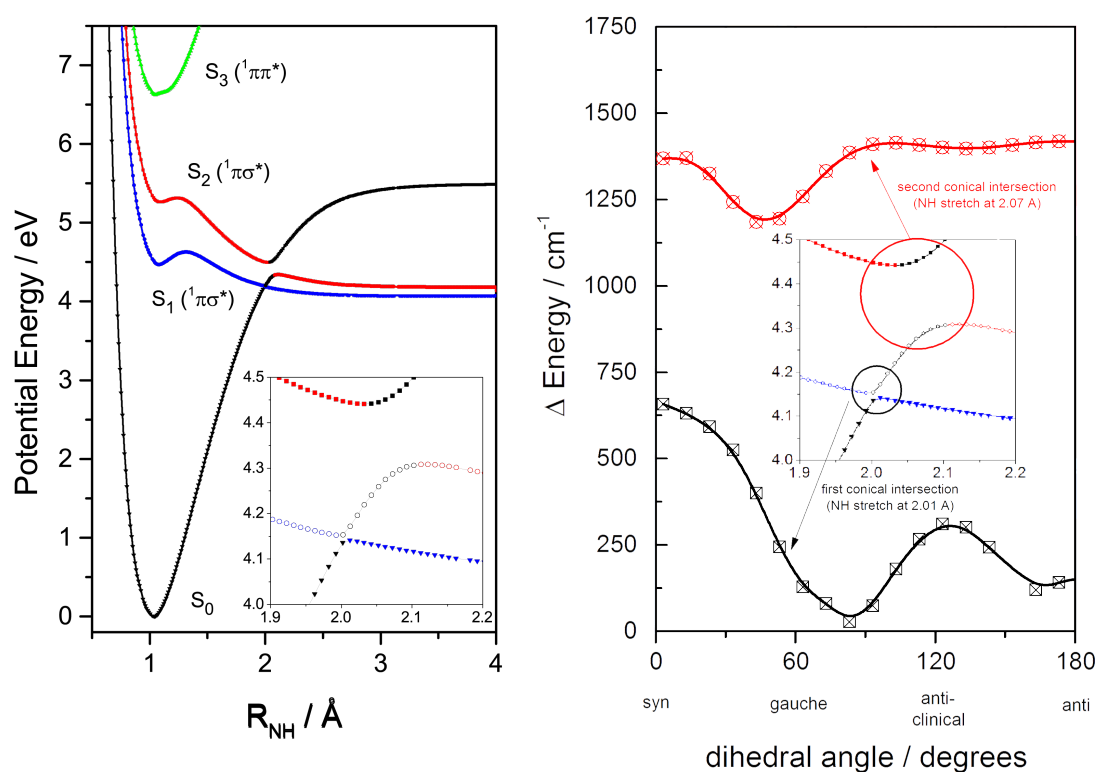


Fig. 6.8 a) CASPT2(8/7) Calculations of the first three excited electronic states in 2-Ethylpyrrole. Showing the first two repulsive $\pi\sigma^*$ and the bound $\pi\pi^*$ states with inset of the intersection region of the ground state surface $S_0(\pi^2)$ with the repulsive $\pi\sigma^*$ S_1 and S_2 surface. b) CASSCF(8/7) of the 2-Ethylpyrrolyl Radical in the conical intersection region as a function of dihedral angle. Showing the S_0/S_1 conical intersection with a minimum for the gauche-conformer.

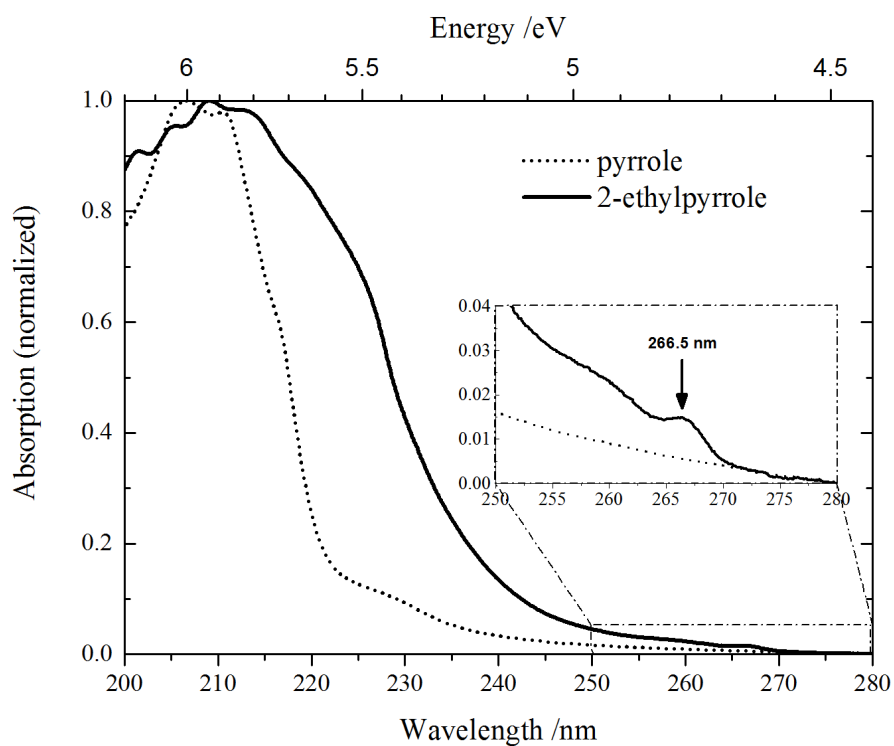


Fig. 6.9 Comparing the UV Absorption Spectrum of 2-Ethylpyrrole and Pyrrole with inset graphic in absorption range 250 to 280 nm. 2-Ethylpyrrole (solid line) with clear absorption onset and first absorption structure at approximately 266.5 nm, pyrrole absorption spectrum (dotted line) shown for comparison.

bilising on the sigma framework and thus lowers the N-H bond strength [48]. Further to this the absorption onset in 2-ethylpyrrole shows a remarkable sharp peak centred at 266.5 nm as shown in the inset of the absorption spectra in figure 6.9. This might indicate a bound population, contrary to pyrrole with a gradual decrease in absorption strength. The evidently weak absorption at $\lambda \geq 240$ nm in the case of 2-ethylpyrrole can be related to weak $1^1\pi\sigma^* \leftarrow S_0$ absorption as in the case of pyrrole and known from the literature [23, 48, 80]. The evident increased in absorption strength at wavelengths shorter than approx. 240 nm, as in the case of pyrrole, can be related to absorption into the optically bright $1^1\pi\pi^*$ state according to Karsili et al. [48]. As mentioned previously the C_{2v} symmetry as observed in pyrrole is broken in 2-ethylpyrrole by the ethyl group and transition to the $S_1(1^1\pi\sigma^*)$ state is not completely forbidden by electronic dipole considerations.

6.4.2 Results: fs-Transient Absorption

Femtosecond transient absorption experiments for 2-ethylpyrrole in ethanol solution were conducted in a wide probe range stretching from the near UV (~ 315 nm) to the near IR (~ 1000 nm) range at magic angle. Excitation at $\lambda_{\text{pump}} = 243$ nm and probing with the UV probe continuum as in the case of pyrrole revealed a broadband absorption component centred at approximately 390 nm. The extracted kinetic cut is shown in figure 6.10. The time evolution was probed over the first 6 ps.

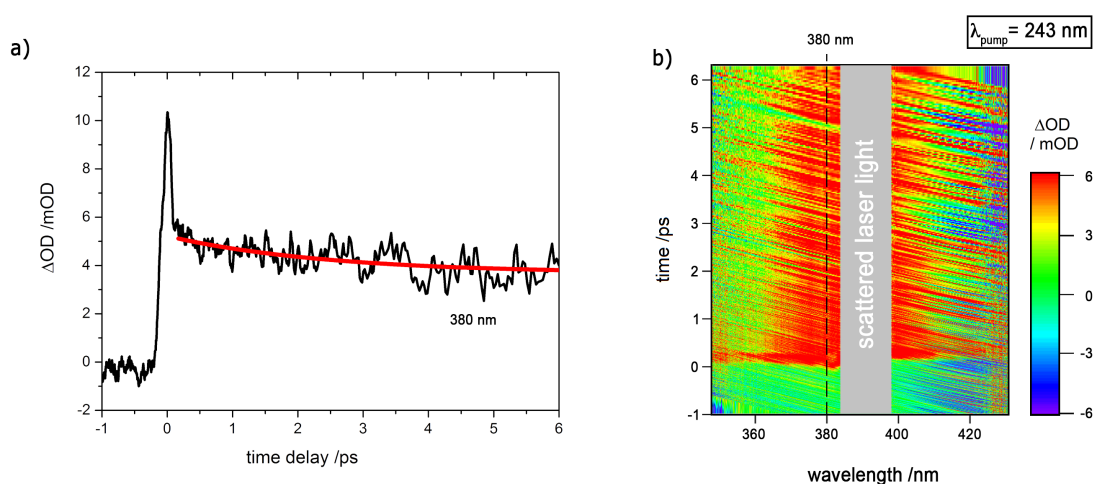


Fig. 6.10 Excited state dynamics over the first 6 ps of 2-ethylpyrrole in ethanol solution excited at 243 nm and probe in the UV range. (a) Transient shows instant absorption component at ~ 380 nm extracted close to the centre of the broadband absorption as shown in (b) the contour plot.

The data show an instant absorption signal with the coherence spike at time zero

followed by a marginal decay as indicated with the single exponential decay function (red line). A decay time constant of (2.48 ± 0.43) ps was determined. However, a large offset is observed at 6 ps indicating a total reduction in magnitude of the absorption signal by only approximately 25 %. Similarly to the dynamics observed in pyrrole the data set for 2-ethylpyrrole (figure 6.11) at an excitation wavelength of 243 nm features a frequency sweep from >1000 nm to 700 nm, which can be seen in the 3D representation and the contour plot of figure 6.11(a,c). Contrary to the dynamics observed in the case of pyrrole, the extracted time constant for the sweep feature is of the order of (15.8 ± 0.8) ps and thus slower than in the case of pyrrole. The fitting was carried out in analogy to the pyrrole data and a single exponential worked well in the range after the first 3 ps for the frequency sweep. The gaussian width (figure 6.11, blue hollow dots) starts off with a narrow bandwidth of approximately 125 nm and after passing the turning point at approximately (24.0 ± 0.5) ps the gaussian FWHM widens significantly (to ~ 900 nm), forming a broadband absorption covering the entire white light continuum range.

Additionally, a narrow absorption band centred at approximately 580 nm is observed in the experiment conducted at an excitation wavelength of 243 nm. The absorption band appears to grow over several picoseconds which is caused by the broadband absorption band sweeping into the absorption range of the narrow band. Experiments conducted at $\lambda_{\text{pump}} < 267$ nm did not result in any significant absorption past the coherence spike. Thus experiments conducted at 267 nm, which correspond closely to the onset known from the UV-vis vapour phase absorption spectrum, show a dramatic change in the transient absorption plot shown in figure 6.12(b). The former prominent sweeping feature in the IR spectral range is vanished leaving a broadband absorption band centred around 750 nm. The absorption onset is instant within the time resolution of the excitation pulse and the kinetic cut for the 750 nm component (green dots) shown in figure 6.12(a). Interestingly, the weak feature observed at approximately 580 nm in figure 6.11(a) at higher energy excitation is now the prominent absorption feature. The kinetic cut for the 580 nm component (black dots) is also shown in figure 6.11(a) together with the transient at 520 nm (blue dots) that shows the coherence spike and provides an indication about the cross-correlation of the white light continuum and the excitation pump pulse at this wavelength. The transient at 580 nm was fit with a single exponential (red solid line) and has a rise time of ~ 300 fs.

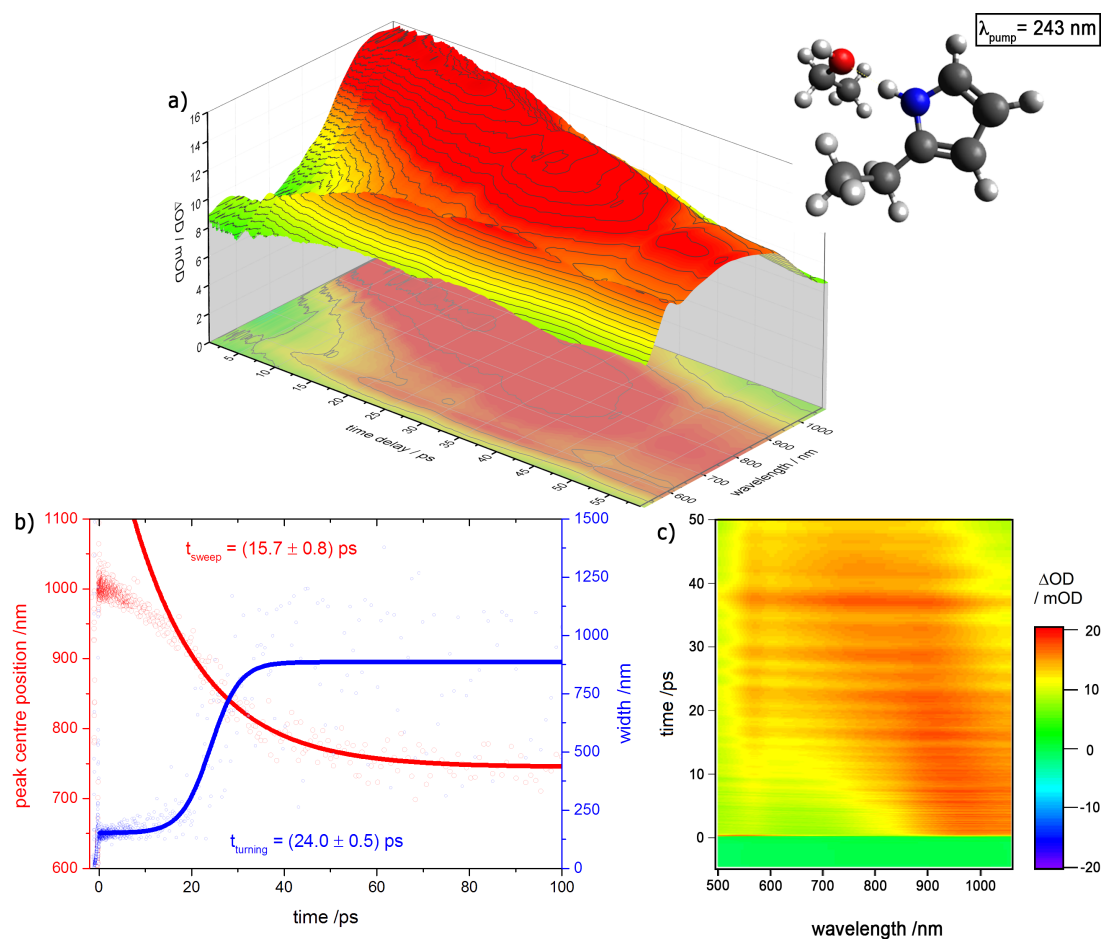


Fig. 6.11 Excited state dynamics over the first 50 ps of 2-ethylpyrrole in ethanol solution excited at 240 nm and probed in the near-IR spectral range between 510 to 1070 nm as (a) 3D representation, (b) fitting of broadband frequency sweep together with the gaussian width of the absorption band as a function of time delay and (c) and as contour plot.

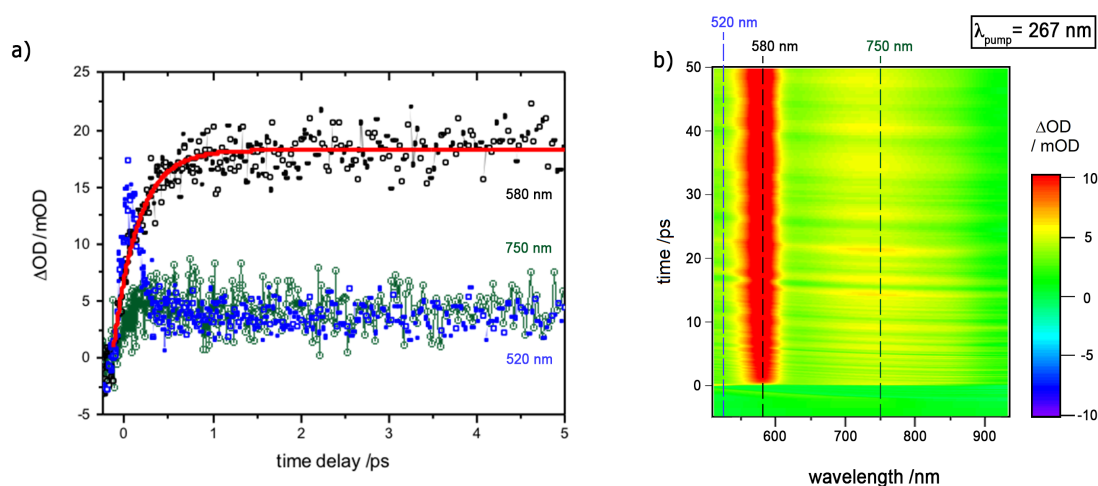


Fig. 6.12 Excited state dynamics over the first 50 ps of 2-ethylpyrrole in ethanol solution excited at 267 nm and probed in the near-IR spectral range between 510 to 1070 nm. (a) Kinetic cuts at 520 nm, 580 nm and 750 nm of the initial 5 ps time evolution, taken from (b) the TA contour plot.

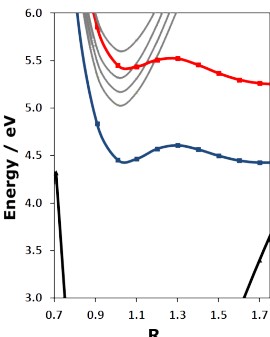
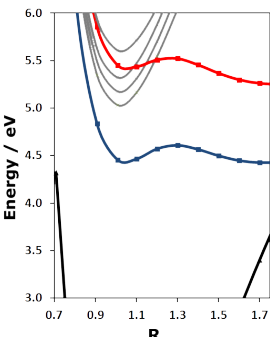
6.4.3 Results: Computational

TD-DFT Calculations

The dihedral angle of the ethyl group in the ground state optimised structure of the DFT calculation presented in table 6.3 was found to be 69.8° and thus is in agreement to the gauche conformer found in Karsili et al. [48]. In the vertical Franck-Condon region the $S_1(\pi\sigma^*)$ state of 2-ethylpyrrole was determined to be at 278 nm (4.46 eV) and is the result of LUMO \leftarrow HOMO electron promotion between orbitals with mainly pseudo- a_2' (LUMO) and pseudo- a_1' (HOMO) character. This is reminiscent to the symmetry forbidden transition known from the HOMO- (a_1) to the LUMO- (a_2) state in pyrrole and leads to the first repulsive $\pi(3s)\sigma^*$ state in 2-ethylpyrrole. Nevertheless, the first excited state transition in 2-ethylpyrrole is not strictly symmetry forbidden, which is reflected in the oscillator strength of the $S_1 \leftarrow S_0$ transition. The data table summarises the vertical excitation energies and oscillator strength for 2-ethylpyrrole as well as the 2-ethylpyrrole radical. The part of the data table related to 2-ethylpyrrole shows an inset that has been derived by scanning along the N-H stretch between 0.7 to 1.7 Å with otherwise rigid structure.

To elucidate on the electronic structure and to allow for further comparison of 2-ethylpyrrole with pyrrole the highest occupied and lowest unoccupied MOs from the results presented in table 6.3 are shown in figure 6.13. The left hand side of the figure shows the transitions that are overlapping between pyrrole and 2-ethylpyrrole. Most importantly the low-lying S_1 state with pseudo 1A_2 state label is as in the case with

Table 6.3 Vertical excitation energies and oscillator strength calculated for 2-ethylpyrrole and 2-ethylpyrrolyl radical using the (TD)-B3LYP/aug-cc-pVDZ level of theory. Also shown is an un-relaxed scan along the N-H stretch (graphic inset).

(TD)-B3LYP / aug-cc-pVDZ Vertical Excitation Energies / eV							
Transition from S ₀ to	2-Ethylpyrrole			Transition from D ₀ to	2-Ethylpyrrolyl Radical		
	Vertical Excitation Energy / eV	<i>f</i>			Vertical Excitation Energy / eV	<i>f</i>	
S ₁	4.4563	0.0119			D ₁	1.5502	0.0008
S ₂	5.0328	0.0419			D ₂	2.2058	0.0000
S ₃	5.1763	0.0021			D ₃	4.5311	0.0011
S ₄	5.3226	0.0160			D ₄	4.5706	0.0198
S ₅	5.4526	0.0009			D ₅	4.7801	0.0004
S ₆	5.6083	0.0409			D ₆	5.3552	0.0335

pyrrole the lowest-lying state. However, a series of intermediate states (S₂ to S₄) is introduced, some with significant oscillator strength, before the pyrrole-like S₅ state with pseudo ¹B₁ is reached as the result of the transition from the pseudo-²b₁' (LUMO-1) to the pseudo-²a₁' (HOMO) orbital. The three intermediate states S₂ to S₄ are orbital transitions originating from the pseudo-²a₂' (HOMO) orbital to the 3p/σ* Rydberg/valence state, which in turn is partially mixed with the antibonding orbitals corresponding to the sigma-bonds of the ethyl group. The S₃ ← S₀ transition is symmetry 'forbidden', involving the pseudo-²a₂' (HOMO) to pseudo-²a₁' (LUMO+2) orbital interaction, resulting in the pseudo S₃(A₂) state label and shows the expected lack in oscillator strength.

In short figure 6.13 can be used to show the similarities of 2-ethylpyrrole with regards to the electronic structure and orbital contribution of pyrrole (*cf.* figure 6.2). The most important low energy transition is defined by the aromatic ring structure and the resulting transition is maintained in 2-ethylpyrrole, but the additional ethyl group perturbs the orbital shape, thus breaking the overall symmetry, which leads to the introduction of additional states.

The well in the Franck-Condon region of the S₁ has been characterised with TD-DFT scans along the N-H stretch as shown with the inset in table 6.3. The barrier height from the minimum of the S₁ state to the saddle point was calculated to be 0.15 eV.

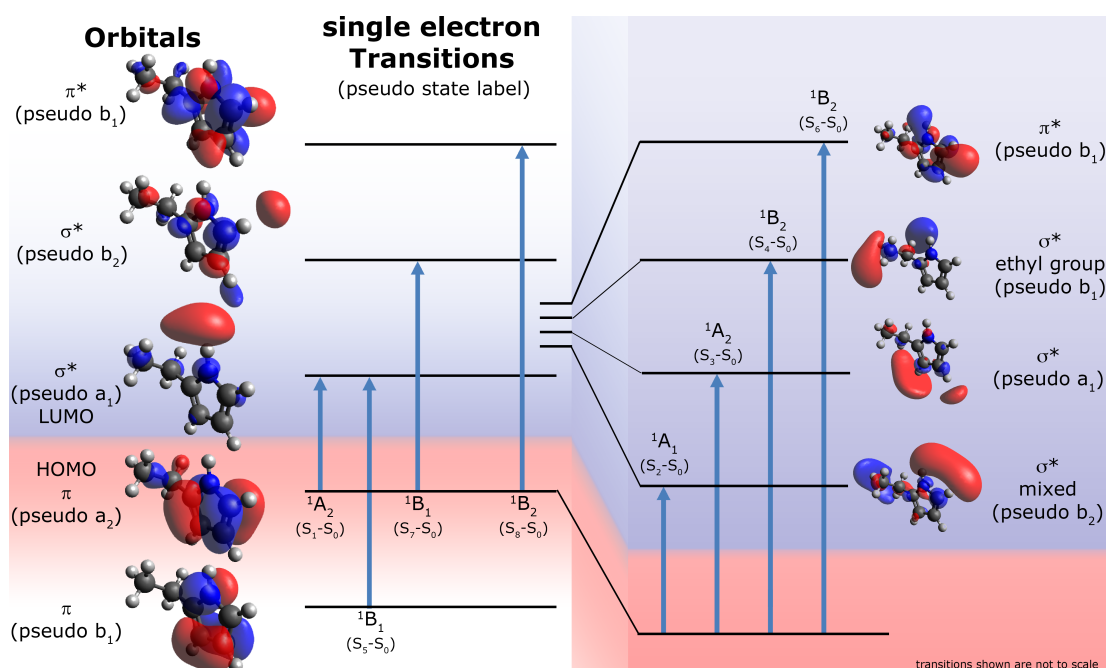


Fig. 6.13 Frontier Orbitals of 2-Ethylpyrrole and the energetically low-lying singlet transitions.

Identical calculations carried out with the long range correlated CAM-B3LYP basis set resulted in a barrier height of 0.26 eV. Table 6.4 also shows the first six radical states together with the corresponding oscillator strength. The D_0 state corresponds to the pseudo- ${}^2A_2'$ state and the D_1 is also equivalent to the pseudo- ${}^2B_1'$ as known from pyrrole. Two more states are introduced among the first six radical states in the calculations with explicit solvent and this is D_3 which is introduced due to an orbital transition to the explicit solvent and D_4 is the result of an orbital transition to the ethyl group.

CASSCF-(SA4) Potential Energy Cuts and Conical Intersection in the Radical

The potential energy cuts presented in the introduction section 6.4 for 2-ethylpyrrole show similarities to the already known pyrrole potential energy cuts. However, the S_1 surface shows a slight barrier with a height of approximately 0.15 eV as determined from the local minimum close to the Franck-Condon region up to the saddle point as the N-H bond is stretched to approximately 1.3 Å. From the saddle point onwards the S_1 cut is repulsive along the N-H bond stretch cutting the S_0 ground state surface at approximately 2 Å as also shown in the magnification inset of figure 6.8(a). Little has been stated regarding figure 6.8(b) that shows the energy separation of the first and second conical intersection as a function of dihedral angle. This has been calculated at

Table 6.4 Vertical excitation energies calculated for 2-ethylpyrrole and 2-ethylpyrrolyl radical with explicit ethanol molecule and PCM using the (TD)-B3LYP/aug-cc-pVDZ level of theory.

(TD)-B3LYP / aug-cc-pVDZ Vertical Excitation Energies / eV					
Transition from S_0 to	2-Ethylpyrrole with explicit ethanol molecule and PCM		Transition from D_0 to	2-Ethylpyrrole Radical with explicit ethanol molecule and PCM	
	Vertical Excitation Energy / eV	f		Vertical Excitation Energy / eV	f
S_1	4.6702	0.0148	D_1	1.6036	0.0014
S_2	5.0502	0.0098	D_2	2.3719	0.0000
S_3	5.1011	0.0293	D_3	3.3353	0.0000
S_4	5.2148	0.0284	D_4	4.4498	0.0015
S_5	5.6087	0.0003	D_5	4.5692	0.0238
S_6	5.6094	0.0535	D_6	4.7179	0.0017

identical level of theory with optimisation towards the first conical intersection S_0/S_1 at long N-H stretch followed by a scan around the dihedral angle. The starting geometry of the optimisation has been chosen close to the intersection known from the potential energy cut presented in figure 6.8(a). The minimum energy separation is shown at a conformer between the gauche and anti-conformer with a dihedral angle of $\sim 85^\circ$. A brief comment regarding the additional bound states observed in the TD-DFT is made at this point: The apparent difference between the missing bound states in the case of the CASPT2 calculations is the result of the limited active space chosen that focuses on the N-H bond breaking coordinate (see section 6.2.2 for active space). However, the involvement of the ethyl group in gauche conformer introduces additional orbitals that give rise to those additional $\sigma^* \leftarrow \pi$ orbital transitions. These σ^* are antibonding orbitals in the C-H stretch of 2-ethylpyrrole, both on the aromatic ring part as well as the ethyl group. The N-H bond dissociation energy in pyrrole is significantly lower than the average C-H bond dissociation energy for pyrrole and other aromatic hydrocarbons has been calculated previously [3]. As a result the dynamics at extended N-H stretch are still determined by the orbitals that have been selected as the active CAS space and explain the missing intermediate bound states in the CASSCF versus TD-DFT calculations. The results presented in figure 6.14 show a comparison between the radical entrance channel for the pyrrolyl and 2-ethylpyrrolyl radical. This can be understood as cross-sections of the calculations presented in figures 6.4 and 6.8 at long N-H stretch with the hydrogen entirely removed from the parent radical fragment. The

ground state surface for pyrrolyl is shown with the black line in the top graphic, showing the adiabatic D_0 surface. In a diabatic representation the surface with 2B_1 character is intersected close to its minimum by the 2A_2 surface forming a conical intersection as previously reported in the literature [98]. The D_0 minimum is of 2A_2 character and corresponds to the 1A_2 first repulsive surface in pyrrole. Similarly the 2B_1 corresponds to the second repulsive surface in pyrrole $S_2(B_1)$ and the 2A_1 surface is the $S_0(A_1)$ surface. The last blue energy surface is of 2B_1 character and corresponds to $S_3(B_1)$.

6.5 Discussion

Femtosecond transient absorption spectroscopy was performed to unveil the excited state dynamics of pyrrole and 2-ethylpyrrole in ethanol solution and was further supported by ab-initio calculations as presented in the result sections 6.3 and 6.4. Static UV-vis vapour phase absorption spectroscopy of pyrrole and 2-ethylpyrrole shows an apparent difference in the absorption spectrum, revealing a strong absorption in 2-ethylpyrrole peaking at 266.5 nm (4.65 eV) followed by the underlying pyrrole typical gradual increase in absorption strength towards the first $\pi^* \leftarrow \pi$ absorption below 225 nm in pyrrole and 240 nm in 2-ethylpyrrole. The S_1 onset in 2-ethylpyrrole in the vapour phase UV-vis is in good agreement with the TD-DFT calculations presented in table 6.3 that state an absorption onset of approximately 278 nm (4.46 eV). Taking a closer look at the oscillator strength between pyrrole and 2-ethylpyrrole for the lowest excited state than in 2-ethylpyrrole the lowest energy transition gains oscillator strength in the vertical Franck-Condon region. This might, in part, be related to the sigma anti-bonding orbitals of the ethyl group that are sticking out of the σ_v (yz) molecular plane and thus allows mixing with the σ^* orbital of the LUMO and as a consequence the pseudo HOMO-(a_1) and LUMO-(a_2) orbitals are not strictly orthogonal to each other, which in turn might be one reason for the gain in oscillator strength for the low energy transition. However, possibly more important, the first transition in 2-ethylpyrrole is strongly mixed ($\sim 14\%$) with the LUMO+1 \leftarrow HOMO transition. The LUMO+1 being the Rydberg ($3p_y$) σ^* orbital of pseudo-' b_2 ' character and shown as part of figure 6.13. States S_2 to S_4 are bound along the N-H stretch and are introduced due to the symmetry breaking ethyl group. The S_5 state is the next state that corresponds to the pyrrole-type $B_1(\pi\sigma^*)$ repulsive state. As the lowest energy excitation in the vertical Franck-Condon (vFC) region shows significant oscillator strength it is proposed that the increased oscillator strength is related to the mixing of the Rydberg $3p_y$ orbital in the gauche conformer of 2-ethylpyrrole. In comparison the ${}^1A_2 \pi(3s)\sigma^*$

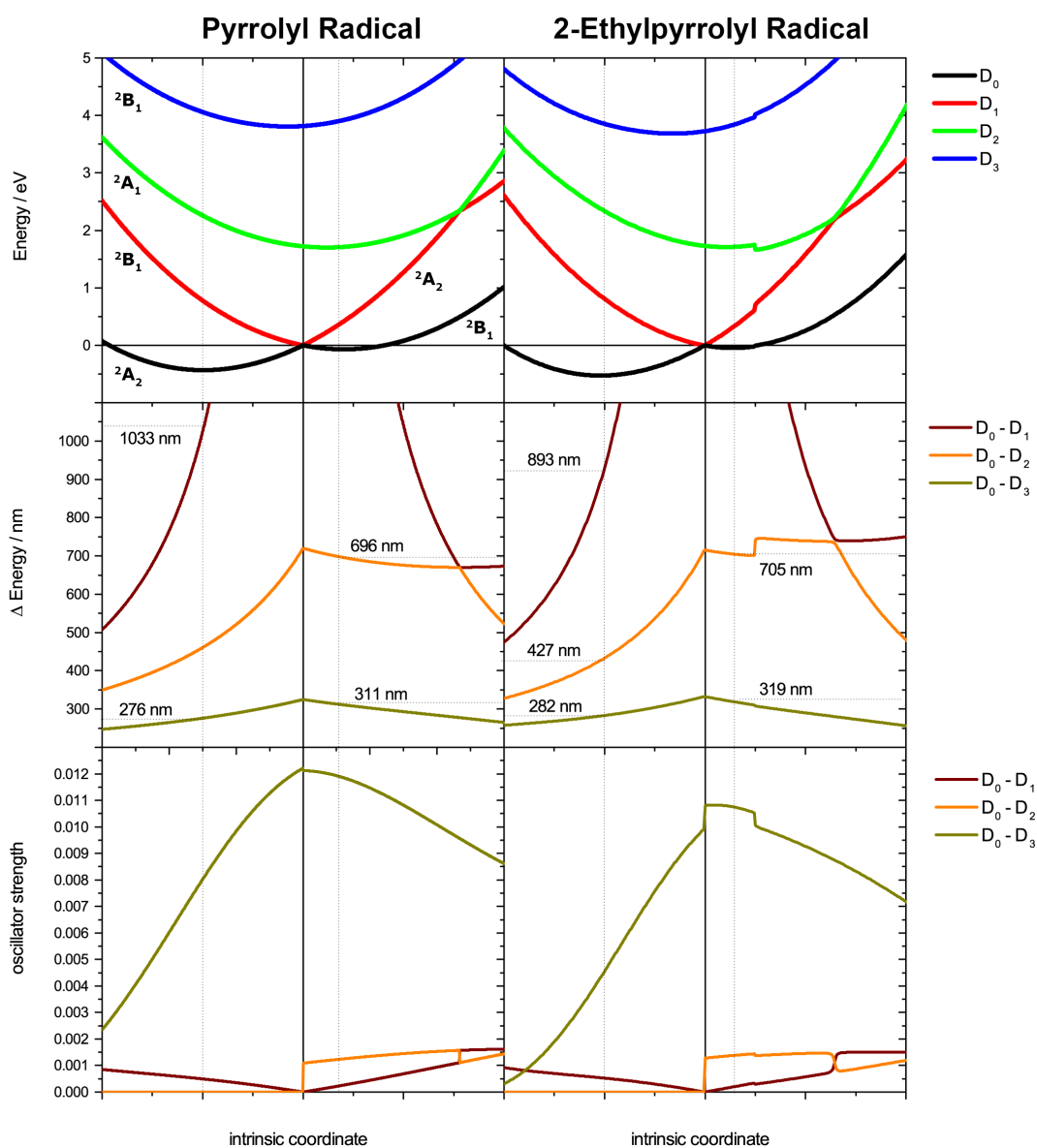


Fig. 6.14 SA4-CASSCF(7/6) Calculations showing Cuts through the PESs of the pyrrolyl (left) and 2-ethylpyrrolyl (right) radical. At the top the figure shows the lowest four states calculated at the SA4-CASSCF(7/6) level with aug(N)-cc-pVDZ basis together with the calculated oscillator strength (in middle figures) originating for the transitions from the D_0 surface and the corresponding transition energies (in bottom figure) represented in wavelength for easier comparison with the experimental data. Shown are adiabatic energy surfaces e.g. the lowest D_0 cut (top figures, black line) changes state character from 2A_2 on the left hand side to 2B_1 once the conical intersection is passed.

state in C_{2v} pyrrole shows a single orbital transition at this level of theory. The second excited state is predominantly made up of the LUMO+1 \leftarrow HOMO transition that carries large oscillator strength and a small contribution of the repulsive LUMO \leftarrow HOMO transition.

The femtosecond transient absorption experiments revealed similarities in the dynamics between pyrrole and 2-ethylpyrrole that are observed in an excitation range above the $S_1(\pi\sigma^*)$ onset of the corresponding molecule. As such the discussion is split into the subsection 6.5.2 concerned with the similar dynamics observed in pyrrole and 2-ethylpyrrole above the $S_1(\pi\sigma^*)$ onset and subsection 6.5.1 that will discuss the dynamics observed in 2-ethylpyrrole at the minimum of the S_1 absorption and suggest possible origins for the absorption signals observed.

6.5.1 Excitation into the S_1 of 2-Ethylpyrrole

Tuning the excitation wavelength to the first absorption maximum observed in the UV-Vis at ~ 267 nm (4.64 eV) results in a narrow absorption band with a FWHM of approximately 40 nm centred at 580 nm in the transient absorption data. The absorption band seems to rise with a time constant of approximately 300 fs as revealed with a single exponential fit. The centre wavelength remains constant throughout the observed delay range, even in the first few picoseconds. At this excitation energy of 4.64 eV only the lowest lying S_1 state can be accessed on energetic grounds as calculated in the TD-DFT calculations with explicit solvent molecule that show the first absorption onset at 4.67 eV and thus appear to be in excellent agreement with the experimental onset. Comparing the narrow and strong feature with the underlying instant broadband absorption centred at approximately 750 nm, then on basis of the early time dynamics, which differ, one can conclude that both absorptions are originating from different states. However, this means that the population that is excited into the vertical Franck-Condon region of the lowest singlet state evolve along the potential energy surface within the temporal resolution of the experiment to form two absorbing populations. The CASPT2 calculations in figure 6.8 and the inset in table 6.3 both show a well on the S_1 . The barrier height depends on the computational method chosen, but in either case predicts a minimum on the $(3s)\sigma^*$ Rydberg state. The barrier is in the range 1200 to 2100 cm^{-1} and thus sufficient to trap population. H atom PTS experiments showed prompt dissociation of 2-ethylpyrrole to 2-ethylpyrrolyl radical and H atom in the gas phase at 267 nm [48]. The kinetic energy of the released hydrogen is centred with a TKER ~ 6000 cm^{-1} . The assignment carried out by Karsili et al. (see figure 4(a) and 5(a) in [48]) with regards to the vibrational modes active in the radical product

formed after photodissociation at 263 nm show almost exclusively the lowest ($v=0$) vibrational level being populated at this excitation energy. Thus, excitation at 263 nm into the vertical Franck-Condon region is predominantly forming S_1 population in its lowest vibrational state and it can be expected that excitation at the onset wavelength 267 nm will further narrow down the vibrational diversity. The solution phase transient absorption data at 267 nm feature two absorption bands; one at 580 nm and the other spread over a wide range with centre at 750 nm. The calculated excitation energies for the lowest $D_1 \leftarrow D_0$ absorption for the isolated radical species and this with explicit ethanol molecule are located at 800 nm (1.55 eV) and 775 nm (1.60 eV), respectively (tables 6.3 and 6.4). Both calculations show a weak oscillator strength associated to this transition, with approximately double the magnitude in oscillator strength for the calculations that include the solvent. Based on the experimentally determined N-H bond strength of $(31650 \pm 50) \text{ cm}^{-1}$ from the H atom PTS data together it is possible to estimate the excess energy in the radical products. The initial energy provided by the excitation laser in the transient absorption experiment was 37450 cm^{-1} (267 nm), leaving a difference energy of approximately 5800 cm^{-1} available for the photodissociation products. Considering that the H atom is ejected with approximately 6000 cm^{-1} in the gas phase then the 2-ethylpyrrolyl fragment is likely to be formed in its vibrational ground state ($v=0$).

The 750 nm component appears to match well with the TD-DFT calculations indicating the formation of the 2-ethylpyrrolyl radical. The second component at 580 nm does not match any of the calculated radical transitions from D_0 that show oscillator strength. However, the kinetic cut shown in figure 6.12 shows a 300 fs rise time of the 580 nm component and is thus showing a different kinetic profile to the 750 nm radical component. It's tempting to assign the narrow absorption to S_1 absorption, but one would expect to see an instant absorption signal upon excitation instead of a rising component. A possibility for the S_1 showing an additional rise time, could be related to a Rydberg to Rydberg absorption. As already stated, a difference in the orbital contributions for the S_1 state is observed, by which the lowest excited state is made up of 3p Rydberg contribution. The higher states and orbital contributions have been studied extensively for the closely related pyrrole molecule [88]. Absorptions in pyrrole to the 3d Rydberg orbitals are known to carry very high oscillator strength for symmetry allowed transitions and thus are strong absorbers in this highly symmetric molecule. The energy gap in pyrrole between the lowest state $3s(\sigma^*)$ Rydberg/valance state to the 3d Rydberg orbital is 2.1 eV (585 nm).

The $3d \leftarrow 3s$ transition in pyrrole doesn't take much oscillator strength due to the non-symmetry allowed transition. However, a $3d \leftarrow 3p$ orbital transition is symmetry allowed. As the $3s(\sigma^*)$ in 2-ethylpyrrole is a mixed state with the $3p$ orbital this might be a possible reason for the strong absorption observed at 580 nm and matches the energy gap for the symmetry forbidden $3d \leftarrow 3s$ transition in pyrrole. The schematic in figure 6.15 shows the possible origin of the 580 nm absorption and the required torsional motion in 2-ethylpyrrole from the gauche to the syn conformer that potentially accounts for the rising component. Rydberg to Rydberg transitions are strong near the equilibrium geometry and give rise to sharp spectral features for 0-0 transitions, meaning absorption from the $v=0$ vibrational level of a Rydberg state to that of another Rydberg state [97]. In 2-ethylpyrrole the optimised S_1 geometry was found to be the syn-conformer, which is approximately 600 cm^{-1} lower in energy than the gauche conformer and the S_0 state showed a minimum for the gauche conformer as determined in the calculations by Karsili et al. [48]. The ground state population in the transient absorption experiment can be expected to be predominantly a mix of gauche (60°) to anti (180°) conformer at room temperature (approximately 60 % gauche) with the syn conformer being at a maximum potential energy in the calculation by Karsili et al [48]. Thus, upon excitation the S_1 potential will be populated with the gauche conformer, which is expected to relax to its energetically stable syn-conformer. The rotation period of the torsion in ethylpyrrole has been studied for a range of other aromatic alkylbenzenes, such as ethylbenzene, and was determined to be between $30\text{-}100\text{ cm}^{-1}$ [14], which corresponds to a time scale of approximately 1 ps to 0.3 ps for the torsional motion. The observed time scale of the rising 580 nm component is approximately 300 fs and thus in proximity to the torsional time constants determined for other alkylbenzenes such as ethylbenzene.

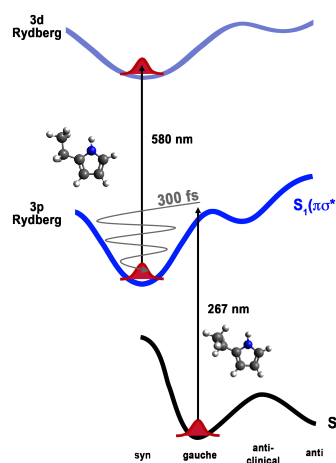


Fig. 6.15 Rydberg ($3p$) to Rydberg ($3d$) Absorption in 2-Ethylpyrrole

6.5.2 Excitation above the $S_1(\pi\sigma^*)$ minimum

The data presented in figures 6.6 and 6.11 focus on the evolution of excited species initially prepared above the S_1 minimum in 2-ethylpyrrole and also above the S_1 onset of pyrrole. The results have been obtained at $\lambda_{\text{pump}} = 243\text{ nm}$ and show a broad and strong IR signal that sweeps from the far IR side to an approximate centre position

of 700 nm. Excitation at this energy in pyrrole leads to population of the S_1 state according to TD-DFT calculations presented in tables 5.1 and 6.1 with the S_2 not being accessed until a wavelength shorter than 230 nm. In the case of 2-ethylpyrrole excitation at this wavelength is leading to excitation of high vibrational states in the vertical Franck-Condon region of S_1 but can in principle also access the lower S_2 bound states as calculated in table 6.3 or up to the bound S_3 in the calculations with explicit solvent molecule (table 6.4). The 2-ethylpyrrole data recorded with the IR probe continuum further show the 580 nm absorption feature, although significantly weaker as in the case of excitation at 267 nm, thus further validating the assignment of the 580 nm to an absorption out of the $S_1(\pi\sigma^*)$ minimum as suggested in section 6.5.1. The reason for the weaker 580 nm signal at an excitation wavelength of 243 nm is this that the calculated barrier of approximately 1200 to 2100 cm^{-1} is overcome as the relative energy difference from S_1 minimum to the excited vertical Franck-Condon region at 243 nm is approximately 3700 cm^{-1} and thus sufficient to overcome the barrier.

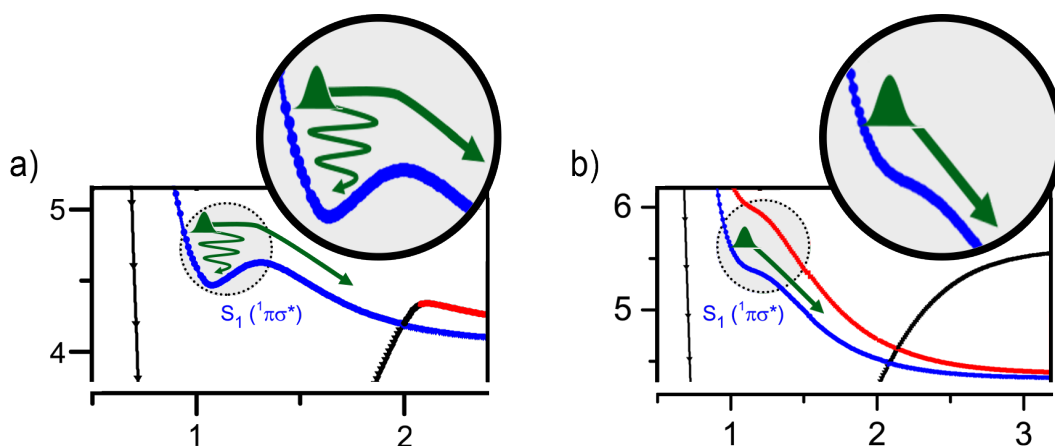


Fig. 6.16 Possible Population Flow upon S_1 Absorption in 2-Ethylpyrrole and Pyrrole. (a) Population bifurcation in 2-ethylpyrrole to the S_1 minimum and over the barrier leading to N-H bond fission via repulsive $\pi\sigma^*$ pathway and (b) no barrier along the $A_2(\pi\sigma^*)$ surface in pyrrole, leading to N-H bond fission.

The weak signal determined at 580 nm could thus be related to a fraction of population that is trapped in the S_1 minimum potential. Schematic 6.16 compares the possible population flow in 2-ethylpyrrole and pyrrole at an excitation of 243 nm. In schematic 6.16(a) population in the vertical Franck-Condon region of 2-ethylpyrrole is bifurcated with the majority of population flowing along the repulsive surface leading to N-H bond dissociation and a small fraction gets trapped in the S_1 minimum. Comparing this with the schematic for pyrrole, then there is no minimum determined on the S_1 surface and population follows the repulsive pathway towards N-H dissociation. To

the best of our knowledge all reported experimental studies in the literature on the excited state dynamics of pyrrole to date have been conducted in the gas phase and comparable studies are not available that investigate the solution phase dynamics of pyrrole or 2-ethylpyrrole. Thus, the gas phase studies of pyrrole [65, 75, 76, 96, 114, 119] and 2-ethylpyrrole [48] are all stating prompt dissociation upon accessing the $S_1(\pi\sigma^*)$ surface and only Roberts et al. [96] state a longer time constant on the $S_1(\pi\sigma^*)$ surface with (126 ± 28) fs due to tunneling out of the quasi-bound part of the potential followed by direct dissociation via the low-lying repulsive $A_2(\pi\sigma^*)$ surface. The suggested prompt dissociation in pyrrole and 2-ethylpyrrole is thus consistent with the gas phase studies. Experimental studies do not support a long-lived pyrrole $A_2(\pi\sigma^*)$ and computational studies only report a small barrier depending on the level of theory. The H atom PTS study by Karsili et al. [48] determined the N-H bond fission in 2-ethylpyrrole, however the experimental method does not allow to conclude on the excited state lifetime as only the time-of-flight of the released H atoms are measured and thus it is only inferred on the final product states observed after the photodissociation event. As such an S_1 absorption component is not contrary to the results by Karsili et al. [48]. Assigning the 580 nm feature in 2-ethylpyrrole to the $3d \leftarrow 3p$ as carried out in section 6.5.1 allows now to focus the attention onto the origin of the IR component.

The assignment of the broadband absorption components for pyrrole and 2-ethylpyrrole in the range 700-900 nm at a delay time larger than 30 ps fits to the TD-DFT calculations that suggest a $D_1 \leftarrow D_0$ absorption for pyrrole and 2-ethylpyrrole at approximately 850 nm and 775 nm, respectively. However, this component appears only instant in the 2-ethylpyrrole data during excitation into the S_1 minimum and at an excitation of 243 nm the sweep from the IR range is observed with time constants of approximately 9 ps and 16 ps for pyrrole and 2-ethylpyrrole. The excess energy with regards to the N-H bond dissociation energies determined for pyrrole of (32850 ± 40) cm^{-1} [23] and (31650 ± 50) cm^{-1} for 2-ethylpyrrole [48] at 243 nm (41150^{-1}) excitation is 8300 cm^{-1} for pyrrole and 9500 cm^{-1} for 2-ethylpyrrole. However, considering that the H atom leaves with a kinetic energy of 7000 cm^{-1} and 6000 cm^{-1} for pyrrole and 2-ethylpyrrole, this leaves approximately 1300 cm^{-1} for the pyrrolyl fragment and 3500 cm^{-1} for the 2-ethylpyrrolyl fragment. From the TKER data [23, 48] it is further known that radical fragments upon N-H photodissociation at 243 nm for pyrrole and 2-ethylpyrrole are vibrationally excited and have been assigned to vibrations in the radical ground state.

Diabatic Population Flow

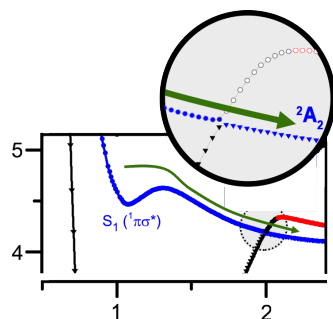


Fig. 6.17 Diabatic Population Flow from $S^1(A_2)$ to $D^0(A_2)$

As such pyrrole molecules prepared in the 1A_2 and pseudo- 1A_2 for 2-ethylpyrrole molecules correlate to the 2A_2 and pseudo- 2A_2 radical states after passing the conical intersection diabatically between the lowest excited 1A_2 and ground state 1A_1 surface. The figure 6.17 shows this diabatic population flow into the radical state, in which the radical species undergo vibrational cooling within the radical ground state D_0 . The observed frequency sweep in the transient absorption data will then be associated to vibrational cooling of the excess energy stored in the vibrational modes of the radical fragment. The observed time constants (9 ps and 16 ps for pyrrole and 2-ethylpyrrole) are reflecting this vibrational cooling time in the solvent ethanol within the radical $D_0(A_2)$ ground state of the respective molecule.

Adiabatic Population Flow

An alternative route, by which the pyrrole and 2-ethylpyrrole molecules excited to $S_1(A_2)$ state can couple, non-adiabatically, to the ground state could arise in the case when the molecules approach the region of the first conical intersection with sufficiently distorted geometries that they actually remain on the upper adiabatic potential energy surface. This has been described by Cronin et al. [23] previously and provides a starting point for a different model to explain the observed transient absorption data. As already referenced with the TKER data [23, 48] both radicals pyrrolyl and 2-ethylpyrrolyl show higher vibrational modes being active after excitation at 243 nm. As such it is possible that the first conical intersection is mostly circumvented due to the fact that the molecules are distorted and miss the intersection point and the population flows mostly adiabatically onto the D_1 radical surface. The figure 6.18 shows the adiabatic population flow that leads to excited radical population.

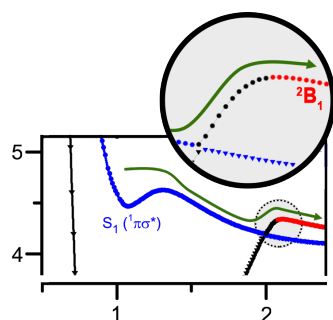


Fig. 6.18 Adiabatic Population Flow from $S^1(A_2)$ to $D^1(B_1)$

Figure 6.18 shows first the adiabatic population flow from the 1A_2 surface at stretched N-H bond length onto the 1A_1 ground state surface via the S_1/S_0 conical intersection followed by diabatic passage onto the first excited $D_1(^2B_1)$ radical surface. The computational data presented figure 6.14 show the entrance channel for the population flowing diabatically into the ground state radical surface

with 2A_2 or adiabatic into the first excited radical surface with 2B_1 character. An adiabatic population flow is in agreement with recent dynamics calculations. On-the-fly multiconfigurational Ehrenfest dynamics calculations for pyrrole by Saita et al. [98] and ab-initio multiple cloning simulations of pyrrole by Makhov et al. [69] both suggest branching at the first S_1/S_0 conical intersection with significant adiabatic population flow onto the D_1 excited radical state of 2B_1 character. Saita et al. [98] calculate a population of approximately 80 % in the 2B_1 state after 25 fs. Thus, photodissociation and the formation of the radicals will be on a timescale shorter than the time resolution of the transient absorption experiment and any absorption signals associated with the radicals can be expected instantly. Comparing the potential between pyrrole and 2-ethylpyrrole, then only marginal differences in energetics and oscillator strengths are observed. The pseudo- ${}^2B_1'$ potential appears slightly steeper in the case of 2-ethylpyrrole with also a slightly deeper pseudo- ${}^2A_2'$ well relative to the conical intersection, which is marked by the crossing of the pseudo- ${}^2A_2'/{}^2B_1'$ surface. Schematic 6.19 summarises the proposed population flow from the initially populated 2B_1 state with key steps assigned from (A) to (D) in the following:

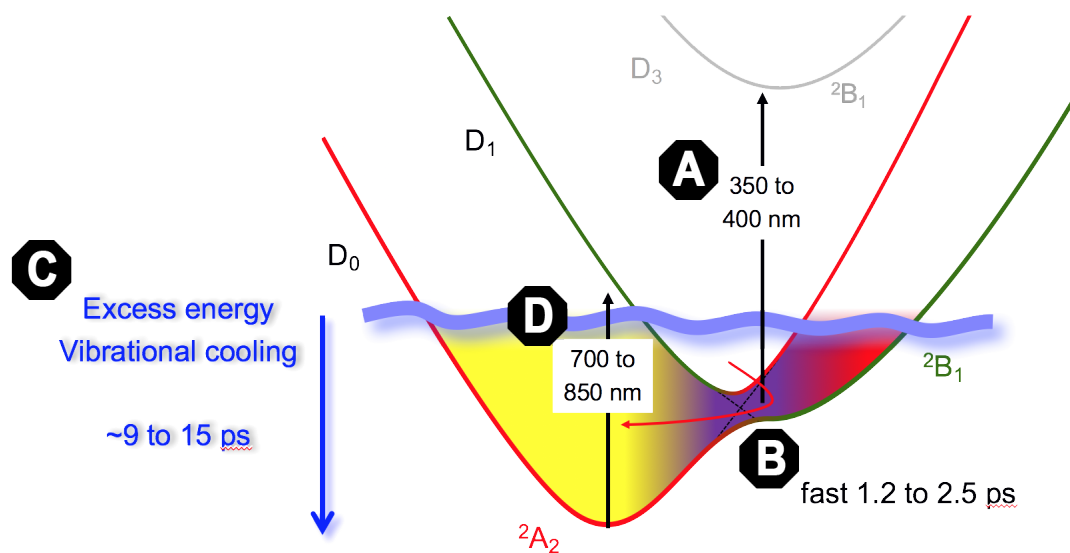


Fig. 6.19 Population flow from Radical 2B_1 to 2A_2 minimum via Conical Intersection

(A) Shows a strong $D_3(B_1) \leftarrow D_1(B_1)$ absorption between the states with same symmetry. A strong absorption in the transient absorption data has been observed (see figures 6.5 and 6.10) at a wavelength of approximately 350 nm and 390 nm for pyrrole and 2-ethylpyrrole, respectively. In both cases a single exponential with offset was

extracted. Considering the calculations presented in table 6.2 as rough estimate of the energy difference between the pyrrolyl radical D_3 and D_1 state, then this corresponds to an energy of 3.26 eV (380 nm). Similarly, table 6.4 shows an energy gap of 2.97 eV (420 nm) for the states that are labelled D_5 and D_1 . The change in labelling is due to the additional states introduced in the TD-DFT calculations. The additional state (D_3) is caused by the explicit solvent molecule, but doesn't carry any oscillator strengths and the ethyl group is the reason for the additional D_4 state, with weak oscillator strengths. Those states are not part of the figure 6.14 as the solvent molecule is not included and the active space is limited as outlined in section 6.2.2. The CASSCF calculations (table 6.14) also confirm the strong oscillator strength for this transition which is shown on the right hand side of the potential energy cuts for each molecule. Further to this the ${}^2A_2 \leftarrow {}^2B_1$ transition out of the 2B_1 minimum, close to the conical intersection, gives rise to an absorption in the IR region, but with small oscillator strength calculated in both the TD-DFT as well as the CASSCF calculations. (B) The observed UV absorption component at 350 nm for pyrrole shows a decay component of approximately 1.2 ps which can be assigned to a fast population flow from the 2B_1 potential onto the 2A_2 potential. These findings are supported by the dynamics calculations by Saita et al. [98] that even after crossing the first conical intersection and a yield of approximately 80 % 2B_1 population still a coupling between the 2B_1 and 2A_2 surfaces that lead to population being transferred onto the 2A_2 surfaces on a timescale of a few hundred femtoseconds. Similarly, in the case of 2-ethylpyrrole a 2.5 ps component was observed in the 390 nm kinetic cut (figure 6.10)). The slightly longer decay time might be related to the slightly steeper gradient to overcome the small barrier from the pseudo-' 2B_1 ' minimum towards the pseudo-' 2A_2 ' potential. As the pseudo-' 2B_1 ' minimum is energetically close to the conical intersection it is unlikely that the delay is caused by rotation of the ethyl group in order to adjust to the required molecular configuration to pass the intersection. The CASSCF calculations (table 6.14) confirmed the syn-conformer for the D_0 optimised geometry as reported by Karsili et al. [48] and identified the gauche conformer with 68° for the optimised geometry at the conical intersection. (C) Vibrational cooling of formed radicals in ethanol solution on a time scale as determined by the sweep feature in figure 6.6(b) with approximately 9 ps for pyrrole and 16 ps for the 2-ethylpyrrole as shown in figure 6.11(b) lead to the observed frequency sweep from the IR range to (D) the equilibrated broadband absorption with an approximate centre wavelength of 730 nm for the pyrrolyl radical and 750 nm for the 2-ethylpyrrolyl radical. The assignment is in agreement with the TD-DFT calculations for the pyrrolyl radical with explicit solvent that calculated an absorption at 850 nm (1.45 eV, table 6.2) and 770 nm (1.60 eV, table 6.4) for 2-ethylpyrrolyl radical.

The transient absorption data recorded at an excitation energy close to the minimum of the S_1 state of 2-ethylpyrrole at 267 nm with the ground vibrational state ($v=0$) predominantly active leads then primarily to D_0 radical population. The first conical intersection between the lowest repulsive $\pi\sigma^*$ and the S_0 ground state surface is 'hit' with low vibrational degree of freedom (such as $v=0$) and leads to diabatic population flow into the radical ground state. The transient absorption data at 267 nm are thus consistent with the a population split at the first conical intersection that leads to diabatic D_0 population if the S_1 state is prepared in it's ground vibrational state and the data in both the pyrrole and 2-ethylpyrrole excited at 243 nm activate higher vibrational modes that leads to molecular distortion and thus population circumvents the first conical intersection leading to adiabatic population flow with population of the $D_1(B_1)$ radical state.

Formation of solvated electrons

A very different interpretation of the observed sweep in the IR range of the transient absorption data is provided with the formation of a solvated electron in ethanol solution. The formation of solvated electrons in diverse solvents has been studied extensively in the literature [28, 38, 39, 42, 73, 99, 104, 106]. The formation of solvated electrons either use precursors or multi-photon absorption processes to ejected electrons into liquids that will then interact with the solvent molecule to form a solvent cage essentially trapping the free electron. Multi-photon absorption experiments reported in the literature are typically performed with short fs-laser pulses of 125 fs duration or less centred around 266 nm with high pulse energies of about 8 μJ [28, 99, 104] to generate solvated electrons in time-resolved photoelectron or transient absorption spectroscopy. Electron solvation in methanol studied that have been generated with 8 μJ at 273 nm excitation in transient absorption spectroscopy studies [42, 104, 105] show an absorption onset in the IR range larger than 1000 nm that evolves to the ground state absorption of solvated electrons in methanol with a centre wavelength of about 700 nm. Toigawa et al. [106] summarises the rise time of transient absorptions of solvated electrons for diverse n-alcohols. The rise time is reported in the literature between 7 to 26 ps for fully solvated electrons in ethanol and between 5 to 17 ps for this in methanol [38, 112, 113] with a maximum absorption wavelength of the solvated electron of 690 nm and 630 nm for ethanol and methanol, respectively. The transient absorption experiment for pyrrole and 2-ethylpyrrole in ethanol solution were performed with a pulse energy of less than 0.2 μJ . Ionisation processes of isolated solvent or the isolated molecule is unlikely via one photon absorption processes as the ionisation

potential of ethanol (10.41 ± 0.05) eV [41], pyrrole (8.2 eV) [15] and 2-ethylpyrrole (7.97 ± 0.05) eV [64] exceeds this of the pump photon source used even at the shortest experimental wavelength. However, the experiment is conducted in solution, as such the referenced ionisation threshold of isolated species might not be applicable for the bulk condition in the fs-TA experiment. Unintended multiphoton processes that lead to an ionisation of either the solvent or the molecules, which in principle can be achieved with two or three photon absorption processes are unlikely considering the low pump fluence as well as comparable experiments conducted in pure ethanol solvent that did not show any absorption signals apart from the coherence spike at time zero. Moreover, the data recorded at 267 nm would then only correspond to the final equilibrated solvated electron in ethanol as the strong IR absorption is not apparent at this excitation wavelength. Very recently the study by Oliver et al. [84] investigated the excited state dynamics of phenol in water with transient absorption spectroscopy at 267 nm and 200 nm excitation. Oliver et al. observed a very short lived absorption feature around 420 nm in the early dynamics ($t < 1$ ps) at 200 nm excitation that has been assigned to the phenol radical cation ($\text{PhOH}^{\bullet+}$) based on absorption spectra in the literature data. Rapid autoionisation to a phenoxyl radical (PhO^{\bullet}), a proton (H^+) and a solvated electron (e^-) leads to a spectral absorption signal at approximately 600 nm close to the edge of their detectable probe window, which has been attributed to phenoxyl radicals and solvated electrons indiscernible by their absorption spectrum. However, excitation into the lowest bound $\pi\pi^*$ state at 267 nm resulted in a much slower (nanosecond) formation time of the radical fragment and the broadband absorption signal of a solvated electron in water. As known from gas phase H atom photofragment translational spectroscopy prompt H atom formation is not accessed until $\lambda_{\text{phot}} \leq 248$ nm with the $1^1\pi\sigma^*$ surface being accessed. As such the observation of the intermediate by Oliver et al. [84] opens up an interpretation via the formation of an intermediate that leads to a radical absorption signal as suggested by the TD-DFT calculations for pyrrolyl and 2-ethylpyrrolyl radical together with the formation of solvated electrons in the protic solvent ethanol via an autoionisation process. As such in this interpretation the radical formation goes along with the formation of the solvated electron. Nevertheless, this interpretation cannot be fully supported without a signature of the intermediate species. The transient absorption data for pyrrole and 2-ethylpyrrole lack such a signature that confirms the radical cation and to the best of our knowledge no absorption spectra of pyrrolyl radical cations or 2-ethylpyrrolyl radical cations are reported in the literature, that would allow to confirm this species with further time-resolved experiments.

6.6 Conclusion

The observed sweep feature in the IR region gains in relative importance on shifting to shorter pump wavelength, as can be seen in the comparison between the signal intensity in the 2-ethylpyrrole experiments. The origin of this IR sweep component observed in both the pyrrole and 2-ethylpyrrole data at excitation energies beyond the S_1 minimum, but below the S_2 absorption onset in the presented data is less clear, but several observations may assist towards identifying the source of this spectral feature. (1) the data presented for 2-ethylpyrrole into the well of the S_1 surface reflect this of a bound population, with only little decay even after a time delay of more than 20 ps, well after the sweep feature is equilibrated in 2-ethylpyrrole, indicating that the population flow is uncoupled between the absorption signal observed at 580 nm and this in the IR. (2) As already stated ionisation processes of the solvent or the molecule is unlikely and (3) unintended multiphoton absorption processes that lead to ionisation are less likely at low pump fluence (4) The effect of dimers contributing to the overall transient spectra are likely minimal. Dimers are known to absorb in the visible spectral range and even small quantities of dimers colour solutions strongly. Samples have been prepared with colourless starting material to form fresh solutions stored in the dark prior to the experiment being conducted. Moreover the strongly diluted conditions of only a few tens of millimoles per litre provide unfavourable conditions for dimer formation. (5) A fast autoionisation process upon excitation above the $\pi\sigma^*$ onset such as described by Oliver et al. [84] could explain the observations of ground state radicals and solvated electrons, but experimental evidence of radical cations in the transient data is yet to be confirmed.

Equipped with the above, and the literature related to dynamics calculations by Saita et al. [98] it appears that the behaviour of the pyrrole in ethanol solution seems to be analogous to that in the gas phase, wherein H atoms and pyrrolyl radicals are formed within the cross-correlation time of the experiment (80 fs). However, the solution phase data show some details of the non-adiabatic dynamics that elude the frequency resolved gas phase HRAPTS experiment. Ehrenfest calculations suggested that the pyrrolyl is in fact formed in the D_1 state (with 2B_1 character), despite initial population of the $S_1(^1A_2)$ state, due to preferential adiabatic pathways at both the $S_0/\pi\sigma^*$ conical intersections along the dissociation pathway. Current data support this view, indicating that an excited state (D_1 in 2B_1) population is formed in < 80 fs, which is observed via its UV absorption to the $D_3(B_1)$ state (at 350 nm). This signal decays within 1.2 ps, in accordance with the Ehrenfest calculation and yields a strong absorption in the IR which corresponds to the generation of a hot ground state D_0 population, exhibiting

excited state absorption to D_1 . This cools over many picoseconds to give a signal centred around 700 nm at the D_0 minimum. The cooling is complete in approximately 9 ps and the signal subsequently fades slowly as a result of geminate recombination. The gas phase H atom phototranslational spectroscopy data [23] show only a D_0 population with a relatively cold internal energy distribution, when excited at 244 nm, indicating that the kinetic energy release distribution of the H atom is not fixed until after the D_1 population has decayed, at around 2 ps. Of course, collisional cooling is not possible in the gas phase, so an internal energy distribution greater than that thermally allowed is persistent. The conclusion is extended to 2-ethylpyrrole that shares the adiabatic dynamics observed in pyrrole at an excitation above the S_1 minimum with the formation of excited radical population with pseudo- 2B_1 character and a UV decay component of 2.5 ps, thus slightly slower than in the benchmark pyrrole. The slightly longer delay can most likely be assigned to the specific topology of the excited radical potential and the required crossing geometry to pass the conical intersection and enter the pseudo- 2A_2 potential. Very different to pyrrole is the appearance of a strong absorption signal at approximately 580 nm that was rationalised with an absorption out of the S_1 minimum, based on the observed 3p Rydberg mixed character within the $S_1(\pi(3s)\sigma^*)$ state and a $3d \leftarrow 3p$ Rydberg transition is proposed to explain the sharp, narrow absorption band. A 300 fs rise time of this very absorption component is explained with the relaxation towards the minimum energy syn conformer from the initially prepared gauche conformer upon S_1 excitation.

Chapter 7

Concluding Remarks

The work presented in this thesis set out to add to the knowledge of excited state dynamics reported in literature by investigating the dynamics in solution phase and thus provide new insights to the photodissociation dynamics of pyrrole and related pyrrole molecules in the gas phase. More than a decade ago the computational work by Sobolewski et al. [102] and gas phase experimental studies [23, 65] raised discussions around the involvement of $\pi\sigma^*$ states in pyrrole and other heteroaromatics. Many studies followed that investigated on the non-radiative decay pathways in these prototype molecules to further widen the understanding of the photostability and mechanisms of biomolecules.

The chapters 5 and 6 add to the discussion by following the excited state dynamics in solution phase. In pyrrole-2-carboxaldehyde the excited state dynamics could be separated into two clearly distinguishable channels. Excitation below the $\pi\sigma^*$ onset resulted in triplet state population with two triplet absorption channels. A dramatic change in the transient absorption experiments was observed upon accessing the $\pi\sigma^*$ state. The previously dominant triplet channels disappeared and a new instant channel appeared in the near-IR spectral range coinciding with the H atom onset in the gas phase PTS data. This new absorption channel in the transient absorption data was associated to prompt formation of radicals as a consequence of N-H bond fission.

The spectral signatures presented for pyrrole and 2-ethylpyrrole upon accessing the $\pi\sigma^*$ state were also assigned to the formation of radicals due to N-H bond fission. The spectral signature that was assigned to the parent radical fragment was in the same spectral range as observed in the study of pyrrole-2-carboxaldehyde. Further to this the solution phase data provided some details of the non-adiabatic dynamics in such

that excitation into the Franck-Condon region of the $\pi\sigma^*$ state provided sufficient vibrational degree of freedom that population following the repulsive $\pi\sigma^*$ surface flew adiabatically, meaning the first S_1/S_0 conical intersection is missed, and the first excited radical state was populated, which then decayed to the radical ground state via a conical intersection. This assignment is in agreement with recent dynamics simulations [98] that predict this population plow from the excited radical surface to the radical ground state by means of a conical intersection connecting the two low-lying radical states. In short the behaviour of the pyrrole, 2-ethylpyrrole and pyrrole-2-carboxaldehyde in ethanol solution seems to be analogous to that in the gas phase in such that the prompt N-H bond dissociation persists in solution phase upon accessing the $1^1\pi\sigma^*$ state.

Chapters 4 investigated the dynamics of CuInS₂/ZnS Quantum Dots in hexane solution upon promotion to the conduction band. The transient absorption study together with the pump-dump-probe setup allowed to verify the involvement of an internal defect state in the photoluminescence adding to a long on-going discussion in literature. Understanding the carrier dynamics in this semiconductor material may assist in further optimisation of charge extraction in solar panels and increasing the photoluminescence quantum yield in bio-imaging.

Transient absorption spectroscopy proved valuable in gaining electronic energy information about the evolution of population on electronically dark states, but one constraint of femtosecond transient absorption spectroscopy is the relatively low spectral resolution. Extending transient absorption data with additional data gathered with techniques like ultrafast transient infrared spectroscopy is one possible way to gain vibrational information in addition to electronic state information provided by femtosecond transient absorption spectroscopy. Newer techniques, such as femtosecond stimulated Raman spectroscopy [71, 121], allow in principle to follow the vibrational energy distribution with high temporal resolution at once. Future work might consist in extending the current femtosecond transient absorption setup by a picosecond non-linear optical parametric amplification stage to allow for the three laser beam setup as required to carry out femtosecond stimulated Raman spectroscopy.

References

- [1] Aloïse, S., Ruckebusch, C., Blanchet, L., Réhault, J., Buntinx, G., and Huvenne, J.-P. (2008). The benzophenone $s\ 1\ (n,*) \rightarrow t\ 1\ (n,*)$ states intersystem crossing reinvestigated by ultrafast absorption spectroscopy and multivariate curve resolution. *The Journal of Physical Chemistry A*, 112(2):224–231.
- [2] Bagchi, A., Huang, Y. H., Xu, Z. F., Raghunath, P., Lee, Y. T., Ni, C. K., Lin, M. C., and Lee, Y. P. (2011). Photodissociation dynamics of benzaldehyde (c_6h_5cho) at 266, 248, and 193 nm. *Chem Asian J*, 6(11):2961–76. Bagchi, Arnab Huang, Yu-Hsuan Xu, Z F Raghunath, P Lee, Yuan T Ni, Chi-Kung Lin, M C Lee, Yuan-Pern Germany Chem Asian J. 2011 Nov 4;6(11):2961-76. doi: 10.1002/asia.201100483. Epub 2011 Sep 23.
- [3] Barckholtz, C., Barckholtz, T. A., and Hadad, C. M. (1999). Ch and nh bond dissociation energies of small aromatic hydrocarbons. *Journal of the American Chemical Society*, 121(3):491–500.
- [4] Barron, A. R. (2014). Physical methods in chemistry and nano science. [Accessed 19 September 2014]. Available from: <http://cnx.org/contents/ba27839d-5042-4a40-afcf-c0e6e39fb454@18.3@18.3>.
- [5] Bass, M., DeCusatis, C., Enoch, J., Lakshminarayanan, V., Li, G., MacDonald, C., Mahajan, V., and Van Stryland, E. (2009). *Handbook of Optics, Third Edition Volume IV: Optical Properties of Materials, Nonlinear Optics, Quantum Optics*. McGraw-Hill Professional.
- [6] Baum, P., Lochbrunner, S., Krok, P., Breuer, M., and Riedle, E. (2014). NOPA - overview and principles [online]. [Accessed 30 May 2014]. Available from: http://www.bmo.physik.uni-muenchen.de/~wwwriedle/projects/NOPA_overview/NOPA_overview.php.
- [7] Becke, A. D. (1993). Densityfunctional thermochemistry. iii. the role of exact exchange. *The Journal of Chemical Physics*, 98(7):5648–5652.
- [8] Berera, R., van Grondelle, R., and Kennis, J. T. (2009). Ultrafast transient absorption spectroscopy: principles and application to photosynthetic systems. *Photosynth Res*, 101(2-3):105–18. Berera, Rudi van Grondelle, Rienk Kennis, John T M Netherlands Photosynth Res. 2009 Aug-Sep;101(2-3):105-18. Epub 2009 Jul 4.
- [9] Berger, M., Goldblatt, I. L., and Steel, C. (1973). Photochemistry of benzaldehyde. *Journal of the American Chemical Society*, 95(6):1717–1725.
- [10] Berger, M. and Steel, C. (1975). Photochemical and photophysical processes in acetophenone. *Journal of the American Chemical Society*, 97(17):4817–4821.

- [11] Booth, M. (2014). *Synthesis and Characterization of CuInS₂ Quantum Dots*. PhD thesis, University of Leeds.
- [12] Booth, M., Brown, A. P., Evans, S. D., and Critchley, K. (2012). Determining the concentration of CuInS₂ quantum dots from the size-dependent molar extinction coefficient. *Chemistry of Materials*, 24(11):2064–2070.
- [13] Born, M. and Oppenheimer, R. (1927). Zur quantentheorie der molekeln. *Annalen der Physik*, 389(20):457–484.
- [14] Breen, P. J., Bernstein, E. R., and Seeman, J. I. (1987). Supersonic molecular jet spectroscopy of ethylbenzene, the ethyltoluenes, and the diethylbenzenes. *J. Chem. Phys.*, 87(6):3269.
- [15] Brom, A. J. v. d., Kapelios, M., Kitsopoulos, T. N., Nahler, N. H., Cronin, B., and Ashfold, M. N. R. (2005). Photodissociation and photoionization of pyrrole following the multiphoton excitation at 243 and 364.7 nm. *Phys. Chem. Chem. Phys.*, 7:892–899.
- [16] Brouard, M. and Vallance, C., editors (2012). *Tutorials in Molecular Reaction Dynamics*. The Royal Society of Chemistry.
- [17] Cadirci, M., Masala, O., Pickett, N., and Binks, D. (2014). Ultrafast charge dynamics in CuInS₂ nanocrystal quantum dots. *Chemical Physics*, 438(0):60 – 65.
- [18] Castro, S. L., Bailey, S. G., Raffaele, R. P., Banger, K. K., and Hepp, A. F. (2004). Synthesis and characterization of colloidal CuInS₂ nanoparticles from a molecular single-source precursor. *The Journal of Physical Chemistry B*, 108(33):12429–12435.
- [19] Chen, B. K., Zhong, H. Z., Zhang, W. Q., Tan, Z. A., Li, Y. F., Yu, C. R., Zhai, T. Y., Bando, Y. S., Yang, S. Y., and Zou, B. S. (2012a). Highly emissive and color-tunable CuInS₂-based colloidal semiconductor nanocrystals: Off-stoichiometry effects and improved electroluminescence performance. *Adv. Funct. Mater.*, 22(10):2081–2088. 942LT Times Cited:15 Cited References Count:60.
- [20] Chen, H., Wang, C.-Y., Wang, J.-T., Hu, X.-P., and Zhou, S.-X. (2012b). First-principles study of point defects in solar cell semiconductor CuInS₂. *J. Appl. Phys.*, 112(8):084513.
- [21] Cook, P. (2001). *Photofragment translational spectroscopy of selected hydride molecules*. Thesis, University of Bristol.
- [22] Cronin, B., Nix, M. G., Devine, A. L., Dixon, R. N., and Ashfold, M. N. (2006). High resolution photofragment translational spectroscopy studies of the near ultraviolet photolysis of 2,5-dimethylpyrrole. *Phys Chem Chem Phys*, 8(5):599–612. Cronin, Brid Nix, Michael G D Devine, Adam L Dixon, Richard N Ashfold, Michael N R England *Phys Chem Chem Phys*. 2006 Feb 7;8(5):599-612. Epub 2005 Nov 23.
- [23] Cronin, B., Nix, M. G. D., Qadiri, R. H., and Ashfold, M. N. R. (2004). High resolution photofragment translational spectroscopy studies of the near ultraviolet photolysis of pyrrole. *Physical Chemistry Chemical Physics*, 6(21):5031–5041.

- [24] Cui, G., Lu, Y., and Thiel, W. (2012). Electronic excitation energies, three-state intersections, and photodissociation mechanisms of benzaldehyde and acetophenone. *Chemical Physics Letters*, 537(0):21–26.
- [25] DeLong, K. W., Trebino, R., Hunter, J., and White, W. E. (1994). Frequency-resolved optical gating with the use of second-harmonic generation. *J. Opt. Soc. Am. B*, 11(11):2206–2215.
- [26] Dunning, T. H. (1989). Gaussian basis sets for use in correlated molecular calculations. i. the atoms boron through neon and hydrogen. *The Journal of Chemical Physics*, 90(2):1007–1023.
- [27] El-Sayed, M. A. (1968). Triplet state. its radiative and nonradiative properties. *Accounts of Chemical Research*, 1(1):8–16.
- [28] Elkins, M. H., Williams, H. L., and Neumark, D. M. (2015). Dynamics of electron solvation in methanol: Excited state relaxation and generation by charge-transfer-to-solvent. *J. Chem. Phys.*, 142(23):234501.
- [29] European Commission (2000). Communication from the commission on the precautionary principle. [Accessed 19 September 2014]. Available from: http://ec.europa.eu/dgs/health_consumer/library/pub/pub07_en.pdf. COM(2000) 1.
- [30] Fang, W. and Phillips, D. (2002). The crucial role of the s1/t2/t1 intersection in the relaxation dynamics of aromatic carbonyl compounds upon n→* excitation. *Chemphyschem : a European journal of chemical physics and physical chemistry*, 10:889.
- [31] Fang, W.-H. (2008). Ab initio determination of dark structures in radiationless transitions for aromatic carbonyl compounds. *Accounts of Chemical Research*, 41(3):452–457.
- [32] Fischer, H. and Gleim, W. (1936). Synthese des porphins. *Justus Liebigs Annalen der Chemie*, 521(1):157–160.
- [Frisch et al.] Frisch, M. J., Trucks, G. W., Schlegel, H. B., Scuseria, G. E., Robb, M. A., Cheeseman, J. R., Scalmani, G., Barone, V., Mennucci, B., Petersson, G. A., Nakatsuji, H., Caricato, M., Li, X., Hratchian, H. P., Izmaylov, A. F., Bloino, J., Zheng, G., Sonnenberg, J. L., Hada, M., Ehara, M., Toyota, K., Fukuda, R., Hasegawa, J., Ishida, M., Nakajima, T., Honda, Y., Kitao, O., Nakai, H., Vreven, T., Montgomery, Jr., J. A., Peralta, J. E., Ogliaro, F., Bearpark, M., Heyd, J. J., Brothers, E., Kudin, K. N., Staroverov, V. N., Kobayashi, R., Normand, J., Raghavachari, K., Rendell, A., Burant, J. C., Iyengar, S. S., Tomasi, J., Cossi, M., Rega, N., Millam, J. M., Klene, M., Knox, J. E., Cross, J. B., Bakken, V., Adamo, C., Jaramillo, J., Gomperts, R., Stratmann, R. E., Yazyev, O., Austin, A. J., Cammi, R., Pomelli, C., Ochterski, J. W., Martin, R. L., Morokuma, K., Zakrzewski, V. G., Voth, G. A., Salvador, P., Dannenberg, J. J., Dapprich, S., Daniels, A. D., Farkas, ., Foresman, J. B., Ortiz, J. V., Cioslowski, J., and Fox, D. J. Gaussian09 Revision D.01. Gaussian Inc. Wallingford CT 2009.
- [34] Giuliano, B. M., Reva, I., and Fausto, R. (2010). Infrared spectra and photochemistry of matrix-isolated pyrrole-2-carbaldehyde. *The Journal of Physical Chemistry A*, 114(7):2506–2517.

- [35] Goossens, A. and Hofhuis, J. (2008). Spray-deposited cuins2 solar cells. *Nanotechnology*, 19(42):424018. Goossens, Albert Hofhuis, Joris England Nanotechnology. 2008 Oct 22;19(42):424018. doi: 10.1088/0957-4484/19/42/424018. Epub 2008 Sep 25.
- [36] Gumy, J.-C. (2000). *Developments and applications of four wave mixing spectroscopies in the picosecond and femtosecond time regimes*. PhD thesis, Université de Fribourg.
- [37] Hirata, Y. and Lim, E. C. (1980). Nonradiative electronic relaxation of gas phase aromatic carbonyl compounds: Benzaldehyde. *The Journal of Chemical Physics*, 72(10):5505–5510.
- [38] Hirata, Y. and Mataga, N. (1991). Solvation dynamics of electron ejected by photoionization of p-phenylenediamine in several alcohols: temperature effect studied by picosecond transient absorption measurements. *J. Phys. Chem.*, 95(23):9067–9071.
- [39] Hirata, Y., Murata, N., Tanioka, Y., and Mataga, N. (1989). Dynamic behavior of solvated electrons produced by photoionization of indole and tryptophan in several polar solvents. *J. Phys. Chem.*, 93(11):4527–4530.
- [40] Hofhuis, J., Schoonman, J., and Goossens, A. (2008). Elucidation of the excited-state dynamics in cuins2 thin films. *J. Phys. Chem. C*, 112(38):15052–15059. 350HD Times Cited:10 Cited References Count:33.
- [41] Holmes, J. L. and Lossing, F. P. (1991). Ionization energies of homologous organic compounds and correlation with molecular size. *Organic Mass Spectrometry*, 26(6):537–541.
- [42] Holpár, P., Megyes, T., and Keszei, E. (1999). Electron solvation in methanol revisited. *Radiation Physics and Chemistry*, 55(5-6):573–577.
- [43] Horner, K. E. and Karadakov, P. B. (2013). Chemical bonding and aromaticity in furan, pyrrole, and thiophene: a magnetic shielding study. *J Org Chem*, 78(16):8037–43. Horner, Kate E Karadakov, Peter B J Org Chem. 2013 Aug 16;78(16):8037-43. doi: 10.1021/jo401319k. Epub 2013 Aug 1.
- [44] Hoshino, K., Gopal, A., Glaz, M. S., Vanden Bout, D. A., and Zhang, X. (2012). Nanoscale fluorescence imaging with quantum dot near-field electroluminescence. *Applied Physics Letters*, 101(4):043118.
- [45] Hsu, T. M. (1991). p-d hybridization of the valence bands of copper indium disulfide. *J. Appl. Phys.*, 69(6):3772–3774.
- [46] Huang, D. and Persson, C. (2012). Stability of the bandgap in cu-poor cuinse2. *J. Phys.: Condens. Matter*, 24(45):455503. Huang, Dan Persson, Clas England J Phys Condens Matter. 2012 Nov 14;24(45):455503. doi: 10.1088/0953-8984/24/45/455503. Epub 2012 Oct 23.
- [47] Huix-Rotllant, M., Siri, D., and Ferre, N. (2013). Theoretical study of the photochemical generation of triplet acetophenone. *Phys Chem Chem Phys*, 15(44):19293–300. Huix-Rotllant, Miquel Siri, Didier Ferre, Nicolas England Phys Chem Chem Phys. 2013 Oct 23;15(44):19293-300. doi: 10.1039/c3cp52703d.

- [48] Karsili, T. N., Marchetti, B., Moca, R., and Ashfold, M. N. (2013). Uv photodissociation of pyrroles; symmetry and substituent effects. *J Phys Chem A*. Karsili, Tolga N V Marchetti, Barbara Moca, Roberta Ashfold, Michael N R J Phys Chem A. 2013 Jun 28.
- [49] Kim, Y.-K., Ahn, S.-H., Chung, K., Cho, Y.-S., and Choi, C.-J. (2012). The photoluminescence of cuins2 nanocrystals: Effect of non-stoichiometry and surface modification. *J. Mater. Chem.*, 22(4):1516–1520.
- [50] Kirkby, O. M. (2015). *The role of pi sigma* states in the ultrafast non-radiative dynamics of pyrrole, aniline and phenol*. PhD thesis, University College London.
- [51] Klimov, V. I. (2000). Optical nonlinearities and ultrafast carrier dynamics in semiconductor nanocrystals. *J. Phys. Chem. B*, 104(26):6112–6123.
- [52] Klimov, V. I. (2003). Nanocrystal quantum dots - from fundamental photophysics to multicolor lasing. *LA Science*, 28:214–220.
- [53] Klimov, V. I., Mikhailovsky, A. A., McBranch, D. W., Leatherdale, C. A., and Bawendi, M. G. (2000). Quantization of multiparticle auger rates in semiconductor quantum dots. *Science*, 287(5455):1011–1013. Klimov VI Mikhailovsky McBranch Leatherdale Bawendi New York, N.Y. Science. 2000 Feb 11;287(5455):1011-3.
- [54] Koyanagi, M., Zwarich, R., and Goodman, L. (1971). Optical studies of the 3(n.*) magnetic sublevels in benzaldehyde. *Chemical Physics Letters*, 9(1):74–76.
- [55] Kraatz, I. T., Booth, M., Whitaker, B. J., Nix, M. G. D., and Critchley, K. (2014). Sub-bandgap emission and intraband defect-related excited-state dynamics in colloidal cuins 2 /zns quantum dots revealed by femtosecond pump–dump–probe spectroscopy. *The Journal of Physical Chemistry C*, 118(41):24102–24109.
- [56] Krustok, J., Schön, J. H., Collan, H., Yakushev, M., Mädasson, J., and Bucher, E. (1999). Origin of the deep center photoluminescence in cugase2 and cuins2 crystals. *Journal of Applied Physics*, 86(1):364–369.
- [57] Kuno, M. K. (1998). *Band edge spectroscopy of CdSe quantum dots*. PhD thesis, Massachusetts Institute of Technology.
- [58] Kuo, K. T., Chen, S. Y., Cheng, B. M., and Lin, C. C. (2008). Synthesis and characterization of highly luminescent cuins2 and cuins2/zns (core/shell) nanocrystals. *Thin Solid Films*, 517(3):1257–1261. 388XO Times Cited:10 Cited References Count:27.
- [59] Le Ru, E. and Etchegoin, P. (2008). *Principles of Surface-Enhanced Raman Spectroscopy: and related plasmonic effects*. ELSEVIER.
- [60] Lee, S.-H., Tang, K.-C., Chen, I.-C., Schmitt, M., Shaffer, J. P., Schultz, T., Underwood, J. G., Zgierski, M. Z., and Stolow, A. (2002). Substituent effects in molecular electronic relaxation dynamics via time-resolved photoelectron spectroscopy: * states in benzenes. *The Journal of Physical Chemistry A*, 106(39):8979–8991.
- [61] Li, J., Zhang, F., and Fang, W.-H. (2005). Probing photophysical and photochemical processes of benzoic acid from ab initio calculations. *The Journal of Physical Chemistry A*, 109(34):7718–7724.

- [62] Li, L., Daou, T. J., Texier, I., Tran, T. K. C., Nguyen, Q. L., and Reiss, P. (2009). Highly luminescent Cu₂/ZnS core/shell nanocrystals: Cadmium-free quantum dots for in vivo imaging. *Chem. Mater.*, 21(12):2422–2429. 458UE Times Cited:119 Cited References Count:52.
- [63] Li, L., Pandey, A., Werder, D. J., Khanal, B. P., Pietryga, J. M., and Klimov, V. I. (2011). Efficient synthesis of highly luminescent copper indium sulfide-based core/shell nanocrystals with surprisingly long-lived emission. *J. Am. Chem. Soc.*, 133(5):1176–1179. Li, Liang Pandey, Anshu Werder, Donald J Khanal, Bishnu P Pietryga, Jeffrey M Klimov, Victor I J Am Chem Soc. 2011 Feb 9;133(5):1176-9. doi: 10.1021/ja108261h. Epub 2011 Jan 5.
- [64] Linda, P., Marino, G., and Pignataro, S. (1971). A comparison of sensitivities to substituent effects of five-membered heteroaromatic rings in gas phase ionization. *J. Chem. Soc., B.*, page 1585.
- [65] Lippert, H., Ritze, H.-H., Hertel, I. V., and Radloff, W. (2004). Femtosecond time-resolved hydrogen-atom elimination from photoexcited pyrrole molecules. *ChemPhysChem*, 5(9):1423–1427.
- [66] Liu, B., Zhu, J., Wang, B., Wang, Y., and Wang, L. (2009). Time-resolved dynamics of NO₂ in its conical intersection region. *J Phys Chem A*, 113(50):13839–44. Liu, Benkang Zhu, Jingyi Wang, Bingxing Wang, Yanqiu Wang, Li J Phys Chem A. 2009 Dec 17;113(50):13839-44.
- [67] Liu, J.-m. (2005). *Photonic Devices*. Cambridge University Press.
- [68] Liu, W., Han, F., Smith, C., and Fang, C. (2012). Ultrafast conformational dynamics of pyranine during excited state proton transfer in aqueous solution revealed by femtosecond stimulated raman spectroscopy. *J Phys Chem B*. Liu, Weimin Han, Fanyuan Smith, Connor Fang, Chong J Phys Chem B. 2012 Jun 19.
- [69] Makhov, D. V., Saita, K., Martinez, T. J., and Shalashilin, D. V. (2015). Ab initio multiple cloning simulations of pyrrole photodissociation: Tker spectra and velocity map imaging. *Phys. Chem. Chem. Phys.*, 17(5):3316–3325.
- [70] Marstokk, K.-M. and Mollendal, H. (1974). Microwave spectrum, conformation, intramolecular hydrogen bond, and dipole moment of pyrrole-2-carboxaldehyde. *Journal of Molecular Structure*, 23(1):93 – 101.
- [71] McCamant, D. W., Kukura, P., and Mathies, R. A. (2003). Femtosecond time-resolved stimulated raman spectroscopy: Application to the ultrafast internal conversion in beta-carotene. *J Phys Chem A*, 107(40):8208–14. McCamant, David W Kukura, Philipp Mathies, Richard A R01 EY002051-27/EY/NEI NIH HHS/ R01 EY002051-27/NEI NIH HHS/ J Phys Chem A. 2003 Oct 9;107(40):8208-14.
- [72] Merz, T., Wenninger, M., Weinberger, M., Riedle, E., Wagenknecht, H.-A., and Schütz, M. (2013). Conformational control of benzophenone-sensitized charge transfer in dinucleotides. *Physical Chemistry Chemical Physics*, 15(42):18607.
- [73] Miyasaka, H., Masuhara, H., and Mataga, N. (1983). Picosecond 266 nm photolysis of neat liquids: Solvated electron formation in water and alcohols. *Chemical Physics Letters*, 98(3):277–281.

- [74] Monmayrant, A., Weber, S., and Chatel, B. (2010). A newcomer's guide to ultra-short pulse shaping and characterization. *Journal of Physics B: Atomic, Molecular and Optical Physics*, 43(10):103001–103001.
- [75] Montero, R., Ovejas, V., Fernández-Fernández, M., Peralta Conde, I., and Longarte, A. (2014). Revisiting the relaxation dynamics of isolated pyrrole. *J. Chem. Phys.*, 141(1):014303.
- [76] Montero, R., Peralta Conde, A., Ovejas, V., Fernandez-Fernandez, M., Castano, F., Vazquez de Aldana, J. R., and Longarte, A. (2012). Femtosecond evolution of the pyrrole molecule excited in the near part of its UV spectrum. *J. Chem. Phys.*, 137(6):064317.
- [77] Nam, D. E., Song, W. S., and Yang, H. (2011). Noninjection, one-pot synthesis of cu-deficient cuins2/zns core/shell quantum dots and their fluorescent properties. *J. Colloid Interface Sci.*, 361(2):491–496. Nam, Da-Eun Song, Woo-Seuk Yang, Heesun J Colloid Interface Sci. 2011 Sep 15;361(2):491-6. doi: 10.1016/j.jcis.2011.05.058. Epub 2011 May 24.
- [78] Nanu, M., Boulch, F., Schoonman, J., and Goossens, A. (2005). Deep-level transient spectroscopy of tio2cuins2 heterojunctions. *Appl. Phys. Lett.*, 87(24):242103.
- [79] Nibbering, E. T. J., Fidler, H., and Pines, E. (2005). Ultrafast chemistry: using time-resolved vibrational spectroscopy for interrogation of structural dynamics. *Annual review of physical chemistry*, 56(1):337–67.
- [80] Nix, M. G. D. (2007). *UV Photoinduced H Atom Loss Dynamics in Heteroaromatic Biomolecular Prototypes*. PhD thesis, University of Bristol.
- [81] Nix, M. G. D., Devine, A. L., Cronin, B., and Ashfold, M. N. R. (2007). Ultraviolet photolysis of adenine: Dissociation via the [sup 1][sup. *The Journal of Chemical Physics*, 126(12):124312.
- [82] Ohmori, N., Suzuki, T., and Ito, M. (1988). Why does intersystem crossing occur in isolated molecules of benzaldehyde, acetophenone, and benzophenone? *The Journal of Physical Chemistry*, 92(5):1086–1093.
- [83] Oliver, T. A., Zhang, Y., Ashfold, M. N., and Bradforth, S. E. (2011). Linking photochemistry in the gas and solution phase: S-h bond fission in p-methylthiophenol following uv photoexcitation. *Faraday Discuss*, 150:439–58; discussion 505–32. Oliver, Thomas A A Zhang, Yuyuan Ashfold, Michael N R Bradforth, Stephen E England Faraday Discuss. 2011;150:439-58; discussion 505-32.
- [84] Oliver, T. A. A., Zhang, Y., Roy, A., Ashfold, M. N. R., and Bradforth, S. E. (2015). Exploring autoionization and photoinduced proton-coupled electron transfer pathways of phenol in aqueous solution. *The Journal of Physical Chemistry Letters*, 6(20):4159–4164.
- [85] Omata, T., Nose, K., Kurimoto, K., and Kita, M. (2014). Electronic transition responsible for size-dependent photoluminescence of colloidal cuins2 quantum dots. *J. Mater. Chem. C*, 2(33):6867–6872.

- [86] Omata, T., Nose, K., and Otsuka-Yao-Matsuo, S. (2009). Size dependent optical band gap of ternary i-iii-vi₂ semiconductor nanocrystals. *J. Appl. Phys.*, 105(7):073106–5.
- [87] Ou, Q. and Subotnik, J. E. (2013). Electronic relaxation in benzaldehyde evaluated via td-dft and localized diabaticization: Intersystem crossings, conical intersections, and phosphorescence. *The Journal of Physical Chemistry C*, 117(39):19839–19849.
- [88] Palmer, M. H., Walker, I. C., and Guest, M. F. (1998). The electronic states of pyrrole studied by optical (vuv) absorption, near-threshold electron energy-loss (eel) spectroscopy and ab initio multi-reference configuration interaction calculations. *Chemical Physics*, 238(2):179–199.
- [89] Park, S. T., Feenstra, J. S., and Zewail, A. H. (2006). Ultrafast electron diffraction: excited state structures and chemistries of aromatic carbonyls. *J Chem Phys*, 124(17):174707. Park, Sang Tae Feenstra, Jonathan S Zewail, Ahmed H J Chem Phys. 2006 May 7;124(17):174707.
- [90] Paschotta, R. (2012). Encyclopedia of laser physics and technology - frequency-resolved optical gating.
- [91] Prabakar, K., Seo, H., Son, M., and Kim, H. (2009). Cds quantum dots sensitized tio₂ photoelectrodes. *Materials Chemistry and Physics*, 117(1):26 – 28.
- [92] Pretzler, G., Kasper, A., and Witte, K. (2000). Angular chirp and tilted light pulses in cpa lasers. 70(1):1–9.
- [93] Rath, S. and Sahu, S. N. (2006). Electronic structure of hgte nanocrystals: An observation of p–d weakening. *Surface Science*, 600(9):L110–L115.
- [94] Rice, C. A., Dauster, I., and Suhm, M. A. (2007). Infrared spectroscopy of pyrrole-2-carboxaldehyde and its dimer: a planar beta-sheet peptide model? *J Chem Phys*, 126(13):134313. Rice, Corey A Dauster, Ingo Suhm, Martin A J Chem Phys. 2007 Apr 7;126(13):134313.
- [95] Roberts, G. M., Marroux, H., Grubb, M. P., Ashfold, M. N., and Orr-Ewing, A. J. (2014). On the participation of photo-induced n–h bond fission in aqueous adenine at 266 and 220 nm: A combined ultrafast transient electronic and vibrational absorption spectroscopy study. *The Journal of Physical Chemistry A*, page 141008135923005.
- [96] Roberts, G. M., Williams, C. A., Yu, H., Chatterley, A. S., Young, J. D., Ullrich, S., and Stavros, V. G. (2013). Probing ultrafast dynamics in photoexcited pyrrole: timescales for pi sigma* mediated h-atom elimination. *Faraday Discuss*, 163:95–116; discussion 117–38. Roberts, Gareth M Williams, Craig A Yu, Hui Chatterley, Adam S Young, Jamie D Ullrich, Susanne Stavros, Vasilios G England Faraday Discuss. 2013;163:95-116; discussion 117-38.
- [97] Roos, B. O., Malmqvist, P.-k., Molina, V., Serrano-Andres, L., and Merchan, M. (2002). Theoretical characterization of the lowest-energy absorption band of pyrrole. *J. Chem. Phys.*, 116(17):7526.

- [98] Saita, K., Nix, M. G. D., and Shalashilin, D. V. (2013). Simulation of ultrafast photodynamics of pyrrole with a multiconfigurational ehrenfest method. *Phys. Chem. Chem. Phys.*, 15:16227–16235.
- [99] Scheidt, T. and Laenen, R. (2003). Ionization of methanol: monitoring the trapping of electrons on the fs time scale. *Chemical Physics Letters*, 371(3-4):445–450.
- [100] Sewall, S. L., Cooney, R. R., Anderson, K. E. H., Dias, E. A., Sagar, D. M., and Kambhampati, P. (2008). State-resolved studies of biexcitons and surface trapping dynamics in semiconductor quantum dots. *J. Chem. Phys.*, 129(8):084701. Sewall, Samuel L Cooney, Ryan R Anderson, Kevin E H Dias, Eva A Sagar, D M Kambhampati, Patanjali J Chem Phys. 2008 Aug 28;129(8):084701. doi: 10.1063/1.2971181.
- [101] Shaislamov, U., Kim, H., and Yang, B. L. (2013). Cds-sensitized tio2 photoelectrodes for quantum dots-based solar cells. *Journal of Materials Research*, 28:497–501.
- [102] Sobolewski, A. L., Domcke, W., Dedonder-Lardeux, C., and Jouvet, C. (2002). Excited-state hydrogen detachment and hydrogen transfer driven by repulsive 1* states: A new paradigm for nonradiative decay in aromatic biomolecules. *Physical Chemistry Chemical Physics*, 4(7):1093–1100.
- [103] Sun, J., Zhu, D., Zhao, J., Ikezawa, M., Wang, X., and Masumoto, Y. (2014). Ultrafast carrier dynamics in cuins2 quantum dots. *Appl. Phys. Lett.*, 104(2):023118.
- [104] Thaller, A., Laenen, R., and Laubereau, A. (2004). Femtosecond spectroscopy of the hydrated electron: novel features in the infrared. *Chemical Physics Letters*, 398(4-6):459–465.
- [105] Thaller, A., Laenen, R., and Laubereau, A. (2006). The precursors of the solvated electron in methanol studied by femtosecond pump-repump-probe spectroscopy. *J. Chem. Phys.*, 124(2):024515.
- [106] Toigawa, T., Gohdo, M., Norizawa, K., Kondoh, T., Kan, K., Yang, J., and Yoshida, Y. (2016). Examination of the formation process of pre-solvated and solvated electron in n-alcohol using femtosecond pulse radiolysis. *Radiation Physics and Chemistry*, 123:73–78.
- [107] Träger, F. (2012). Springer handbook of lasers and optics.
- [108] Tran, T. K. C., Le, Q. P., Nguyen, Q. L., Li, L., and Reiss, P. (2010). Time-resolved photoluminescence study of cuins2/zns nanocrystals. *Adv. Nat. Sci.: Nanosci. Nanotechnol.*, 1(2):025007.
- [109] Trebino, R. (2000). *Frequency-Resolved Optical Gating: The Measurement of Ultrashort Laser Pulses*. Kluwer Academic Publishers, Boston, Dordrecht, London.
- [110] Tyagi, P. and Kambhampati, P. (2011). False multiple exciton recombination and multiple exciton generation signals in semiconductor quantum dots arise from surface charge trapping. *J. Chem. Phys.*, 134(9):094706–10.

- [111] Vallet, V., Lan, Z., Mahapatra, S., Sobolewski, A. L., and Domcke, W. (2005). Photochemistry of pyrrole: Time-dependent quantum wave-packet description of the dynamics at the [sup 1][sup. *The Journal of Chemical Physics*, 123(14):144307.
- [112] Walhout, P. K., Alfano, J. C., Kimura, Y., Silva, C., Reid, P. J., and Barbara, P. F. (1995). Direct pump/probe spectroscopy of the near-IR band of the solvated electron in alcohols. *Chemical Physics Letters*, 232(1-2):135–140.
- [113] Wang, Y., Crawford, M., McAuliffe, M., and Eisinger, K. (1980). Picosecond laser studies of electron solvation in alcohols. *Chemical Physics Letters*, 74(1):160–165.
- [114] Wei, J., Kuczmann, A., Riedel, J., Renth, F., and Temps, F. (2002). Photofragment velocity map imaging of h atom elimination in the first excited state of pyrrole. *Physical Chemistry Chemical Physics*, 5(2):315–320.
- [115] Wei, J., Riedel, J., Kuczmann, A., Renth, F., and Temps, F. (2004). Photodissociation dynamics of pyrrole: Evidence for mode specific dynamics from conical intersections. *Faraday Discussions*, 127:267.
- [116] Werner, H.-J., Knowles, P. J., Knizia, G., Manby, F. R., Schütz, M., Celani, P., Korona, T., Lindh, R., Mitrushenkov, A., Rauhut, G., Shamasundar, K. R., Adler, T. B., Amos, R. D., Bernhardsson, A., Berning, A., Cooper, D. L., Deegan, M. J. O., Dobbyn, A. J., Eckert, F., Goll, E., Hampel, C., Hesselmann, A., Hetzer, G., Hrenar, T., Jansen, G., Köppl, C., Liu, Y., Lloyd, A. W., Mata, R. A., May, A. J., McNicholas, S. J., Meyer, W., Mura, M. E., Nicklass, A., O'Neill, D. P., Palmieri, P., Pflüger, K., Pitzer, R., Reiher, M., Shiozaki, T., Stoll, H., Stone, A. J., Tarroni, R., Thorsteinsson, T., Wang, M., and Wolf, A. (2010). Molpro, version 2010.1, a package of ab initio programs. see <http://www.molpro.net>.
- [117] Wollenhaupt, M., Assion, A., and Baumert, T. (2007). *Femtosecond Laser Pulses: Linear Properties, Manipulation, Generation and Measurement*, volume 49, pages 937–983. Springer, New York.
- [118] Wright, J. T. and Meulenbergh, R. W. (2012). Modification of the conduction band edge energy via hybridization in quantum dots. *Appl. Phys. Lett.*, 101(19):193104.
- [119] Wu, G., Neville, S. P., Schalk, O., Sekikawa, T., Ashfold, M. N. R., Worth, G. A., and Stolow, A. (2015). Excited state non-adiabatic dynamics of pyrrole: A time-resolved photoelectron spectroscopy and quantum dynamics study. *J. Chem. Phys.*, 142(7):074302.
- [120] Yoodie, K., Woolley, J. C., and Sa-yakanit, V. (1984). Effects of p-d hybridization on the valence band of i-iii-vi₂ chalcopyrite semiconductors. *Phys. Rev. B: Condens. Matter Mater. Phys.*, 30(10):5904–5915. PRB.
- [121] Yoshizawa, M. and Kurosawa, M. (1999). Femtosecond time-resolved raman spectroscopy using stimulated raman scattering. *Physical Review A*, 61(1):1–6.
- [122] Zhao, H., Farah, A., Morel, D., and Ferekides, C. (2009). The effect of impurities on the doping and {VOC} of cdte/cds thin film solar cells. *Thin Solid Films*, 517(7):2365 – 2369. Thin Film Chalogenide Photovoltaic Materials (EMRS, Symposium L).

- [123] Zhong, H., Lo, S. S., Mirkovic, T., Li, Y., Ding, Y., Li, Y., and Scholes, G. D. (2010). Noninjection gram-scale synthesis of monodisperse pyramidal CuInS₂ nanocrystals and their size-dependent properties. *ACS Nano*, 4(9):5253–5262. Zhong, Haizheng Lo, Shun S Mirkovic, Tihana Li, Yunchao Ding, Yuqin Li, Yongfang Scholes, Gregory D ACS Nano. 2010 Sep 28;4(9):5253-62. doi: 10.1021/nn1015538.
- [124] Zhong, H. Z., Zhou, Y., Ye, M. F., He, Y. J., Ye, J. P., He, C., Yang, C. H., and Li, Y. F. (2008). Controlled synthesis and optical properties of colloidal ternary chalcogenide CuInS₂ nanocrystals. *Chem. Mater.*, 20(20):6434–6443. 363FY Times Cited:123 Cited References Count:80.

